Nanoscale Structures in Near-Equiatomic Fe-Ni Films and Particles

---

A Dissertation Presented to

the Faculty of the School of Engineering and Applied Science

University of Virginia

---

in partial fulfillment

of the requirements for the degree

Doctor of Philosophy

by

Qiyuan Lin

May

2022

APPROVAL SHEET

This

is submitted in partial fulfillment of the requirements
for the degree of

Author:

Advisor:

Advisor:

Committee Member:

Committee Member:

Committee Member:

Committee Member:

Committee Member:

Committee Member:

Accepted for the School of Engineering and Applied Science:

Jennifer L. West, School of Engineering and Applied Science

Table of Contents

Acknowledgement

I would like to acknowledge my advisor Prof. Giovanni Zangari, for accepting me as one of his students, and for his constant support and encouragement over the entire course of my PhD study. I would like to acknowledge all the professors on my committee, including Prof. James M. Howe, Prof. Leonid V. Zhigilei, Prof. Jerrold A. Floro, and Prof. Joshua J. Choi. I appreciate the time and efforts they spent on helping me to make progress on my PhD study. I would like to thank all the professors who had taught me in one or more of their classes, including Prof. Jerrold A. Floro, Prof. Elizabeth J. Opila, Prof. Gary J. Shiflet, Prof. Sean R. Agnew, Prof. Giovanni Zangari, Prof. William Soffa, Prof. Petra Reinke, Prof. Leonid V. Zhigilei, Prof. James M. Howe, and Prof. Keivan Esfarjani. I would like to thank the entire NMCF staff, including Prof. James M. Howe, Richard White, Diane Dickie, Catherine Dukes, Helge Heinrich, and Joe Thompson, for helping and training me to perform the material characterizations I need to make progress during my PhD study. I would like to thank the current staff of the MSE department, including Tanner R. Fitzgerald, Sherri Sullivan, Jerry Weaver, and Bryana Amador, as well as the former staff, including Barry Baber, Kimberly Fitzhugh-Higgins, and Kari Werres.

I thank Eric Hoglund for helping me with the S/TEM characterization and analyses. I thank Prof. James Fitz-Gerald and Jonathan Skelton for helping me with the laser irradiation and the vacuum annealing. I thank Luke Daemen and Yongqiang Cheng for helping me to perform the NVS characterization and analyses at Oak Ridge National Laboratory. I thank Prof. Filippo Mangolini, Robert R. Chrostowski, and Zixuan Li for helping me to perform the AFM characterization and

the PSD analyses at the University of Texas at Austin. I thank Prof. Bilal Gökce, Ruksan Nadarajah, and Inna Yusnila Khairani for helping me to perform PLAL and prepare the Fe-Ni nanoparticles at the University of Duisburg-Essen and the University of Wuppertal. I thank Anna Semisalova for helping me to perform the PPMS characterization at the University of Duisburg-Essen. I thank Evguenia Karapetrova for helping me to perform the SXRD characterization at Argonne National Laboratory. I thank Hao Huang and Chaobo Chen for providing computational insights to my study of the Fe-Ni nanoparticles from PLAL. I thank Prof. Mool C. Gupta and R. Elisa Pantoja for helping with the laser processing, and Caixia Bu for helping with the SIMS characterization and analyses. I thank Parasmani Rajput for helping me to perform the XAFS and the XANES characterization and analyses at the Bhabha Atomic Research Centre.

I also appreciate the help and support from my current and former colleagues in Prof. Zangari's research group, including Yin Xu, Ahmed Rasin, Begum Unveroglu Abdioglu, Jae Kim, Yunkai Sun, Amir Chamaani, Lee Kendall, Bilal Bawab, Paloma Boeck Souza, and Ali Akbari Sehat.

I am grateful to my parents, my wife, my friends for their love and support.

Last but not least, I acknowledge the financial support of the Basic Energy Sciences (BES) program award No. DE-SC0019191 from the Office of Science in U.S. Department of Energy (DOE).

List of Publications

1. **Q. Lin**, G. Zangari, "The Evolution of Composition and Morphology during the Initial Growth of Electrodeposited Ni-Fe Films: Comparison between the Potentiostatic Mode and the Pulse-Reverse Potential Mode" *Electrochimica Acta*, **2022**, 409: 139978.
2. **Q. Lin**, R. Nadarajah, E. Hoglund, J. M. Howe, B. Gökce, G. Zangari, "Towards Synthetic $L1_0$-FeNi: Detecting the Absence of Cubic Symmetry in Laser-Ablated Fe-Ni Nanoparticles" *Applied Surface Science*, **2021**, 150664.
3. Y. Xu, **Q. Lin**, R. Ahmed, G. Zangari, "Photoelectrochemical Oxidation Performance via a Protective, Catalytic Self-Limiting Ni-Co Alloys by Electrodeposition" *Electrochimica Acta*, **2021**, 382: 138305.
4. Y. Xu, R. Ahmed, J. Zheng, E. R. Hoglund, **Q. Lin**, E. Berretti, A. Lavacchi, G. Zangari, "Photoelectrochemistry of Self-Limiting Electrodeposition of Ni Film onto GaAs" *Small*, **2020**, 2003112.
5. **Q. Lin**, E. Hoglund, G. Zangari, "Electrodeposition of Fe-Ni alloy on Au(111) substrate: Metastable BCC growth via hydrogen evolution and interactions" *Electrochimica Acta*, **2020**, 338: 135876.
6. Y. Xu, R, Ahmed, **Q. Lin**, G. Zangari, "(Photo) Electrochemical Water Oxidation at Anodic TiO_2 Nanotubes Modified by Electrodeposited NiFe Oxy-hydroxides Catalysts" *Electrochimica Acta*, **2019**, 308: 91-98.
7. S. Ge, **Q. Lin***, S. Wodarz, S. Hashimoto, M. Kambe, T. Homma, G. Zangari, "Electrodeposition of Fe-Ni-Pt Alloy Films for Heat-Assisted Magnetic Recording Media: Synthesis, Structure and Magnetic Properties" *Electrochimica Acta*, **2019**, 302: 92-101.

8. R. Ahmed, **Q. Lin**, Y. Xu, G. Zangari, "Growth, Morphology and Crystal Structure of Electrodeposited Bi_2Se_3 Films: Influence of the Substrate" *Electrochimica Acta*, **2019**, 299: 654-662.

9. Y. Xu, **Q. Lin**, R. Ahmed, G. Zangari, "Synthesis of TiO_2-based Nanocomposites by Anodizing and Hydrogen Annealing for Efficient Photoelectrochemical Water Oxidation" *Journal of Power Sources*, **2019**, 410-411: 59-68.

10. Z. Hoffman, T. Gray, Y. Xu, **Q. Lin**, T. Gunnoe, G. Zangari, "High Selectivity Towards Formate Production by Electrochemical Reduction of Carbon Dioxide at Copper-Bismuth Dendrites" *ChemSusChem*, **2018**, 11: 1-10.

11. R. Ahmed, Y. Xu, M. Sales, **Q. Lin**, S. McDonnell, G. Zangari, "Synthesis and Material Properties of Bi_2Se_3 Nanostructures Deposited by SILAR" *The Journal of Physical Chemistry C*, **2018**, 122: 12052-12060.

* Q. Lin and S. Ge contributed equally to this paper.

Abstract

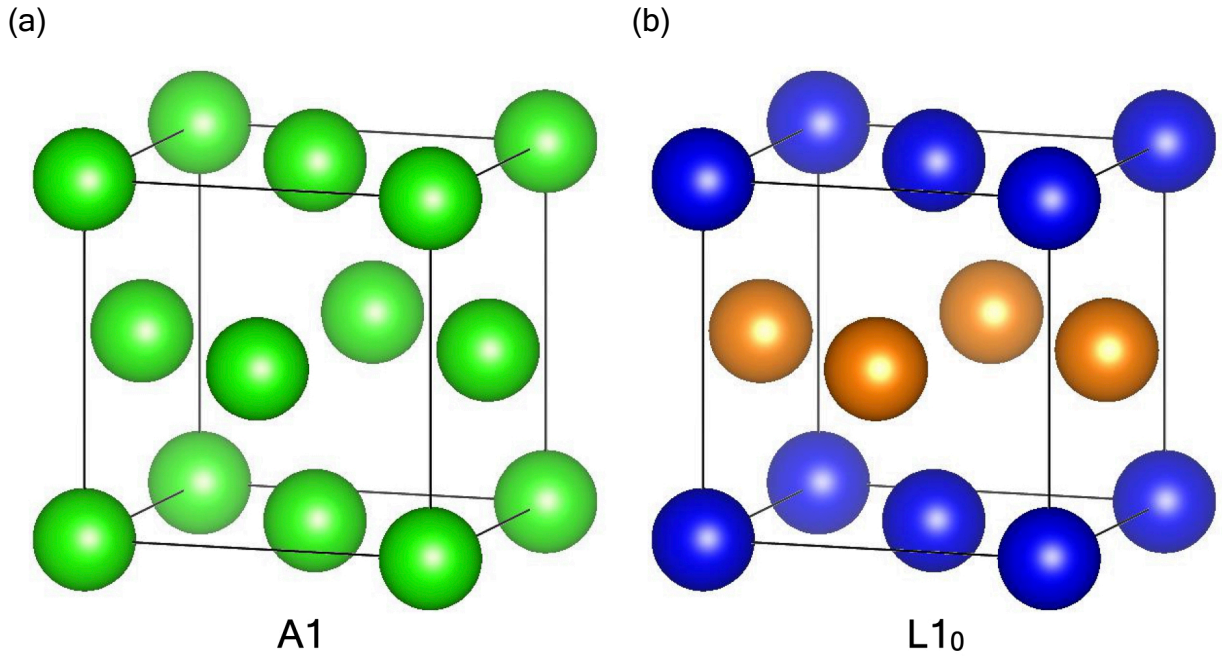

Figure 1.1. (a) The A1 crystal structure. **(b)** The $L1_0$ crystal structure. The VESTA 3 software [5] was used to draw the crystal structures.

The Fe-Ni binary system is ferromagnetic, electrically conductive, and displays a high dimensional stability in the composition range between 30 and 45 at.%Ni. The material is consisting of earth-abundant elements and continues to find applications in digital memory devices [1], precision instruments [2], and micro-electromechanical systems (MEMS) [2-4]. The Fe-Ni components being used in these applications are predominantly of the A1-type crystal structure, a chemically disordered crystal structure that belongs to the cubic system (**Figure 1.1a**). As a soft ferromagnet, A1 Fe-Ni are used for the linear control and sensing of magnetic fields, but they are not suitable for any of the permanent magnet applications, such as the traction

motors in electric or hybrid vehicles and the generators in wind turbines. However, the discovery of $L1_0$ Fe-Ni, a chemically ordered crystal structure that belongs to the tetragonal system (**Figure 1.1b**), first in high-flux neutron targets and later in meteorites, revealed a high first-order magnetocrystalline anisotropy constant on the order of 0.84 MJ/m^3 (i.e., 84 × 10^5 erg/cm^3) or higher, giving rise to the possibility of producing a permanent magnet based on a material system free of rare-earths and precious metals [6, 7].

The synthesis of $L1_0$ Fe-Ni has been a longstanding challenge. So far, the human-made synthesis of $L1_0$ Fe-Ni were only realized in the laboratories in the form of thin films, nanoprecipitates, or nanoparticles by a few methods that are far from viable for the production of bulk materials (i.e., phases that are well above 100 nm in all three dimensions) [8-13]. In order to synthesize $L1_0$ Fe-Ni, one has to circumvent the sluggish ordering kinetics and the limited thermodynamic driving force imposed by the low order-disorder temperature ($T_{OD,\ L10}$ ~ 320 ^{o}C) of the system [6]. A fundamental understanding of the relationship between the nanoscale structure and the synthesis condition may provide critical insights for one to implement a phase transformation landscape, at which the ordered phase can form within a timescale viable for bulk production.

The A1-to-$L1_0$ Fe-Ni chemical ordering phase transformation is a first-order phase transformation [14, 15]. Based on the thermodynamic and the kinetic parameters of the order-to-disorder phase transformation [16], the synthetic challenge of $L1_0$ Fe-Ni can be tackled from at least two directions: (1) increase the thermodynamic driving force of the ordering transformation; (2) decrease the kinetic barrier of the ordering transformation.

The thermodynamic driving force for the ordering transformation can be increased by replacing the A1 Fe-Ni phase with an initial phase that has a higher molar Gibbs free energy ($G_{initial}$) than that of the A1 Fe-Ni phase. A search for alternative metastable Fe-Ni phases with a near-equiatomic composition (i.e., 40 ~ 60 at.%Ni) is therefore of a significant importance for the synthesis of $L1_0$ Fe-Ni.

On the other hand, the ordering kinetics can be accelerated by lowering the activation barrier of lattice diffusion (E_L), which is a sum of both the vacancy formation energy (E_{Vf}) and the vacancy migration energy (E_{Vm}). In the neighborhood of a non-equilibrium crystal defect, such as a surface, a grain boundary, or a dislocation, the activation energy required for lattice diffusion is expected to be reduced, because the vacancy concentrations in the neighborhoods of these crystal defects are supposed to be higher than the equilibrium level. A nanoscale structure indicative of a high density of any of these non-equilibrium defects is therefore also of a significant importance for the synthesis of $L1_0$ Fe-Ni.

In this dissertation, the nanoscale structures of near-equiatomic Fe-Ni synthesized by different methods are investigated with an aim to provide insights for the synthesis of $L1_0$ Fe-Ni. Chapter 1 is an introduction. Chapter 2 - 4 are dedicated to the electrodeposition of Fe-Ni films. Chapter 2 investigated the conditions under the activation limit, during the deposition of which a metastable BCC phase was observed to form. Chapter 3 investigated the anomalous codeposition mechanism encountered under the activation limit, in order to understand the origin of the

through-thickness composition gradient. Chapter 4 investigated the conditions close to the mass transfer limit, during the deposition of which a high surface area growth front was observed to form. Chapter 5 and 6 are dedicated to two methods based on the use of pulsed laser. Chapter 5 investigated the structures arise from the pulsed laser irradiation of electrodeposited Fe-Ni films. It was demonstrated that the pulsed laser irradiation affects the crystallographic texture of the Fe-Ni films. Chapter 6 investigated the structures in the Fe-Ni nanoparticles synthesized by pulsed laser ablation in liquids. A nano-size metastable non-cubic phase and a high density of planar defects (either twins or stacking faults) were observed. The significances of these observations upon the synthesis of $L1_0$ Fe-Ni are discussed in the respective chapter.

Keywords: Fe-Ni, chemical ordering, crystal defects, electrodeposition, pulsed laser.

1 Introduction

1.1 Permanent Magnet Materials for Clean Energy Technologies

As the key component of two important types of clean energy technologies — electric vehicle and wind energy, the global demand for permanent magnet materials is projected to surge and may surpass the projected supply significantly in the next 10 ~ 30 years, considering that the estimated lifetimes of a typical electric car and wind turbine are 9 ~ 13 years and 25 ~ 35 years respectively [17]. The function of a permanent magnet is to provide an external magnetic field. The figure of merit that characterizes the performance of a permanent magnet material is the maximum energy product — $(BH)_{max}$ — defined as the maximum rectangular area in quadrant II within the *B*-*H* loop (**Figure 1.2a**), where *B* is called the magnetic flux density and *H* is called the magnetic field strength. The $(BH)_{max}$ should not be confounded with the maximum rectangular area in quadrant II within the *M*-*H* loop (**Figure 1.2b**), where *M* is called the magnetization. *B*, *H*, and *M* are related at every point in space any time by

$$B^{cgs} = H^{cgs} + 4\pi M^{cgs} \qquad \text{eq. 1.1}$$

if the cgs units are used, and by

$$B^{SI} = \mu_0 (H^{SI} + M^{SI}) \qquad \text{eq. 1.2}$$

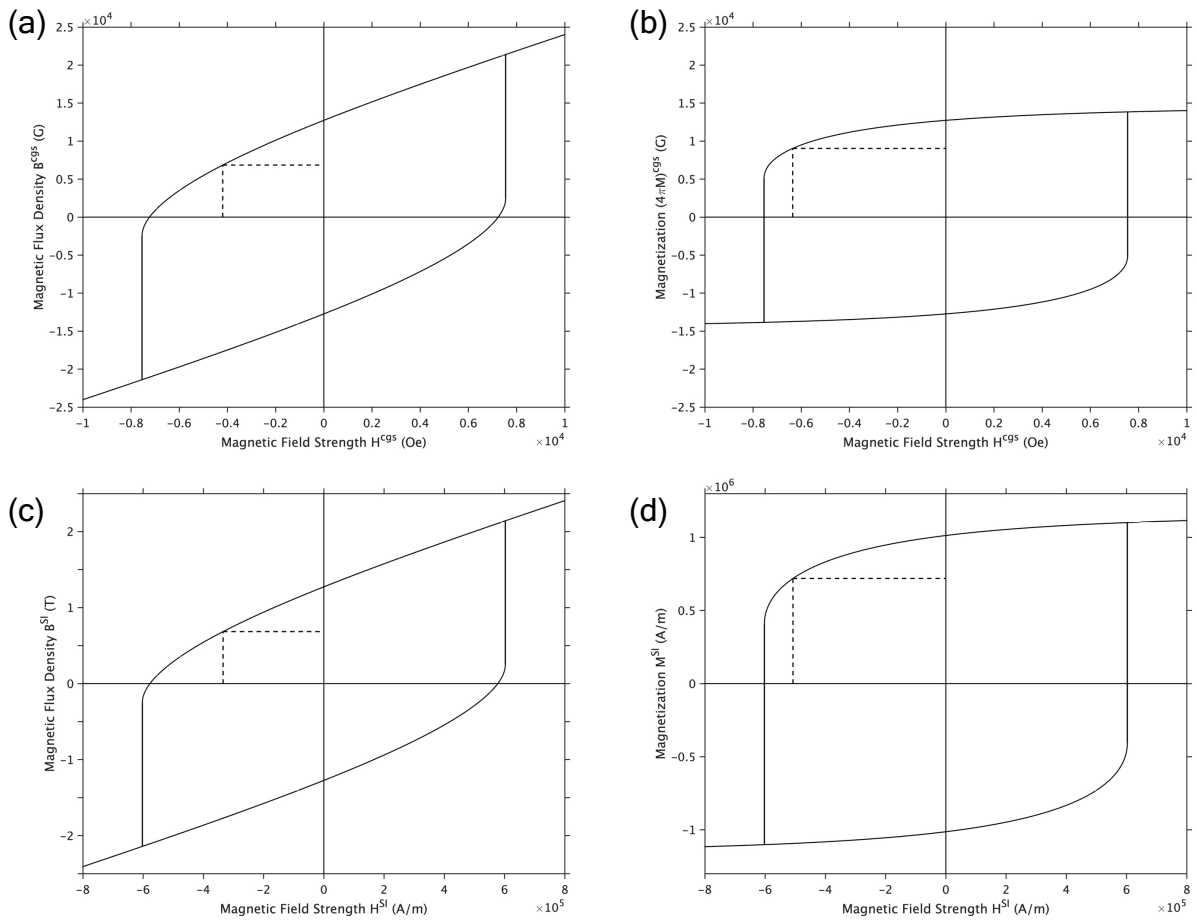

Figure 1.2. (a) The B-H loop in cgs units. **(b)** The M-H loop in cgs units. **(c)** The B-H loop in SI units. **(d)** The M-H loop in SI units. The dashed lines outline the largest box in quadrant II within each loop. The magnetization process of a single-domain particle is described here by following the approach developed by E. C. Stoner and E. P. Wohlfarth [18]. The single-domain particle was assumed to have a unique easy axis resulted from magnetocrystalline anisotropy. The first order magnetocrystalline anisotropy constant (K_1 = 0.84 MJ/m^3) and the saturation magnetization (M_s = 1.17 × 10^6 A/m) extracted from the $L1_0$ Fe-Ni phase in the NWA 6259 meteorite [7] were used. The angle between the magnetic field and the easy axis was arbitrarily chosen to be 30^o. The $(BH)_{max}$ of the particle was calculated to be 29 MGOe.

if the SI units are used, where μ_0 is the permeability of the free space. For clarification, **Figure 1.2a** and **Figure 1.2c** show a *B-H* loop in the cgs and the SI units respectively. **Figure 1.2b** and **Figure 1.2d** show the corresponding *M-H* loops in the two unit systems respectively. Based on

the **eq. 1.1** and **eq. 1.2** and a careful conversion between the two unit systems, one should be able to generate all the other loops from any one of the loops. All the equations in this dissertation are written in the SI units if not specified.

The $(BH)_{max}$ is limited by the remanent magnetic flux density — B_r — defined as the intercept of the *B*-*H* loop at the positive *B* direction, and by the coercive field — H_c — defined as the intercept of the *B*-*H* loop at the negative *H* direction. Since the *B*-*H* loop and the *M*-*H* loop are isomorphic, one can equivalently state that $(BH)_{max}$ is limited by the remanent magnetization — M_r — defined as the intercept of the *M*-*H* loop at the positive *M* direction, and by the intrinsic coercive field — H_{ci} — defined as the intercept of the *M*-*H* loop at the negative *H* direction.

The remanent magnetization, M_r, is bounded by the saturation magnetization, M_s. The intrinsic coercive field, H_{ci}, is bounded by the magnetocrystalline anisotropy field, H_k. Both M_s and H_k are magnetic properties intrinsic to the crystal structure of the material, in the sense that they are independent of the microstructure of the material.

The saturation magnetization, M_s, is defined as the magnitude of the vector sum of the magnetic moments in a volume when all the magnetic moments within this volume are parallel to each other. That is

$$M_s = | \sum \boldsymbol{m} |_{\max} / V \qquad \text{eq. 1.3}$$

where $\sum \boldsymbol{m}$ is the vector sum of all the magnetic moments within the volume of V occupied by the magnetic moments.

The magnetocrystalline anisotropy field, H_k, is a function of the magnetocrystalline anisotropy constants. The magnetocrystalline anisotropy constants characterize the increment in the anisotropy energy density when the magnetization direction deviates from a certain crystallographic direction. When the magnetocrystalline anisotropy of a crystal structure is uniaxial, only the first-order magnetocrystalline anisotropy constant — K_1 — remains non-zero. In this case, the anisotropy energy density is given by

$$E_k|_{0+\theta} = E_k|_0 + K_1 \sin^2\theta \qquad \text{eq. 1.4}$$

where $E_k|_0$ is the anisotropy energy density of the magnetic moments when the magnetization direction is parallel to the easy axis, which is unique when the magnetocrystalline anisotropy is uniaxial, and θ is the angular deviation of the magnetization direction from the easy axis. And H_k is given by

$$H_k = 2\,K_1 / (\mu_0 M_s) \qquad \text{eq. 1.5}$$

Based on the magnetic characterization of the NWA 6259 meteorite, which contains 95 vol.% of $L1_0$ Fe-Ni in the composition of 43 ± 1.3 at.% Ni and 5 vol.% of non-ferromagnetic Fe-Ni phosphides and sulfides, the magnetocrystalline anisotropy of $L1_0$ Fe-Ni is indeed uniaxial. The

first-order magnetocrystalline anisotropy constant was characterized to be K_1 = 0.84 MJ/m^3 (*i.e.*, 84 × 10^5 erg/cm^3). The saturation magnetization was M_s = 1.17 × 10^6 A/m (*i.e.*, 1170 emu/cm^3), corresponding to $(4\pi M_s)^{cgs}$ = 14.7 kG. The magnetocrystalline anisotropy field was calculated with **eq. 1.5** to be H_k = 1.15 × 10^6 A/m (*i.e.*, 14.4 kOe). A theoretical maximum energy product of $[(BH)_{max}]^{cgs}$ ~ 40 MGOe was anticipated by E. Poirier et al. [7], which amounts to ~ 18.9% of $(4\pi M_s H_k)^{cgs}$. This theoretical value projected from the intrinsic magnetic properties of $L1_0$ Fe-Ni falls into the $(BH)_{max}$ range (*i.e.*, 25 ~ 50 MGOe) typical of the $Nd_2Fe_{14}B$-based rare-earth magnets, which remains the market dominant material system for electric vehicle and wind energy nowadays.

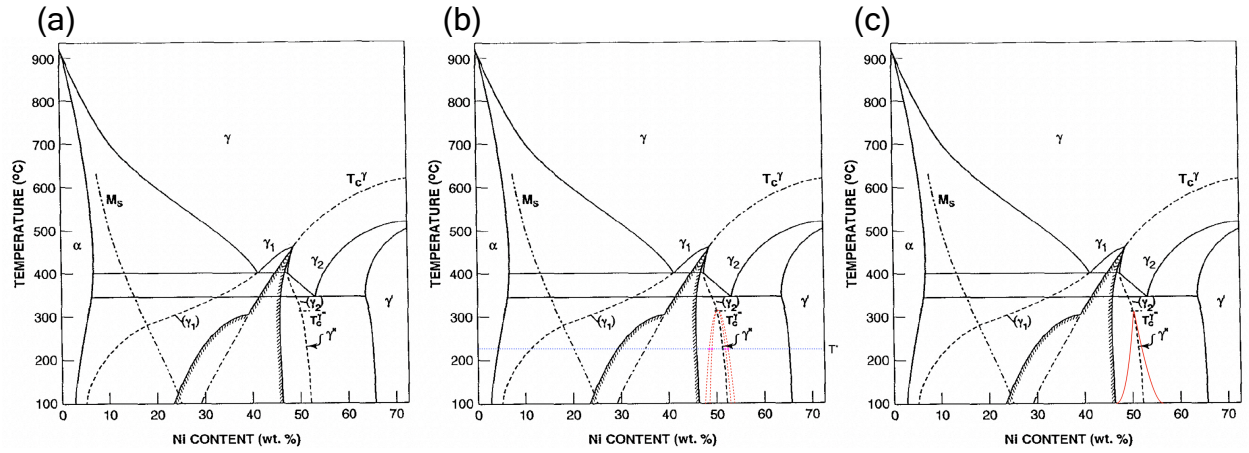

Figure 1.3. (a) The Fe-Ni phase diagram proposed by C. -W. Yang et al. [19]. **(b)** A derivative of the phase diagram in (a) in which the $L1_0$ Fe-Ni structure (*i.e.*, the γ'' phase) is metastable below T_{OD}. **(c)** A derivative of the phase diagram in (a) in which the $L1_0$ Fe-Ni structure is stable below T_{OD}.

1.2 The Fe-Ni Binary Phase Diagram

The motivation to synthesize $L1_0$ Fe-Ni has been demonstrated by the intrinsic magnetic properties of the crystal structure. In order to understand the synthetic challenge of synthesizing $L1_0$ Fe-Ni, the Fe-Ni phase diagram deserves a careful examination. **Figure 1.3a** shows the Fe-Ni phase diagram proposed by C. -W. Yang et al. [19], the features in the low temperature part (*i.e.*, $< \sim 400\ ^oC$) of which were determined from the microstructures and microcompositions found in a few meteorites. Staring from the Fe-rich side of the phase diagram, the chemical crystal structure of the α phase is the body-centered cubic (BCC) structure, which is also called the A2 structure. The chemical crystal structure of the γ phase, the field of which occupies the high temperature part of the phase diagram, is the face-centered cubic (FCC) structure, which is also called the A1 structure. The γ' phase with a phase field around 70 wt.% Ni is an intermetallic with the $L1_2$ structure. The order-disorder temperature of $L1_2$ Fe-Ni was determined by Deen and Woude to be $T_{OD,\ L12} \sim 516\ ^oC$ at 74 wt.% Ni [20, 21]. The dot-dash line — T_C γ— in the γ phase field separates the paramagnetic phase at and above the line and the ferromagnetic phase below the line. The Curie line T_C γ is a higher-order phase boundary, at which the Gibbs phase rule does not apply [22]. T_C γ intersects the first-order phase boundary at a tricritical point near the equiatomic composition. This tricritical point is the tip of a horn-shape miscibility gap under the γ phase field. The γ_1 phase and the γ_2 phase, the field of which are located at the high-Ni side and the low-Ni side of the miscibility gap, respectively, are paramagnetic and ferromagnetic, respectively. The dashed line (γ_1) and (γ_2) are the metastable extensions of the high-Ni side and the low-Ni side of the miscibility gap, respectively. The pair of hatched lines, branching from the tricritical point, bound the composition range for spinodal decomposition

(SD). As the temperature decreases from the tricritical point, the low-Ni SD curve initially coincides with the Curie line (T_C γ) and then diverges from T_C γ below the temperature of ~ 300°C.

There are two invariant three-phase lines in the Fe-Ni phase diagram (**Figure 1.3a**), both of which are first-order phase boundaries at which the Gibbs phase rule applies. The one at the higher temperature of T_{MO} ~ 400 °C is a monotectoid from γ_1 to $\alpha + \gamma_2$. The one at the lower temperature of T_{EU} ~ 345 °C is a eutectoid from γ_2 to α + γ'. The dot-dot-dash line — M_S — is the martensitic start line. Quenching the γ phase to a temperature below M_s triggers a diffusionless phase transformation towards the α phase [23]. The γ'' phase, which has the chemically ordered $L1_0$ structure, is another intermetallic, whose phase field is a line — γ'' — coinciding the low temperature part of the metastable extension of the high-Ni side of the miscibility gap — (γ_2). Along the γ'' phase line, the $L1_0$ structure is at a metastable equilibrium below the the critical point T_C γ'' at the order-disorder temperature $T_{OD,\ L10}$ ~ 320 °C. According to **Figure 1.3a**, within the phase field bounded by the metastable extensions of the miscibility gap — dashed lines (γ_1) and (γ_2), and between the two invariant three-phase lines (*i.e.*, T_{MO} and T_{EU}), a γ solid solution may decompose into a stable microconstituent of $\alpha + \gamma_2$, or a metastable microconstituent of $\gamma_1 + \gamma_2$. Between T_{EU} and $T_{OD,\ L10}$, a quenched γ solid solution may decompose into a stable microconstituent of α + γ', or a metastable microconstituent of $\gamma_1 + \gamma_2$. Below T_{OD}, a quenched γ solid solution may decompose into a stable microconstituent of α + γ', or a metastable microconstituent of γ_1 + γ''.

Notice that, in **Figure 1.3a**, the γ'' phase field is a dashed line. This is equivalent to say that the single-phase composition range of the γ'' phase is a single value at any given temperature. According to **Figure 1.3a**, such a composition value should be at or above 50.9 ± 1.4 wt.% Ni at any given temperature. The meteorites contributed to the determination of the γ'' phase line in **Figure 1.3a** include the iron or stony-iron meteorites — Dayton, Tazewell, Carlton, Grant, and Estherville — reported by K. B. Reuter et al. in 1989 [24], and the stony-iron meteorites — Estherville and RKPA 79015 — reported by C. -W. Yang et al. in 1996 [19]. Notice that the iron meteorite NWA 6259 discussed previously, the recovery of which was reported by J. T. Wasson in 2011 [15], did not contribute to the determination of the γ'' phase line in **Figure 1.3a**. As mentioned previously, NWA 6295 contains 95 vol.% of $L1_0$ Fe-Ni (γ'') in the composition of 43 ± 1.3 at.% Ni (= 44 ± 1.4 wt.% Ni), which is smaller than 50.9 ± 1.4 wt.% Ni by at least 4 wt.% Ni [7]. Based on this level of supersaturation, it is not unreasonable to speculate that it might be possible for the γ'' phase to have a finite range of metastable compositions, as large as a few weight percents, at a given temperature below $T_{OD,\ L10}$. If this is the case, the Gibbs free energy vs. composition curve (*i.e.*, the *G-x* curve) of the γ'' phase will not be a vertical line, but a parabolic curve, which will have two common tangents with the *G-x* curve of the γ phase below $T_{OD,\ L10}$, giving rise to a set of metastable phase fields, an example of which is speculated and outlined by the red dashed curves in **Figure 1.3b**. The inner curve defines the metastable single-phase field of the γ'' phase. The two regions bounded by the inner and the outer curves are the metastable two-phase fields of the γ'' phase and the γ phase.

In fact, it still remains an open question whether or not the γ'' phase is in a stable equilibrium or a metastable equilibrium below $T_{OD,\ L10}$ [16]. The phase diagram in **Figure 1.3a** described by C. -W. Yang et al. [19] indicates that the microconstituent of α + γ' is more stable than the γ'' phase. However, the thermodynamic parameters extracted from the NWA 6259 meteorite suggests that the opposite might instead be true. **Figure 1.4** shows the enthalpy vs. composition curves (*i.e.*, the *H-x* curves) of Fe-Ni reported by N. Bordeaux et al. in 2016 [16]. The enthalpy of transformation of the $L1_0$-to-A1 disordering ($\Delta H_{L10\text{-}A1}$) at the composition of 43 at.%Ni was extracted from the NWA 6259 meteorite to be + 4.0 ± 0.2 kJ/mol of atoms. The enthalpy of transformation of the $L1_2$-to-A1 disordering ($\Delta H_{L12\text{-}A1}$) at the composition of 75 at.%Ni was characterized to be + 4.1 or + 2.4 kJ/mol of atoms by W. Gasior et al. or J. Liu et al. respectively [26, 27]. The relative entropy contribution to the Gibbs free energy between the γ'' phase and the α + γ' microconstituent is not known [16]. Considering the enthalpy contribution only, based on the value from W. Gąsior et al., the γ'' phase is marginally more stable than the microconstituent of α + γ' at 43 at.%Ni (**Figure 1.4a**). Based on the value from J. Liu et al., the γ'' phase is significantly more stable (*i.e.*, by ~ 1.5 kJ/mol of atoms) than the microconstituent of α + γ' at 43 at.%Ni (**Figure 1.4b**).

If the γ'' phase is more stable than the α + γ' microconstituent at the composition defined by the γ'' phase field, and if the γ'' phase is not a line compound in the most rigorous definition, the *G-x* curve of the γ'' phase (below $T_{OD,\ L10}$) will have two common tangents with the *G-x* curves of the α phase and the γ' phase, respectively, giving rise to a stable phase field, an example of which is speculated and outlined by the red solid curves in **Figure 1.3c**, and a three-phase-invariant

peritectoid (α + γ' to γ'') at $T_{PE} = T_{OD,\,L1_0}$. Notice that **Figure 1.3c** does not necessarily contradict with the observation of the α / γ' interface in the RKPA 79015 meteorite reported by C. -W. Yang [19], in precisely the sense that, if it is quenched to a temperature between T_{EU} and $T_{OD,\,L1_0}$, a γ solid solution will still transform towards an α + γ' microconstituent (where an α / γ' interface can be found) as the equilibrium configuration, even though the γ'' phase is more stable than the α + γ' microconstituent below $T_{OD,\,L1_0}$.

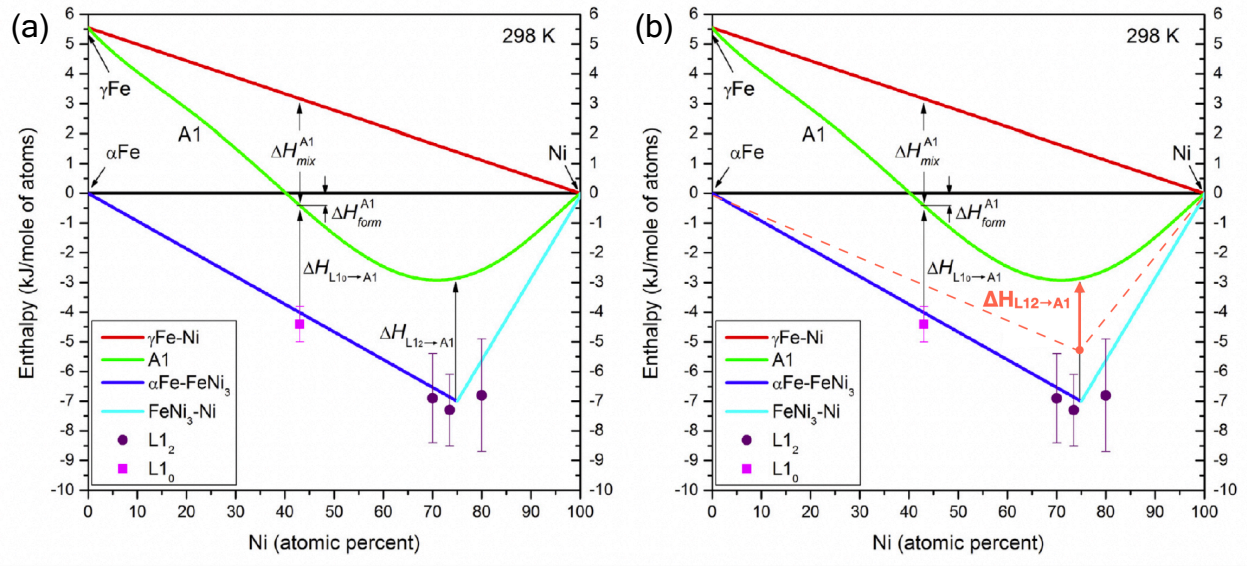

Figure 1.4. (a) The enthalpy vs. composition (*H-x*) curves reported by N. Bordeaux et al. [16]. The red line is a linear combination of the enthalpy of γ Fe and the enthalpy of γ Ni. The deviation of the green curve from the red curve was determined by the enthalpy of mixing of A1 Fe-Ni (ΔH^{A1}_{mix}). The deviation of the magenta square from the green curve was determined by the enthalpy of the $L1_0$-to-A1 disordering ($\Delta H_{L10\text{-}A1}$). The deviation of the minimum point of the convex envelope from the zero enthalpy level was determined by the formation enthalpy of $L1_2$ Fe-Ni (ΔH^{L12}_{form}) values reported by W. Gasior et al. [26]. The blue line is a linear combination of the enthalpy of α Fe and the minimum point of the convex envelope. The cyan line is a linear combination of the enthalpy of γ Ni and the minimum point of the convex envelope. **(b)** Overlaying on (a), the deviation of the minimum point of the orange dashed convex envelope from the green curve was determined by the enthalpy of the $L1_2$-to-A1 disordering ($\Delta H_{L12\text{-}A1}$) reported by J. Liu [27].

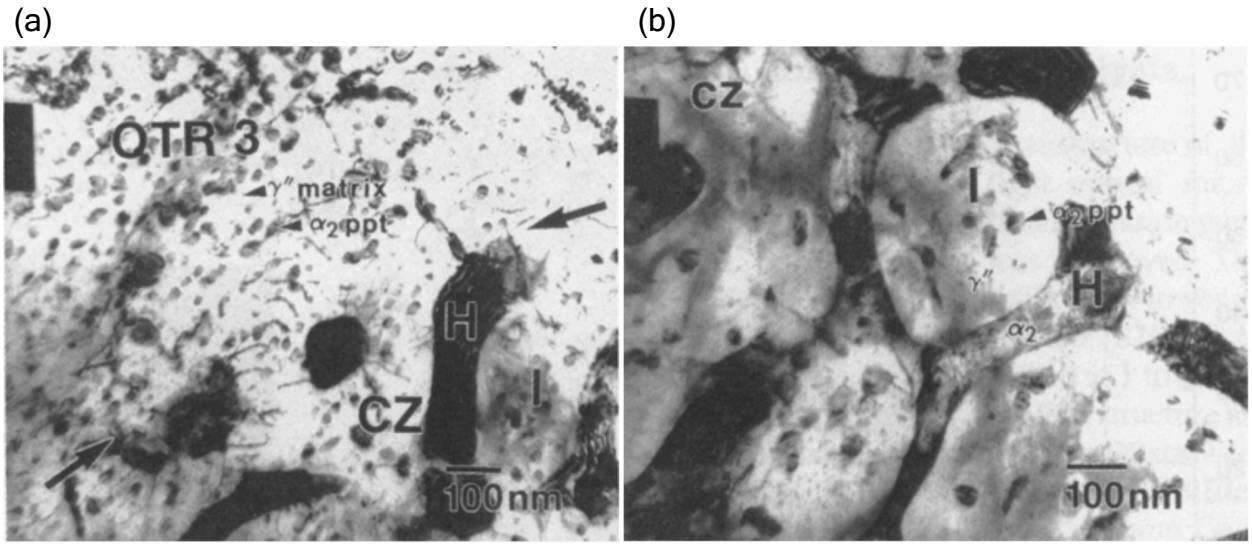

Figure 1.5. (a) Transmission electron microscopy (TEM) bright field (BF) image of the outer taenite rim (OTR) and the cloudy zone (CZ) in the RKPA 79015 meteorite, reported by C. -W. Yang et al. [19]. The OTR denoted as "OTR 3" locates at the upper left. The CZ locates at the lower right. A pair of arrows indicates the boundary between the OTR and the CZ. The OTR contains a number of α precipitates, denoted as "α_2 ppt", in the γ'' matrix. The CZ is consisting of the γ'' islands, denoted as "I", in the α percolating network, denoted as "H". The γ'' islands contain the α precipitates. **(b)** TEM BF image of the CZ in the RKPA 79015 meteorite, reported by C. -W. Yang et al. [19], showing the percolating network ("H") of the α phase ("α_2") and the islands ("I") of the γ'' phase. The γ'' islands also contain the α precipitates ("α_2 ppt").

Based on the Fe-Ni phase diagrams in **Figure 1.3**, some reaction paths of the A1-to-$L1_0$ chemical ordering can be envisioned to understand the microstructures in the meteorites, where the γ'' phase was found. Notice that, at a given temperature below $T_{OD,\ L10}$, the composition point (**Figure 1.3a**) or the composition ranges (**Figure 1.3b and c**), at which the γ'' phase is more stable than the γ phase, overlaps with the metastable miscibility gap of the γ phase. Consider a near-equiatomic solid solution of the γ phase quenched to a temperature below the order-disorder temperature, $T_{OD,\ L10}$. (i) When the composition is in the high-Ni region outside the miscibility

gap, the γ phase may transform to the γ'' phase, without being accompanied by the precipitation of the α phase. (ii) When the composition is within the miscibility gap but outside the spinodal region, the formation of the γ'' phase may be accompanied by the precipitation of the low-Ni γ phase, which may further transform to the α phase, forming a microstructure consisting of a matrix of the γ'' phase and precipitates of the α phase. The microstructure in the outer Taenite rim (OTR) of the RKPA 79015 meteorite [19] may result from this reaction path (**Figure 1.5a**). (iii) When the composition is within the spinodal region, the γ phase may first decompose into a low-Ni γ phase and a high-Ni γ phase, then the low-Ni γ phase may transform into the α phase, while the high-Ni γ phase may transform into the γ'' phase, forming a microstructure consisting of a percolating network of the α phase and islands of the γ'' phase. The microstructures in the cloudy zone (CZ) of the Tazewell [24, 28], the Estherville [24, 19], and the RKPA 79015 [19] meteorite may result from such a reaction path (**Figure 1.5**). Subsequent to the formation of the CZ microstructure, γ precipitates may nucleate and grow within the γ'' islands. This post-ordering precipitation can be rationalized by following the graphical thermodynamic method described in detail by Soffa et al. [29]. **Figure 1.6** shows a hypothetical configuration of the *G*-*x* curves of the γ phase (red) and the γ'' phase (blue) around the equiatomic composition at a temperature below $T_{OD,\,L1_0}$ (the isotherm at T^* in **Figure 1.3b**). The four intersections (magenta points) between the T^* isotherm and the metastable boundaries (red dashed curves) in **Figure 1.3b** correspond to the points of tangency (magenta points) in **Figure 1.6**. Following the ordering transformation from the γ phase (point A) to the γ'' phase (point B), the system can lower the Gibbs free energy by precipitating a low-Ni γ phase (point C_γ) and arrive at point C at the common tangent construction. The low-Ni γ phase may further transform into the α phase,

forming the microstructure (γ'' islands embedded with α precipitates) shown in **Figure 1.5**. It also worth mentioning that the ordering transformation from the γ to the γ'' phase (*e.g.*, point A to point B in **Figure 1.6**) can be either congruous or continuous, depending on the Gibbs free energy vs. order parameter curve (*i.e.*, the *G*-η curve) of the transformation [29]. With no consideration of the strain energy and the interfacial energy associating with the formation of the ordered phase, if there is an energy barrier in the *G*-η curve between the two phases, the γ phase will be metastable with respect to the γ'' phase, and the ordering transformation will occur congruously through nucleation and growth; if there is no energy barriers between the two phases, the γ phase will be unstable with respect to γ'' phase, and the ordering transformation will occur continuously through spinodal decomposition. The absence of an energy barrier in the *G*-η curve, however, can only be achieved, when the γ phase is quenched below the ordering instability temperature (T_i), which could be much lower than the order-disorder temperature, $T_{OD,\ L10}$. To the best of my knowledge, the T_i of the γ-to-γ'' ordering transformation has not been experimentally characterized nor computationally estimated. Yet, considering that the $T_{OD,\ L10}$ (~ 320 ^{o}C) of the γ-to-γ'' ordering transformation being low in the sense that the lattice diffusion is extremely slow below $T_{OD,\ L10}$, the ordering transformation that can be facilitated within a viable timescale will most likely be congruous instead of continuous.

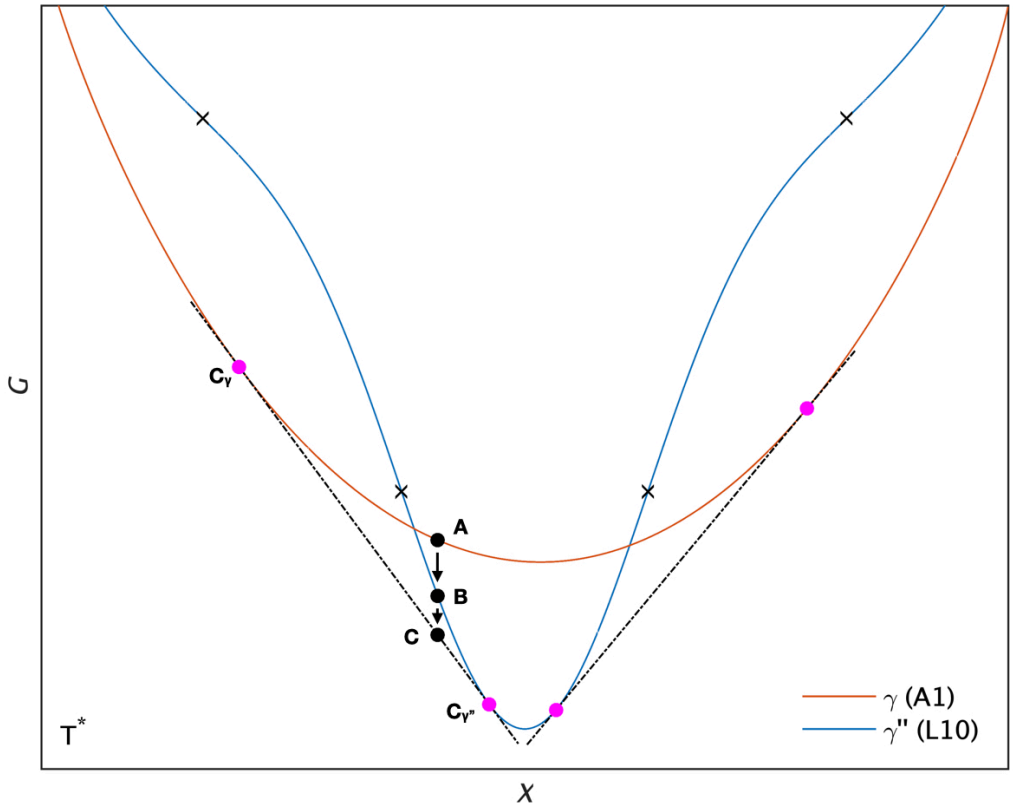

Figure 1.6. Hypothetical *G*-*x* curves of the γ (A1, disordered) and the γ'' ($L1_0$, ordered) phase near the equiatomic composition of Fe-Ni. The magenta points are the points of tangency of the two common tangent constructions between the two *G*-*x* curves. The crosses are the inflection points on the *G*-*x* curve of the γ'' phase. The arrow from point A to point B indicates the reaction path of the A1-to-$L1_0$ ordering transformation. The arrow from point B to point C indicates the reaction path of the precipitation of the low-Ni γ phase from the γ'' phase.

1.3 The Kinetics of the Chemical Ordering towards $L1_0$ Fe-Ni

1.3.1 Diffusion Kinetics

The chemical ordering from A1 Fe-Ni (*i.e.*, the γ phase) to $L1_0$ Fe-Ni (*i.e.*, the γ'' phase) occurs via either the nucleation and growth or the spinodal decomposition mechanism, both of which are diffusional and rely on the creation and/or migration of vacancies. The vacancy mediated diffusivity (D) can be calculated from the activation energy for lattice diffusion (E_L) and the pre-exponential factor of diffusivity (D_0) according to the Arrhenius equation:

$$D = D_0 \exp[-E_L/(k_B T)] \qquad \text{eq. 1.6}$$

where $k_B = 8.617 \times 10^{-5}$ eV/K is the Boltzmann constant and T is the absolute temperature. The jump rate (Γ) can be calculated from the diffusivity by:

$$\Gamma = 6D/a_{NN}^2 \qquad \text{eq. 1.7}$$

where a_{NN} is the nearest neighbor distance between atoms in the defect-free crystal [30]. For example, a_{NN} is related to the lattice parameter by $a_{NN} = (\sqrt{2}/2)\, a$ in the A1 crystal structure.

The vacancy formation energy in A1 Fe-Ni with 73.6 at.% Ni was measured by N. A. Koneva et al. to be $E_{V,f,Fe\text{-}Ni} \sim 1.4 \pm 0.1$ eV/atom [31], comparable to the vacancy formation energy in FCC Ni ($E_{V,f,Ni} \sim 1.54 \pm 0.2$ eV/atom) measured by K. G. Lynn et al. [32], and the value ($E_{V,f,Ni} \sim 1.43$ eV/atom) calculated by C. Zhang et al. [33]. The vacancy migration energy in A1 Fe-Ni with

73.6 at.% Ni was measured to be $E_{V, m, Fe\text{-}Ni} \sim 1.7 \pm 0.2$ eV/atom by N. A. Koneva et al. [31], comparable to the activation energy for interdiffusion ($E_{a, Fe/Ni} \sim 1.6 \pm 0.1$ eV/atom) extracted from the Fe/Ni multilayer thin films by J. Liu et al. [34]. The closeness between $E_{V, m, Fe\text{-}Ni}$ and $E_{a, Fe/Ni}$ implied that the interdiffusion in the Fe/Ni multilayer was dominated by the diffusion in the grain boundaries, which eliminated the vacancy formation energy barrier by providing excess vacancy sources and sinks. The activation energy for lattice diffusion in A1 Fe-Ni is the sum of $E_{V, f, Fe\text{-}Ni}$ and $E_{V, m, Fe\text{-}Ni}$, and was measured to be $E_{L, Fe\text{-}Ni} \sim 3.1 \pm 0.3$ eV/atom in the Fe-Ni with 73.6 at.% Ni by N. A. Koneva et al. [31], comparable to the activation energy for self diffusion in FCC Fe ($E_{L, Fe} \sim 2.92 \pm 0.08$ eV/atom [35], ~ 2.94 eV/atom [36]) and FCC Ni ($E_{L, Ni} \sim 2.94 \pm 0.4$ eV/atom [35], ~ 2.87 eV/atom [36]), the activation energy for the diffusion of Fe in A1 Fe-Ni with 45.3 at.% Ni ($E_{L, Fe, Fe\text{-}Ni} \sim 3.13 \pm 0.08$ eV/atom) and the diffusion of Ni in A1 Fe-Ni with 45.3 at.% Ni ($E_{L, Ni, Fe\text{-}Ni} \sim 3.14 \pm 0.16$ eV/atom) [35], the activation energy for tracer diffusion of Fe in FCC Ni ($E_{L, Fe, Ni} \sim 2.79$ eV/atom) [36], the activation energy for the $L1_0$-to-A1 disordering transformation ($E_{a, L10\text{-}A1} \sim 3.08 \pm 0.07$ eV/atom) measured by N. Bordeaux et al. [16], and the activation energy for the $L1_2$-to-A1 disordering transformation ($E_{a, L12\text{-}A1} \sim 3.1 \pm 0.1$ eV/atom) measured by J. Liu [27]. The closeness between $E_{L, Fe\text{-}Ni}$, $E_{a, L10\text{-}A1}$, and $E_{a, L12\text{-}A1}$ implies that the two disordering transformations require both the creation and the migration of vacancies, which further implies that the creation of vacancies is a necessary step even for the short-range diffusion across the interphase interface between the ordered and the disordered phase.

The pre-exponential factors of the diffusivity of Fe and Ni in A1 Fe-Ni with 45.3 at.% Ni are $D_{0, Fe} \sim 2.6 \pm 1.3 \times 10^{-4}$ m^2/s and $D_{0, Ni} \sim 2.5 \pm 1.8 \times 10^{-4}$ m^2/s, respectively [35], comparable to the

pre-exponential factor of the tracer diffusion of Fe in FCC Ni ($D_{0,\,Fe,\,Ni}$ ~ 1.0 × 10^{-4} m^2/s) [36], but a factor of about 3 ~ 5 larger than the values of the self diffusion in FCC Fe ($D_{0,\,Fe,\,Fe}$ ~ 0.49 × 10^{-4} m^2/s) and FCC Ni ($D_{0,\,Ni,\,Ni}$ ~ 0.85 × 10^{-4} m^2/s) [36].

Based on the values reported by B. Million et al. (*i.e.*, $E_{L,\,Fe,\,Fe\text{-}Ni}$ ~ 3.13 ± 0.08 eV/atom, $E_{L,\,Ni,\,Fe\text{-}Ni}$ ~ 3.14 ± 0.16 eV/atom, $D_{0,\,Fe}$ ~ 2.6 ± 1.3 × 10^{-4} m^2/s, $D_{0,\,Ni}$ ~ 2.5 ± 1.8 × 10^{-4} m^2/s) [35], the vacancy mediated diffusivity of Fe and Ni in A1 Fe-Ni with a near-equiatomic composition at 45.3 at.% Ni are calculated with **eq. 1.6** to be D_{Fe} ~ 6.6 × 10^{-31} m^2/s and D_{Ni} ~ 5.2 × 10^{-31} m^2/s, respectively, at the order-disorder temperature ($T_{OD,\,L10}$ ~ 320 ^oC) of $L1_0$ Fe-Ni. And the values at 300 ^oC are D_{Fe} ~ 7.8 × 10^{-32} m^2/s and D_{Ni} ~ 6.1 × 10^{-32} m^2/s. The lattice parameter of A1 Fe-Ni with a near-equiatomic composition is a ~ 3.58 Å [37]. The jump rate (Γ) is calculated with **eq. 1.7** to be on the order of 6 × 10^{-12} /s (300 ^oC) ~ 6 × 10^{-11} /s (320 ^oC), which is equivalent to say that each atomic jump occurs on the order of every 500 (320 ^oC) ~ 5000 (300 ^oC) years. This is what it means quantitatively by saying that the lattice diffusion below $T_{OD,\,L10}$ is extremely slow. Nevertheless, the cooling rate that an iron meteorite has experienced can be as low as ~ 0.1 ^oC per million years [38]. It follows that it is not impossible for an iron meteorite to have stayed between 300 and 320 ^oC for as long as ~ 200 million years, during which 4 × 10^4 ~ 4 × 10^5 atomic jumps could have happened for every single atom in an A1 Fe-Ni phase, which may allow for the ordering transformation to occur.

1.3.2 Nucleation Kinetics

According to the classical nucleation theory (CNT) [39], the rate of homogeneous nucleation (I_v), defined as the number of clusters surpassing the size of the critical nucleus (r^*) per unit volume per unit time, scales with the product of the rate at which an atom that borders a critical nucleus jumps across the interface (ω^*) and the concentration of the critical nuclei (C^*):

$$I_v = (A^* S^*)\, \omega^* C^* \qquad \text{eq. 1.8}$$

where A^* is the surface area of a critical nucleus, and S^* is the areal density of atoms at the surface of a critical nucleus. Similar to the jump rate of lattice diffusion (Γ), the jump rate across the interface (ω^*) depends on the vacancy formation energy ($E_{V,f}$) and the vacancy migration energy ($E_{V,m}$). In situations where there is a plethora of vacancies in vicinity of the interface, similar to the neighborhood of a grain boundary, the contribution from the vacancy formation energy to the activation energy of the interfacial jump can be eliminated. In the case of the $L1_0$-to-A1 disordering transformation of Fe-Ni, however, N. Bordeaux reported that the activation energy of the $L1_0$-to-A1 disordering transformation ($E_{a,\,L10\text{-}A1} \sim 3.08 \pm 0.07$ eV/atom) was very close to the activation energy of the lattice diffusion ($E_{L,\,Fe\text{-}Ni} \sim 3.1 \pm 0.3$ eV/atom), indicating that the creation of a vacancy, in this case, is a necessary step for the interfacial jump [16, 31]. Considering the A1-to-$L1_0$ ordering transformation, the interfacial jump rate therefore scales with the Boltzmann factor involving both $E_{V,f}$ and $E_{V,m}$:

$$\omega^* = \omega_0 \exp[-(E_{V,f}+E_{V,m})/(k_B T)] \qquad \text{eq. 1.9}$$

where the vibrational frequency ω_0 is on the order of 10^{12} s^{-1} [39]. On the other hand, the concentration of the critical nuclei scales with the Boltzmann factor involving the nucleation barrier:

$$C^* = [C_0 / (N_A V^*/V_m)] \exp[-(\Delta G^* V_m)/(N_A k_B T)] \quad \text{eq. 1.10}$$

where $N_A = 6.022 \times 10^{23}$ mol^{-1} is the Avogadro constant, V_m is the molar volume of A1 Fe-Ni, $C_0 = N_A/V_m$ is the number of atoms per unit volume, V^* is the volume of a critical nucleus, $N_A V^*/V_m$ is the number of atoms in a critical nucleus assuming that the molar volume of $L1_0$ Fe-Ni can be approximated by that of A1 Fe-Ni, ΔG^* is the nucleation barrier per unit volume of the critical nuclei, and $\Delta G^* V_m/N_A$ is the nucleation barrier per atom of the critical nuclei. The nucleation barrier (ΔG^*) depends on the interfacial energy (σ), the strain energy (ΔG_S), and the thermodynamic driving force (ΔG). Assuming that the critical nuclei are spherical, the nucleation barrier can be calculated by:

$$\Delta G^* = 16\pi\sigma^3/[3(\Delta G + \Delta G_S)^2] \quad \text{eq. 1.11}$$

And the radius of the critical nuclei can be calculated by:

$$r^* = -2\sigma/(\Delta G + \Delta G_S) \quad \text{eq. 1.12}$$

Considering the negligible difference in the unit cell dimensions between near-equiatomic A1 Fe-Ni and $L1_0$ Fe-Ni, it is assumed here that σ can be approximated by the grain boundary energy of near-equiatomic A1 Fe-Ni. The grain boundary energy (γ_{gb}) can be estimated based on the equation described by G. S. Rohrer [40]:

$$\gamma_{gb} = 2\gamma_s - B \qquad \text{eq. 1.13}$$

where the surface energy (γ_s) can be estimated from the Young's modulus (E) by $\gamma_s \sim (E/8) \times 10^{-10}$ m, and the binding energy (B) can be estimated as $\gamma_s/2 \leq B/2 \leq 3\gamma_s/4$. The Young's modulus of near-equiatomic A1 Fe-Ni is on the order of 150 GPa based on the values compiled by H. M. Ledbetter and R. P. Reed [41]. Using **eq. 1.13**, it follows that γ_{gb} of near-equiatomic A1 Fe-Ni is on the order of 1 J/m^2. The anisotropic grain boundary energies of both BCC Fe and FCC Ni are in the range of 0.7 ~ 1.3 J/m^2 [42, 43], which the estimated γ_{gb} value falls within. The anisotropic surface energies of BCC Fe and FCC Ni are on the order of 2.5 J/m^2 and 2.1 J/m^2, respectively [44], roughly twice as large as the estimated γ_{gb}, agreeing with **eq. 1.13**.

The molar thermodynamic driving force ($\Delta G^m_{A1\text{-}to\text{-}L10}$) is a function of the molar transformation enthalpy ($\Delta H^m_{A1\text{-}to\text{-}L10}$) and the molar transformation entropy ($\Delta S^m_{A1\text{-}to\text{-}L10}$):

$$\Delta G^m_{A1\text{-}to\text{-}L10} = \Delta H^m_{A1\text{-}to\text{-}L10} - T\Delta S^m_{A1\text{-}to\text{-}L10} \qquad \text{eq. 1.14}$$

The molar transformation enthalpy extracted from the NWA 6259 meteorite ($\Delta H^{m}_{A1\text{-}to\text{-}L10} \sim -4.0 \pm 0.2$ kJ/mol of atoms) [16] is used here for the estimation of $\Delta G^{m}_{A1\text{-}to\text{-}L10}$. It is further assumed that the molar transformation entropy can be approximated by the molar configurational entropy change ($\Delta S^{m}_{A1\text{-}to\text{-}L10,\ Conf}$). The molar configurational entropy of A1 Fe-Ni is calculated here based on statistical thermodynamics [45] by:

$$S^{m}_{A1,\ Conf}(X) = -R\,[X \ln(X) + (1\text{-}X) \ln(1\text{-}X)] \qquad \text{eq. 1.15}$$

where $R = 8.314$ J·K^{-1}·mol^{-1} is the gas constant, and X is the atomic fraction of Ni. The molar configurational entropy of $L1_0$ Fe-Ni is calculated here using the equation described by A. G. Khachaturyan [46, 47]:

$$S^{m}_{L10,\ Conf}(X, \eta) = -(R/4)\ \{2X\,(1+\eta) \ln[X\,(1+\eta)] + 2X\,(1-\eta) \ln[X\,(1-\eta)] + 2(1-X)\,(1+\eta) \ln[(1-X)\,(1+\eta)] + 2(1-X)\,(1-\eta) \ln[(1-X)\,(1-\eta)]\} \qquad \text{eq. 1.16}$$

where η is the long-range order parameter, with $\eta = 0$ for a random alloy and $\eta = 1$ for an ordered intermetallic. Notice that **eq. 1.16** is the same as **eq. 1.15** when $\eta = 0$, and that $S^{m}_{L10,\ Conf} = 0$ when $\eta = 1$ and $X = 0.5$. As for the equiatomic composition (*i.e.*, $X = 0.5$), $\Delta S^{m}_{A1\text{-}to\text{-}L10,\ Conf}$ can then be calculated by subtracting $S^{m}_{A1,\ Conf}$ from $S^{m}_{L10,\ Conf}$ to be $-5.76 \sim -4.11$ J·K^{-1}·mol^{-1} for the transformation from A1 to $L1_0$ structure with the long-range order parameter in the range of 0.9 ~ 1.0. At 300 °C, $\Delta G^{m}_{A1\text{-}to\text{-}L10}$ can be calculated accordingly with **eq. 1.14** to be $-1.64 \sim -0.70$ kJ/mol of atoms. The thermodynamic driving force can be calculated from $\Delta G^{m}_{A1\text{-}to\text{-}L10}$ via the

molar volume, V^m = 6.91 × 10^{-6} m^3/mol (calculated from the lattice parameter of A1 Fe-Ni a ~ 3.58 Å), to be ΔG = − 2.38 × 10^8 ~ − 1.01 × 10^8 J/m^3. Assuming that the strain energy (ΔG_S) can be neglected in comparison to ΔG, the nucleation barrier can be calculated with **eq. 1.11** to be ΔG^* = 3.0 × 10^{-16} ~ 1.6 × 10^{-15} J/m^3, and the critical radius can be calculated with **eq. 1.12** to be r^* = 8 ~ 20 nm. The critical area and the critical volume are 8.9 × 10^{-16} ~ 4.9 × 10^{-15} m^2 and 2.5 × 10^{-24} ~ 3.3 × 10^{-23} m^3, respectively. It follows that the nucleation barrier per atom of the critical nuclei is $\Delta G^* V_m / N_A$ = 3.4 × 10^{-45} ~ 1.9 × 10^{-44} J/atom = 2.1 × 10^{-26} ~ 1.2 × 10^{-25} eV/atom, which is negligible in comparison to the vacancy formation energy ($E_{V,f}$ ~ 1.4 ± 0.1 eV/atom [31]) and the vacancy migration energy ($E_{V,m}$ ~ 1.7 ± 0.2 eV/atom [31]). Therefore, the nucleation rate (I_v) is limited by the interfacial jump frequency (ω^*) rather than the concentration of the critical nuclei (C^*).

Further assume that the areal density of atoms on the surface of a critical nucleus can be approximated by the areal density of atoms on the (111) facet of A1 Fe-Ni, which can be calculated from the lattice parameter (a ~ 3.58 Å) to be S^* ~ 2/[(√3/4)a^2] = 3.6 × 10^{19} m^{-2}. Putting everything together, the nucleation rate can be written as:

$$I_v = (A^* S^*)\, \omega_0 \left[C_0 / (N_A V^* / V_m)\right] \exp\left[-(E_{V,f} + E_{V,m} + \Delta G^* V_m / N_A)/(k_B T)\right] \qquad \text{eq. 1.17}$$

The value of I_v at 300 °C can then be calculated by **eq. 1.17** to be on the order of 3 × 10^{12} ~ 7 × 10^{12} $s^{-1}m^{-3}$. Consider a 8 mm × 8 mm square Fe-Ni film with a thickness of 50 nm (*i.e.*, a volume of 3.2 × 10^{-12} m^3), the number of critical nuclei being created per second is on the order of 10 ~

20. It follows that the time it takes to transform the entire volume of the film (8 mm × 8 mm × 50 nm) from A1 Fe-Ni to $L1_0$ Fe-Ni by nucleation only (*i.e.*, without growth) at 300 °C is on the order of t = 300 ~ 1800 years. The pre-exponential factor of I_v can be obtained by:

$$K_0 = (A^* S^*)\, \omega_0 [C_0 / (N_A V^*/V_m)] \qquad \text{eq. 1.18}$$

The value of K_0 is calculated by **eq. 1.18** to be $5.5 \times 10^{39} \sim 1.3 \times 10^{40}$ $s^{-1}m^{-3}$, which falls within the order of magnitude range described in CNT [39]. Furthermore, the value of t is very sensitive to $E_{V,f}$ and $E_{V,m}$. For example, if the vacancy formation energy ($E_{V,f}$) drops by 50% to ~ 0.7 eV/ atom, the value of t will drop accordingly to 2 ~ 10 hours, a laboratory achievable timescale potentially relevant for production.

1.3.3 Growth Kinetics

The growth kinetics can be estimated based on the elementary rate theory [39]. Assuming that the growth of the stable nuclei occurs via vacancy mediated jump across the interface, the forward flux of atoms from the A1 phase to the $L1_0$ phase can be described by:

$$dN_{A1\text{-}to\text{-}L10}/dt = S\, \omega_0 \exp[-(E_{V,f}+E_{V,m})/(k_B T)] \qquad \text{eq. 1.19}$$

And the backward flux from the $L1_0$ phase to the A1 phase can be described by:

$$dN_{L10\text{-}to\text{-}A1}/dt = S\, \omega_0 \exp\{-[E_{V,f}+E_{V,m}-(\Delta G^m_{A1\text{-}to\text{-}L10}/N_A)/(k_B T)] \qquad \text{eq. 1.20}$$

where the thermodynamic driving force per atom ($\Delta G^m_{A1\text{-}to\text{-}L10}/N_A$) is on the order of − 0.02 ~ − 0.01 eV/atom based on the range of $\Delta G^m_{A1\text{-}to\text{-}L10}$ estimated in **section 1.3.2**. The growth rate can be characterized by the net flux described as the net amount of atoms jump across the interface from the $L1_0$ phase to the A1 phase per unit area of the interface per unit time, which can be obtained by subtracting **eq. 1.20** from **eq. 1.19**:

$$dN/dt = dN_{A1\text{-}to\text{-}L10}/dt - dN_{L10\text{-}to\text{-}A1}/dt = S\,\omega_0 \exp[-(E_{V,f}+E_{V,m})/(k_BT)] \times\{1-\exp[+(\Delta G^m_{A1\text{-}to\text{-}L10}/N_A)/(k_BT)]\} \quad \text{eq. 1.21}$$

The value of dN/dt at 300 °C can then be calculated by **eq. 1.21** to be on the order of 3000 ~ 6000 $m^{-2}\cdot s^{-1}$. For a critical nuclei with a radius of 8 ~ 20 nm, it follows that it takes about t' = 2000 ~ 6000 years for it to grow by another atom. Similar to the nucleation rate (I_v), dN/dt is very sensitive to the $E_{V,f}$ and $E_{V,m}$. If the vacancy formation energy ($E_{V,f}$) drops by 50% to ~ 0.7 eV/atom, the value of t' is reduced accordingly to 15 ~ 38 hours. Recall from **section 1.3.2** that at 300 °C it only takes about 2 ~ 10 hours to transform by nucleation without growth the entire volume of the 8 mm × 8 mm × 50 nm film from A1 Fe-Ni to $L1_0$ Fe-Ni, provided that $E_{V,f}$ is discounted by 50%. In such a hypothetical case, the ordering transformation is limited by the growth rate, and the product being obtained consists of nanocrystalline $L1_0$ Fe-Ni with an average grain size about the size of a critical nuclei (r^* = 8 ~ 20 nm).

Furthermore, **eq. 1.21** can be expanded to the first order as follow:

$$dN/dt = S\,\omega_0 \exp[-(E_{V,f}+E_{V,m})/(k_BT)] \times [-\Delta G^m_{A1\text{-}to\text{-}L10}/(RT)] \quad \text{eq. 1.22}$$

According to **eq. 1.22**, when $\Delta G^m_{A1\text{-}to\text{-}L10}/(RT)$ is small, the net flux (dN/dt) scales linearly with the magnitude of the molar thermodynamic driving force ($\Delta G^m_{A1\text{-}to\text{-}L10}$). This is different from the situation in nucleation, where the nucleation rate is insensitive to the thermodynamic driving force. Being more quantitative about the error introduced by the expansion, $\Delta G^m_{A1\text{-}to\text{-}L10}$ is about 0.15 ~ 0.35 RT at 300 °C, and the deviation from **eq. 1.22** to **eq. 1.21** is about +7% ~ +18%. In addition to the 50% discount on $E_{V,f}$, if the magnitude of the thermodynamic driving force can be enlarged by a factor of 2, the growth time t' at 300 °C will be further reduced to 8 ~ 22 hours, which is more comparable to the nucleation time t. In such a hypothetical case, the ordering transformation is limited by both the nucleation rate and the growth rate, obtaining an average grain size larger than r^* becomes possible.

1.4 The Strategies of Synthesizing $L1_0$ Fe-Ni

After surveying the ordering transformation from the angle of thermodynamics (**section 1.2**) and kinetics (**section 1.3**), two strategies can be conceived to accelerate the ordering transformation towards $L1_0$ Fe-Ni. (1) Based on **eq. 1.17** and **eq. 1.21**, both the nucleation rate and the growth rate can be increased by decreasing the kinetic barrier. More specifically, non-equilibrium defects such as grain boundaries and dislocations may provide excess vacancies and reduce the kinetic barrier locally. (2) Based on **eq. 1.21**, the growth rate can also be increased by increasing the magnitude of the thermodynamic driving force. A far-from-equilibrium initial phase may be used

to raise the driving force and accelerate the growth globally. On the other hand, a survey of laboratory methods reported in the literature may provide practical insights complementary to the theoretical ones.

1.4.1 Neutron Bombardment

The first report of human-made $L1_0$ Fe-Ni dates back to 1960s by a group of scientists, including Nobel laureate Louis Néel, from The nuclear research center at Grenoble (C. E. N. G.), France. After being irradiated by a neutron fluence of 170×10^{17} neutrons/cm^2 (> 1 MeV) at 300^{o}C under a magnetic field, polycrystalline equiatomic A1 Fe-Ni showed a first-order magnetocrystalline anisotropy constant of $K_1 \sim 0.20$ MJ/m^3, which was too high to be explained by a disordered structure [6]. The team further investigated monocrystalline equiatomic A1 Fe-Ni in the form of disk or sphere processed under similar conditions [48, 49]. The magnetization curves measured along different crystallographic directions were consistent with the magnetization behavior of an ensemble of $L1_0$ Fe-Ni crystallites whose four-fold rotation axes were orthogonal to each other. The electron diffraction pattern showed the 001 superstructure spots indicative of the existence of $L1_0$ Fe-Ni (**Figure 1.7a**). The dark field image corresponding to the 001 superstructure spots further revealed that the crystallite size of the $L1_0$ Fe-Ni phase was about 5 ~ 15 nm. Notice that the $L1_0$ Fe-Ni crystallites with their four-fold rotation axes along the applied magnetic field (**Figure 1.7b**) were in a higher density and larger than those with their four-fold rotation axes perpendicular to the applied magnetic field (**Figure 1.7c**), indicating the effects of the applied magnetic field to the nucleation and growth of the $L1_0$ Fe-Ni crystallites. It was also found that

replacing the neutron irradiation by the electron irradiation with a fluence of 920×10^{17} electrons/ cm^2 (2 MeV) developed $L1_0$ Fe-Ni crystallites as large as 40 nm (**Figure 1.7d**).

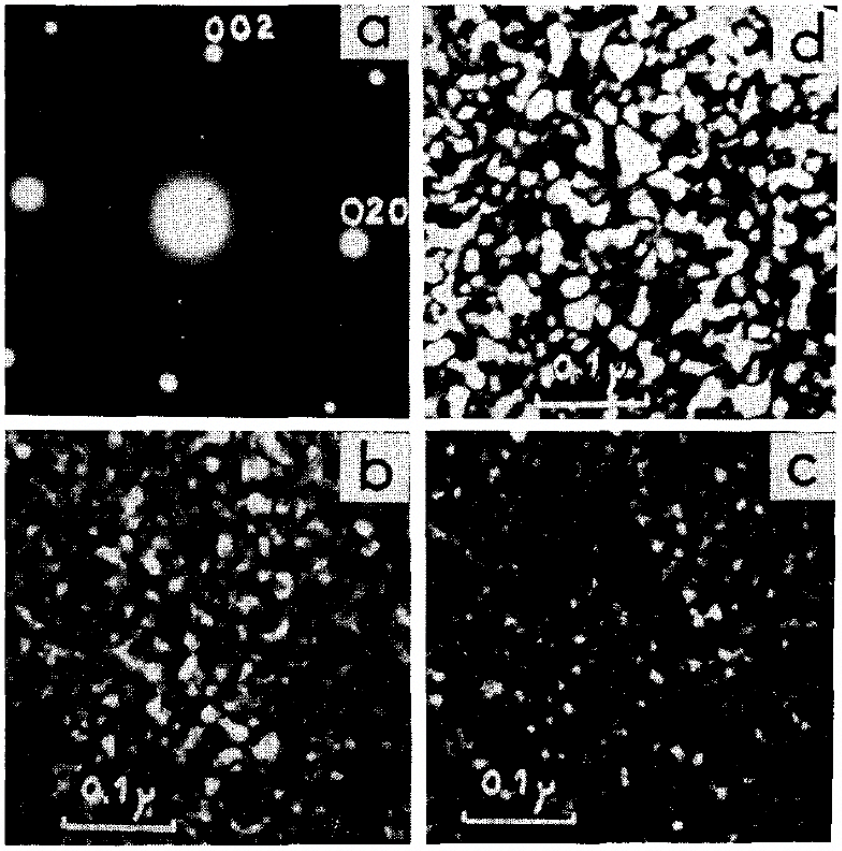

Figure 1.7. Transmission electron microscopy (TEM) characterizations reported by J. Paulevé et al. [49] of monocrystalline equiatomic A1 Fe-Ni ordered by neutron bombardment with an applied magnetic field along [001] or by electron irradiation: (a) electron diffraction pattern of the [100] zone of the monocrystalline A1 Fe-Ni after neutron bombardment; (b) dark field image corresponding to the 001 spots in (a); (c) dark field image corresponding to the 010 spots in (a); (d) dark field image (corresponding to the superstructure spots on the applied field direction) of the monocrystalline equiatomic A1 Fe-Ni ordered by electron irradiation.

1.4.2 Alternate Monoatomic Layer Deposition

The $L1_0$ Fe-Ni crystal structure can be considered as a face center cubic lattice decorated by alternating Fe and Ni monoatomic layers along the [001] direction (**Figure 1.1b**), which in principle can be prepared by alternate monoatomic layer deposition (AMLD). T. Shima et al. first reported such an effort, using an ultra-high vacuum (UHV) deposition system to prepare the superlattice of $(Fe\ 1ML / Ni\ 1ML)_{50}$ (~ 18 nm) on the Ni (001) buffer layer with a deposition rate of 0.01 nm/sec [8]. The superlattice deposited at a growth temperature of 240 ^oC showed the maximum order parameter of $\eta \sim 0.6$ and the maximum first-order anisotropy constant of $K_1 \sim 0.63$ MJ/m^3. The lattice parameter $c \sim 3.62$ Å was found to be larger than the bulk value (~ 3.58 Å), which was hypothesized to be generated by the compressive strain in the Fe-Ni thin film imposed by the Ni (001) buffer layer. T. Kojima et al. used molecular beam epitaxy (MBE) to perform AMLD on the $Au_6Cu_{51}Ni_{43}$ (001) buffer layer at a rate of 0.01 nm/sec [50]. The $Au_6Cu_{51}Ni_{43}$ (001) buffer layer had an estimated lattice parameter of ~ 3.598 Å, close to those (both a and c) of $L1_0$ Fe-Ni. A superlattice of $(Fe\ 1ML / Ni\ 1ML)_{50}$ (~ 18 nm) was obtained, showing an order parameter of $\eta \sim 0.4$ and a first-order anisotropy constant of $K_1 \sim 0.7$ MJ/m^3. The first 10 bilayers — $(Fe\ 1ML / Ni\ 1ML)_{10}$ — were deposited at 100 ^oC to suppress the intermixing between the superlattice and the buffer layer. The next 40 bilayers were instead deposited at a higher temperature (190 ^oC), which promoted the surface diffusion. Curiously however, a significantly higher first-order anisotropy constant of $K_1 \sim 0.93$ MJ/m^3 was obtained from a sub-stoichiometric superlattice — $(Fe\ 0.6ML / Ni\ 0.4ML)_{50}$ (~ 18 nm) — with a significantly smaller order parameter of $\eta \sim 0.2$. The lattice parameter ratios (c/a) were less than unity for all the superlattices, including the stoichiometric and the sub-stoichiometric one. Saito

et al. used pulsed laser deposition (PLD) to perform AMLD, preparing a superlattice of (Fe 1ML / Ni 1ML)$_{25}$ (~ 9 nm) on the Cu (001) buffer layer [12]. The deposition rates were 0.024 and 0.025 nm/sec for Fe and Ni respectively. The superlattice deposited at a growth temperature of 300 ^{o}C showed the highest order parameter η ~ 0.38 and the highest first-order anisotropy constant of K_1 ~ 0.13 MJ/m^3. The lattice parameters were measured to be a ~ 3.58 Å and c ~ 3.53 Å (c/a ~ 0.986). The relatively small K_1 were said due to the intermixing between the superlattice and the buffer layer.

1.4.3 Nitrogen Insertion and Topotactic Extraction

A method to synthesize $L1_0$ Fe-Ni based on the nitriding and de-nitriding of Fe-Ni nanoparticles was first reported by S. Goto et al. [10]. The Fe-Ni nanoparticles (~ 40 nm) were prepared by the thermal plasma method, and it was shown by TEM that the particles had an oxide film (~ 2 nm) on the surface. It was found that the intercalation of nitrogen atoms could trigger the chemical ordering. The nitrogen insertion was implemented by exposing the nanoparticles to high purity ammonia flow of 5 L/min at 300 ^{o}C for 50 hours, during which the ordering of the Fe-Ni substructure was activated. The intercalated nitrogen was then extracted by high purity hydrogen flow (1 L/min at 250 ^{o}C for 2 hour), which did not destroy the ordered substructure. The method was called nitrogen insertion and topotactic extraction (NITE). After NITE, the nanoparticles showed an order parameter of η ~ 0.7. The first-order anisotropy constant was not measured due to the sintering of the nanoparticles, but was estimated to be K_1 = 0.14 ~ 0.30 MJ/m^3. Y. Sakanaka et al. implemented the nitriding and de-nitriding process electrochemically by the potentiostatic electrolysis of Fe-Ni powders in the LiCl-KCl-CsCl molten salt at 320 ^{o}C. The

order parameter of powders after the electrolysis was estimated to be $\eta \sim 0.7$. The magnetic properties were not reported [11].

1.4.4 Amorphized Precursors

Another method is introducing amorphizing elements (*e.g.*, Si, B, P) into Fe-Ni and annealing the amorphous precursor at the recrystallization temperature in order to utilize the fast diffusion kinetics during the recrystallization process. A. Makino et al. used melt spinning to produce amorphous $Fe_{42}Ni_{41.3}Si_8B_4P_4Cu_{0.7}$ ribbons from ingots of about the same composition, and then annealed the amorphous ribbon at 400^o C for 288 hours [9]. The scanning transmission electron microscopy energy dispersive X-ray spectroscopy (STEM-EDS) map showed equiatomic Fe-Ni nanoprecipitates (30 ~ 50 nm) with an areal fraction of 23%. Nano-beam electron diffraction (NBED) was used to further identified the crystal structure of the nanoprecipitates as $L1_0$ Fe-Ni. The X-ray diffraction (XRD) pattern showed the 001 superstructure reflection indicative of the existence of $L1_0$ Fe-Ni, and the lattice parameters were extracted from the pattern to be $a = 3.56$ Å and $c = 3.62$ Å ($c/a = 1.015$). The volume fraction of the $L1_0$ Fe-Ni phase was estimated to be ~ 8%, and the order parameter was estimated to be $\eta \sim 0.8$. The first-order anisotropy constant was not reported.

References

1. Cullity, B. D., and C. D. Graham. “Magnetic Materials for Recording and Computers.” In Introduction to Magnetic Materials, 505–15. John Wiley & Sons, Ltd, 2008.
2. Hirano, Toshiki, and Long-Sheng Fan. “Invar Electrodeposition for MEMS Application.” In Micromachining and Microfabrication Process Technology II, edited by Stella W. Pang and Shih-Chia Chang, 2879:252–59. SPIE, 1996.
3. Datta, M., and D. Landolt. “Fundamental Aspects and Applications of Electrochemical Microfabrication.” Electrochimica Acta 45, no. 15 (May 3, 2000): 2535–58.
4. Zangari, Giovanni. “Microelectromechanical Systems.” In Modern Electroplating, edited by Mordechay Schlesinger and Milan Paunovic, 617–36. John Wiley & Sons, Ltd, 2010.
5. Momma, Koichi, and Fujio Izumi. “VESTA3 for Three-Dimensional Visualization of Crystal, Volumetric and Morphology Data.” Journal of Applied Crystallography 44, no. 6 (December 2011): 1272–76.
6. Paulevé, J., Dautreppe, D., Laugier, J., and Néel, L. “Une Nouvelle Transition Ordre-Désordre Dans Fe-Ni (50-50).” J. Phys. Radium 23, no. 10 (1962): 841–43.
7. Poirier, Eric, Frederick E. Pinkerton, Robert Kubic, Raja K. Mishra, Nina Bordeaux, Arif Mubarok, Laura H. Lewis, Joseph I. Goldstein, Ralph Skomski, and Katayun Barmak. “Intrinsic Magnetic Properties of L10 FeNi Obtained from Meteorite NWA 6259.” Journal of Applied Physics 117, no. 17 (2015): 17E318.
8. Shima, T., M. Okamura, S. Mitani, and K. Takanashi. “Structure and Magnetic Properties for L10-Ordered FeNi Films Prepared by Alternate Monatomic Layer Deposition.” Journal of Magnetism and Magnetic Materials 310, no. 2, Part 3 (2007): 2213–14.

9. Makino, Akihiro, Parmanand Sharma, Kazuhisa Sato, Akira Takeuchi, Yan Zhang, and Kana Takenaka. “Artificially Produced Rare-Earth Free Cosmic Magnet.” Scientific Reports 5, no. 1 (November 16, 2015): 16627.
10. Goto, Sho, Hiroaki Kura, Eiji Watanabe, Yasushi Hayashi, Hideto Yanagihara, Yusuke Shimada, Masaki Mizuguchi, Koki Takanashi, and Eiji Kita. “Synthesis of Single-Phase L10-FeNi Magnet Powder by Nitrogen Insertion and Topotactic Extraction.” Scientific Reports 7, no. 1 (October 16, 2017): 13216.
11. Sakanaka, Y., E. Watanabe, Y. Hayashi, and T. Goto. “New Route of the Formation of Ordered FeNi by Electrochemical Nitriding and De-Nitriding Processes.” Journal of The Electrochemical Society 164, no. 14 (2017): E525–28.
12. Saito, Masahiro, Hisaaki Ito, Yuta Suzuki, Masaki Mizuguchi, Tomoyuki Koganezawa, Toshio Miyamachi, Fumio Komori, Koki Takanashi, and Masato Kotsugi. “Fabrication of L10-FeNi by Pulsed-Laser Deposition.” Applied Physics Letters 114, no. 7 (2019): 072404.
13. Rodríguez, V. A. Peña, C. Rojas-Ayala, J. Medina Medina, P. Paucar Cabrera, J. Quispe-Marcatoma, C. V. Landauro, J. Rojas Tapia, E. M. Baggio-Saitovitch, and E. C. Passamani. “Fe50Ni50 Synthesized by High Energy Ball Milling: A Systematic Study Using X-Ray Diffraction, EXAFS and Mössbauer Methods.” Materials Characterization 149 (2019): 249–54.
14. Barmak, Katayun, Bincheng Wang, Andrew T. Jesanis, David C. Berry, and Jeffrey M. Rickman. “Quantitative Kinetic Models of the A1 to L10 Transformation in FePt and Related Ternary Alloy Films.” IEEE Transactions on Magnetics 50, no. 1 (2014): 1–4.

15. Montes-Arango, A. M., N. C. Bordeaux, J. Liu, K. Barmak, and L. H. Lewis. “L10 Phase Formation in Ternary FePdNi Alloys.” Journal of Alloys and Compounds 648 (2015): 845–52.
16. Bordeaux, N., A.M. Montes-Arango, J. Liu, K. Barmak, and L.H. Lewis. “Thermodynamic and Kinetic Parameters of the Chemical Order–Disorder Transformation in L10 FeNi (Tetrataenite).” Acta Materialia 103 (January 15, 2016): 608–15.
17. Alves Dias, P., S. Bobba, S. Carrara, and B. Plazzotta. “The Role of Rare Earth Elements in Wind Energy and Electric Mobility.” Anticipation and foresight. Luxembourg (Luxembourg): Publications Office of the European Union, 2020.
18. Stoner, E.C., and E.P. Wohlfarth. “A Mechanism of Magnetic Hysteresis in Heterogeneous Alloys.” IEEE Transactions on Magnetics 27, no. 4 (1991): 3475–3518.
19. Yang, C. -W., D. B. Williams, and J. I. Goldstein. “A Revision of the Fe-Ni Phase Diagram at Low Temperatures (<400 °C).” Journal of Phase Equilibria 17, no. 6 (December 1, 1996): 522–31.
20. Van Deen, J. K. and Van Der Woude, F. “PHASE DIAGRAM OF THE ORDER-DISORDER TRANSITION IN Ni3Fe.” J. Phys. Colloques 41, no. C1 (1980): C1-367-C1-368.
21. Deen, J. K. Van, and F. Van Der Woude. “Phase Diagram of the Order-Disorder Transition in Ni3Fe.” Acta Metallurgica 29, no. 7 (1981): 1255–62.
22. Laughlin, David E. “Magnetic Transformations and Phase Diagrams.” Metallurgical and Materials Transactions A 50, no. 6 (June 1, 2019): 2555–69.

23. Bhadeshia, H. K. D. H., and C. M. Wayman. “Phase Transformations: Nondiffusive.” In Physical Metallurgy (Fifth Edition), edited by David E. Laughlin and Kazuhiro Hono, Fifth Edition., 1021–72. Oxford: Elsevier, 2014.
24. Reuter, K. B., D. B. Williams, and J. I. Goldstein. “Determination of the Fe−Ni Phase Diagram below 400°C.” Metallurgical Transactions A 20, no. 4 (April 1, 1989): 719–25.
25. Wasson, John T. “Relationship between Iron-Meteorite Composition and Size: Compositional Distribution of Irons from North Africa.” Geochimica et Cosmochimica Acta 75, no. 7 (April 1, 2011): 1757–72.
26. Gąsior, W., Z. Moser, and A. Dębski. “Heat of Formation of FeNi70, FeNi73.5 and FeNi80 Ordered Alloys from the Homogenous Region of the FeNi3 Phase.” Journal of Alloys and Compounds 487, no. 1 (2009): 132–37.
27. Liu, J., L. J. Riddiford, C. Floristean, F. Goncalves-Neto, M. Rezaeeyazdi, L. H. Lewis, and K. Barmak. “Kinetics of Order-Disorder Transformation of L12 FeNi3 in the Fe-Ni System.” Journal of Alloys and Compounds 689 (2016): 593–98.
28. Einsle, Joshua F., Alexander S. Eggeman, Ben H. Martineau, Zineb Saghi, Sean M. Collins, Roberts Blukis, Paul A. J. Bagot, Paul A. Midgley, and Richard J. Harrison. “Nanomagnetic Properties of the Meteorite Cloudy Zone.” Proceedings of the National Academy of Sciences 115, no. 49 (2018): E11436–45.
29. Soffa, William A., and David E. Laughlin. “Decomposition and Ordering Processes Involving Thermodynamically First-Order Order-Disorder Transformations.” Acta Metallurgica 37 (1989): 3019–28.

30. Cai, Wei, and William D. Nix. Imperfections in Crystalline Solids. MRS-Cambridge Materials Fundamentals. Cambridge: Cambridge University Press, 2016.
31. Koneva, N. A., A. D. Korotaev, and M. A. Bol'shanina. "Ordering Processes and Activation Energy in Ni3Fe-Based Ternary Alloys." Soviet Physics Journal 9, no. 1 (January 1, 1966): 94–99.
32. Lynn, K. G., C. L. Snead, and J. J. Hurst. "Positron Lifetime Studies of Pure Ni from 4.2 to 1700K." Journal of Physics F: Metal Physics 10, no. 8 (August 1980): 1753–61.
33. Zhang, Changjun, and Ali Alavi. "First-Principles Study of Superabundant Vacancy Formation in Metal Hydrides." Journal of the American Chemical Society 127, no. 27 (July 13, 2005): 9808–17.
34. Liu, Jiaxing, and Katayun Barmak. "Method for Measurement of Diffusivity: Calorimetric Studies of Fe/Ni Multilayer Thin Films." Scripta Materialia 104 (July 15, 2015): 1–4.
35. Million, B., J. Růžičková, J. Velíšek, and J. Vřešťál. "Diffusion Processes in the Fe-Ni System." Materials Science and Engineering 50, no. 1 (September 1, 1981): 43–52.
36. Gale, W.F., and T.C. Totemeier, eds. "13 - Diffusion in Metals." In Smithells Metals Reference Book (Eighth Edition), 13–1. Oxford: Butterworth-Heinemann, 2004.
37. Dobroeol'skii, V. D., S. M. Karal'nik, and A. V. Koval'. "X-Ray Spectroscopic Study of Some Alloys in Relation with Deviations from the Additivity Rule." Metallofizika (Akademiya Nauk Ukrainskoi SRR, Institut Metallofiziki) 41 (1972): 73–77.
38. Wood, John A. "The Cooling Rates and Parent Planets of Several Iron Meteorites." Icarus 3, no. 5 (December 1, 1964): 429–59.

39. Soffa, W.A., and David E. Laughlin. “8 - Diffusional Phase Transformations in the Solid State.” In Physical Metallurgy (Fifth Edition), edited by David E. Laughlin and Kazuhiro Hono, 851–1020. Oxford: Elsevier, 2014.
40. Rohrer, Gregory S. “Grain Boundary Energy Anisotropy: A Review.” Journal of Materials Science 46, no. 18 (September 1, 2011): 5881–95.
41. Ledbetter, H. M., and R. P. Reed. “Elastic Properties of Metals and Alloys, I. Iron, Nickel, and Iron-Nickel Alloys.” Journal of Physical and Chemical Reference Data 2, no. 3 (July 1, 1973): 531–618.
42. Sarochawikasit, Rajchawit, Cong Wang, Poom Kumam, Hossein Beladi, Taira Okita, Gregory S. Rohrer, and Sutatch Ratanaphan. “Grain Boundary Energy Function for α Iron.” Materialia 19 (September 1, 2021): 101186.
43. Rohrer, Gregory S., Elizabeth A. Holm, Anthony D. Rollett, Stephen M. Foiles, Jia Li, and David L. Olmsted. “Comparing Calculated and Measured Grain Boundary Energies in Nickel.” Acta Materialia 58, no. 15 (September 1, 2010): 5063–69.
44. Lee, J.-Y., M.P.J. Punkkinen, S. Schönecker, Z. Nabi, K. Kádas, V. Zólyomi, Y.M. Koo, et al. “The Surface Energy and Stress of Metals.” Surface Science 674 (August 1, 2018): 51–68.
45. Porter, D. A., and K. E. Easterling. Phase Transformations in Metals and Alloys. 2nd ed. CRC Press, 1992.
46. Khachaturyan, A. G. Theory of Structural Transformation in Solids. Newburyport: Dover Publications, 2013.

47. Tian, Li-Yun, Oliver Gutfleisch, Olle Eriksson, and Levente Vitos. “Alloying Effect on the Order–Disorder Transformation in Tetragonal FeNi.” Scientific Reports 11, no. 1 (March 4, 2021): 5253.
48. Néel, L., J. Pauleve, R. Pauthenet, J. Laugier, and D. Dautreppe. “Magnetic Properties of an Iron—Nickel Single Crystal Ordered by Neutron Bombardment.” Journal of Applied Physics 35, no. 3 (March 1, 1964): 873–76.
49. Paulevé, J., A. Chamberod, K. Krebs, and A. Bourret. “Magnetization Curves of Fe–Ni (50–50) Single Crystals Ordered by Neutron Irradiation with an Applied Magnetic Field.” Journal of Applied Physics 39, no. 2 (February 1, 1968): 989–90.
50. Kojima, Takayuki, Misako Ogiwara, Masaki Mizuguchi, Masato Kotsugi, Tomoyuki Koganezawa, Takumi Ohtsuki, Taka-Yuki Tashiro, and Koki Takanashi. “Fe–Ni Composition Dependence of Magnetic Anisotropy in Artificially Fabricated L10-Ordered FeNi Films.” Journal of Physics: Condensed Matter 26, no. 6 (January 2014): 064207.

2 Electrodeposition of Near-Equiatomic BCC Fe-Ni

2.1 Introduction

2.1.1 Anomalous Codeposition

Electrodeposition is a simple and efficient method to grow Fe-Ni films of high quality from ~ 10 nm to ~ 100 μm and more. The composition and phase control of electrodeposited Fe-Ni however is complicated by the mechanism called anomalous codeposition. The mechanism of this process was derived from the Fe deposition mechanism first described by J. O'M. Bockris, D. Drazic, and A. R. Despic [1]. The understanding of this mechanism had been developed and refined over time, fueled by the technological importance of Fe-group alloy coatings for recording heads [2], magnetic shields [3], sensors [4, 5], and micro-electro-mechanical systems (MEMS) [6, 7]. The Bockris-Drazic-Despic (BDD) mechanism can be summarized by the following reactions in series:

Step 1: $Me^{++} + 2H_2O \leftrightarrow Me(OH)^{+} + H_3O^{+}$ (2.1)

Step 2: $Me(OH)^{+} + e^{-} \rightarrow Me(OH)_{ads}$ (R. D. S.) (2.2)

Step 3: $Me(OH)_{ads} + H_3O^{+} + e^{-} \rightarrow Me(solid) + 2H_2O$ (2.3)

where reaction (2.2) is the rate-determining step (R. D. S.), and Me^{++} represents a bivalent cation of a 3d transition metal atom having between 25 and 30 electrons, except that Me^{++} cannot be Cu^{++} [8]. If such a mechanism is encountered, deposition of the more noble metal (*i.e.*, the metal with a higher equilibrium reduction potential, which is Ni in the case of Fe and Ni) will be inhibited. The anomalous codeposition of Fe-Ni was first considered by Dahms and Croll as a consequence of the preferential adsorption of ferrous hydroxide — $Fe(OH)_2$ — at the cathode surface [9]. Hessami and Tobias, however, pointed out that the cathode surface, under some deposition conditions where the anomalous behavior was encountered, was not sufficiently alkaline to form the metal hydroxides described by Dahms and Croll. Accordingly, they proposed that it was the metal hydroxide ions — $Fe(OH)^+$ and $Ni(OH)^+$ — instead of the metal hydroxides — $Fe(OH)_2$ and $Ni(OH)_2$ — that were competing for the surface adsorption sites [10]. Matlosz instead proposed a different model, whereby the competitive adsorption of the metal hydroxide ions was described as a result of the difference in the adsorption kinetics (*i.e.*, the rate constants of reaction (2.2) and (2.3) in the BDD mechanism) instead of the difference in the hydrolysis equilibrium (*i.e.*, the hydrolysis constant, K_{sp}) between $Fe(OH)^+$ and $Ni(OH)^+$. This model can explain the anomalous codeposition behavior without requiring an assumption of the exact nature of the adsorbed species, and therefore was consistent with the observation that the anomalous codeposition behavior was encountered in a wide range of local pH [11]. Zech, Podlaha, and Landolt further demonstrated that the codeposition mechanism of the iron group metals should explain not only the inhibition of the more noble metal, but also the enhancement of the less noble metal [12]. In parallel to reaction (2.2) and (2.3) in the BDD mechanism, Zech et al.

proposed that the less noble metal was reduced alternatively via the catalytic reactions as follows:

Step 2: $Me^1(II) + Me^2(II) + e^- \rightarrow [Me^1(II)Me^2(I)]_{ads}$ (R. D. S.) (2.4)

Step 3: $[Me^1(II)Me^2(I)]_{ads} + e^- \rightarrow Me^1(II) + Me^2(solid)$ (2.5)

where metal Me^1 was more noble than metal Me^2. Both $Me^1(II)$ and $Me^2(II)$ were unreduced soluble species, while $Me^1(II)$ served as a catalyst for the reduction of $Me^2(II)$. Similar to the competitive adsorption model described by Matlosz [11], the exact chemical formulae of the soluble species need not be specified. The reaction intermediate — $[Me^1(II)Me^2(I)]_{ads}$ — competed with the elemental intermediates — $Me^1(I)_{ads}$ and $Me^2(I)_{ads}$ — for the adsorption sites on the cathode surface [13].

2.1.2 Hydrogen Evolution

Another complication in the electrodeposition of Fe group elements arises from hydrogen evolution, due to the fact that the applied potential for Fe reduction is more negative than hydrogen. While hydrogen evolution was not considered as a prerequisite for the occurrence of anomalous codeposition [12-14], some have suggested that hydrogen may contribute to structural idiosyncrasies that cannot arise from a hydrogen-free deposition environment [15, 16]. Few experimental works investigated these hypotheses, and the relationship between hydrogen evolution reaction (HER) and the crystal structure was rarely clarified. The scanning tunneling

microscopy (STM) work from H. F. Jurca et al. for example suggested that the initial epitaxial growth of Fe on FCC Au (111) surface was not pseudomorphic, as it would be if the deposition occurred under ultra-high vacuum [17], but followed instead the BCC structure with the Nishiyama-Wassermann (NW) orientation, which was attributed to the presence of the adsorbed hydrogen (H_{ads}) [18]. The crystal structure of the first few layers, whether it was truly BCC or FCC, was still under debate [18].

On the other hand, the thermal desorption spectroscopy (TDS) study from Y. Fukai et al. showed that electrodeposited Ni after prolonged aging under ambient condition had retained a significant amount of hydrogen within the lattice [19]. In the same work they proposed that the retained hydrogen was lattice interstitial complexed by vacancies in the vicinity, and suggested that the vacancy concentration in the electrodeposited Ni was much higher than the equilibrium level.

The study from L. Yang on electrodeposited Ni demonstrated the correlation between the higher hydrogen content in the deposit and the occurrence of the metastable hexagonal close packed (HCP) structure [20]. However, the study also showed that the electrolyte (*i.e.*, chloride based) that gave rise to HCP Ni actually occurred under a lower HER current efficiency than the electrolyte (*i.e.*, sulfate based) that did not give rise to HCP Ni, suggesting that increasing the HER current efficiency was not necessarily conducive to the formation of the metastable HCP structure. L. Yang further suggested that only the absorbed hydrogen (H_{ads}) contributed to the formation of the metastable HCP structure. Nevertheless, the study was not able to resolve

whether it was the difference in the anion type or the difference in the hydrogen content or both that resulted in the formation of HCP Ni.

The work from A. Vicenzo compared the XRD patterns of compositionally similar Fe-Ni samples prepared from different applied current densities. The nuances in the peak asymmetry of the FCC (111) reflection suggested that varying the deposition condition can change the phase fractions of FCC and BCC Fe-Ni [16]. A. Vicenzo further suggested that the incorporated hydrogen promoted the supersaturation of Ni in BCC Fe-Ni, reaching a Ni fraction of ~ 35 at.%.

2.1.3 Motivation

During the electrodeposition of Fe-Ni films, the total current consists of the partial currents of three subprocesses: the deposition of Fe, the deposition of Ni, and the HER. The partial current density indicates the rate of each subprocess, which can be affected by the deposition conditions, including the electrolyte composition, the electrolyte pH, the applied potential, etc. Changing any of these conditions usually changes the rates of one or more subprocesses, leading to the difficulty in controlling the composition and the phase fractions of the as-deposited Fe-Ni. This chapter seeks to reveal the connections among the deposition conditions, the partial current densities, and the phase fractions of electrodeposited Fe-Ni thin films (< 30 nm), focusing on the near-equiatomic composition range. This study intends to shed light on the mechanism that controls the phase fraction of electrodeposited Fe-Ni in the presence of anomalous codeposition and hydrogen evolution.

2.2 Experimental Methods

2.2.1 Electrodeposition

Table 2.1 The metal ion concentrations, the metal ion concentration ratio, the pH, the total charge, and the associated applied potentials of each electrolyte being used to deposit the Fe-Ni films reported in this chapter.

Electrolyte	C_{Ni2+} / mM	C_{Fe2+} / mM	C_{Ni2+}/C_{Fe2+}	pH	Q_{TOT} / mC	E_{app} (V vs. MSE)
E-a	1000	90	11:1	2.8	70	-1.525, -1.475, -1.425, -1.375, -1.325
E-b	1000	90	11:1	1.4	176	-1.525, -1.475, -1.425, -1.375, -1.325
E-c1	1000	102	9.8:1	2.8	70	-1.325
E-c2	1000	125	8.0:1	2.8	70	-1.325
E-c3	1000	143	7.0:1	2.8	70	-1.325
E-c4	1000	286	3.5:1	2.8	70	-1.325

Fe-Ni films were prepared by potentiostatic electrodeposition from six different aqueous electrolytes. The pH, the metal ion concentrations, and the metal ion concentration ratio (C_{Ni2+}/ C_{Fe2+}) of each electrolyte are listed in **Table 2.1**. All chemicals were used as purchased. $FeSO_4$ was used as the Fe source. The 1000 mM Ni^{2+} source consists of 180 mM of $NiCl_2$ and 820 mM of $NiSO_4$. Each electrolyte also contains 3 mM of saccharin ($C_7H_5NO_3S$) and 550 mM of boric acid (H_3BO_3). The pH of the solution was adjusted by adding H_2SO_4. Milli-Q™ deionized water with a resistivity of 18.2 MOhm was used throughout. The potentials and the total charges are also listed accordingly in **Table 2.1**. The Fe-Ni films were grown under potential control onto a Au (120 nm) / SiO_2 /Si substrate, where the Au layer has a (111) texture and a random in-plane orientation. The exposure area was 0.8 × 0.8 cm^2, defined by the Kapton® tape. The electrical contact was made from the front side of the substrate using the 3M™ copper conductive tape.

Electrodeposition experiments were carried out with an EG&G PAR(263A) potentiostat/ galvanostat, using a vertical three-electrode setup with the sample/substrate as the working electrode, a platinum mesh as the counter electrode, and a saturated mercury mercurous sulfate electrode as the reference electrode (MSE, + 0.65 V vs. SHE). The electrodepositions were performed at room temperature without intentional stirring.

2.2.2 Electrochemical Quartz Crystal Microbalance

Electrochemical quartz crystal microbalance (EQCM) measurements were performed in three electrolytes, E-a, E-b, and E-c3 (see **Table 2.1**), from which a set of Fe-Ni films with nominally the same composition but different phase fractions was generated. A PAR (QCM922) EQCM was used to simultaneously record the current density and the mass change at the working electrode, enabling the separation of the alloy deposition current from that of the side reactions. The EQCM study carried out during cyclic voltammetry (CV) allows for the determination of the alloy deposition onset potential and the current efficiency as a function of the applied potential. The scan rate ($\Delta E/\Delta t$) was 20 mV/sec. A vertical three electrode setup was used. The working electrode of the EQCM study was an Au coated AT-cut quartz resonator with a diameter of 0.5 cm (a working area of A = 0.196 cm^2) and a resonant frequency of 9 MHz. The resonant frequency of the working electrode decreases as the mass of the film increases. The mass change (Δm) can be calculated from the measured resonant frequency change (Δf) through the Sauerbrey equation [21]:

$$\Delta m = - K \Delta f \qquad \text{eq. 2.1}$$

The constant K in **eq. 2.1** is calculated from the physical constants of the quartz resonator [21], including the working area (0.196 cm^2), the elastic constant of the AT-cut quartz crystal (2.947×10^{11} $g/cm^{-1}/s^{-2}$), the density of the quartz crystal (2.65 g/cm^3), and the frequency of the quartz crystal (9.00 MHz). The constant K is calculated to be 1.068 ng/Hz. The calculated mass change of the deposited alloy is further converted into the deposition charge transfer by the Faraday law:

$$\Delta Q_{FeNi} = \Delta m \, (zF/M) \qquad \text{eq. 2.2}$$

In **eq. 2.2**, F is the Faraday constant (F = 96485.3 C/mol), z is the valency number of the ions ($z = z_{Fe2+} = z_{Ni2+} = 2$), and M is the molar mass in unit of g/mol of the deposit. Here, the film composition experimentally determined by EDS is used to calculate the molar mass. Notice that the charge transfer (Q_{FeNi}) in **eq. 2.2** is indexed by the subscript "FeNi". This charge transfer refers to the deposition process only, which is different from the total charge (Q_{TOT}) in **Table 2.1**. The total charge (Q_{TOT}) involves the charge transfer from both the deposition process and the HER by-process. The deposition charge transfer is then converted into the current density by:

$$J_{FeNi} = (\Delta Q_{FeNi}/\Delta E)\,(\Delta E/\Delta t\,) / A \qquad \text{eq. 2.3}$$

In **eq. 2.3**, $\Delta Q_{FeNi}/\Delta E$ is extracted from the slope of the $Q_{FeNi}(E)$ curve, $\Delta E/\Delta t$ is the scan rate, and A is the working area. For each of the three electrolytes (E-a, E-b, E-c3) of the EQCM study, the partial current density extracted from the EQCM measurement is therefore most accurate in vicinity of the potential or the potential range, with which Fe-Ni films were grown under potential control (**Table 2.1**).

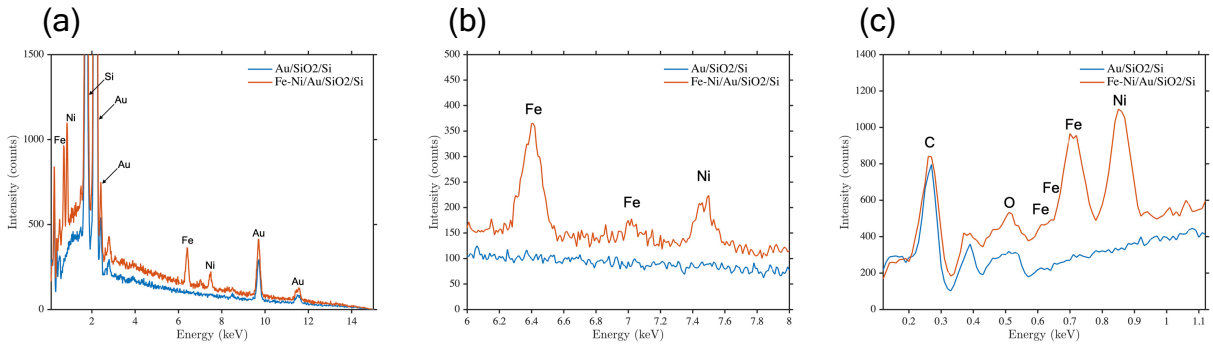

Figure 2.1. (a) Energy dispersive X-ray spectra (EDS) of Fe-Ni film on Au/SiO2/Si substrate (red curve) and bare Au/SiO2/Si substrate (blue curve). The sample was deposited from electrolyte E-b (**Table 2.1**) under condition D (**Table 2.2**) with a composition of ca. 40 at.%Ni. **(b)** The region in (a) showing the Fe/Ni K Lines (6 ~ 8 keV). (c) The region in (a) showing the Fe/Ni L lines (0.6 ~ 0.9 keV).

2.2.3 Characterization

The film composition was determined using the EDS instrument attached to a FEI Quanta LV200 scanning electron microscope with an acceleration voltage of 15 kV. The elements Fe and Ni were identified by the respective K lines. Standardless quantifications were performed with the Oxford Instruments software AZtec (Appendix **A 2.2**). A spectrum was collected from the Au (120 nm) / SiO_2 /Si substrate with the same acceleration voltage (**Figure 2.1**). In comparison to the sample spectrum, the absence of Fe and Ni lines in the substrate spectrum indicated that the

Fe and Ni lines in the sample spectrum were detected from the film region. The sample spectrum can thus be used to gauge the Fe-Ni composition of the film region, despite that the information depth was larger than the film thickness. For each Fe-Ni film, EDS spectra from five different locations on the film surface were collected, from which the mean and the standard deviation of the composition were extracted. The composition uncertainties reported later in **Figure 2.2** and **Table 2.2** were derived from the aforementioned point-to-point variation only. The surface morphology was characterized using a FEI Quanta 650 scanning electron microscope with an acceleration voltage of 5 kV.

The FEI TITAN Transmission Electron Microscope (TEM) was used to investigate the cross-section morphology. High resolution imaging (HR-TEM) was performed by Eric Hoglund at the University of Virginia. The cross section specimen was prepared by focus ion beam (FIB) milling using the Helios UC G4 Dual Beam FIB-SEM also by Eric Hoglund at the University of Virginia. The standard milling methods were used. The milling was performed at 30 kV. A carbon layer, an e-beam Pt layer, and then a Ga-beam Pt layer were deposited to protect the sample surface. After creating the trenches with a 9300 pA beam, both sides of the cross section were milled with a 430 pA beam. A “U-cut” was made at the bottom of the sample. The sample was attached to the needle with Pt, and then cut free. Subsequently, the sample was attached to the TEM grid with Pt, and the needle was cut off the sample. The sample was then thinned, with the current being reduced from 230 to 80 pA. A final clean was performed at 5 kV.

The crystal structure and phase constitution of the alloy films were investigated in the Bragg−Brentano geometry using the Empyrean multipurpose X-ray diffractometer, which has a Cu Kα (λ = 1.5406 Å) radiation source. The $\theta/2\theta$ scan mode was used to collect XRD patterns for the comparison of the phase fraction. The $\omega/2\theta$ scan mode was used to collect XRD patterns for confirming the existence of the highly textured BCC phase. In the diffractometer coordinate frame, ω is defined as the angle between the incident beam and the horizontal plane, 2θ is defined as the angle between the incident beam and the detected diffracted beam, ω offset is defined by:

$$\omega \text{ offset} = \omega - 0.5\times(2\theta) \qquad \text{eq.2.4}$$

Therefore, ω offset is the tilt angle of the scattering vector ($\boldsymbol{S}$) with respect to the vertical direction. In the $\theta/2\theta$ scan mode, ω offset = 0^{o} and thus $\omega = \theta$, so $\boldsymbol{S}$ is always along the vertical direction during the scan. In the $\omega/2\theta$ scan mode, ω offset is non-zero and thus $\omega \neq \theta$, and $\boldsymbol{S}$ is always along the direction tilted with respect to the vertical direction by the ω offset. The $\omega/2\theta$ scan is particularly useful when the sample is so highly textured that only one or two peaks of each phase can be identified from the $\theta/2\theta$ scan pattern. The $\omega/2\theta$ scan was used by M. Fayette et al. to differentiate the FCC phase from the HCP phase of electrodeposited Co [22].

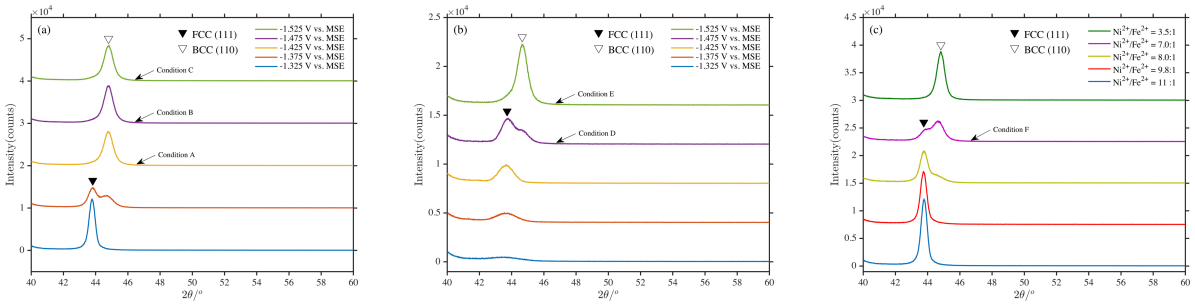

Figure 2.2. (a) XRD patterns of Fe-Ni films (S-01) deposited under different applied potentials from −1.325 to −1.525 V vs. MSE (from the bottom to the top) from the same electrolyte (E-a) in which pH = 2.8 and C_{Ni2+}/C_{Fe2+} = 11:1. **(b)** XRD patterns of Fe-Ni films (S-02) deposited under different applied potentials from −1.325 to −1.525 V vs. MSE (from the bottom to the top) from the same electrolyte (E-b) in which pH = 1.4 and C_{Ni2+}/C_{Fe2+} = 11:1. **(c)** XRD patterns of Fe-Ni films (S-03) deposited from different electrolytes (E-a, E-c1 ~ E-c4) with the C_{Ni2+}/C_{Fe2+} ratio varying from 11:1 to 3.5:1 (from the bottom to the top) with the same pH of 2.8 under the same applied potential of −1.325 V vs. MSE. The text arrows annotate the 6 deposition conditions (A - F) listed in **Table 2.2** that result in ca. 40 at.%Ni but different phase fractions.

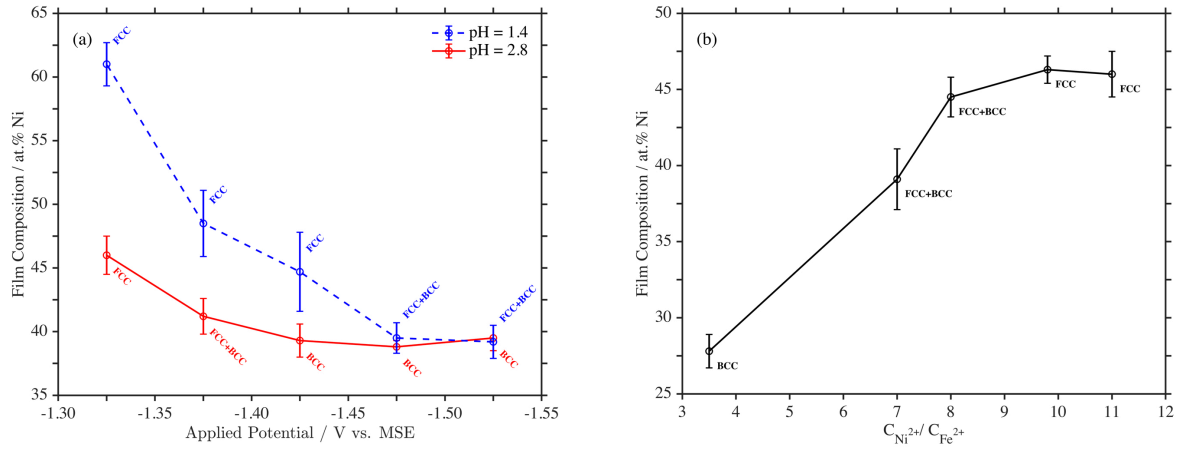

Figure 2.3. (a) Red solid curve: composition of Fe-Ni films (S-01) deposited under different applied potentials from −1.325 to −1.525 V vs. MSE from the electrolyte (E-a) in which pH = 2.8 and C_{Ni2+}/C_{Fe2+} = 11:1; blue dashed curve: composition of Fe-Ni films (S-02) deposited under different applied potentials from −1.325 to −1.525 V vs. MSE from the electrolyte (E-b) in which pH = 1.4 and C_{Ni2+}/C_{Fe2+} = 11:1. **(b)** composition of Fe-Ni films (S-03) deposited from different electrolytes (E-c4, E-c3, E-c2, E-c1, E-a) with the C_{Ni2+}/C_{Fe2+} ratio increasing from 3.5:1 to 11:1 with the same pH of 2.8 under the same applied potential of −1.325 V vs. MSE.

2.3 Results

2.3.1 Phase fraction and composition relationship

Three sets of films were grown to investigate the effect of three deposition conditions: (1) the applied potential; (2) the electrolyte pH; (3) the metal ion ratio (C_{Ni2+}/C_{Fe2+}) of the electrolyte. These sets are denoted as S-01, S-02, and S-03 in the following. XRD patterns in **Figure 2.2** show that both the FCC phase and the BCC phase have a well-defined preferred orientation. The FCC phase is dominantly (111), and the BCC phase is dominantly (110). Both are the lowest energy facets for these two structures. The XRD patterns in **Figure 2.2a** show that as the applied potential becomes more negative from −1.325 to −1.525 V_{MSE}, the BCC phase fraction increases. **Figure 2.2b** shows that the samples deposited from an electrolyte of lower pH follow a similar trend. A decrease in Ni^{2+}/Fe^{2+} ratio shown in **Figure 2.2c** results in a transition from FCC to BCC. The red solid curve in **Figure 2.3a** shows that as the applied potential becomes more negative, the Ni content first decreases and then flattens at ca. 40 at.%Ni. The blue dashed curve in **Figure 2.3a** shows that the samples deposited from a lower pH electrolyte follow a similar trend, reaching a similar composition. Notice that the composition becomes insensitive to the applied potential when the BCC phase starts to develop. Also notice that such a behavior appears both at high and low pH. At constant pH, the formation of the BCC phase is favored over the FCC one at a more negative applied potential. With the same applied potential, a less acidic electrolyte seems to favor the BCC phase over the FCC phase.

Figure 2.3b shows that as the ratio C_{Ni2+}/C_{Fe2+} increases, the Ni fraction in the film increases. The Ni/Fe ratio in the electrolyte being much larger than the Ni/Fe ratio in the film is a sign of

anomalous codeposition, which also indicates that the electrodeposition is not under the diffusion control. **Figure 2.2c** shows that as C_{Ni2+}/C_{Fe2+} decreases, *i.e.*, as the Ni fraction in the Fe-Ni film decreases, the phase fraction changes from being purely FCC, to a mixture FCC/BCC phase, and finally to a pure BCC phase.

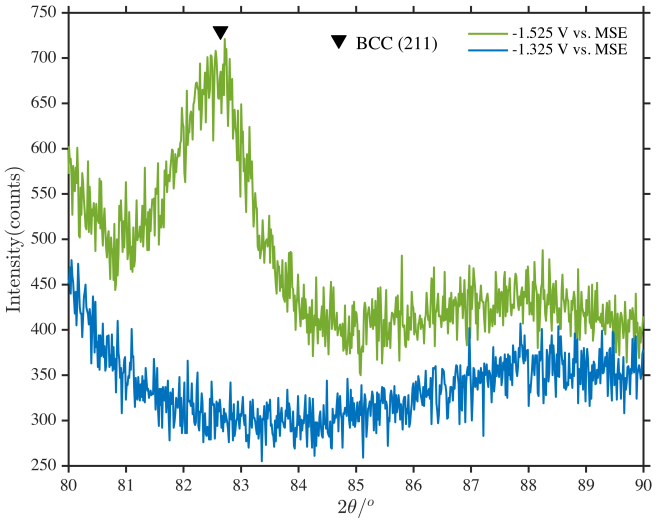

Figure 2.4. XRD ω/2θ scan patterns (ω offset = −30°) taken from the Fe-Ni films (S-01) deposited under different applied potentials from the electrolyte (E-a) in which pH = 2.8 and C_{Ni2+}/C_{Fe2+} = 11:1. The pattern in blue is taken from the Fe-Ni film deposited under − 1.325 V vs. MSE, corresponding to the θ/2θ pattern in blue in **Figure 2.2a**. The pattern in green is taken from the Fe-Ni film deposited under − 1.525 V vs. MSE, corresponding to the θ/2θ pattern in green in **Figure 2.2a**.

Throughout our discussion of the XRD patterns, the Bragg reflections at ~ 43.8° and ~ 44.8° are identified as the FCC (111) and the BCC (110) reflections, respectively. The peak assignments are further confirmed with XRD $\omega/2\theta$ scan by setting the ω offset to be −30°, *i.e.*, the angle between the [110] and the [211] direction in a BCC lattice. Based on the peak assignments, when the scattering vector (***S***) is tilted by 30° from the film normal, a highly (110) textured BCC film should show the (211) reflection at ~ 82.6°, while a highly (111) textured FCC film should not show a Bragg reflection at the same 2θ position. This was indeed observed experimentally: the pattern in blue in **Figure 2.4** corresponds to the same sample as the pattern in blue in **Figure 2.2a**; the pattern in green in **Figure 2.4** corresponds to the same sample as the pattern in green in **Figure 2.2a**. When the $\theta/2\theta$ scan only shows a peak at ~ 43.8°, the $\omega/2\theta$ scan does not show a peak at ~ 82.6°, indicating the existence of the FCC phase. When the $\theta/2\theta$ scan only shows a peak at ~ 44.8°, the $\omega/2\theta$ scan shows a peak at ~ 82.6°, indicating the existence of the BCC phase. The broad peak at ~ 88.1° present in both the blue and the green patterns in **Figure 2.4** corresponds to the diamond cubic (422) reflection of the Si wafer. The tail between 80° ~ 83° is due to the Au FCC (311) reflection. Notice that the angle between [311] and [111] directions in an FCC lattice is 29.5°, which is very close to 30°. The existence of the Au FCC (311) reflection indicates that the (111) textured Au substrate has a finite degree of mosaicity.

So far, six different sets of electrodeposition conditions (A-F) have been used to prepare Fe-Ni films of about the same composition (ca. 40 at.%Ni) but not necessarily the same phase fraction. These conditions are listed in **Table 2.2**. The film composition is an indicator of the relative

deposition rate of Fe and Ni (J_{Fe}/J_{Ni}); controlling J_{Fe}/J_{Ni} allows for the investigation of the effects of the rate of hydrogen evolution (J_H) upon the phase fraction.

Table 2.2 The six sets of deposition conditions (A-F) that lead to the alloy composition of ca. 40 at.%Ni but different phase fractions. The corresponding Fe-Ni deposition partial current density ($|J_{Fe\text{-}Ni}|$), hydrogen evolution partial current density ($|J_H|$), total current density ($|J_{TOT}|$), current efficiency (η), and estimated thickness (h).

Condition	Electrolyte	E_{app} (V vs. MSE)	C_{Ni} (at.%)	Phase	$\|J_{Fe\text{-}Ni}\|$ (mA/cm²)	$\|J_H\|$ (mA/cm²)	$\|J_{TOT}\|$ (mA/cm²)	η (%)	h (nm)
A	E-a	-1.425	39.3 ± 1.3	BCC	3.5	2.0	5.5	64	25
B	E-a	-1.475	38.8 ± 0.5	BCC	5.1	2.6	7.8	66	26
C	E-a	-1.525	39.5 ± 1.0	BCC	7.7	3.5	11.2	69	27
D	E-b	-1.475	39.5 ± 1.2	BCC+FCC	1.1	12.8	13.9	8	8
E	E-b	-1.525	39.2 ± 1.3	BCC+FCC	1.7	14.6	16.2	10	10
F	E-c3	-1.325	39.1 ± 2.0	BCC+FCC	1.2	0.7	1.9	62	24

2.3.2 Phase constitution and partial currents relationship

EQCM was used to separate the partial current density of Fe-Ni deposition ($J_{FeNi} = J_{Fe}+J_{Ni}$) from the total current density ($J_{TOT} = J_{Fe}+J_{Ni}+J_H$). The three electrolytes (E-a, E-b, and E-c3) that generate the electrodeposition conditions in **Table 2.2** were studied individually. **Figure 2.5** shows the mass change during the potential sweep for each of the three electrolytes. **Figure 2.6** compares the partial current density loops of Fe-Ni deposition (dashed curves) and the total current density loops (solid curves) of the three electrolytes. A deviation of the partial current loop from the total current loop yields the hydrogen evolution current. Note that the mass change of the crystal resonator (**Figure 2.5**) was converted into the deposition current by the Faraday's

law (**eq. 2.2**), which requires knowing the alloy composition in order to calculate the molar mass (M). To study the deposition conditions in **Table 2.2** that result in a film composition of ca. 40 at. %Ni, we assume the Invar (35 at.%Ni) and the equiatomic compositions as the lower and the upper bounds of the alloy composition. As a result, the partial current loops in **Figure 2.6** are most accurate in vicinity of the applied potentials listed in **Table 2.2**. The region on the negative (cathodic) sweep of the current density loop between −1.60 and −1.20 V_{MSE} was fitted with a 3rd-order polynomial using a least-square method (**Figure 2.7**). This applied potential range includes all potentials that were used to prepare the samples being reported in this work. **Figure 2.8a** shows the fitted partial current densities of Fe-Ni (J_{FeNi}) from the three electrolytes of interest. **Figure 2.8b** shows the partial current of hydrogen (J_H) calculated by subtracting the fitted partial current of the alloy deposition from the fitted total current (J_{TOT}). **Figure 2.9** shows the current efficiencies ($\eta = J_{FeNi}/J_{TOT}\times 100\%$) of the three electrolytes. Based on **Figure 2.8** and **Figure 2.9**, the deposition current ($J_{Fe\text{-}Ni}$), the hydrogen evolution current (J_H), and the current efficiency (η) of the deposition conditions (A-F) are listed in **Table 2.2**.

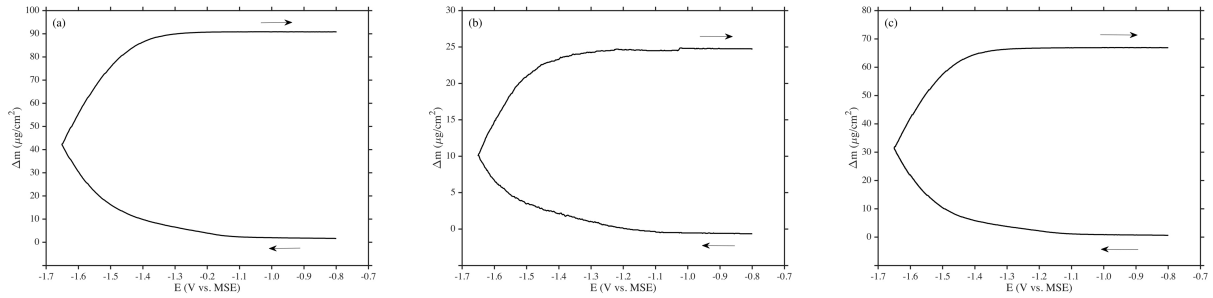

Figure 2.5. (a) mass change per active area from the electrolyte (E-a) in which pH = 2.8 and C_{Ni2+}/C_{Fe2+} = 11:1.**(b)** mass change per active area from the electrolyte (E-b) in which pH = 1.4 and C_{Ni2+}/C_{Fe2+} = 11:1. **(c)** mass change per active area from the electrolyte (E-c3) in which pH = 2.8 and C_{Ni2+}/C_{Fe2+} = 7:1. A scan rate of 20 mV/sec was used.

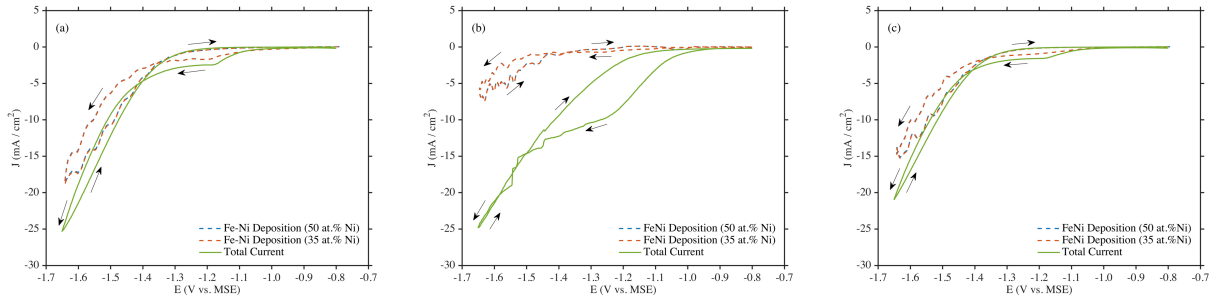

Figure 2.6. Partial (red/blue dashed) and total (solid green) current densities (the red and blue dashed curves assume a composition of 35 and 50 at.%Ni respectively) of **(a)** the electrolyte (E-a) in which pH = 2.8 and C_{Ni2+}/C_{Fe2+} = 11:1. **(b)** the electrolyte (E-b) in which pH = 1.4 and C_{Ni2+}/C_{Fe2+} = 11:1. **(c)** the electrolyte (E-c3) in which pH = 2.8 and C_{Ni2+}/C_{Fe2+} = 7:1.

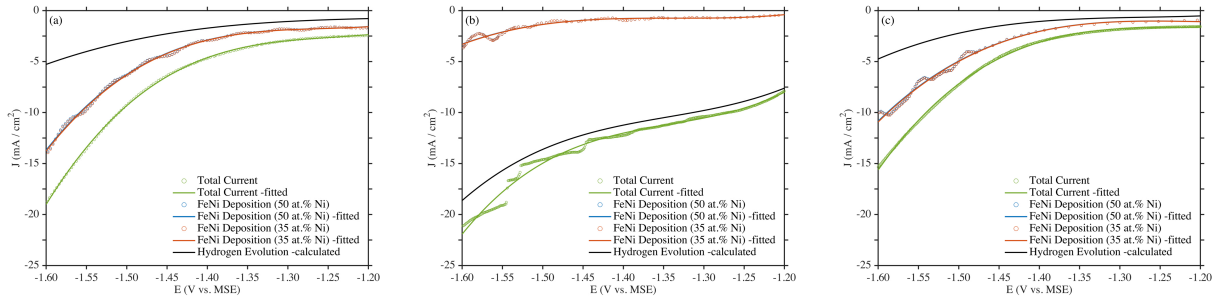

Figure 2.7. Hydrogen evolution (black), alloy deposition (red/blue) and total (green) current densities in the cathodic branch (the red and blue curves assume a composition of 35 and 50 at.%Ni respectively); the blue, red and green circles are the raw data; the blue, red and green solid lines are 3rd-order polynomials fitted to the raw data; the black line (hydrogen evolution) is calculated by subtracting the average alloy deposition current density from the total current density: **(a)** the electrolyte (E-a) in which pH = 2.8 and C_{Ni2+}/C_{Fe2+} = 11:1; **(b)** the electrolyte (E-b) in which pH = 1.4 and C_{Ni2+}/C_{Fe2+} = 11:1; **(c)** the electrolyte (E-c3) in which pH = 2.8 and C_{Ni2+}/C_{Fe2+} = 7:1.

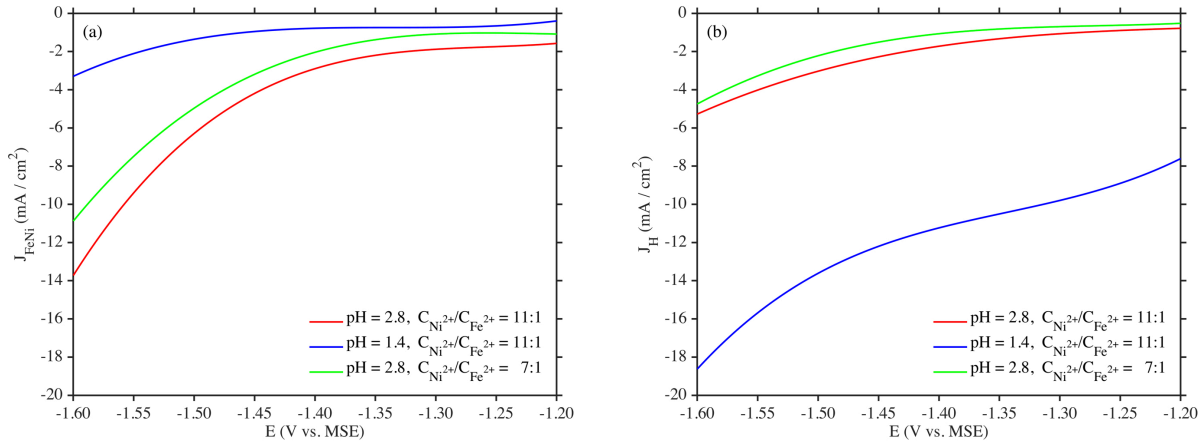

Figure 2.8. Partial current densities of Fe-Ni alloy deposition **(a)** and partial current densities of hydrogen evolution **(b)** from the three different electrolytes: red curve: the electrolyte (E-a) in which pH = 2.8 and C_{Ni2+}/C_{Fe2+} = 11:1; blue curve: the electrolyte (E-b) in which pH = 1.4 and C_{Ni2+}/C_{Fe2+} = 11:1; green curve: the electrolyte (E-c3) in which pH = 2.8 and C_{Ni2+}/C_{Fe2+} = 7:1.

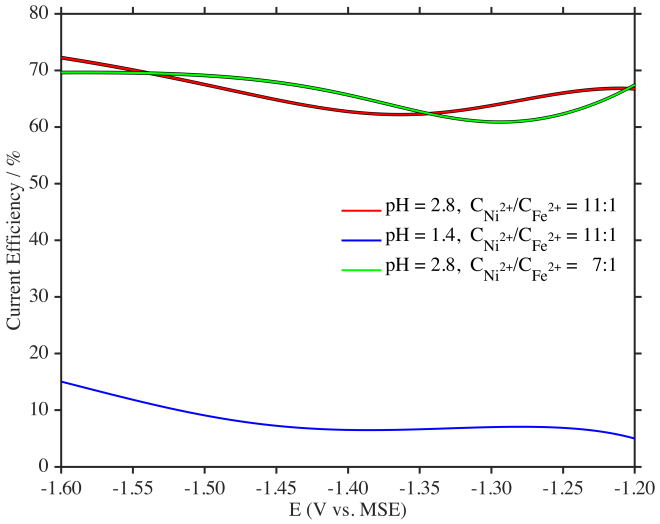

Figure 2.9. Current efficiency of alloy deposition in: red band: the electrolyte in which pH = 2.8 and C_{Ni2+}/C_{Fe2+} = 11:1; blue band: the electrolyte in which pH = 1.4 and C_{Ni2+}/C_{Fe2+} = 11:1; green band: the electrolyte in which pH = 2.8 and C_{Ni2+}/C_{Fe2+} = 7:1. The width of each band is bounded by the two curves that assume a composition of 35 and 50 at.%Ni respectively.

By examining **Table 2.2**, one can see that an increase in the alloy deposition partial current (J_{FeNi}) was observed whenever the phase fraction of the BCC phase increased. The larger J_{FeNi} of condition A, B, and C (> 3 mA/cm^2) leads to a pure BCC phase, while the smaller J_{FeNi} of condition D, E, and F (< 2 mA/cm^2) leads to a mixture of BCC/FCC phase. Further examine condition D, E, and F. On one hand, the XRD patterns in **Figure 2.2b** and **Figure 2.2c** show that the fraction of the BCC phase follows: D < F < E. On the other hand, **Table 2.2** shows that J_{FeNi} follows the same sequence: D < F < E. Such a direct correlation between the phase fraction and the deposition partial current (J_{FeNi}), however, was not observed between the phase fraction and

the hydrogen current (J_H), nor was it observed between the phase fraction and the current efficiency (η). In other words, increasing the hydrogen evolution rate does not necessarily give rise to an increase in the phase fraction of the BCC phase unless the alloy deposition rate was also increased. Although this does not exclude the possibility that the presence of hydrogen is critical to the formation of the BCC Fe-Ni, our results strongly suggest that a sufficiently high alloy deposition rate is required for the formation of the Invar-to-equiatomic BCC Fe-Ni on the Au (111) substrate.

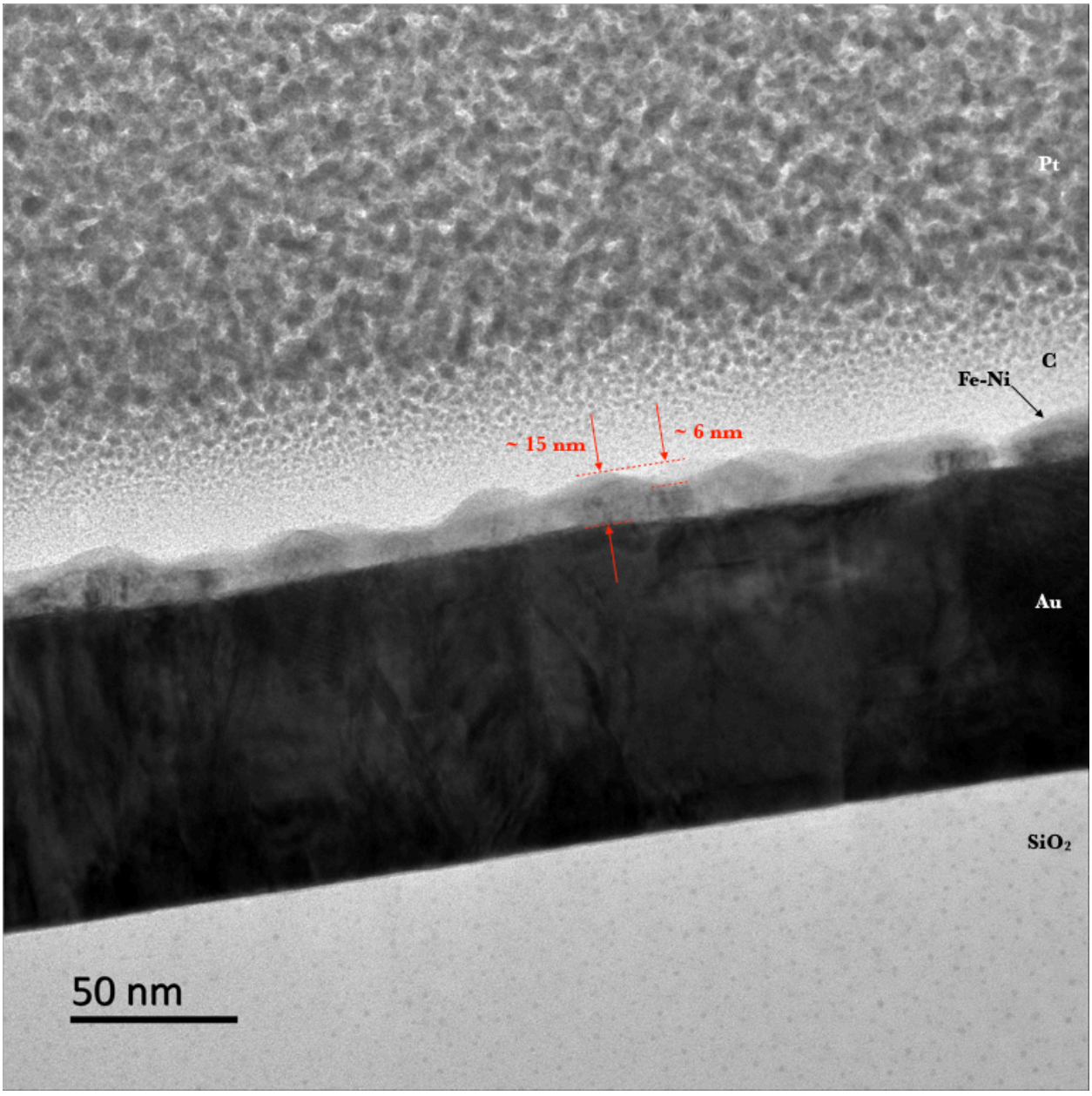

Figure 2.10. Cross section TEM image of the Fe-Ni film deposited from electrolyte E-b in which pH = 1.4 and C_{Ni2+}/C_{Fe2+} = 11:1 under the applied potential of − 1.475 V_{MSE} (condition D).

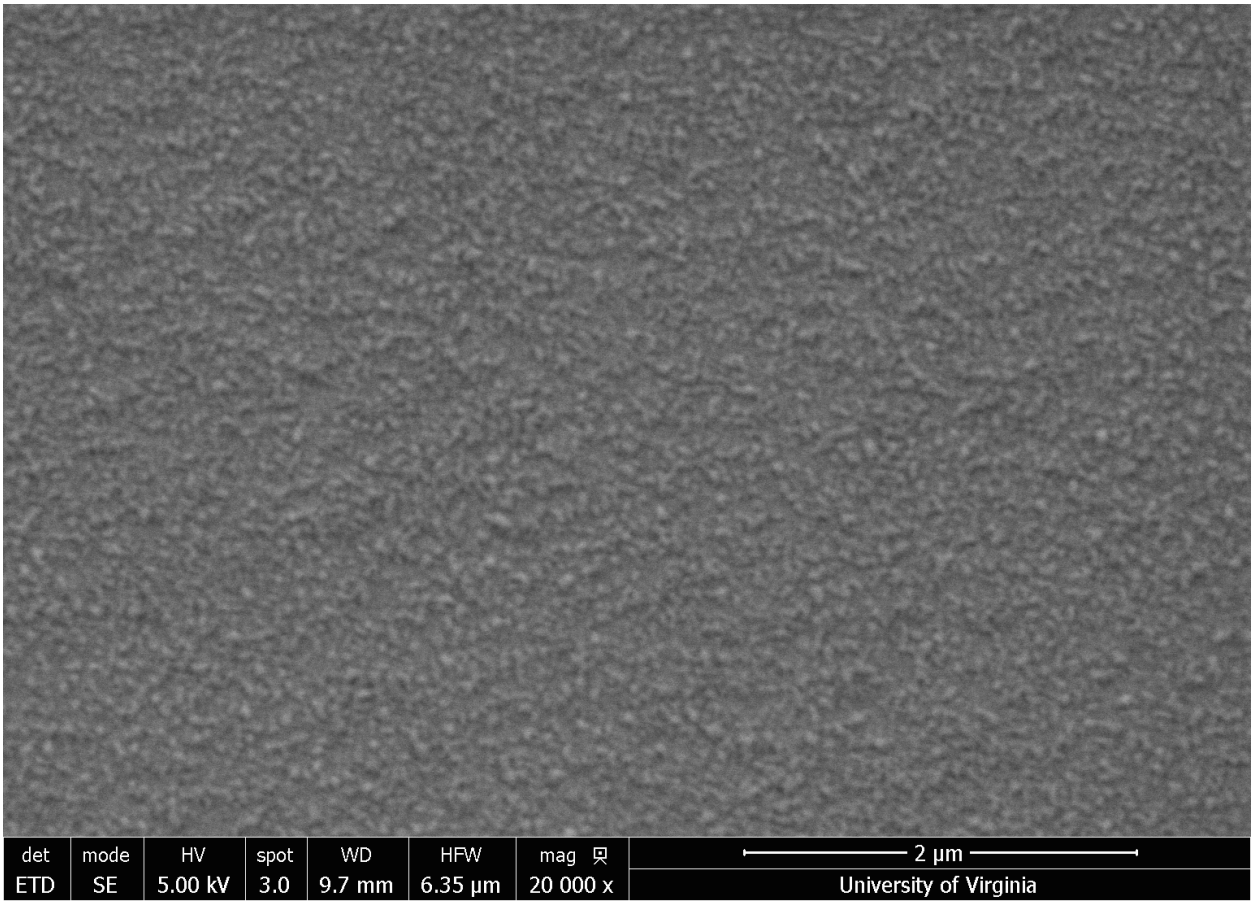

Figure 2.11. Plane view SEM image of the Fe-Ni film deposited from electrolyte E-b in which pH = 1.4 and C_{Ni2+}/ C_{Fe2+} = 11:1 under the applied potential of − 1.475 V_{MSE} (condition D).

2.3.3 Film morphology and epitaxy

Figure 2.10 and **Figure 2.11** show the cross section TEM image and the plane view SEM image of a Fe-Ni film (electrolyte E-b, condition D; see **Table 2.2**), which exhibits mixed BCC/FCC phases. The ~ 12 nm thick continuous film with a peak-to-valley thickness fluctuation of ~ 3 nm was formed on the Au under layer. The observed thickness is comparable to the estimated thickness (~ 8 nm) calculated from the total charge (Q_{TOT} in **Table 2.1**) and the current efficiency (η in **Table 2.2**). The cross section TEM image features coalesced islands with spherical caps, suggesting that the deposition flux is quite fast with respect to the adatom diffusion, preventing the development of well-defined facets. Assuming that the nucleation and growth of the electrodeposited layer follows the Volmer-Weber mode, we provide a rule-of-thumb estimation of the lateral grain size and the wetting angle of the spherical caps. The lateral grain size (L) is estimated to be ~ 33 nm, by counting the number of spherical caps (~ 10) along the field of view of ~ 330 nm in length. By gauging the vertical distance between the top of the spherical cap and the level of the triple junction between two adjacent caps, the minimum thickness (d_{min}) for island coalescence is ~ 6 nm. Further applying the Pythagoras theorem, the radius (R) of the spherical cap is calculated from L and d_{min} to be ~ 26 nm, where $R = [(L/2)^2+(d_{min})^2] / (2d_{min})$. The wetting angle ($\theta_c$) of the spherical cap is extracted from L and R to be ~ 39°, where $\theta_c = 90^o - \arccos[L/(2R)]$. The relationship between island shape and growth condition was discussed theoretically by L. Guo et al. [23]. Although examining the growth stress is out of the scope of this work, the lateral grain size (L) and the wetting angle (θ_c) are key parameters in the kinetic model formulated by E. Chason et al. that targets on the stress evolution during the Volmer-Weber growth of electrodeposited films [24].

Figure 2.12a shows the high resolution TEM (HR-TEM) image of the Fe-Ni film. **Figure 2.12b** shows the Fast Fourier Transform (FFT) of the Fe-Ni film region highlighted by the cyan dashed box in the HR-TEM image. **Figure 2.12c** shows the FFT of the Au substrate region highlighted by the yellow dashed box in the HR-TEM image. The lattice parameter extracted from **Figure 2.12b** agrees with the lattice parameter of the FCC Fe-Ni (3.58 Å) from the XRD pattern (purple curve) in **Figure 2.2b** with a deviation less than 0.1 Å. The lattice parameter extracted from **Figure 2.12c** matches the lattice parameter of the FCC Au (4.07 Å), with a deviation less than 0.1 Å. Although the lattice parameter determined from the FFT is less accurate than that from the XRD pattern, it is precise enough to differentiate the FCC Fe-Ni phase from the FCC Au phase. Furthermore, the FFT patterns show that the Fe-Ni film region and the Au substrate region highlighted in the HR-TEM image are both imaged along the FCC[110] zone axis with the FCC[111] direction aligned perpendicular to the film surface. This strongly suggests that the FCC Fe-Ni grew epitaxially (locally) onto the FCC Au substrate.

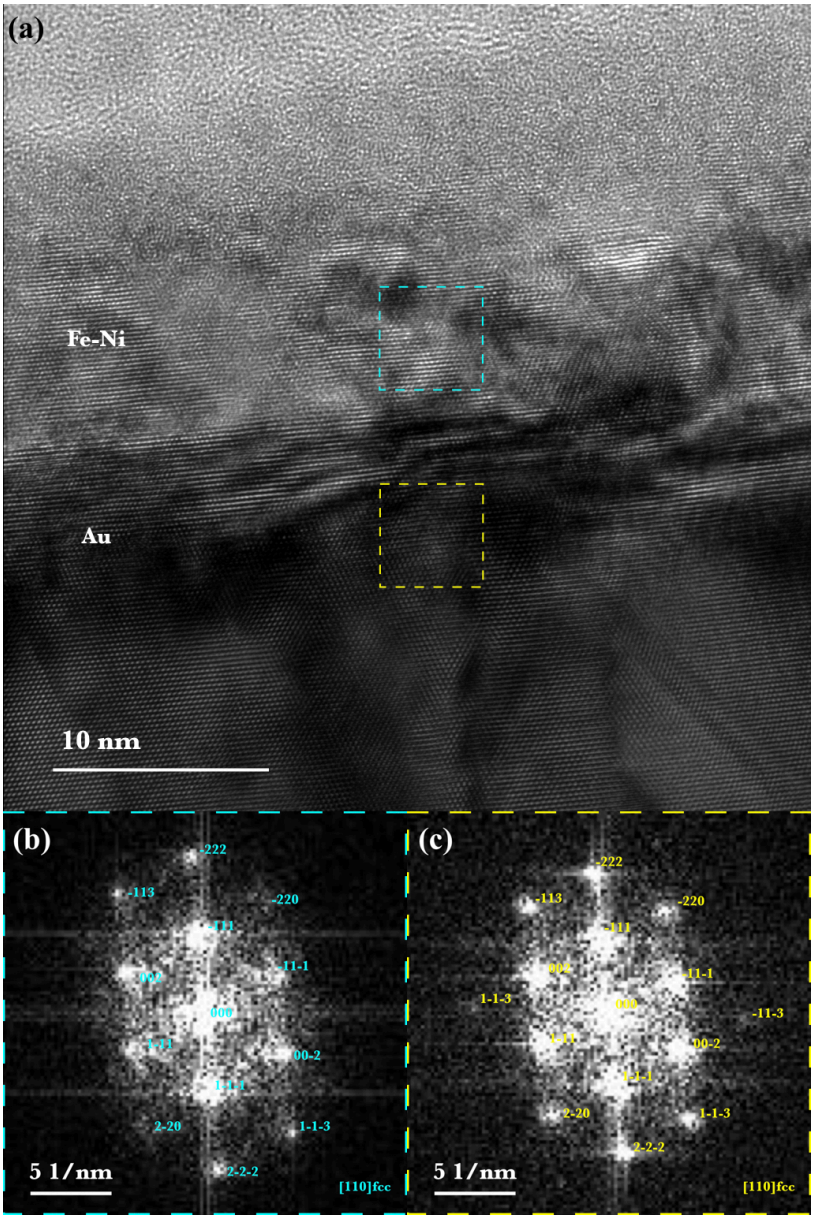

Figure 2.12. (a) Cross section high-resolution TEM image of the Fe-Ni film deposited from electrolyte E-b in which pH = 1.4 and C_{Ni2+}/C_{Fe2+} = 11:1 under the applied potential of − 1.475 V_{MSE} (condition D). **(b)** Fast Fourier Transform (FFT) of the Fe-Ni film region in the HR-TEM image highlighted by the cyan dashed box. **(c)** FFT of the Au substrate region in the HR-TEM image highlighted by the yellow dashed box.

2.4 Discussion

2.4.1 The formation of BCC Fe-Ni with ca. 40 at.%Ni

The XRD patterns in **Figure 2.2** show that both of the Fe-Ni phases have their unique textures, (111) and (110) texture for the FCC and BCC phase, respectively. This suggests that the phase fraction is strongly influenced by the initial growth on the Au (111) substrate. We begin our discussion with the effect of the Au (111) substrate upon the phase fraction. The scanning tunneling microscopy (STM) work by J. A. Stroscio et al. shows that under ultra-high vacuum (UHV) environment the epitaxial growth of Fe on Au (111) substrate is pseudomorphic by the FCC structure in the first 2-3 monolayers (ML); when the film grows above 3 ML, a transition from the FCC phase to the BCC phase occurs [17]. Furthermore, the epitaxial relationship between the BCC Fe (formed at thickness > 3ML) and the Au (111) substrate is BCC Fe (110) [1-10] ||FCC Au (111) [11-2], which is known as the Nishiyama-Wassermann (NW) orientation [25]. The lattice parameter of FCC Fe is 3.63 Å; a pseudomorphic FCC structure Fe on Au (111) (a = 4.07 Å) has a lattice mismatch of ε = +12%. The interatomic spacing along [001] of the BCC Fe is 2.87 Å, comparing to the interatomic spacing of 2.88 Å along [1-10] of Au. On the other hand, the interatomic spacing along [1-10] of the BCC Fe is 4.05 Å, comparing to the interatomic spacing of 4.98 Å along [11-2] of Au. The lattice mismatch of BCC Fe epitaxially grown on Au (111) by the NW mode is ε = +0.3% along BCC Fe [001] and ε = +23% along BCC Fe [1-10]. The epitaxial growth of the metastable FCC Fe on Au (111) in the first 2-3 ML is due to the smaller strain of the pseudomorphic FCC phase in comparison to the BCC phase, while the transition from the metastable FCC Fe to BCC Fe at thickness larger than 3 ML is driven by the smaller Gibbs free energy of the BCC phase of pure Fe. Extracted from the XRD patterns shown

in **Figure 2.2**, the lattice parameter of the FCC Fe-Ni with ca. 40 at.%Ni is 3.58 ± 0.01 Å, while the lattice parameter of the BCC Fe-Ni with ca. 40 at.%Ni is 2.86 ± 0.01 Å. The lattice mismatch corresponding to the FCC Fe-Ni is +14%. The lattice mismatch corresponding to the BCC Fe-Ni is +0.7% and +23% along the Fe [001] and the Fe [1-10], respectively. Therefore, after alloying ca. 40 at.%Ni, the lattice mismatch of the BCC structure remains significantly larger than that of the FCC structure, which indicates that the Au (111) substrate favors the formation of the FCC phase if we only consider the strain energy difference.

According to the Fe-Ni phase diagram, a Ni content of 40 at.% is far beyond the equilibrium solubility limit of Ni (~ 6 at.%) in the BCC Fe-Ni, which should also favor the formation of the FCC phase [26]. Despite the formation of BCC Fe-Ni with ca. 40 at.%Ni not being favored by the epitaxial effect of the Au (111) substrate, nor by the supersaturation of the Ni content, pure BCC Fe-Ni with ca. 40 at.%Ni was obtained experimentally from the potentiostatic electrodeposition in this work, specifically from deposition conditions A, B, and C (**Table 2.2**). It is precisely in this sense we suggest that the presence of hydrogen in the electrochemical environment may play a critical role in the formation of the BCC phase Fe-Ni with a composition in the Invar-to-equiatomic range.

The presence of hydrogen in the electrochemical environment may contribute to the formation of the BCC phase Fe-Ni through different mechanisms: (i) the surface adsorbed atomic hydrogen (H_{ads}) at the growth front between the electrode/electrolyte interface; (ii) through the interstitial hydrogen (H_{ins}) incorporated into the lattice of the deposited alloy.

The STM and the Φ scan XRD results from H. F. Jurca et al. suggest that under electrochemical (EC) environment the crystal structure of the first three epitaxial monolayers of Fe on Au (111) substrate is BCC instead of FCC, which follows the Nishiyama-Wassermann (NW) orientation [18]. This difference in the initial crystal structure was attributed to the presence or absence of the adsorbed atomic hydrogen (H_{ads}) on the Fe surface during the deposition in EC and UHV environment, respectively. It was suggested that the H_{ads} on the Fe surface reduces the interaction between the two topmost atomic planes; and in the case of the initial growth of Fe on Au (111), the H_{ads} reduces the interaction between Fe and the Au substrate underneath, which could lead to the absence of pseudomorphism [18]. It was suggested in the same work that the presence of H_{ads} enhanced surface mobility [18]. **Figure 2.13** shows the difference in the epitaxial growth schematically.

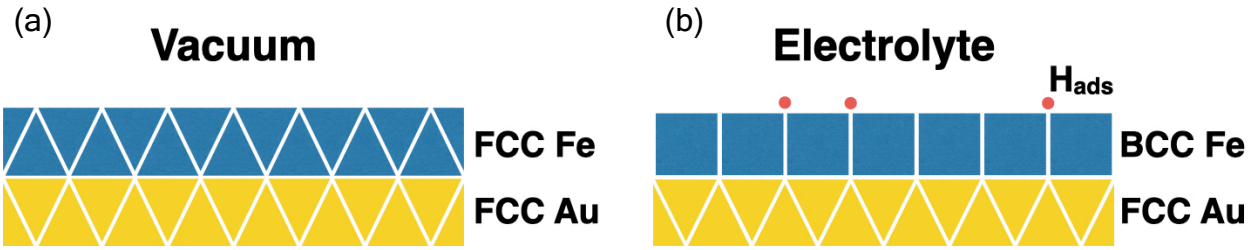

Figure 2.13. (a) Pseudomorphic FCC Fe grown on FCC Au (111) in a vacuum environment. **(b)** Non-pseudomorphic BCC Fe epitaxially grown on FCC Au (111) in an electrochemical environment. The yellow triangles represent Au atoms. The blue triangles represent Fe atoms in the FCC structure. The blue squares represent Fe atoms in the BCC structure. The red circles represent hydrogen adatoms at the growth front in an electrochemical environment.

As discussed above, alloying ca. 40 at.%Ni does not cause a significant change to the relative strain energy difference between the FCC and the BCC phase. In other words, the Au (111) surface prefers the formation of the FCC phase rather than the BCC phase when the Fe-Ni has a composition of ca. 40 at.%Ni. The observation of pure BCC Fe-Ni with ca. 40 at.%Ni in this work (**Figure 2.2**) leads us to speculate that the presence of H_{ads} may affect the phase fraction of the initially grown Fe-Ni alloy on Au (111) in a similar fashion as the crystal structure of the epitaxial Fe on Au (111) was affected: the H_{ads} weakens the bonding between the initially grown Fe-Ni film and the substrate as well compromises the preference to form FCC Fe-Ni on Au (111).

On the other hand, it was suggested that atomic hydrogen can be incorporated into the lattice in the form of hydrogen interstitial (H_{ins}) during electrodeposition. The presence of H_{ins} in electrodeposited Ni and Fe-Ni ([H]/[M]~10^{-4}) was demonstrated by Y. Fukai et al. and N. Mukaibo et al. with thermal desorption spectroscopy (TDS); these results suggest that a substantial amount of lattice vacancies form vacancy-hydrogen clusters with the hydrogen interstitials [19, 27]. The first principle calculation by C. Zhang et al. indicates that the vacancy formation energy in Ni hydride is lower than that in pure Ni, which is consistent with the experimental suggestion that the presence of hydrogen interstitials contribute to the incorporation of more vacancies [28]. Notice the parallelism between the formation of BCC phase and the incorporation of vacancies: they both evolve towards a more open or less close-packed structure. D. Ikuta et al. has recently revised the phase diagram of Fe-H based on in-situ neutron diffraction measurements under high pressure conditions; these results show that the BCC/FCC phase

boundary of Fe-H extends to higher temperatures in comparison to the BCC/FCC phase boundary of pure Fe [29]. On the other hand, it is generally accepted that the FCC/liquid phase boundary drops to substantially lower temperatures (i.e., the melting point decreases) in the presence of hydrogen [29-32]. In other words, in the presence of hydrogen under high pressures, the FCC phase field contracts while the BCC phase field and the liquid phase field expand. These observations may be extrapolated as another indication that a more open structure is being favored in the presence of hydrogen. Moreover, the work from Vicenzo on galvanostatically electrodeposited Fe-Ni suggests that the maximum concentration of Fe achieved in the metastable FCC Fe-Ni is lower when the hydrogen evolution is more intense, which is aligned with the theory that hydrogen incorporation destabilizes the more close-packed crystal structure [16].

To summarize the discussion in this section, we speculate that the formation of highly textured BCC Fe-Ni with ca. 40 at.%Ni on Au (111) substrate found in this work could be explained by the two-fold effect of hydrogen in the electrochemical environment: (1) the presence of surface adsorbed hydrogen (H_{ads}) weakens the bonding between the initially grown Fe-Ni film and the Au substrate, reducing the strain energy associated with the non-pseudomorphic growth of the BCC phase on the FCC (111) surface; (2) the presence of incorporated hydrogen, probably in the form of hydrogen interstitial (H_{ins}), extends the Ni solubility limit in the BCC lattice of Fe-Ni in the favor of a more open structure.

Tangential to this topic, Appendix **A 2.1** summarized an attempt to investigate the chemical state of the hydrogen atoms in electrodeposited Ni foils by neutron vibrational spectroscopy (NVS). The absolute amount of hydrogen atoms within the electrodeposited Ni sample was shown to be strictly less than 1 mmol. Accordingly, the concentration, defined as the amount of hydrogen atoms normalized by the amount of Ni atoms in the sample, is strictly less than 2×10^{-3}.

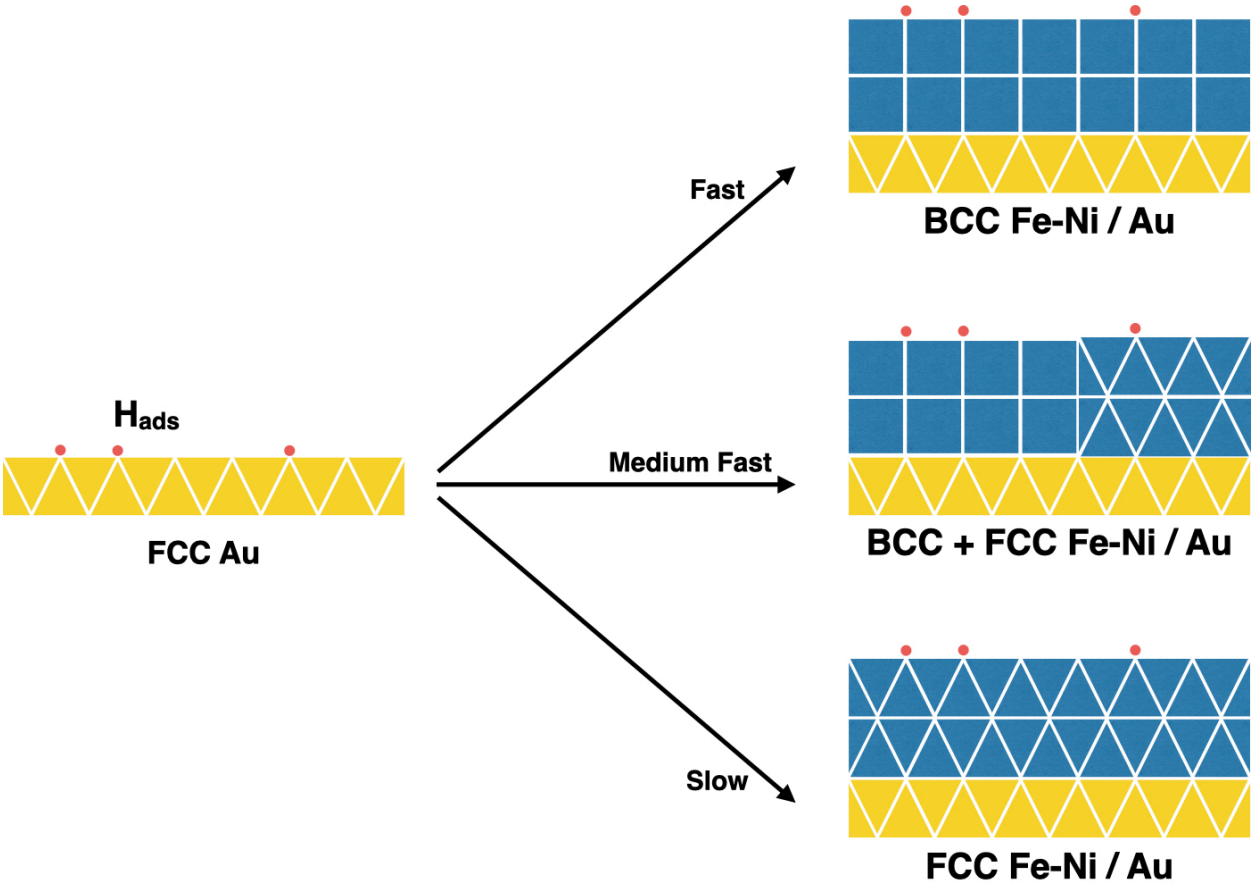

Figure 2.14. The correlation between the phase fraction and the deposition current density (i.e., the growth rate) hypothesized to be a consequence of the competition between the BCC-to-FCC relaxation kinetics and the growth kinetics at the growth front. The yellow triangles represent Au atoms. The blue triangles represent Fe atoms in the FCC structure. The blue squares represent Fe atoms in the BCC structure. The red circles represent hydrogen adatoms at the growth front.

2.4.2 The effects of deposition condition on phase fraction of Fe-Ni with ca. 40 at.%Ni

The effect of deposition conditions on the phase fraction of Fe-Ni in the Invar-to-equiatomic composition is addressed in this section. Specifically, we examine what deposition conditions favor the formation of the BCC phase, and conjecture what could be the mechanism behind. Our electrochemistry study of the electrodeposition conditions demonstrates that the alloy deposition rate can affect the phase fraction of the electrodeposited Fe-Ni alloy, since increasing the alloy deposition current (J_{FeNi}) favors the formation of the BCC over the FCC phase (**Table 2.2**). On the other hand, the crystallographic texture and the epitaxy of the Fe-Ni samples reported in this work (**Figure 2.2** and **Figure 2.12**) suggest that the phase fraction is influenced by the initial growth on the Au (111) substrate. We speculate the following theory to account for both the local epitaxial growth and the phase fraction variation under different J_{FeNi}. Due to the effects of H_{ads} and H_{ins} described in the previous section (**2.4.1**), the Fe-Ni nuclei on Au (111) show the BCC instead of FCC structure. Immediately after the nucleation, however, a structural relaxation from the BCC to the FCC phase may occur, driven by the epitaxial effect of the Au (111) substrate, which is weaker in the presence of H_{ads}, but still contributing at some level. Based on **Table 2.2**, such a structural relaxation occurs when J_{FeNi} is relatively small (~ 1.5 mA/cm^2). When J_{FeNi} is sufficiently large (> 3.5 mA/cm^2), the growth process becomes much faster than the competing relaxation process, and the BCC nuclei initially grown on Au are quickly buried underneath the growth front and becomes unable to undergo the BCC-to-FCC relaxation. Whether the relaxation occurs or not, once the nuclei starts to grow, the subsequently grown lattice is less prone to undergo any structural relaxation or transformation, because the bond between the Fe-Ni layers is stronger than the bond between the initially grown Fe-Ni layer and the Au substrate. This

difference in the binding energy was confirmed by H. F. Jurca et al., showing that Fe is more strongly bound to Ni than to Au, based on the positive shift of the dissolution potential of Fe from Ni respective to that of Fe from Au [18]. The occurrence and the extent of such structural relaxation depends on the competition between the structural relaxation kinetics and the growth kinetics, which manifests as a correlation between the phase fraction and the partial current (J_{FeNi}). **Figure 2.14** illustrates the proposed theory schematically.

Recall from section **2.3.2** that increasing J_H does not necessarily lead to a larger fraction of the BCC phase. This seems to contradict with the theory that the presence of hydrogen in the electrochemical environment favors the formation of the BCC phase. The apparent contradiction is resolved by noticing that not all H^+ being reduced remain adsorbed on the film surface — they can recombine to form H_2. The result from this work suggests that a higher J_H does not guarantee a higher level of hydrogen incorporation — a relatively high J_{FeNi} is also required to trap the adsorbed hydrogen before they recombine to from H_2. Notice that such behavior is very similar to that observed in the galvanostatic electrodeposition of Ni by L. Yang, where the formation of the metastable HCP phase Ni was not correlated with the higher hydrogen evolution current (J_H) but with the higher overall current (J_{TOT}) and the higher incorporated hydrogen [20]. A comment that differentiates the adsorbed hydrogen and the recombined hydrogen was made by L. Yang to explain this behavior, and it was suggested that only those adsorbed hydrogen that remained trapped contributed to the formation of the metastable HCP phase [20].

2.5 Conclusion

Pure BCC Fe-Ni films (< 30 nm) with (110) texture and a composition in the Invar-to-equiatomic range (ca. 40 at.%Ni) were grown by potentiostatic electrodeposition on Au (111) substrate. Based on the epitaxial strain and the high supersaturation of Ni content associated with its formation, the presence of hydrogen in the electrochemical environment was suggested to play a critical role in the formation of the metastable BCC Fe-Ni. Different electrodeposition conditions were found to change the phase constitution without varying the composition of the Fe-Ni alloy (ca. 40 at.%Ni). Investigation of these conditions with the electrochemical quartz crystal microbalance (EQCM) further indicates that a sufficiently large alloy deposition partial current (J_{FeNi}) is always associated with the formation of the metastable BCC phase. The EQCM study also reveals that increasing the hydrogen evolution current density (J_H) does not guarantee an increase in the phase fraction of the BCC Fe-Ni. A mechanism that emphasizes the initial epitaxial growth on the Au (111) substrate was proposed to explain the observed relationship between the alloy deposition rate and the phase fraction. The influence of the Fe-Ni deposition conditions on the metastable phase constitution observed in this work resembles the behavior observed in the Ni electrodeposition that produced the metastable HCP phase [20]. Understanding the formation mechanism and controlling the phase fraction of near-equiatomic BCC Fe-Ni might be significant to the synthesis of $L1_0$ Fe-Ni in the sense that the BCC phase has a higher Gibbs free energy than the FCC phase in the near-equiatomic composition range, and may therefore provide a larger thermodynamic driving force, conducive to accelerate the growth kinetics of the ordering transformation.

Appendix A 2.1 Neutron Vibrational Spectrum of Electrodeposited Nickel

A 2.1.1 Electrodeposition of Ni foils

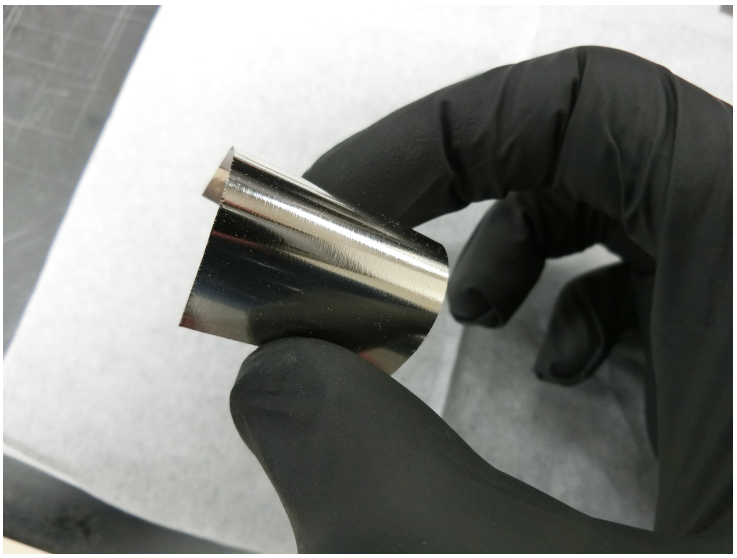

Figure 2.15. Free-standing Ni foil prepared by electrodeposition.

Ni foils were prepared by galvanostatic electrodeposition from an electrolyte consisting of 3 mM saccharin ($C_7H_5NO_3S$), 550 mM boric acid (H_3BO_3), 180 mM of nickel chloride ($NiCl_2$), and 820 mM of nickel sulfate ($NiSO_4$). All chemicals were used as purchased. Milli-Q™ deionized water with a resistivity of 18.2 MOhm was used. The pH of the electrolyte was adjusted to 3 ~ 4 by the addition of 1M H_2SO_4 droplets. The electrolyte was deaerated by N_2 purging for 15 min before each of the depositions. The Ni foils were grown under galvanostatic control on 410 stainless steel substrates. The exposure area was 3 × 5 cm^2, defined by the Kapton® tape. The electrical contact was made from the front side of the substrate using the 3M™ copper conductive tape. Electrodeposition experiments were carried out with a VersaSTAT 4 potentiostat/galvanostat (PAR), using a vertical three-electrode setup with the sample/substrate as

the working electrode, a metallurgical Ni plate (Caswell Inc.) as the counter electrode, and a Ag/AgCl (in saturated KCl) electrode as the spectating reference electrode (Ag/AgCl sat'd KCl, + 0.199 V vs. SHE). The applied current was 0.3 A, and the corresponding applied current density was 20 mA/cm^2. The electrodepositions were performed at room temperature without intentional stirring. Each of the depositions lasted for 2 hours. The Ni foils grown were pealed off from the stainless steel substrates after each of the depositions. **Figure 2.15** shows an example of the free-standing electrodeposited Ni foils. Each foil weighed ~ 0.62 g, and the current efficiency was ~ 95%. Such an electrodeposition process was conducted for 48 times, accumulating a stack of Ni foils in the weight of 30 g as 1 sample for the neutron vibrational spectroscopy characterization.

A 2.1.2 Neutron vibrational spectroscopy (NVS)

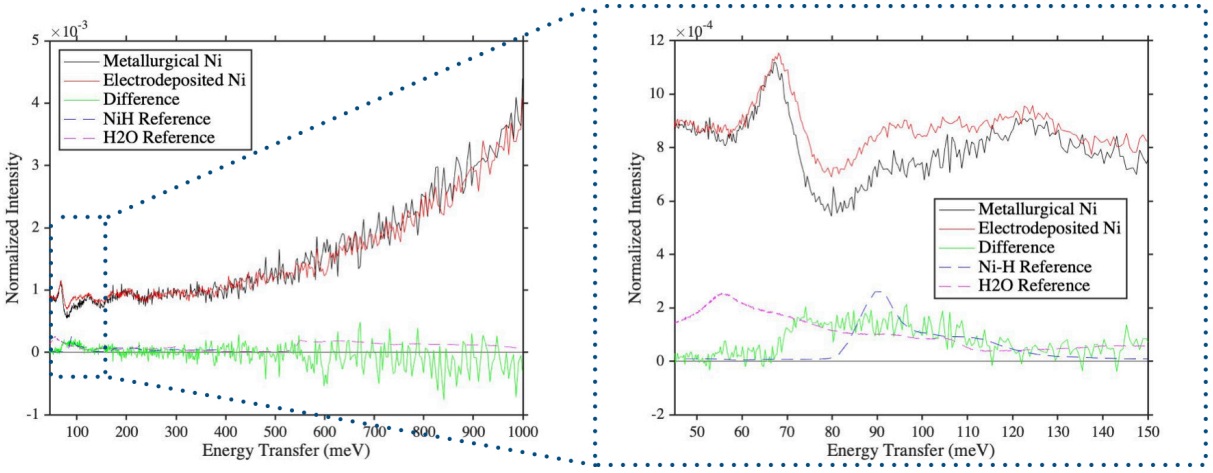

Figure 2.16. Neutron vibrational spectra of electrodeposited Ni and metallurgical Ni.

Neutron vibrational spectra of the electrodeposited Ni sample and the metallurgical Ni sample (Caswell Inc.) were collected with the vibrational spectrometer in the VISION beamline

(BL-16B | SNS) in Oak Ridge National Laboratory (ORNL). The NVS spectra were collected and analyzed by Luke Daemen and Yongqiang Cheng at ORNL. The sample was sealed in a flat Al sample holder with In. The sealed sample holder was mounted on a sample stick and inserted at room temperature to the sample chamber. The sample chamber was then purged 3 times with He gas (*i.e.*, 3 evacuation / He gas backfilling cycles). The spectra were collected at 5 K. **Figure 2.16** shows the NVS spectra of the electrodeposited Ni (red) and the metallurgical Ni (black). The difference spectrum (green) was compared to Ni-H reference spectrum (blue) and the ice (H_2O) reference spectrum (magenta). The difference spectrum shows a broad feature around 70 ~ 110 meV, centering at 90 meV. Notice that Ni has the FCC crystal structure, and only the acoustic modes (< 40 meV) are present in the dispersion diagram. And the overtone of the 33 meV peak (corresponding to the X point extremum in the dispersion diagram) at 66 meV is unlikely to give rise to such a broad feature centered around 90 meV. The plausible origins of the broad feature in the difference spectrum include: (1) H_2O bound near the surface of the Ni foils; (2) $Ni(OH)_2$ and/or NiO(OH) at the surface of the Ni foils; (3) non-crystalline Ni-H. Based on the detection limit of the instrument, whatever status the hydrogen atoms were, the amount of hydrogen atoms within the electrodeposited Ni sample of 30 g is strictly less than 1 mmol, corresponding to a concentration strictly less than 0.2% (*i.e.*, [H] / [M] < 2×10^{-3}). Such an upper bound does not contradict with the hydrogen level reported by Y. Fukai (*i.e.*, [H] / [M] ~ 10^{-4}) [19].

Appendix A 2.2 EDS Spectra and Quantifications

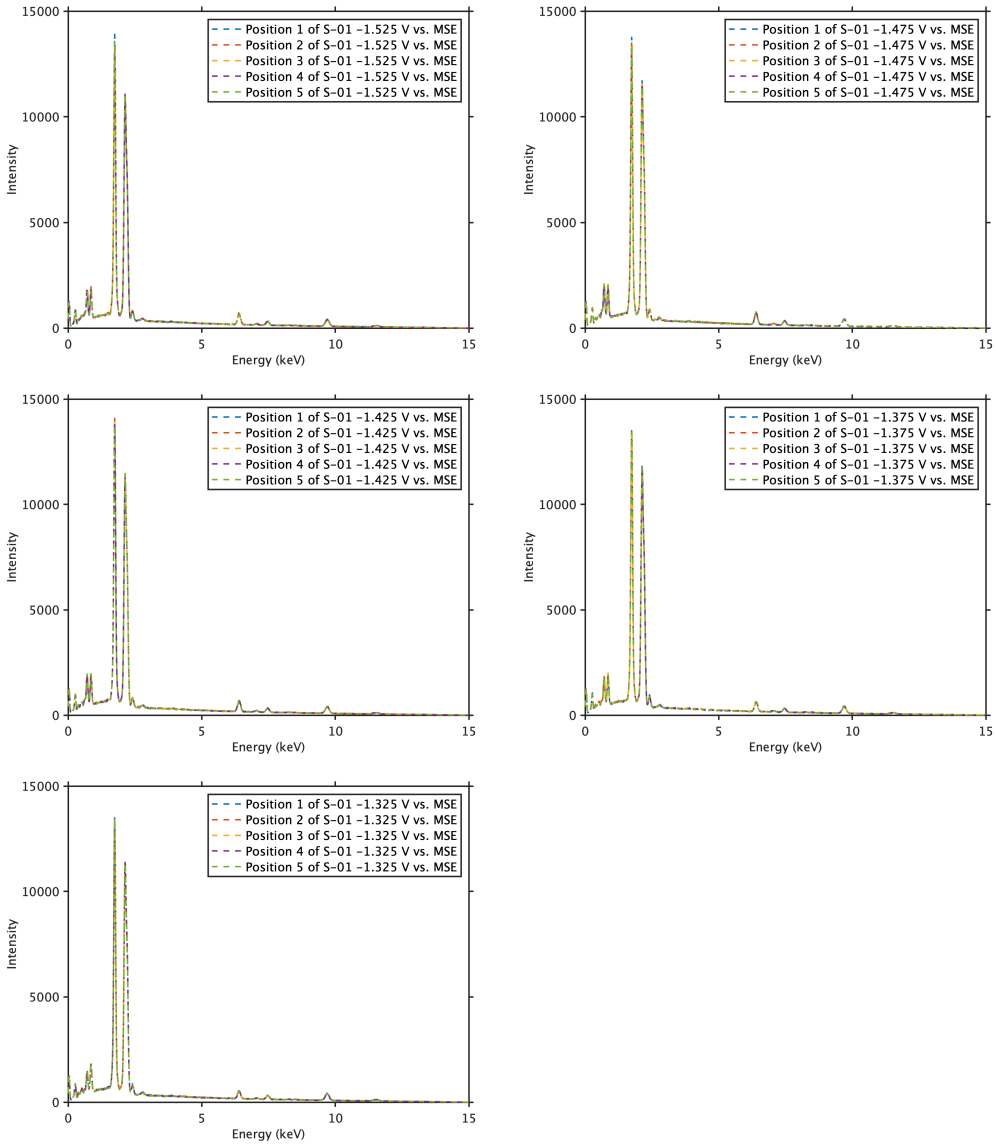

Figure 2.17. EDS spectra of Fe-Ni films in set S-01. Note that S-01 -1.325 V vs. MSE is also in set S-03.

Position 1 of S-01 -1.525 V vs. MSE

Element	Line Type	Apparent Concentration	Intensity Correction	k Ratio	Wt%	Wt% Sigma	At%	Standard Label	Factory Standard
Fe	K series	9.09	1.04	0.09093	60.40	1.52	61.59	Fe	Yes
Ni	K series	5.48	0.96	0.05477	39.60	1.52	38.41	Ni	Yes
Total:					100.00		100.00		

Position 1 of S-01 -1.475 V vs. MSE

Element	Line Type	Apparent Concentration	Intensity Correction	k Ratio	Wt%	Wt% Sigma	At%	Standard Label	Factory Standard
Fe	K series	10.21	1.04	0.10212	59.94	1.39	61.14	Fe	Yes
Ni	K series	6.27	0.96	0.06266	40.06	1.39	38.86	Ni	Yes
Total:					100.00		100.00		

Position 1 of S-01 -1.425 V vs. MSE

Element	Line Type	Apparent Concentration	Intensity Correction	k Ratio	Wt%	Wt% Sigma	At%	Standard Label	Factory Standard
Fe	K series	9.63	1.04	0.09630	61.61	1.51	62.79	Fe	Yes
Ni	K series	5.52	0.96	0.05517	38.39	1.51	37.21	Ni	Yes
Total:					100.00		100.00		

Position 1 of S-01 -1.375 V vs. MSE

Element	Line Type	Apparent Concentration	Intensity Correction	k Ratio	Wt%	Wt% Sigma	At%	Standard Label	Factory Standard
Fe	K series	8.19	1.05	0.08186	58.09	1.64	59.30	Fe	Yes
Ni	K series	5.42	0.96	0.05416	41.91	1.64	40.70	Ni	Yes
Total:					100.00		100.00		

Position 1 of S-01 -1.325 V vs. MSE

Element	Line Type	Apparent Concentration	Intensity Correction	k Ratio	Wt%	Wt% Sigma	At%	Standard Label	Factory Standard
Fe	K series	7.11	1.06	0.07109	51.68	1.57	52.93	Fe	Yes
Ni	K series	6.06	0.96	0.06061	48.32	1.57	47.07	Ni	Yes
Total:					100.00		100.00		

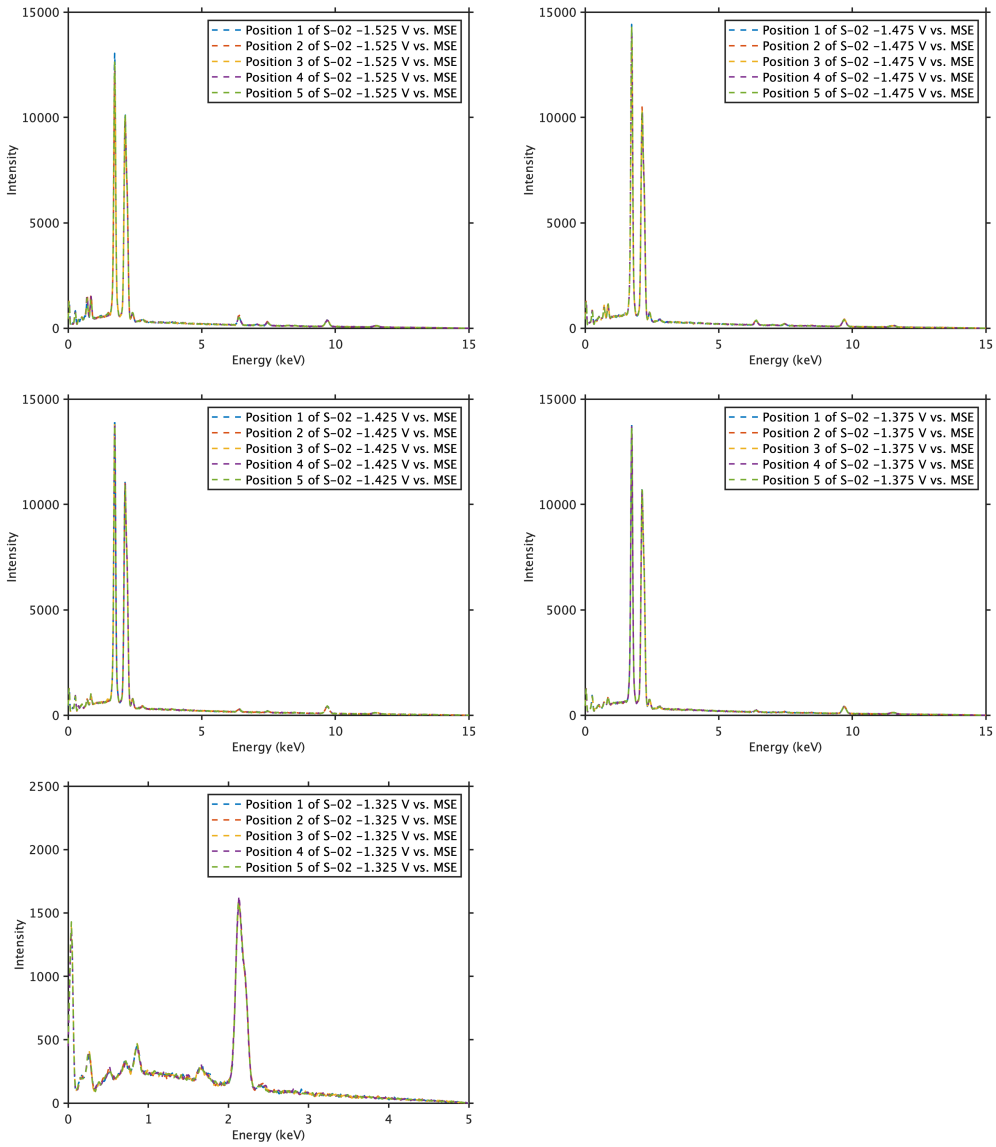

Figure 2.18. EDS spectra of Fe-Ni films in set S-02. Note that S-02 -1.325 V vs. MSE was collected under 5 kV.

Position 1 of S-02 -1.525 V vs. MSE

Element	Line Type	Apparent Concentration	Intensity Correction	k Ratio	Wt%	Wt% Sigma	At%	Standard Label	Factory Standard
Fe	K series	6.27	1.04	0.06270	61.29	2.06	62.47	Fe	Yes
Ni	K series	3.64	0.96	0.03640	38.71	2.06	37.53	Ni	Yes
Total:					100.00		100.00		

Position 1 of S-02 -1.475 V vs. MSE

Element	Line Type	Apparent Concentration	Intensity Correction	k Ratio	Wt%	Wt% Sigma	At%	Standard Label	Factory Standard
Fe	K series	3.89	1.05	0.03888	57.05	2.84	58.27	Fe	Yes
Ni	K series	2.68	0.96	0.02682	42.95	2.84	41.73	Ni	Yes
Total:					100.00		100.00		

Position 1 of S-02 -1.425 V vs. MSE

Element	Line Type	Apparent Concentration	Intensity Correction	k Ratio	Wt%	Wt% Sigma	At%	Standard Label	Factory Standard
Fe	K series	2.03	1.06	0.02026	49.88	4.32	51.13	Fe	Yes
Ni	K series	1.85	0.96	0.01853	50.12	4.32	48.87	Ni	Yes
Total:					100.00		100.00		

Position 1 of S-02 -1.375 V vs. MSE

Element	Line Type	Apparent Concentration	Intensity Correction	k Ratio	Wt%	Wt% Sigma	At%	Standard Label	Factory Standard
Fe	K series	1.57	1.06	0.01567	49.99	5.41	51.24	Fe	Yes
Ni	K series	1.43	0.96	0.01429	50.01	5.41	48.76	Ni	Yes
Total:					100.00		100.00		

Position 1 of S-02 -1.325 V vs. MSE

Element	Line Type	Apparent Concentration	Intensity Correction	k Ratio	Wt%	Wt% Sigma	At%	Standard Label	Factory Standard
Fe	L series	0.97	1.01	0.00972	38.99	5.51	40.19	Pure Element	Yes
Ni	L series	1.23	0.82	0.01233	61.01	5.51	59.81	Pure Element	Yes
Total:					100.00		100.00		

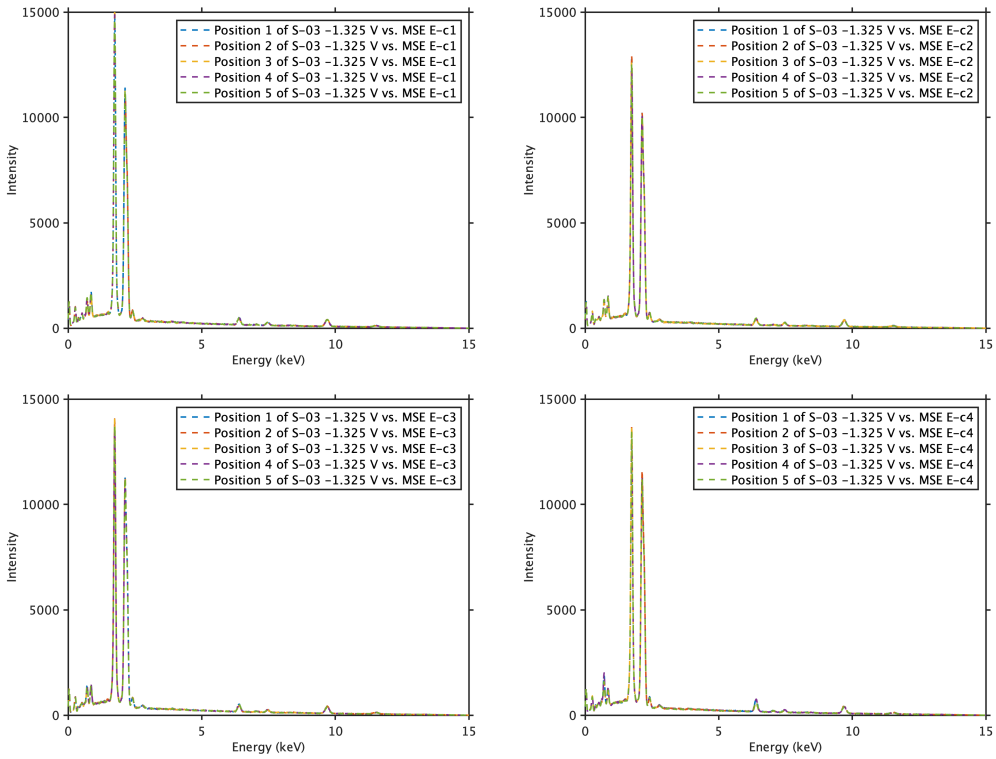

Figure 2.19. EDS spectra of Fe-Ni films in set S-03. Note that S-01 -1.325 V vs. MSE is also in set S-03.

Position 1 of S-03 -1.325 V vs. MSE E-c1

Element	Line Type	Apparent Concentration	Intensity Correction	k Ratio	Wt%	Wt% Sigma	At%	Standard Label	Factory Standard
Fe	K series	6.64	1.05	0.06644	52.97	1.70	54.21	Fe	Yes
Ni	K series	5.39	0.96	0.05386	47.03	1.70	45.79	Ni	Yes
Total:					100.00		100.00		

Position 1 of S-03 -1.325 V vs. MSE E-c2

Element	Line Type	Apparent Concentration	Intensity Correction	k Ratio	Wt%	Wt% Sigma	At%	Standard Label	Factory Standard
Fe	K series	5.45	1.05	0.05446	52.99	1.94	54.24	Fe	Yes
Ni	K series	4.41	0.96	0.04410	47.01	1.94	45.76	Ni	Yes
Total:					100.00		100.00		

Position 1 of S-03 -1.325 V vs. MSE E-c3

Element	Line Type	Apparent Concentration	Intensity Correction	k Ratio	Wt%	Wt% Sigma	At%	Standard Label	Factory Standard
Fe	K series	6.59	1.04	0.06593	59.91	1.99	61.11	Fe	Yes
Ni	K series	4.05	0.96	0.04050	40.09	1.99	38.89	Ni	Yes
Total:					100.00		100.00		

Position 1 of S-03 -1.325 V vs. MSE E-c4

Element	Line Type	Apparent Concentration	Intensity Correction	k Ratio	Wt%	Wt% Sigma	At%	Standard Label	Factory Standard
Fe	K series	10.77	1.03	0.10769	72.29	1.65	73.28	Fe	Yes
Ni	K series	3.82	0.95	0.03817	27.71	1.65	26.72	Ni	Yes
Total:					100.00		100.00		

References

1. Bockris, J. O'M, D. Drazic, and A. R. Despic. "The Electrode Kinetics of the Deposition and Dissolution of Iron." *Electrochimica Acta* 4, no. 2 (1961): 325–61.
2. P. C. Andricacos, L. T. Romankiw, Magnetically Soft Materials in Data Storage: Their Properties and Electrochemistry, in: H. Gerischer, C. W. Tobias (Eds.), Advances in Electrochemical Science and Engineering, Volume 3, VCH Verlagsgesellschaft mbH, 1994, pp. 227-321.
3. Z. An, X. Zhang, H. Li, A Preliminary Study of the Preparation and Characterization of Shielding Fabric Coated by Electrical Deposition of Amorphous Ni–Fe–P Alloy, Journal of Alloys and Compounds 621 (2015) 99–103.
4. J. Torrejón, G. Badini-Confalonieri, M. Vázquez, Fabrication and Magnetic Properties of Hard/Soft Magnetostatically Coupled FePt/FeNi Multilayer Microwires, Journal of Applied Physics 103 (2008) 07E712.
5. M. T. Tung, D. V. A. Dung, N. D. Long, Anh-Tuan Le, Effects of Electrolytic Current Density on Structural, Magnetic Properties and GMI Behavior in Electrodeposited Bilayer FeNi/Cu Composite Wires, Journal of Superconductivity and Novel Magnetism 25 (2012) 2499–2505.
6. M. Datta, D. Landolt, Fundamental Aspects and Applications of Electrochemical Microfabrication, Electrochimica Acta 45 (2000) 2535–2558.
7. G. Zangari, Microelectromechanical systems, in: M. Schlesinger (Eds.), Modern Electroplating, 5th Edition, John Wiley & Sons, Inc., 2010, pp. 617-636.

8. A. Brenner, Electrodeposition of Alloys Principles and Practice, vol. II, Academic Press, 1963.
9. H. Dahms, I. M. Croll, The Anomalous Codeposition of Iron-Nickel Alloys, Journal of The Electrochemical Society 112 (1965) 771.
10. S. Hessami, C. W. Tobias, A Mathematical Model for Anomalous Codeposition of Nickel-Iron on a Rotating Disk Electrode, Journal of The Electrochemical Society 136 (1989) 3611–3616.
11. M. Matlosz, Competitive Adsorption Effects in the Electrodeposition of Iron-Nickel Alloys, Journal of The Electrochemical Society 140 (1993) 2272–2279.
12. N. Zech, E. J. Podlaha, D. Landolt, Anomalous Codeposition of Iron Group Metals: I. Experimental Results, Journal of The Electrochemical Society 146 (1999) 2886–2891.
13. N. Zech, E. J. Podlaha, D. Landolt, Anomalous Codeposition of Iron Group Metals: II. Mathematical Model, Journal of The Electrochemical Society 146 (1999): 2892–2900.
14. Michael Matlosz, Competitive Adsorption Effects in the Electrodeposition of Iron-Nickel Alloys, J. Electrochem. Soc. 140 (1993) 2272-2279.
15. Tomio Nagayama, Takayo Yamamoto, Toshihiro Nakamura, Thermal expansions and mechanical properties of electrodeposited Fe-Ni alloys in the Invar composition range, Electrochimica Acta 205 (2016) 178-187.
16. Antonello Vicenzo, Structure and Mechanical Properties of Electrodeposited Nanocrystalline Ni-Fe Alloys, J. Electrochem. Soc. 160 (2013) D570-D577.

17. Joseph A. Stroscio, D. T. Pierce, R. A. Dragoset, P. N. First, Microscopic Aspects of the Growth of Metastable fcc Iron on the Au (111) Surface, J. Vac. Sci. Technol. A, 10 (1992) 1981-1985.

18. H. F. Jurca, A. Damian, C. Gougaud, D. Thiaudière, R. Cortès, F. Maroun, P. Allongue, Epitaxial Electrodeposition of Fe on Au (111): Structure, Nucleation, and Growth Mechanisms, J. Phys. Chem. C 120 (2016) 16080-16089.

19. Y. Fukai, M. Mizutani, S. Yokota, M. Kanazawa, Y. Miura, T. Watanabe, Superabundant vacancy-hydrogen clusters in electrodeposited Ni and Cu, Journal of Alloys and Compounds 356-357 (2003) 270-273.

20. Ling Yang, Electrolytic Hexagonal Nickel, J. Electrochem. Soc. 97 (1950) 241-244.

21. Daniel A. Buttry, Measurement of Interfacial Processes at Electrode Surfaces with the Electrochemical Quartz Crystal Microbalance, Chem. Rev. 92 (1992) 1355-1379.

22. M. Fayette, U. Bertocci, G. R. Stafford, In Situ Stress Measurements during Cobalt Electrodeposition on (111)-Textured Au, J. Electrochem. Soc. 163 (2016) D146-D153.

23. Lian Guo, Peter C. Searson, On the influence of the nucleation overpotential on island growth in electrodeposition, Electrochimica Acta 55 (2010) 4086-4091.

24. E. Chason, J. W. Shin, S. J. Hearne, L. B. Freund, Kinetic model for dependence of thin film stress on growth rate, temperature, and microstructure, Journal of Applied Physics 111 (2012) 083520.

25. F. Donati, A. Mairov, C. S. Casari, M. Passoni, A. Li Bassi, Nucleation and growth mechanisms of Fe on Au (111) in the sub-monolayer regime, Surface Science 606 (2012) 702-710.

26. K. B. Reuter, D. B. Williams, J. I. Goldstein, Determination of the Fe-Ni Phase Diagram below 400^{o}C, Metallurgical Transactions A, 20A (1989) 719-725.

27. Nagatsugu Mukaibo, Yasuo Shimizu, Yuh Fukai, Toshiaki Hiroi, Heat Treatment for the. Stabilization of Hydrogen and Vacancies in Electrodeposited Ni-Fe Alloy Films, 49 (2008) 2815-2822.

28. Changjun Zhang, Ali Alavi, First-Principle Study of Superabundant Vacancy Formation in Metal Hydrides, J. Am. Chem. Soc. 127 (2005) 9808-9817.

29. Daijo Ikuta, Eiji Ohtani, Asami Sano-Furukawa, Yuki Shibazaki, Hidenori Terasaki, Liang Yuan, Takanori Hattori, Interstitial hydrogen atoms in face-centered cubic iron in the Earth's core, Scientific Reports, 9 (2019) 7108.

30. V. E. Antonov, M. Baier, B. Dorner, V. K. Fedotov, G. Grosse, A. I. Kolesnikov, E. G. Ponyatovsky, G. Schneider, F. E. Wagner, High-pressure hydrides of iron and its alloys, J. Phys.: Condens. Matter 14 (2002) 6427-6445.

31. Y. Fukai, K. Mori, H. Shinomiya, The phase diagram and superabundant vacancy formation in Fe-H alloys under high hydrogen pressures, Journal of Alloys and Compounds 348 (2003) 105-109.

32. S. Klotz, Y. Le Godec, Th. Strässle, U. Stuhr, The α-γ-ε triple point of iron investigated by high pressure-high temperature neutron scattering, Applied Physics Letters, 93 (2008) 091904.

3 Composition Gradient in Electrodeposited Fe-Ni Films

3.1 Introduction

3.1.1 Overview

In addition to the complications arising from the hydrogen evolution reaction (HER), the effect of which on the crystal structure and phase fraction was studied in **chapter 2**, the anomalous codeposition of Fe-Ni tends to develop a composition gradient zone along the growth direction within the near-substrate region, particularly in the thickness range of a few tens to a few hundreds of nanometers [1-3]. The Fe fraction (*i.e.*, the less noble metal) within the composition gradient zone decreases as the film thickness increases and is higher than the Fe fraction within the far-from-substrate region. In other words, the initial growth is even more anomalous — preferentially depositing the less noble metal in a greater extent. The composition depth profile along the composition gradient zone was not characterized until more recently by Gao et al. [4] and Neuróhr et al. [5]. Tabakovic et al. [6] and Białostocka et al. [7] further studied the influence of the substrate material on the composition gradient zone. Tabakovic et al., in particular, showed that the composition gradient was correlated with the increase of roughness at the growth front during the initial growth [6]. To the best of our knowledge, despite of the various works on the subject, the origin of the composition gradient zone has not yet been fully understood. In this chapter, we proposed that the concentration gradient developed during the initial growth of Fe-Ni codeposition could be explained by the theory described as follows in **section 3.1.2** based on the original BDD mechanism described in **section 2.1.1** in **chapter 2** [8].

3.1.2 Theory and Hypothesis

$$1: Me^{++} + 2H_2O \leftrightarrow Me(OH)^{+} + H_3O^{+} \quad (3.1)$$

$$2: Me(OH)^{+} + S_0 \rightarrow Me(OH)^{+}_{ads} \quad \text{(R. D. S.)} \quad (3.2)$$

$$3a: Me(OH)^{+}_{ads} + e^{-} \rightarrow Me(OH)_{ads.} \quad (3.3)$$

$$3b1: Me(OH)^{+}_{ads} + 2H_2O \leftrightarrow Me(OH)_{2,\,ads} + H_3O^{+} \quad (3.4)$$

$$3b2: Me(OH)_{2,\,ads} + H_3O^{+} + e^{-} \rightarrow Me(OH)_{ads} + 2H_2O \quad (3.5)$$

$$4: Me(OH)_{ads} + H_3O^{+} + e^{-} \rightarrow Me\ (solid) + 2H_2O \quad (3.6)$$

According to the reactions (3.1) - (3.6) described above, the metal ion — Me^{++} — can be reduced into the metal atom — Me(solid) — via two reaction paths, either following reaction (3.1), (3.2), (3.3), (3.6) in series or following reaction (3.1), (3.2), (3.4), (3.5), (3.6) in series. The R. D. S. of both paths is the adsorption of $Me(OH)^{+}$, *i.e.*, reaction (3.2), in which S_0 represents an empty adsorption site at the growth front. Subsequent to the R. D. S., the adsorbate ($Me(OH)^{+}_{ads}$) can act as a local pH buffer against the pH increase near the growth front via reaction (3.4). By definition, any species that can react with either H_3O^{+} or OH^{-} can be considered as a pH buffer [9]. Here, we hypothesize that the local pH in vicinity of the growth front is less buffered at the

beginning, due to the smaller amount of $Me(OH)^{+}_{ads}$ at the growth front, and becomes more buffered during the initial growth, resulting from the increasing amount of $Me(OH)^{+}_{ads}$ at the growth front. When the local pH is less buffered, the local pH is higher due to the consumption of H_3O^{+} by HER. At a higher local pH, the position of the hydrolysis equilibrium, *i.e.*, reaction (3.1), shifts to the product side, favoring the formation of $Me(OH)^{+}$ over Me^{++} near the growth front. This shift of the equilibrium position could be described mathematically as follows:

$$d\{[Me(OH)^{+}]/[Me^{++}]\} = (1/K_{sp})\, d[OH^{-}] \qquad \text{eq. 3.1}$$

where $[Me(OH)^{+}]$, $[Me^{++}]$, and $[OH^{-}]$ are the local concentrations of $Me(OH)^{+}$, Me^{++}, and OH^{-}, respectively. The same extent of increase in the local pH — a positive $d[OH^{-}]$ — shifts the hydrolysis equilibrium to the product side by a different extent, depending on the magnitude of the hydrolysis constant (K_{sp}). The K_{sp} of $Fe(OH)^{+}$ is 5.78×10^{-8}, while the K_{sp} of $Ni(OH)^{+}$ is 4.5×10^{-5} [10, 6], *i.e.*, $[Fe(OH)^{+}]/[Fe^{++}]$ is about three orders of magnitude more sensitive to a local pH change than $[Ni(OH)^{+}]/[Ni^{++}]$. The concentration gradient observed during the initial growth of electrodeposited Fe-Ni could then be rationalized based on the change in the buffering extent of the local pH. As the initial growth progresses, the amount of $Me(OH)^{+}_{ads}$ at the growth front increases, and thus the local pH becomes more buffered. In response to the change in the buffering extent, the local concentration of $Fe(OH)^{+}$ decreases more quickly than $Ni(OH)^{+}$, as a result of the K_{sp} of $Fe(OH)^{+}$ being much smaller than that of $Ni(OH)^{+}$. The relative decrease in the local concentration of $Fe(OH)^{+}$ causes a relative decrease in the rate of $Fe(OH)^{+}$ adsorption, which then causes a relative decrease in the rate of Fe deposition, giving rise to the composition

gradient observed in the deposit. As the deposition progresses further, the composition gradient declines as the extent of the buffering action settles. The co-deposition process remains anomalous, because the rate of $Fe(OH)^+$ adsorption remains larger than that of $Ni(OH)^+$ adsorption.

The amount of $Me(OH)^+_{ads}$ at the growth front, which is hypothesized above to play the key role of a localized pH buffer, could be affected by both the surface coverage and the surface morphology. To the best of our understanding, the correlation between the surface roughness and the composition during the initial growth of Fe-Ni electrodeposition observed by Tabakovic *et al.* is in line with our hypothesis. The exact growth mode that resulted in the surface roughening during the initial growth, however, was not revealed in the work from Tabakovic *et al.* [6]. On the other hand, though it has been shown that the pulse-current method could mitigate the composition gradient occurred during the initial growth of Fe-Ni electrodeposition [5, 6], the influence of the pulse-reverse potential method, which controls the applied potential instead of the applied current, has not been studied before.

3.1.3 Motivation

The HRTEM study reported in **section 2.3.3** in **chapter 2** demonstrates the local epitaxial relationship of Fe-Ni thin films (< 30 nm) grown on Au (111) substrates by the potentiostatic method. In this chapter, we extend the anomalous codeposition of Fe-Ni on Au (111) substrates beyond the thickness limit of the epitaxial growth, which is indicated by a morphological transition observed with scanning electron microscopy (SEM). We also investigate the initial

growth of Fe-Ni films grown by the pulse-reverse potential method. The effects of the reverse potential are discussed based on the mechanism of anomalous codeposition described in **section 3.1.2**.

3.2 Experimental Methods

3.2.1 Electrodeposition

Table 3.1. The conditions of the Fe-Ni films grown by potentiostatic electrodeposition. E is the applied potential. σ is the applied charge density. h is the thickness.

Set	E (V_{MSE})	σ (C/cm^2)	h (nm)
I	-1.35	0.1, 0.4, 0.8, 1.0, 2.0	33(6), 69(22), 170(30), 209(31), 458(84)
II	-1.42	0.1, 0.4, 0.8, 1.0, 2.0	42(4), 112(18), 219(16), 256(29), 579(30)
III	-1.50	0.16, 0.47, 0.78, 1.10, 2.35	38(20), 107(31), 197(57), 310(102), 532(171)

Table 3.2. The conditions of the Fe-Ni films grown by pulse-reverse potential electrodeposition. E_P is the pulse potential. E_R is the reverse potential. N is the number of pulse-reverse cycles. h is the thickness.

Set	E_P (V_{MSE})	E_R (V_{MSE})	N	h (nm)
IV	-1.50	-0.90	160, 408, 716, 1576	29(5), 44(8), 169(21), 412(52)
V	-1.50	-1.12	200, 408, 716, 836, 1576	7(3), 97(12), 189(22), 234(32), 444(50)

The aqueous electrolyte used for the electrodepositions was made of 3 mM saccharin ($C_7H_5NO_3S$), 550 mM boric acid (H_3BO_3), 180 mM nickel (II) chloride hexahydrate ($NiCl_2 \cdot 6H_2O$), 820 mM nickel (II) sulfate hexahydrate ($NiSO_4 \cdot 6H_2O$), and 90 mM iron (II) sulfate

heptahydrate ($FeSO4 \cdot 7H_2O$). The recipe was the same as that of the electrolyte E-a in **Table 2.1** in **chapter 2**. Milli-Q™ deionized (DI) water with a resistivity of 18.2 MOhm was used as the solvent of the electrolyte. The pH of the electrolyte was kept around 2.8. The electrodepositions were carried out by potential control using an EG&G PAR (263A) potentiostat/galvanostat. A vertical three-electrode setup was used. The Fe-Ni films were grown at the working electrode (*i.e.*, the cathode) on the Au (111) / SiO_2 / Si substrates. The exposure region at the working electrode was a 0.8 × 0.8 cm^2 square defined by Kapton® tape. The counter electrode (*i.e.*, the anode) was a Pt mesh. The mercury mercurous sulfate ($Hg/HgSO_4$) electrode in saturated potassium sulfate (sat'd K_2SO_4) was used as the reference electrode (0.00 V vs. MSE = + 0.64 V vs. SHE). All the electrodepositions were performed at room temperature without intentional stirring. Cyclic voltammetry was performed in the same setup in a scan rate of 10 mV/s between −1.7 and −0.2 V vs. MSE.

Three sets of Fe-Ni films (set I, II, and III) were deposited with the electrolyte described above by potentiostatic electrodeposition under three different applied potentials (E), which were −1.35, −1.42, and −1.50 V vs. MSE, respectively. Each set consists of films that were deposited with a series of applied charge densities (σ) ranging from ~ 0.1 to ~ 2.3 C/cm^2, targeting a range of thicknesses (h) from ~ 30 to ~ 500 nm (**Table 3.1**). Another two sets of Fe-Ni films (set IV and V) were deposited with the same electrolyte by pulse-reverse potential electrodeposition. The pulse potentials (E_P) for both sets were −1.50 V vs. MSE. The reverse potentials (E_R) were −0.90 and −1.12 V vs. MSE for set IV and V, respectively. The reasons behind the selection of the applied potentials were described in **section 3.3.4**. Each pulse-reverse cycle (T) was 0.5

second, consisting of a pulse potential time (T_P) of 0.1 second and a reverse potential time (T_R) of 0.4 second. The number of pulse-reverse cycles (N) ranged from 160 to 1576, also targeting the thickness range of ~ 30 to ~ 500 nm (**Table 3.2**).

3.2.2 Characterization

The composition of each film was characterized by energy dispersive X-ray spectroscopy (EDS) using a FEI Quanta LV200 SEM. Each EDS spectrum was acquired at 15 kV from a field of view of 2.12 × 3.18 μm. The Mα peak at ~ 2.1 keV from the Au (111) underlayer (see **Figure 2.1a**) was always observed, and thus the composition extracted from each spectrum should be interpreted as a through-thickness average. For each film, five EDS spectra were collected from different locations across the film surface, from which the through-volume average and the standard deviation were calculated. The surface and the cross-section morphologies were characterized by the FEI Quanta 650 SEM with a field emission gun. The crystal structure was characterized by X-ray diffraction (XRD) using the Empyrean X-ray diffractometer with the Cu $K\alpha$ X-ray source (λ = 1.54 Å) in the θ-2θ geometry. The thickness was characterized by scanning white light interferometry (SWLI) using the ZYGO NewView 7300 optical profiler (see **Figure 3.11** in the Appendix **A 3.1** for the height profiles from which the thicknesses were extracted).

3.3 Results

3.3.1 Composition

Figure 3.1 shows the composition as a function of thickness for each set of films in **Table 3.1** and **3.2**. All the films had a Fe-to-Ni ratio, $R_{film} = C_{Fe} / C_{Ni}$ = 0.5 ~ 1.7, significantly larger than

the Fe^{2+}-to-Ni^{2+} ratio, $R_{electrolyte} = C_{Fe2+} / C_{Ni2+} = 0.09$, in the electrolyte, showing the preferential deposition of Fe (*i.e.*, the less noble metal) over Ni (*i.e.*, the more noble metal) during the codeposition process, thus signifying the anomalous codeposition behavior. The films deposited under the potentiostatic mode (set I, II, and III) showed a composition gradient of increasing Ni fraction during the initial growth (solid curves in **Figure 3.1**). The films deposited under the pulse-reverse potential mode (set IV and V), on the other hand, showed a composition gradient of decreasing Ni fraction during the initial growth (dashed curves in **Figure 3.1**). All the curves were obtained by fitting the data with the non-linear least squares method (see Appendix **A 3.2** for the details of the fitting method). In the potentiostatic mode, the films (set I) deposited with the least negative applied potential showed a larger Ni fraction than the films (set II and III) deposited with more negative applied potentials. In the pulse-reverse potential mode, the films (set IV) deposited with a less negative reverse potential also showed a larger Ni fraction than the films (set V) deposited with a more negative reverse potential. The composition gradient of set V was the least extended among all, indicating that the pulse-reverse potential mode could be applied to mitigate the composition gradient occurred during the initial growth. Notice that the composition gradients of set III (green solid curve in **Figure 3.1**), with an applied potential of -1.50 V vs. MSE, and set IV (purple dashed curve in **Figure 3.1**), with a pulse potential of -1.50 V vs. MSE and a reverse potential of -0.90 V vs. MSE, both approached the nominally equiatomic level at the composition plateau. On the other hand, the composition gradient of set V (yellow dashed curve in **Figure 3.1**), with a pulse potential of -1.50 V vs. MSE and a reverse potential of -1.12 V vs. MSE, flattened at a Ni-lean near-equiatomic composition level, suggesting that the reverse potential could be used to adjust the level of the composition plateau.

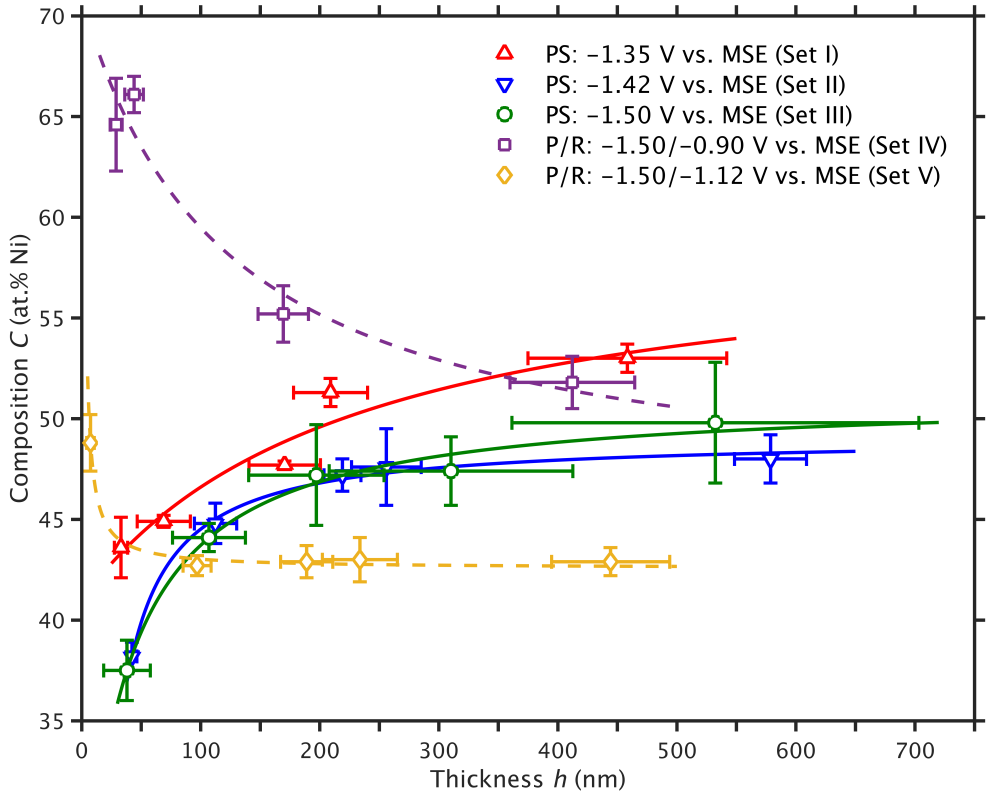

Figure 3.1. Composition as a function of thickness of the Fe-Ni films from potentiostatic (PS) deposition (set I, II and III) and pulse-reverse potential (P/R) deposition (set IV and V).

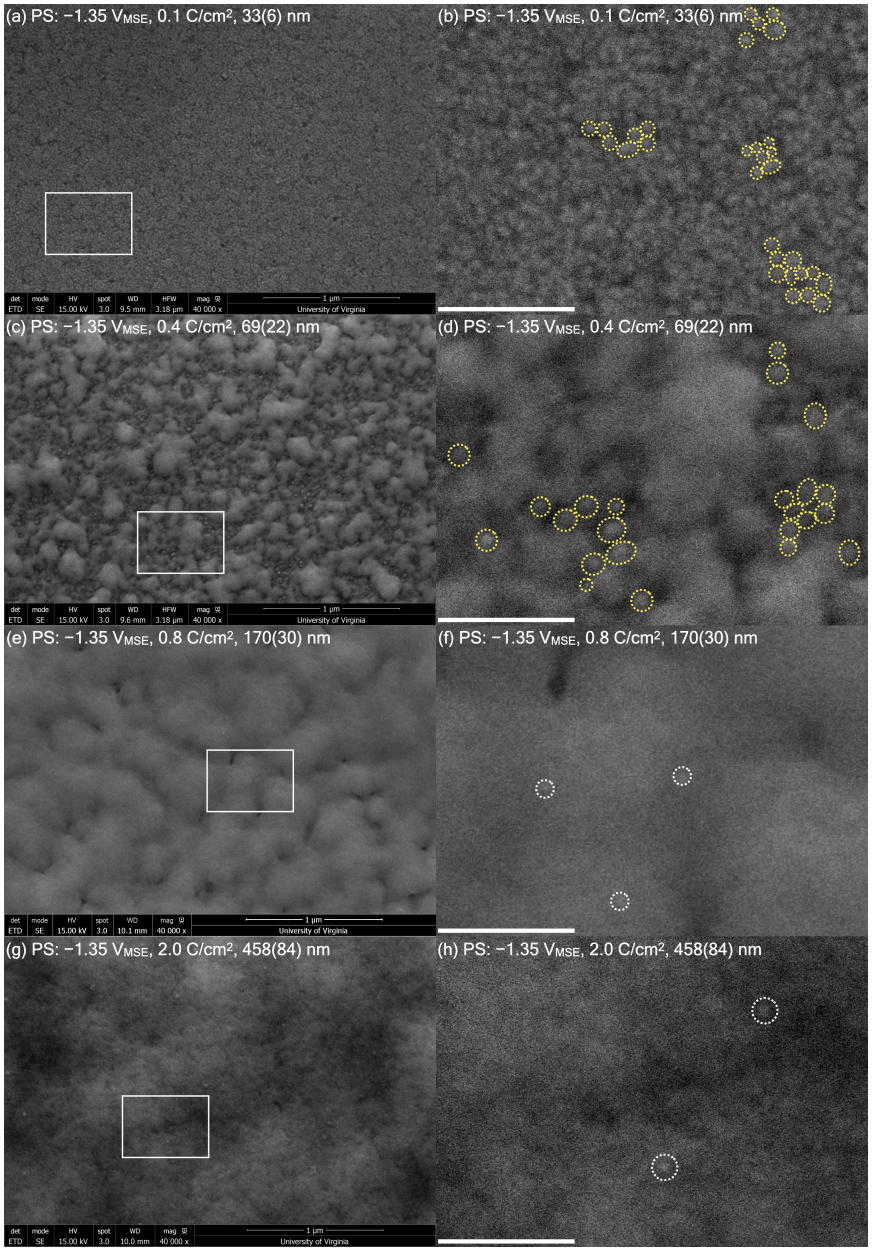

Figure 3.2. SEM micrographs of the Fe-Ni films (Set I) from the potentiostatic (PS) deposition at −1.35 V vs. MSE with increasing thickness: **(a)** 33(6) nm; **(c)** 69(22) nm; **(e)** 170(30) nm; **(g)** 458(84) nm. Micrographs **(b, d, f, h)** are the magnified views of the rectangles in (a, c, e, g), respectively. The scale bars in (b, d, f, h) are all 200 nm.

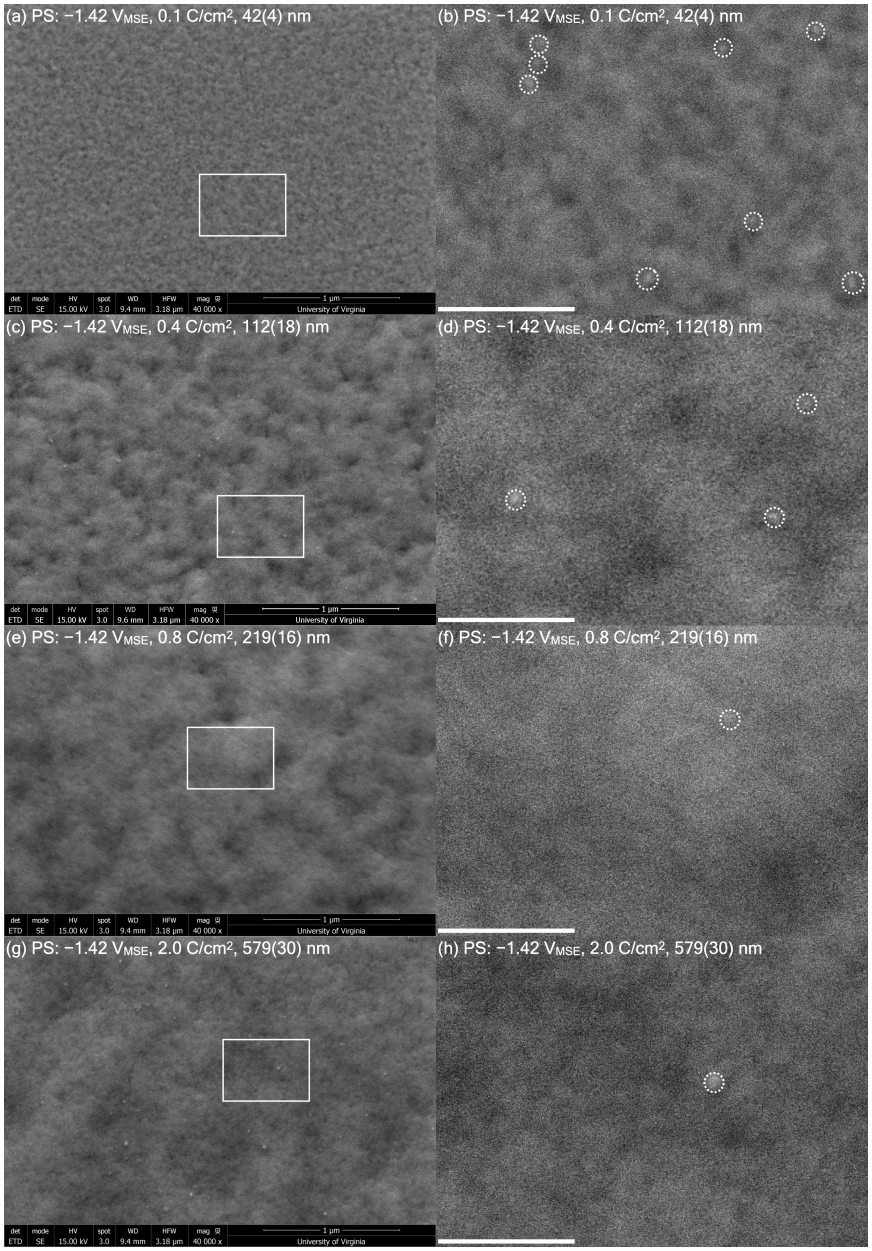

Figure 3.3. SEM micrographs of the Fe-Ni films (Set II) from the potentiostatic (PS) deposition at −1.42 V vs. MSE with increasing thickness: **(a)** 42(4) nm; **(c)** 112(18) nm; **(e)** 219(16) nm; **(g)** 579(30) nm. Micrographs **(b, d, f, h)** are the magnified views of the rectangles in (a, c, e, g), respectively. The scale bars in (b, d, f, h) are all 200 nm.

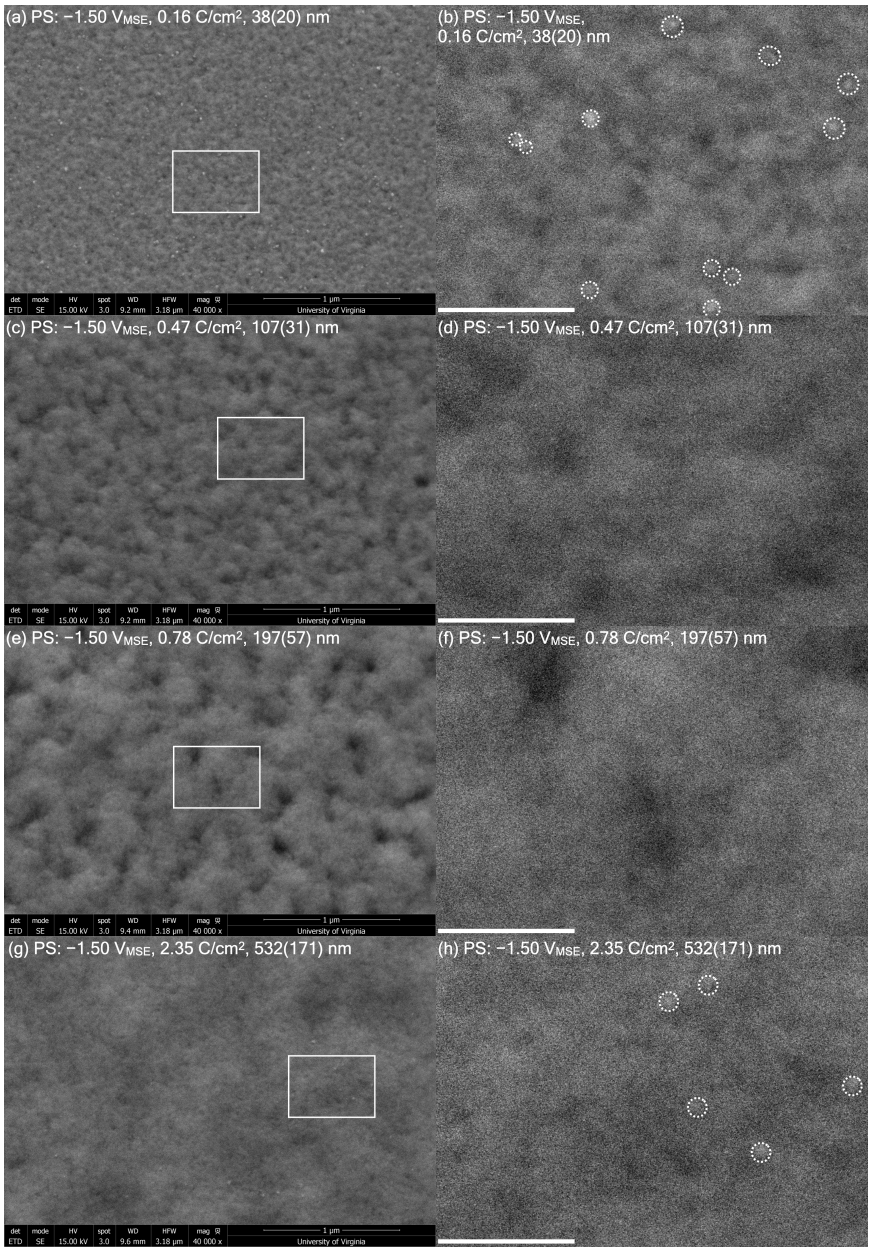

Figure 3.4. SEM micrographs of the Fe-Ni films (Set III) from the potentiostatic (PS) deposition at −1.50 V vs. MSE with increasing thickness: **(a)** 38(20) nm; **(c)** 107(31) nm; **(e)** 197(57) nm; **(g)** 532(171) nm. Micrographs **(b, d, f, h)** are the magnified views of the rectangles in (a, c, e, g), respectively. The scale bars in (b, d, f, h) are all 200 nm.

3.3.2 Morphology

The SEM images in **Figure 3.2 – 3.4** show the morphological evolution for each set of films grown under the potentiostatic mode (set I, II, and III). The films (set I) shown in **Figure 3.2** were deposited at the applied potential of -1.35 V vs. MSE, varying in thickness from ~ 33 nm to ~ 458 nm. **Figure 3.2b**, **d**, **f**, and **h** are the magnified views of **Figure 3.2a**, **c**, **e**, and **g**, respectively. A morphological transition onset was detected between the thickness of ~ 33 nm and ~ 69 nm. **Figure 3.2a** shows that the primary layer consisted of closely packed grains with a lateral (*i.e.*, in-plane) dimension on the order of 20 nm (examples marked by yellow circles in **Figure 3.2b**). **Figure 3.2c** shows that, at a thickness of ~ 69 nm, mounds — clusters of nanocrystalline grains — with a lateral dimension on the order of 200 nm were developed on top of the primary layer. At a higher thickness (*i.e.*, ~ 170 nm), the primary layer was fully covered by the coalesced mounds, as shown in **Figure 3.2e**. At such a thickness, grains with a lateral dimension on the order of 25 nm were observed (examples marked by white circles in **Figure 3.2f**), but they were not closely packed as they were in the primary layer, suggesting a change of the growth mode. The relatively uniform lateral dimension of the closely packed grains in **Figure 3.2a** suggests that the primary layer was developed via a growth-rate-limited process (*i.e.*, fast nucleation). The variation in size and shape of the mounds in **Figure 3.2c** suggests that the secondary layer was developed by a nucleation-rate-limited process (*i.e.*, fast growth).

The SEM images in **Figure 3.3** and **Figure 3.4** show two sets of films (set II and III) deposited under the more negative applied potentials at -1.42 and -1.50 V vs. MSE, respectively. The thicknesses of the films in **Figure 3.3a** and **3.4a** were 42(4) and 38(20) nm, respectively, close to

the thickness of the film in **Figure 3.2a**, *i.e.*, 33(6) nm. However, the morphologies were different. The closely packed grains found in **Figure 3.2a** were not found in **Figure 3.3a** and **3.4a**. Instead, **Figure 3.3a** and **3.4a** both show (1) a landscape of mounds consisting of nanocrystalline grains that had a lateral dimension smaller than the resolution limit, (2) separated grains with a lateral dimension on the order of 25 ~ 30 nm (examples marked by white circles in **Figure 3.3b** and **3.4b**). Such a difference in the morphology suggests a difference in the growth mode. In fact, according to the XRD patterns, the crystal structure of the film in **Figure 3.2a** was face-centered cubic (FCC) (see the red pattern in **Figure 3.9a**), while the films in **Figure 3.3a** and **3.4a** were body-centered cubic (BCC) (see the red patterns in **Figure 3.9b** and **3.9c**). Despite being similar qualitatively, **Figure 3.4a** shows a larger areal density of the separated grains than **Figure 3.3a**. Such a comparison suggests that, under the same growth mode, the nucleation of the separated grains was faster at a more negative applied potential.

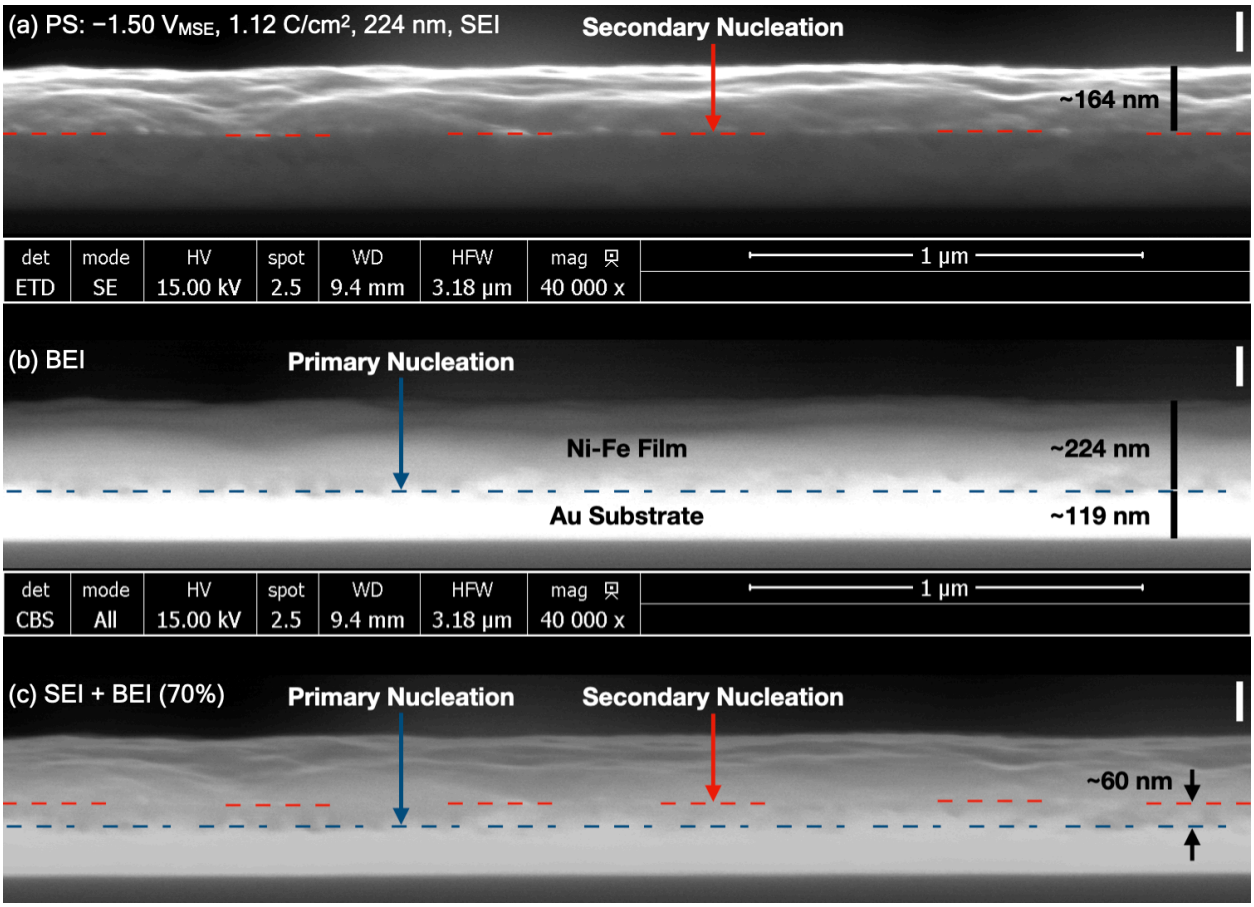

Figure 3.5. Cross-section SEM micrograph of the Fe-Ni film from the potentiostatic (PS) deposition at -1.50 V vs. MSE with the thickness of ~ 224 nm: **(a)** the secondary electron image (SEI); **(b)** the backscattered electron image (BEI); **(c)** the SEI in (a) overlaid with the BEI in (b) with 70% opacity. The vertical scale bars on the right are all 100 nm.

The SEM images in **Figure 3.5** show the cross-section morphology of a film deposited at -1.50 V vs. MSE under the potentiostatic mode (*i.e.*, the same as the films in set III). **Figure 3.5a** and **3.5b** show the secondary electron image (SEI) and the back scattered electron image (BEI), respectively. The composition contrast of the BEI shows the level of the primary nucleation, sandwiched between the Au substrate (~ 119 nm) and the Fe-Ni film (~ 224 nm). The topography

contrast of the SEI shows the level of the secondary nucleation, sandwiched between the primary layer and the secondary layer (~ 164 nm). The thickness of the primary layer was estimated to be ~ 60 nm, as shown in **Figure 3.5c**. According to the XRD patterns of the films in set III (**Figure 3.9c**), the film thinner than this estimated thickness was BCC Fe-Ni, while the films thicker than this estimated thickness contained both BCC and FCC Fe-Ni, suggesting that the secondary nucleation initiated the growth of the FCC phase.

Figure 3.6 and **3.7** show the morphological evolutions under the pulse-reverse potential mode. **Figure 3.6** shows the films (set IV) deposited with a pulse potential of -1.50 V vs. MSE (i.e., the same as the applied potential of set III) and a reverse potential of -0.90 V vs. MSE. Comparing set IV to set III, the separated grains easily found in **Figure 3.4a** (set III) were hardly found in **Figure 3.6a** (set IV). Instead, **Figure 3.6a** shows more and deeper gaps between the mounds (examples marked by cyan circles in **Figure 3.6b**). Such a comparison suggests (1) the gaps between the mounds were preferred sites for the nucleation of the separated grains in the potentiostatic mode (examples marked by white circles in **Figure 3.4b**), (2) the nucleation of the separated grains was suppressed by the pulse-reverse potential mode.

Figure 3.7 shows the films (set V) deposited with a pulse potential of -1.50 V vs. MSE and a more negative reverse potential at -1.12 V vs. MSE. **Figure 3.7a** shows the initially grown morphology at a thickness of ~ 7 nm. **Figure 3.8a** shows a higher magnification image of the same film. **Figure 3.7a** and **Figure 3.8a** show (1) faceted grains with a lateral dimension on the order of 130 ~ 150 nm (examples outlined by broken lines in **Figure 3.7b** and **Figure 3.8b**), (2)

nanoscale pits with a lateral dimension less than ~ 20 nm distributed across the surface of the faceted grains (examples marked by yellow circles in **Figure 3.8b**). Such an initial morphology was drastically different from those of any other films (set I, II, III, and IV), indicating that the initial morphology was very sensitive to the deposition mode and condition. However, at a thickness of 400 ~ 600 nm, the morphologies of all the films (set I, II, III, IV, and V) are qualitatively similar to each other, regardless of the differences in the deposition mode and condition (**Figure 3.2g**, **3.3g**, **3.4g**, **3.6g**, and **3.7g**), suggesting that the ultimate morphology was relatively insensitive to the deposition mode and condition.

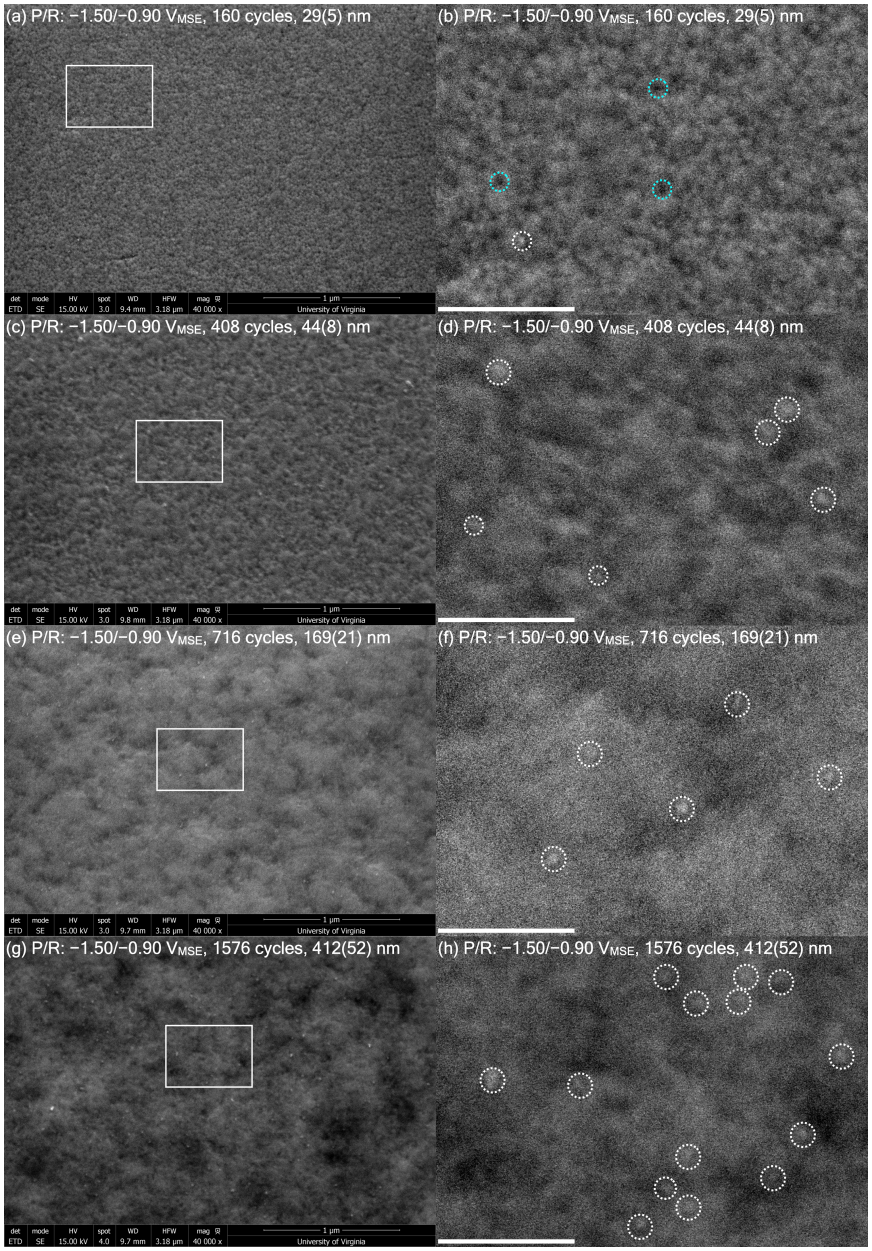

Figure 3.6. SEM micrographs of the Fe-Ni films (Set IV) from the pulse-reverse potential (P/R) deposition at −1.50 / −0.90 V vs. MSE with increasing thickness: **(a)** 29(5) nm; **(c)** 44(8) nm; **(e)** 169(21) nm; **(g)** 412(52) nm. Micrographs **(b, d, f, h)** are the magnified views of the rectangles in (a, c, e, g), respectively. The scale bars in (b, d, f, h) are all 200 nm.

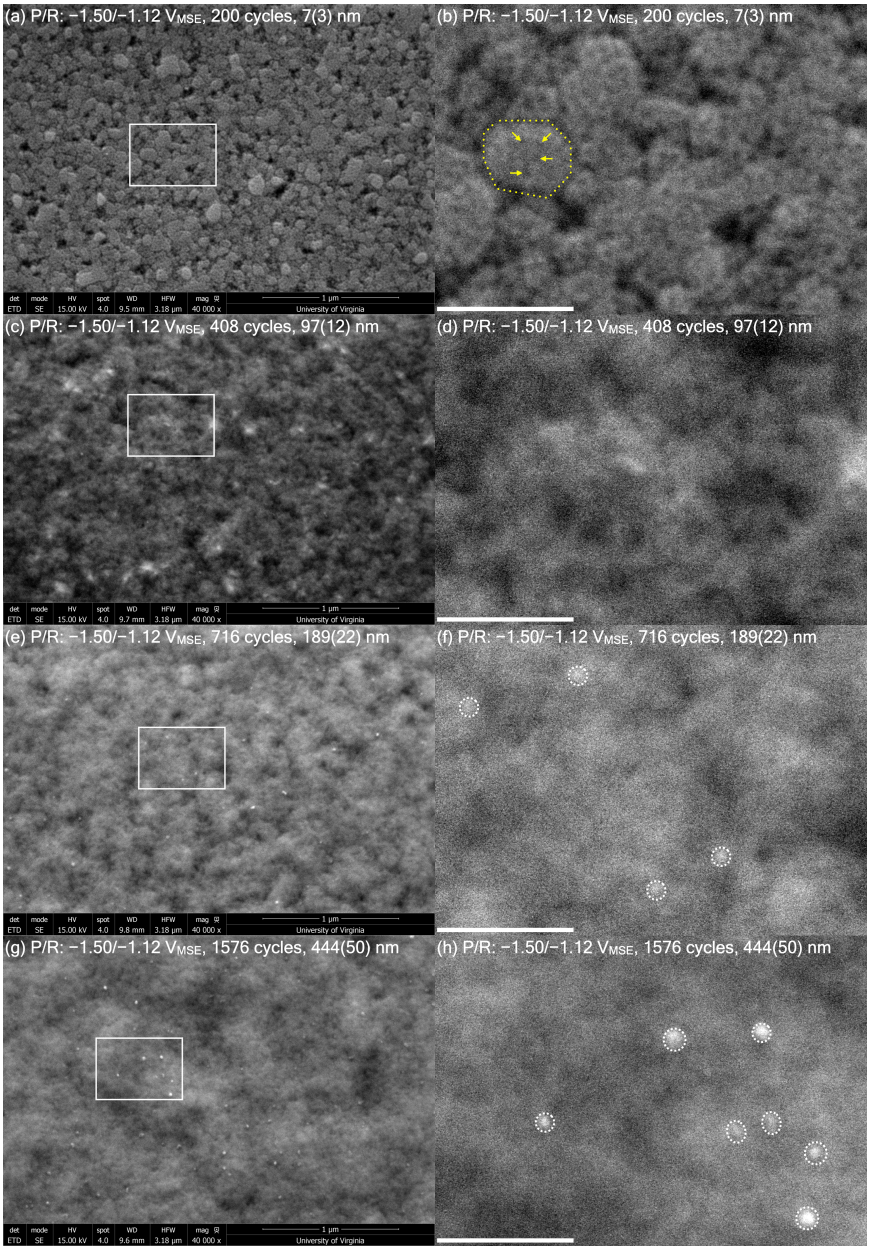

Figure 3.7. SEM micrographs of the Fe-Ni films (Set V) from the pulse-reverse potential (P/R) deposition at −1.50 / −1.12 V vs. MSE with increasing thickness: **(a)** 7(3) nm; **(c)** 97(12) nm; **(e)** 189(22) nm; **(g)** 444(50) nm. Micrographs **(b, d, f, h)** are the magnified views of the rectangles in (a, c, e, g), respectively. The scale bars in (b, d, f, h) are all 200 nm.

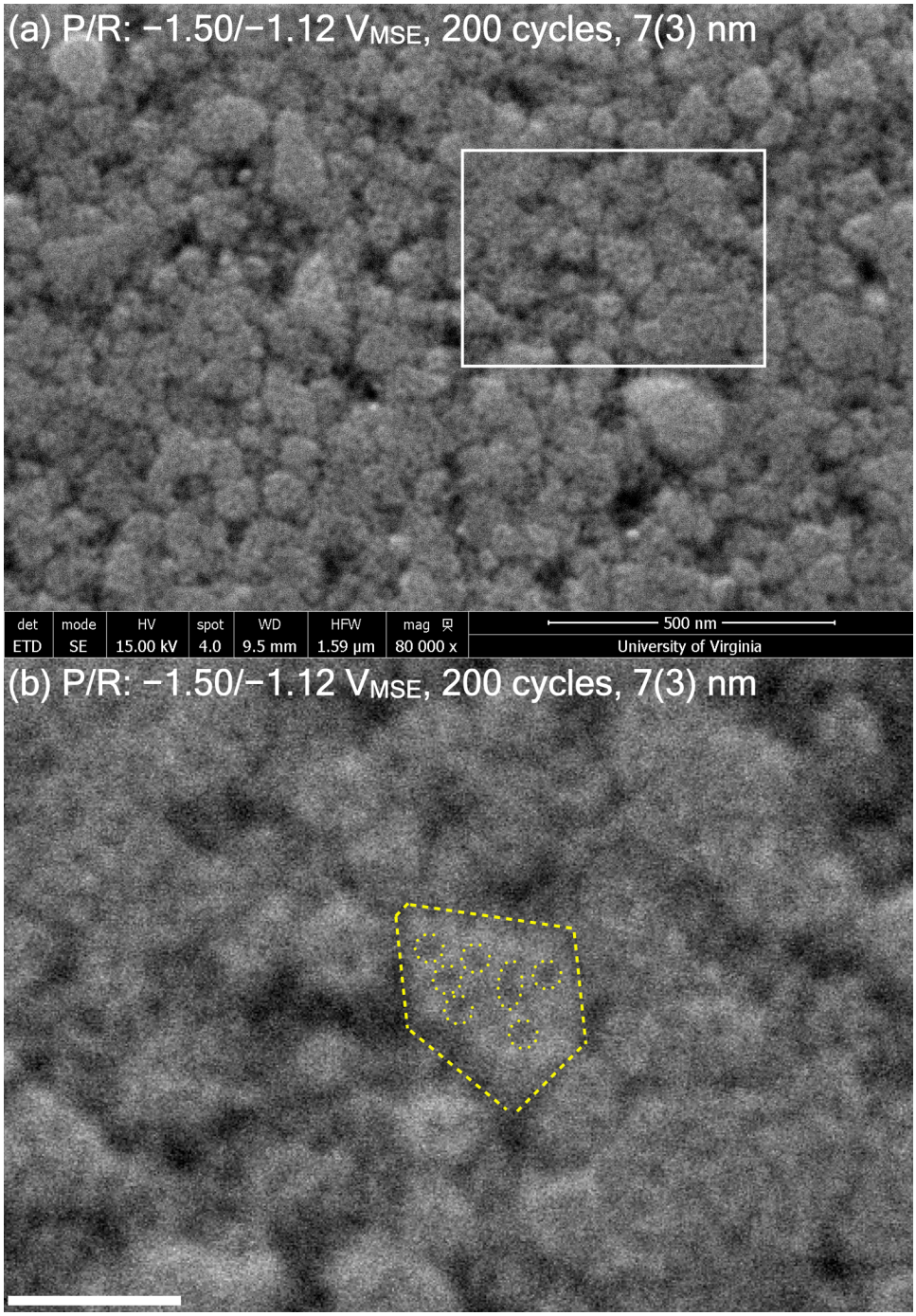

Figure 3.8. SEM micrograph of the Fe-Ni film from the pulse-reverse potential (P/R) deposition at -1.50 /-1.12 V vs. MSE and the thickness of 7(3) nm. The micrograph in (b) is the magnified view of the rectangle in (a). The scale bar in (b) is 100 nm.

3.3.3 Crystal Structure

The XRD patterns of all the films (set I, II, III, IV, and V) are shown in **Figure 3.9a – 3.9e**. The peak around 43.8^{o} was identified as the (111) reflection of FCC Fe-Ni (filled triangle in black). The peak around 50.8^{o} peak was identified as the (200) reflection of FCC Fe-Ni (filled triangle in red). The peak around 44.8^{o} was identified as the (110) reflection of BCC Fe-Ni (unfilled triangle). There was a sharp peak around 38.2^{o}, identified as the (111) reflection of FCC Au, of which the tail on the high angle side could be recognized in the patterns. The lattice parameters in **Table 3.5** and **3.6** (Appendix **A 3.3**) were extracted from the XRD patterns by the individual profile-fitting method [11]. **Figure 3.9f** shows the XRD profile-fitting of the thickest film in set III as an example. The crosses in blue show the raw data. The line in green shows the calculated profile. The red line shows the difference between the raw data and the calculated profile. The agreement between the raw data and the calculated profile indicates that the peak positions extracted from such a fitting procedure are accurate. The lattice parameters (in **Table 3.5** and **3.6**) were calculated from the peak positions extracted. The fitting of all the patterns and the details of the method were in Appendix **A 3.3**. The Rietveld method [11] was then employed to analyze the XRD patterns of the films consisting of both FCC and BCC Fe-Ni (the yellow, blue, and green patterns in **Figure 3.9b**, **3.9c**, and **3.9e**), with which the weight fractions of the two phases were extracted and listed in **Table 3.7** and **3.8** in Appendix **A 3.4**. The Rietveld method differs from the individual profile-fitting method in that physical constraints were imposed upon the positions and the intensities of the peaks belonging to the same phase. This method, however, is quite susceptible to false minima in general [11]. In order to circumvent the false minima, the lattice parameters extracted from the individual profile-fitting method were used as the initial

parameters in the Rietveld method. The details of the procedure were described in Appendix **A 3.4**.

The XRD patterns in **Figure 3.9a** show that FCC Fe-Ni was the dominant phase in set I. The thinnest film (the red pattern at the bottom) does not show the FCC (200) reflection around 50.8^{o}, suggesting that the initial growth was locally epitaxial. The thickest film (the green pattern at the top), however, clearly shows the FCC (200) reflection, suggesting (1) the preferred orientation of the FCC (111) reflection decreased as the thickness increased, (2) secondary nucleation and growth occurred, (3) the grains resulted from the secondary nucleation and growth were not epitaxial. These structural results can be correlated with the morphological results, in that a morphological transition onset was detected between the thickness of ~ 33 nm and ~ 69 nm (**Figure 3.2a** and **3.2c**). It follows that the morphological transition was probably caused by the secondary nucleation and growth of non-epitaxial FCC Fe-Ni.

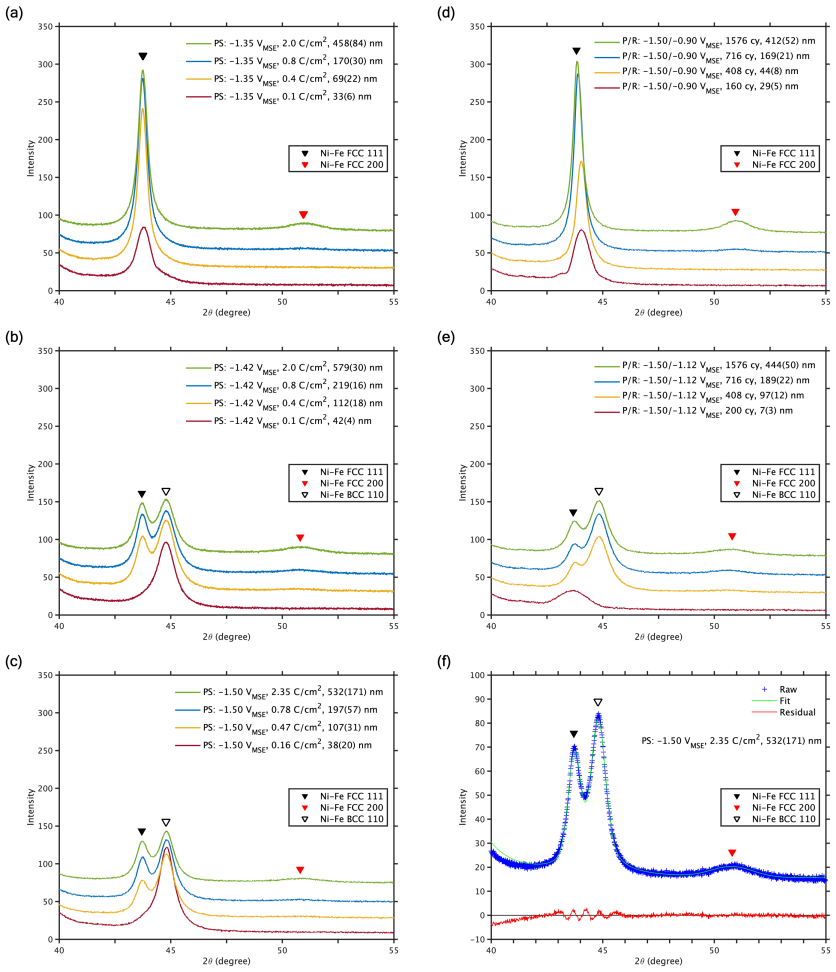

Figure 3.9. XRD patterns of the Fe-Ni films from the potentiostatic (PS) deposition at **(a)** -1.35 V vs. MSE, **(b)** -1.42 V vs. MSE, **(c)** -1.50 V vs. MSE; and the pulse-reverse potential (P/R) deposition at **(d)** -1.50 / -0.90 V vs. MSE, **(e)** -1.50 / -1.12 V vs. MSE. **(f)** Profile-fitting of the Fe-Ni film from the PS deposition at -1.50 V vs. MSE and the thickness of 532(171) nm. The blue cross shows the raw data ('Raw'). The green curve shows the calculated pattern ('Fit'). The red curve shows the difference between the raw data and the calculated pattern ('Residual'). The filled triangles in black and red denote the Fe-Ni FCC 111 and 200 reflections, respectively. The unfilled triangle denotes the Fe-Ni BCC 110 reflection.

Figure 3.9b and **3.9c** show the XRD patterns of the films in set II and III, respectively. Comparing to set I (**Figure 3.9a**), the initially grown films (the red patterns at the bottom) were BCC Fe-Ni instead of FCC Fe-Ni, suggesting that a more negative applied potential favored the formation of BCC Fe-Ni. Moreover, the films in set III had a larger weight fraction of the BCC phase than the films in set II in every higher thickness level being measured (see **Table 3.7** and **Figure 3.17a** in Appendix **A 3.4**), also suggesting that a more negative applied potential was conducive to the formation of the BCC phase. These observations are consistent with the study of the deposition electrolyte with electrochemical quartz crystal microbalance (EQCM) in **chapter 2**, in that a larger deposition partial current was shown to promote the formation of BCC Fe-Ni. Similar to set I, both set II and III showed a more prominent FCC (200) reflection as the thickness increased, suggesting a decreasing preferred orientation of the FCC (111) reflection. Quantitatively, this trend is captured by a decrease in the March coefficient extracted by the Rietveld method (see **Figure 3.17b** in Appendix **A 3.4**), which represents the strength of the preferred orientation [11-13].

Figure 3.9d shows the XRD patterns of the films in set IV from the pulse-reverse potential mode. The thinnest film shows a small peak on top of the low angle tail of the Fe-Ni FCC (111) peak (also see **Figure 3.15a** in Appendix **A 3.3**). Such a small peak was identified as the (111) reflection of a secondary FCC phase, which was absent in set III from the potentiostatic mode. As the film thickness increased, the position of the (111) peak of the primary FCC phase shifted from ~ 44.06^{o} to ~ 43.87^{o}, and the lattice parameter increased monotonically from 3.557 Å to 3.572 Å (**Table 3.6**). The lattice parameter of FCC Fe-Ni increases as the Ni fraction decreases

[14]. The peak shift in the XRD patterns is therefore consistent with the gradient of decreasing Ni fraction measured by EDS (**Figure 3.1**).

Figure 3.9e shows the XRD patterns of the films in set V. The thinnest film shows a broad FCC (111) peak, which is significantly wider than the thinnest films in any other sets (set I – IV). The full-width-at-half-maximum (H_k) of the FCC (111) peak of the thinnest film was extracted to be $H_k \sim 1.19^o$. According to the Scherrer equation, $B = 0.94\lambda/(H_k \times \cos(\theta))$ [15], the grain size perpendicular to the FCC (111) planes was roughly estimated (*i.e.*, by neglecting the contributions from the instrumental and the microstrain broadening) to be $B \sim 7$ nm. And since the FCC (111) planes were the preferably oriented planes, B was also a rough estimation of the vertical (*i.e.*, out-of-plane) grain size. That the vertical grain size ($B \sim 7$ nm) and the thickness ($h \sim 7$ nm) closely matching each other suggests that the initially grown layers in set V were locally epitaxial.

In comparison to **Figure 3.9c**, the thinnest film in **Figure 3.9e** did not form the BCC phase. However, at the thickness of ~ 97 nm, the fraction of the BCC phase had already been substantial (> 50 wt.%) and continued to be so at larger thicknesses (**Table 3.8** in Appendix **A 3.4**). This observation is noteworthy, because it indicates that the epitaxial growth on Au (111) was not a prerequisite for the formation of the BCC phase. The discussion in **section 2.4.1** in **chapter 2** suggested that the formation of the BCC phase was related to the electrochemical environment at the electrodeposited growth front. The observation described here supports this hypothesis.

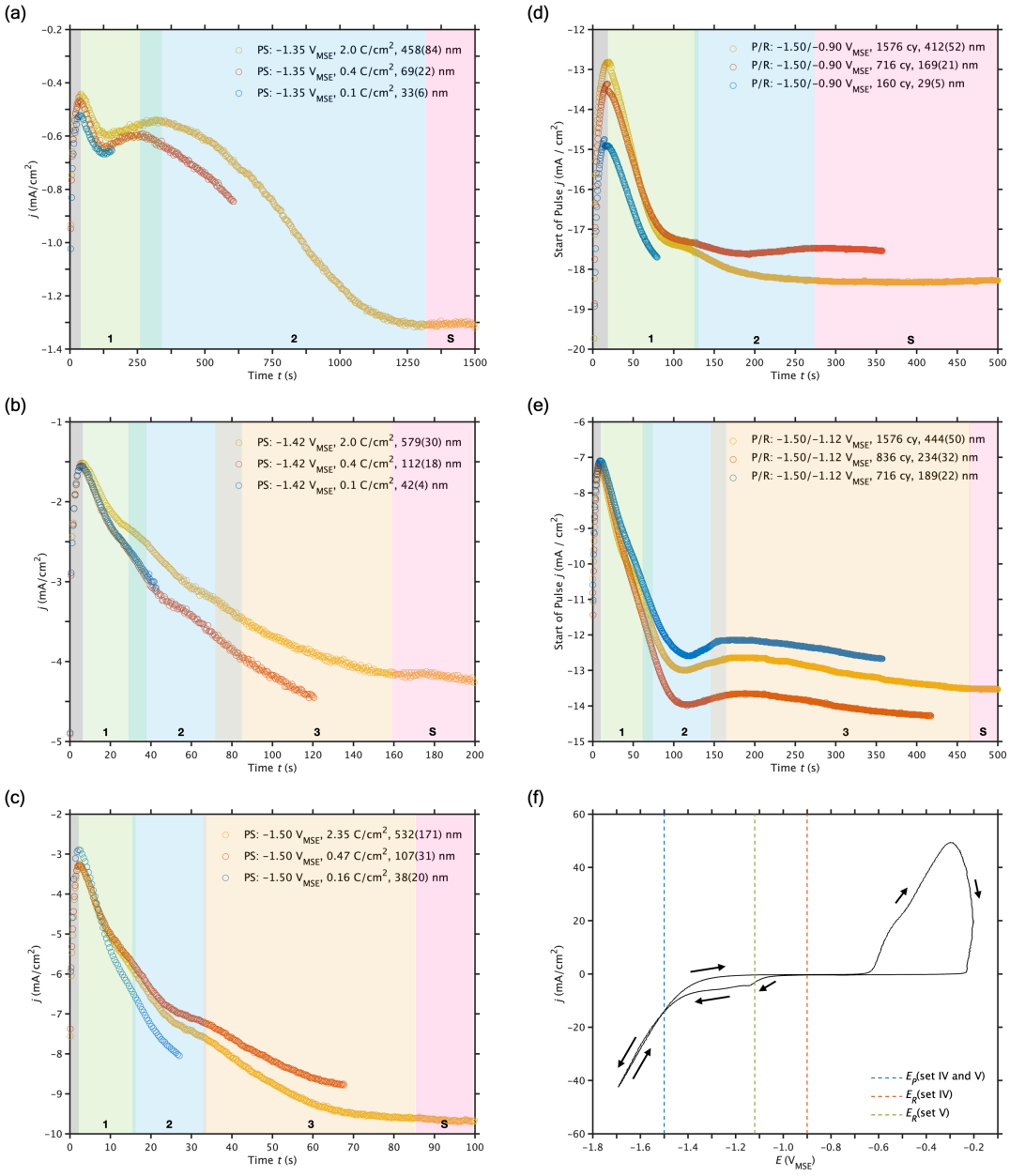

Figure 3.10. The current density vs. time curves of the Fe-Ni films from the potentiostatic (PS) deposition at **(a)** -1.35 V vs. MSE, **(b)** -1.42 V vs. MSE, **(c)** -1.50 V vs. MSE. The start of pulse cycle current density vs. time curves from the pulse-reverse potential (P/R) deposition at **(d)** -1.50 / -0.90 V vs. MSE, **(e)** -1.50 / -1.12 V vs. MSE. **(f)** The cyclic voltammogram measured at the scan rate of 10 mV/s. The arrows indicate the direction of the potential scan.

3.3.4 Electrochemistry

Chronoamperometry (CA) was used to further the understanding of the processes occurring during the early state of the deposition. **Figure 3.10a – 3.10c** show the current density vs. time curves (*i.e.*, the CA curves) of the films from the potentiostatic mode (set I, II, and III). The current density vs. time curves from the pulse-reverse potential mode (set IV and V) are more complicated. Each curve shown in **Figure 3.10d** and **3.10e** consists of the data point at the start of all the pulse cycles, with all the other data points excluded. The complete set of data points were provided in Appendix **A 3.5**. **Figure 3.10f** shows the cyclic voltammogram (*i.e.*, the CV loop) that was used to guide the selection of the applied potentials at the pulse and the reverse cycles. To clarify, whenever the current density is said to increase (decrease) in this work, we mean that the magnitude of the current density increases (decreases).

The anomalous codeposition behavior evidenced by the composition measurements (**Figure 3.1**) suggests that the depositions were under the kinetic or the mixed controlled growth instead of the diffusion-controlled growth. More importantly, hydrogen evolution as a side reaction contributed to the current density during the deposition. For these reasons, the Scharifker-Hill method cannot be directly applied to extract the nucleation mode and parameters from the CA data [16]. The visually distinguishable CA stages (in different colors) in **Figure 3.10a – 3.10c**, however, can still be interpreted qualitatively. All the CA curves begin with a current density decrease resulting from the charging of the double layer (in gray). Subsequently, the current density increase was interpreted as the onset of the primary nucleation (stage 1 in green), for the surface area increased during the nucleation process. Within the same stage, the decrease in the

rate that the current density increased (*i.e.*, the second-order decrease) signifies the saturation of the primary nucleation sites [16]. Thereafter, the second-order increase in the current density signifies the onset of the secondary nucleation (stage 2 in blue). All the features described up to this point can be found in **Figure 3.10a – 3.10c**. In **Figure 3.10a**, the CA curve in stage 2 transitions into the steady state plateau (stage s in red). In contrast, the CA curves in **Figure 3.10b** and **3.10c** encounter firstly a second-order decrease (*i.e.*, the saturation of the secondary nucleation sites) and then a second-order increase (*i.e.*, the onset of the tertiary nucleation – stage 3 in yellow), before transitioning into the steady state plateau. For comparison, the curves in **Figure 3.10d** and **3.10e** were partitioned into different stages based on the same school of reasoning. We notice that all the BCC-forming conditions (set II, III, and V) consist of 3 stages prior to the steady state, while all the other conditions (set I and IV) consist of 2 stages prior to the steady state. We also notice that, as the thickness increased, the weight fraction of the BCC phase first decreased and then increased in all the BCC-forming conditions (set II, III, and V) (see **Table 3.7** and **3.8** in Appendix **A 3.4**). The tertiary nucleation may be related to the formation of the BCC phase. Future investigations are required to verify this conjecture.

The identifications of the CA stages under the potentiostatic mode were supported by the morphological observations. A morphological transition was clearly detected (**Figure 3.2a** and **3.2c**) between the film ceased in stage 1 (the blue curve in **Figure 3.10a**) and the film ceased in stage 2 (the red curve in **Figure 3.10a**), showing the connection between the SEM images and the CA data. As for **Figure 3.10c**, the film ceased in stage 2 (the blue curve) show (1) a landscape of mounds, (2) separated grains in the SEM image (**Figure 3.4a**), which may result

from the primary and the secondary nucleation, respectively. A similar connection can be found between the CA curve in **Figure 3.10b** and the SEM image in **Figure 3.3a**.

The CV loop in **Figure 3.10f** was used to guide the selection of applied potentials for the pulse-reverse potential depositions. The pulse potential (EP = -1.50 V vs. MSE) was close to the crossover potential, where the cathodic and the anodic cycles intersected. The presence of the crossover in the CV loop is indicative of a 3-D nucleation mechanism [17, 18]. The two reverse potentials, $E_{R,a}$ = -0.90 V vs. MSE (set IV) and $E_{R,b}$ = -1.12 V vs. MSE (set V), were less and more negative than the onset potential at E_a ~ -1.00 V vs. MSE, respectively. A magnified view of the CV loop (**Figure 3.23** in Appendix **A 3.6**) shows that there was a second onset at E_b ~ -1.15 V vs. MSE, which was slightly more negative than $E_{R,b,}$ followed by the third onset at ~ -1.35 V vs. MSE resulted from the hydrogen evolution reaction. Based on the Nernst equation, the equilibrium reduction potentials of Ni^{2+}/Ni and Fe^{2+}/Fe were estimated from the cation concentrations (C_{Ni2+} = 1000 mM, C_{Fe2+} = 90 mM) to be $E_{Ni2+/Ni}$ = -0.897 V vs. MSE and $E_{Fe2+/Fe}$ = -1.118 V vs. MSE, respectively. The two onsets in the CV loop, E_a and E_b, were close to and slightly more negative than the estimated equilibrium reduction potentials, $E_{Ni2+/Ni}$ and $E_{Fe2+/Fe}$, respectively, strongly suggesting that they were the onsets of the Ni^{2+}/Ni and the Fe^{2+}/Fe reduction reactions, respectively.

We then selected the reverse potentials of $E_{R,a} \approx E_{Ni2+/Ni}$ (set IV) and $E_{R,b} \approx E_{Fe2+/Fe}$ (set V) as a strategy to mitigate the anomalous codeposition behavior. During the reverse cycles at $E_{R,a}$ (set IV), the reductions of both Fe^{2+} and Ni^{2+} were expected to halt, while more Fe than Ni atoms

were expected to dissolve into Fe^{2+} and Ni^{2+}, respectively (*i.e.*, the dealloying of Fe). During the reverse cycles at $E_{R,b}$ (set V), the reduction of Fe^{2+} was still expected to halt, while the dissolution of Fe and the reduction of Ni^{2+} were expected to occur. In either case, an effective dissolution of Fe (*i.e.*, the less noble metal) was expected to occur during the reverse cycles, which should mitigate the anomalous codeposition behavior. According to the composition measurements, however, this strategy was efficient only during the initial growth. A plausible explanation based on the effect of $Me(OH)^{+}_{ads}$ as a barrier against dissolution was discussed in **section 3.4**.

3.4 Discussion

In **section 3.1.2**, a mechanism was proposed to explain how the anomalous codeposition of Fe-Ni developed a composition gradient during the initial growth. The key assumptions include:

- The adsorption of $Me(OH)^{+}$ at the electrodeposited growth front, *i.e.*, reaction (3.2), was the R. D. S. of the codeposition mechanism.

- The adsorbed metal hydroxide ion — $Me(OH)^{+}_{ads}$ — functioned as a localized pH buffer at the growth front, via reaction (3.4), during the codeposition.

Based on this mechanism, the composition gradient was a result of the gradual accumulation of $Me(OH)^{+}_{ads}$ at the growth front during the initial growth. The decline of the composition gradient in the subsequent growth was a consequence of the saturation of $Me(OH)^{+}_{ads}$ at the growth front.

In the following, this mechanism was further used to rationalize the pulse-reversed potential deposition behavior.

As shown in **Figure 3.1**, the films grown under the potentiostatic and the pulse-reverse potential mode had opposite composition gradients — an increasing Ni fraction under the potentiostatic mode, as opposed to a decreasing Ni fraction under the pulse-reverse potential mode. This observation strongly suggests that Fe (*i.e.*, the less noble metal) was dealloyed during the initial growth under the reverse cycles. The inter-mound gaps shown in **Figure 3.6b** and the nanopits shown in **Figure 3.7b** and **3.8b** evidence the dealloying process. During the subsequent growth, the composition gradient declined under both deposition modes (**Figure 3.1**). And the surface morphologies of the films were similar to each other, despite of the difference in the deposition mode and condition (**Figure 3.2g**, **3.4g**, **3.6g**, and **3.7g**). This was in contrast to the drastically dissimilar surface morphologies of the initially grown films (**Figure 2a**, **4a**, **6a**, and **7a**). Both the compositional and the morphological behavior suggest that the dealloying process that was present during the initial growth was suppressed during the subsequent growth. The suppression of the dealloying process was rationalized based on the mechanism proposed in **section 3.1.2**:

- Under the potentiostatic mode, $Me(OH)^{+}_{ads}$ functioned as a localized pH buffer.

- Under the pulse-reverse potential mode, $Me(OH)^{+}_{ads}$ functioned not only as a localized pH buffer, but also as a barrier against dealloying during the reverse cycles.

In other words, the Fe atoms covered by $Me(OH)^{+}_{ads}$ at the growth front were less susceptible to being dealloyed. Therefore, as $Me(OH)^{+}_{ads}$ accumulated during the initial growth, the Fe fraction increased, showing the gradient of decreasing Ni fraction. When the growth front was saturated with $Me(OH)^{+}_{ads}$, the gradient declined, and the composition approached a plateau. Notice that $Me(OH)^{+}_{ads}$ was not the only species that adsorbed at the growth front. The anions (*i.e.*, SO_4^{2-}, and Cl^-) specifically adsorbed at the growth front may affect the exchange current density of the deposition [8]. Boric acid is a buffer that suppresses the pH increase due to hydrogen evolution [19]. In addition to the buffering action, Yin and Lin suggested that boric acid competed with $NiOH^+$ and $FeOH^+$ for the adsorption sites, and that the boric acid adsorbed at the growth front selectively blocked the passage and reduction of $NiOH^+$, thus augmenting the composition anomaly [20]. The adsorption of saccharin reduces the grain size [21]. Wasekar et al. demonstrated that the adsorbed saccharin favored the lateral growth over the vertical growth, resulting in the cauliflower-like morphology [23], which resembled the morphology shown in **Figure 3.2g**, **3.4g**, **3.6g**, and **3.7g**. Further efforts may be required to clarify the roles of these adsorbed species with respect to the composition gradients occurred in different deposition modes and conditions.

3.5 Conclusions

Composition control is critical to the synthesis of $L1_0$ Fe-Ni. In this chapter, we demonstrated the evolution of composition and morphology during the anomalous codeposition of Fe-Ni films. During the initial growth, the potentiostatic mode and the pulse-reverse potential mode both developed a composition gradient, but in opposite signs; during the subsequent growth, the

composition gradients under both deposition modes declined, approaching a composition plateau (**Figure 3.1**). On the other hand, the surface morphologies resulted from the two deposition modes were drastically different during the initial growth, but became increasingly more similar during the subsequent growth (**Figure 3.2-3.4**, **3.6**, and **3.7**). In particular, the initial growth under the pulse-reverse potential mode showed morphological features indicative of a dealloying process (**Figure 3.6a**, **3.7a**, and **3.8a**), but the subsequent growth under the same mode did not show such features (**Figure 3.6g** and **3.7g**). Combining the compositional and the morphological insights, we formulated a Fe-Ni codeposition mechanism based on the Fe deposition mechanism originally proposed by Bockris, Drazic, and Despic [8]. Notice that the original BDD mechanism only accounted for the composition difference between the deposit and the electrolyte, but not the occurrence of the composition gradient. The mechanism we proposed here, however, accounted for both the composition difference and the composition gradient. More specifically, the accumulation and the saturation of the adsorbed metal hydroxide ion — $Me(OH)^{+}_{ads}$ at the growth front were used to rationalize not only the occurrence and the decline of the composition gradient under the potentiostatic mode and the pulse-reverse potential mode, but also the opposite signs of the composition gradients under the two deposition modes.

Appendix A 3.1 The Height Profiles

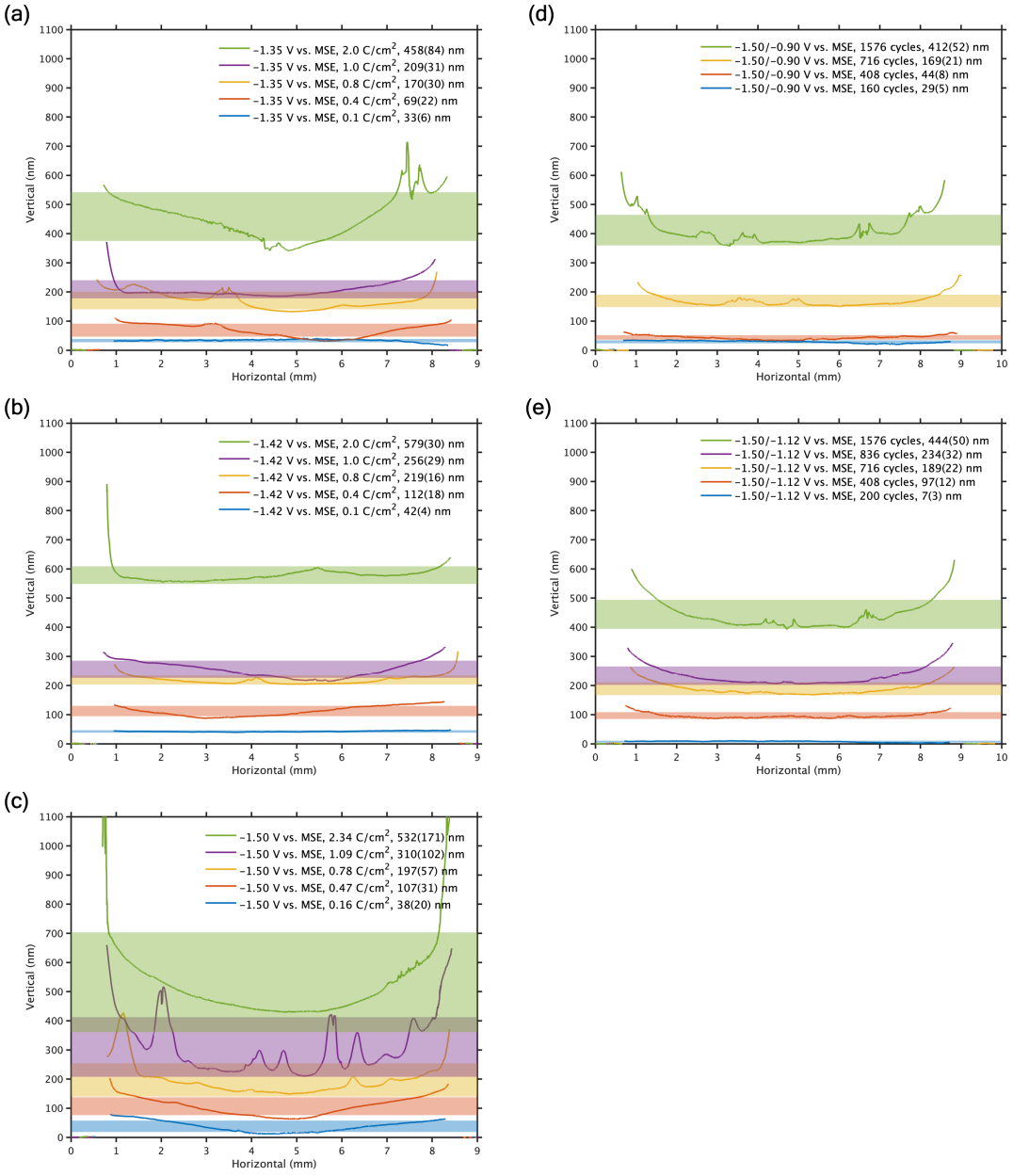

Figure 3.11. Height profiles of the Fe-Ni films from the potentiostatic deposition at **(a)** -1.35 V vs. MSE, **(b)** -1.42 V vs. MSE, **(c)** -1.50 V vs. MSE; and the pulse-reverse potential deposition at **(d)** -1.50 / -0.90 V vs. MSE, **(e)** -1.50 / -1.12 V vs. MSE. The vertical center and half width of each band show the average (*i.e.*, the thickness, *h*) and the standard deviation of the corresponding height profile (in the same color), respectively.

Appendix A 3.2 The Composition vs. Thickness Curves

Table 3.3. The thickness and the composition of the Fe-Ni films (set I, II, and III) from potentiostatic deposition. *E* is the applied potential. σ is the applied charge density. *h* is the thickness. *C* is the composition. *R* is the deposition rate as the thickness normalized by the total deposition time. *Q* is the estimated Faradaic efficiency (see the text below for the details of the calculation).

E **(V_{MSE})**	σ **(C/cm^2)**	***h*** **(nm)**	***h*** **Std. (nm)**	***C*** **(at.% Ni)**	***C*** **Std. (at.% Ni)**	***R*** **(nm/s)**	***Q*** **(%)**
-1.35	0.1	33	6	43.6	1.5	0.21	88 ~ 99
-1.35	0.4	69	22	44.9	0.3	0.11	46 ~ 52
-1.35	0.8	170	30	47.7	0.2	0.18	57 ~ 64
-1.35	1.0	209	31	51.3	0.7	0.15	55 ~ 63
-1.35	2.0	458	84	53.0	0.7	0.23	61 ~ 69
-1.42	0.1	42	4	38.2	0.7	0.99	112 ~ 127
-1.42	0.4	112	18	44.8	1.0	0.93	75 ~ 84
-1.42	0.8	219	16	47.2	0.8	1.05	73 ~ 82
-1.42	1.0	256	29	47.6	1.9	0.98	68 ~ 77
-1.42	2.0	579	30	48.0	1.2	1.15	77 ~ 87
-1.50	0.16	38	20	37.5	1.5	1.41	64 ~ 73
-1.50	0.47	107	31	44.1	0.7	1.58	60 ~ 68
-1.50	0.78	197	57	47.2	2.5	2.09	67 ~ 76
-1.50	1.10	310	102	47.4	1.7	2.47	75 ~ 85
-1.50	2.35	532	171	49.8	3.0	2.04	60 ~ 68

Table 3.4. The thickness and the composition of the Fe-Ni films (set IV and V) from pulse-reverse potential deposition. E_P is the pulse potential. E_R is the reverse potential. N is the number of cycles. h is the thickness. C is the composition. R_{eff} is the effective deposition rate as the thickness normalized by the total pulse potential time (*i.e.*, $N \times T_P$). Q is the estimated Faradaic efficiency (see the text below for the details of the calculation).

E_P (VMSE)	E_R (VMSE)	N	h (nm)	h Std. (nm)	C (at.% Ni)	C Std. (at.% Ni)	R_{eff} (nm/s)	Q (%)
-1.50	-0.90	160	29	5	64.6	2.3	1.81	109 ~ 123
-1.50	-0.90	408	44	8	66.1	0.9	1.08	78 ~ 88
-1.50	-0.90	716	169	21	55.2	1.4	2.36	84 ~ 95
-1.50	-0.90	1576	412	52	51.8	1.3	2.61	77 ~ 87
-1.50	-1.12	200	7	3	48.8	1.4	0.37	45 ~ 50
-1.50	-1.12	408	97	12	42.7	0.5	2.38	84 ~ 95
-1.50	-1.12	716	189	22	42.9	0.8	2.64	77 ~ 87
-1.50	-1.12	836	234	32	43.0	1.1	2.80	71 ~ 81
-1.50	-1.12	1576	444	50	42.9	0.7	2.82	72 ~ 82

The expressions of the composition vs. thickness curves shown in **Figure 3.1** are listed here:

$C_I = \{[59.35 \times (h/nm) + 9321] / [(h/nm) + 227.4]\}$ at.%Ni

$C_{II} = \{[49.08 \times (h/nm) - 489.1] / [(h/nm) - 0.7425]\}$ at.%Ni

$C_{III} = \{[51.15 \times (h/nm) + 835.9] / [(h/nm) + 36.13]\}$ at.%Ni

$C_{IV} = \{[45.63 \times (h/nm) + 8658] / [(h/nm) + 122.3]\}$ at.%Ni

$C_V = \{[42.58 \times (h/nm)^2 - 282.9 \times (h/nm) - 226.7] / [(h/nm)^2 - 7.692 \times (h/nm) + 2.385]\}$ at.%Ni

These expressions were extracted empirically from the (thickness, composition) data (**Table 3.3** and **3.4**) of the films (set I, II, III, IV, and V) prepared with the deposition conditions listed in **Table 3.1** and **3.2**, respectively, by the "FIT" function of MATLAB with the "Rational" model

and the "Non-linear Least Squares" method. The degree of the rational function was selected in order to provide a monotonic function with as few parameters as possible over the fitting range.

The range of the Faradaic efficiency (Q) was estimated based on the on the density of Ni and Fe (*i.e.*, ρ_{Ni} = 8.902 g/cm^3, ρ_{Fe} = 7.874 g/cm^3):

$$Q = h/\{[\sigma/(z\times F\times\rho)]\,[(c_{Ni}/100\times M_{Ni}) + (100-c_{Ni})/100\times M_{Fe}]\}\times 100\%$$

where $z = z_{Fe2+} = z_{Ni2+} = 2$ is the valence of the cations, F = 96485.3329 C/mol is the Faraday constant, M_{Ni} = 58.6934 g/mol and M_{Fe} = 55.845 g/mol are the molar mass of Ni and Fe.

The height (*i.e.*, the thickness h) profiles (**Figure 3.11**) were extracted from the data measured by the scanning white light interferometry (SWLI) in the magnification of 5X with a lateral pixel size of 2.18 μm. Thus, any pores or gaps smaller than the pixel size (for example, those shown in **Figure 3.6a**, **3.7a** and **3.8a**) were not picked up by SWLI and could lead to the overestimation of the Faradaic efficiency, in particular for the relatively thin films whose thicknesses were more comparable to the length scales of the pores and/or gaps.

Appendix A 3.3 The Individual Profile-Fitting of the XRD Patterns

Table 3.5. The peak positions extracted from the individual profile-fitting (shown in **Figure 3.12 – 3.14**) of the XRD patterns of the films (set I, II, and III) from potentiostatic deposition, and the lattice parameters calculated from the peak positions extracted. a is the lattice parameter of FCC Fe-Ni. a' is the lattice parameter of BCC Fe-Ni.

E (V_{MSE})	σ (C/cm^2)	$(2\theta)_{Bragg}$ (°)	Lattice Parameter (Å)
-1.35	0.1	$(111)_{FCC}$ 43.7812	a = 3.5785
-1.35	0.4	$(111)_{FCC}$ 43.7435	a = 3.5814
-1.35	0.8	$(111)_{FCC}$ 43.7404	a = 3.5817
-1.35	2.0	$(111)_{FCC}$ 43.7501, $(200)_{FCC}$ 50.9801	a = 3.5809
-1.42	0.1	$(110)_{BCC}$ 44.7722	a' = 2.8604
-1.42	0.4	$(111)_{FCC}$ 43.7461, $(110)_{BCC}$ 44.7909	a = 3.5812, a' = 2.8593
-1.42	0.8	$(111)_{FCC}$ 43.7374, $(110)_{BCC}$ 44.7929, $(200)_{FCC}$ 50.8759	a = 3.5819, a' = 2.8591
-1.42	2.0	$(111)_{FCC}$ 43.7181, $(110)_{BCC}$ 44.7846, $(200)_{FCC}$ 50.7813	a = 3.5834, a' = 2.8596
-1.50	0.16	$(110)_{BCC}$ 44.8052	a' = 2.8584
-1.50	0.47	$(111)_{FCC}$ 43.7505, $(110)_{BCC}$ 44.7984	a = 3.5809, a' = 2.8588
-1.50	0.78	$(111)_{FCC}$ 43.7496, $(110)_{BCC}$ 44.8132, $(200)_{FCC}$ 51.0600	a = 3.5810, a' = 2.8579
-1.50	2.35	$(111)_{FCC}$ 43.7464, $(110)_{BCC}$ 44.7962, $(200)_{FCC}$ 50.7873	a = 3.5812, a' = 2.8589

Table 3.6. The peak positions extracted from the individual profile-fitting (shown in **Figure 3.15** and **3.16**) of the XRD patterns of the films (set IV and V) from pulse-reverse potential deposition, and the lattice parameters calculated from the peak positions extracted. a is the lattice parameter of FCC Fe-Ni. a' is the lattice parameter of BCC Fe-Ni, a'' is the lattice parameter of the secondary FCC Fe-Ni.

E_P (VMSE)	E_R (VMSE)	N	$(2\theta)_{Bragg}$ (°)	Lattice Parameter (Å)
-1.50	-0.90	160	$(111)_{FCC(2)}$ 43.0823, $(111)_{FCC}$ 44.0627	a = 3.5568, a'' = 3.6337
-1.50	-0.90	408	$(111)_{FCC}$ 44.0479	a = 3.5579
-1.50	-0.90	716	$(111)_{FCC}$ 43.9091	a = 3.5686
-1.50	-0.90	1576	$(111)_{FCC}$ 43.8671, $(200)_{FCC}$ 50.9855	a = 3.5719
-1.50	-1.12	200	$(111)_{FCC}$ 43.6626	a = 3.5878
-1.50	-1.12	408	$(111)_{FCC}$ 43.7608, $(200)_{FCC}$ 50.5662, $(110)_{BCC}$ 44.8291	a = 3.5801, a' = 2.8569
-1.50	-1.12	716	$(111)_{FCC}$ 43.7540, $(200)_{FCC}$ 50.6353, $(110)_{BCC}$ 44.8383	a = 3.5806, a' = 2.8564
-1.50	-1.12	1576	$(111)_{FCC}$ 43.7409, $(200)_{FCC}$ 50.6352, $(110)_{BCC}$ 44.8251	a = 3.5817, a' = 2.8572

The individual profile-fitting of the XRD patterns (**Figure 3.12 – 3.16**) were obtained by the "NLINFIT" function of MATLAB, with the weight function specified by

$$w_i = 1/y_i$$

where w_i is the weight of the ith data point, and y_i is the observed value of the ith data point. According to Prince *et al.* [11], this weight function is adequate in general. The profile function of each Bragg reflection was labeled in **Figure 3.12 – 3.16**, which was either "G", "L", or "PV", representing the Gaussian function, the Lorentzian function, and the pseudo-Voigt function, respectively [11]:

$$\Phi_{K,G}(2\theta_i) = [C_0^{1/2}/(H_K \times \pi^{1/2})]\exp[-C_0(2\theta_i - 2\theta_K)^2/H_K^2]$$

$$\Phi_{K,L}(2\theta_i) = [C_1^{1/2}/(\pi \times H_K)]/[1+ C_1(2\theta_i - 2\theta_K)^2/H_K^2]$$

$$\Phi_{K,PV}(2\theta_i) = \eta L(2\theta_i) + (1\text{-}\eta)G(2\theta_i)$$

with $C_0 = 4 \ln 2$, $C_1 = 4$

where H_K and $2\theta_K$ are the full-width-at-half-maximum (FWHM) and the position of the Kth Bragg peak, and η is the mixed parameter of the pseudo-Voigt function. When $\eta = 0$, the pseudo-

Voigt function is reduced into a Gaussian function. When η = 1, the pseudo-Voigt function is reduced into a Lorentzian function. The calculated intensity was a linear combination of the profile functions plus a flat background (*i.e.*, $y_{bi} = b$):

$$y_{ci} = \sum S_K \Phi_K + y_{bi}$$

The peak positions extracted from each of the XRD patterns, and the lattice parameters calculated from the peak positions were listed in **Table 3.5** and **3.6**.

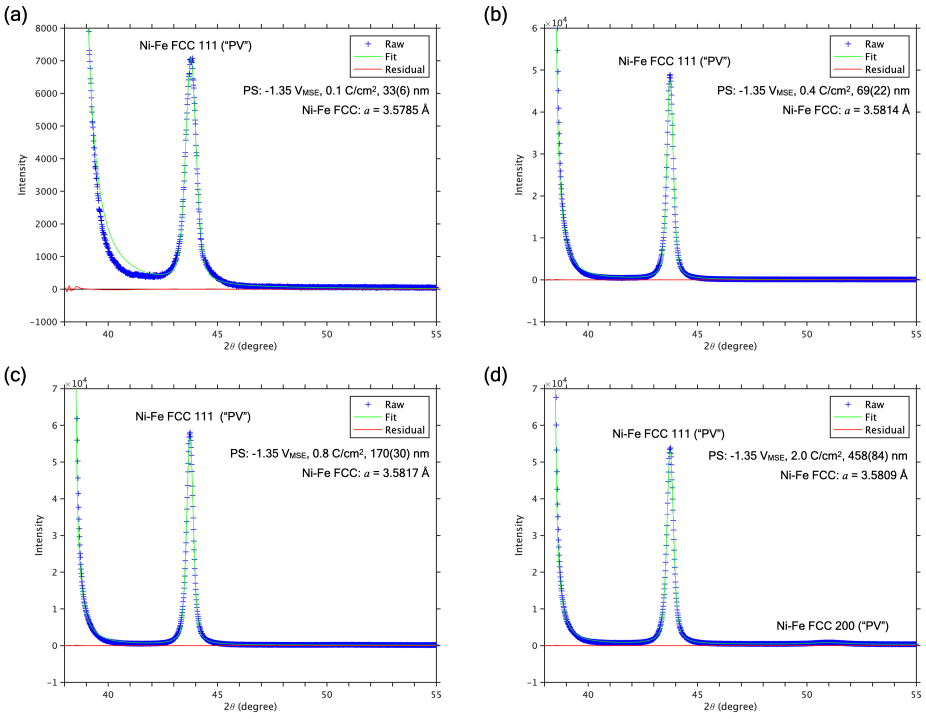

Figure 3.12. Individual profile-fitting of the XRD patterns of the films in set I.

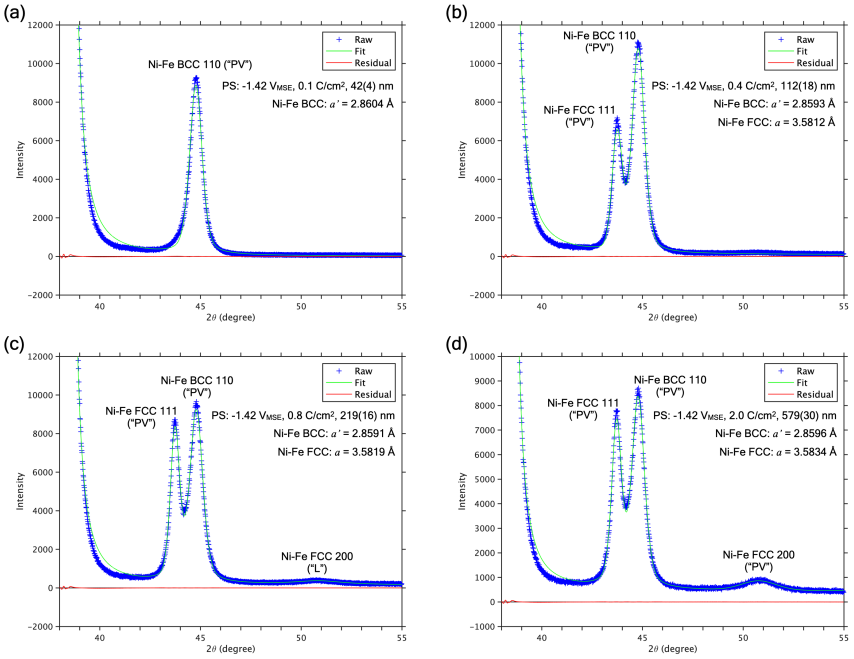

Figure 3.13. Individual profile-fitting of the XRD patterns of the films in set II.

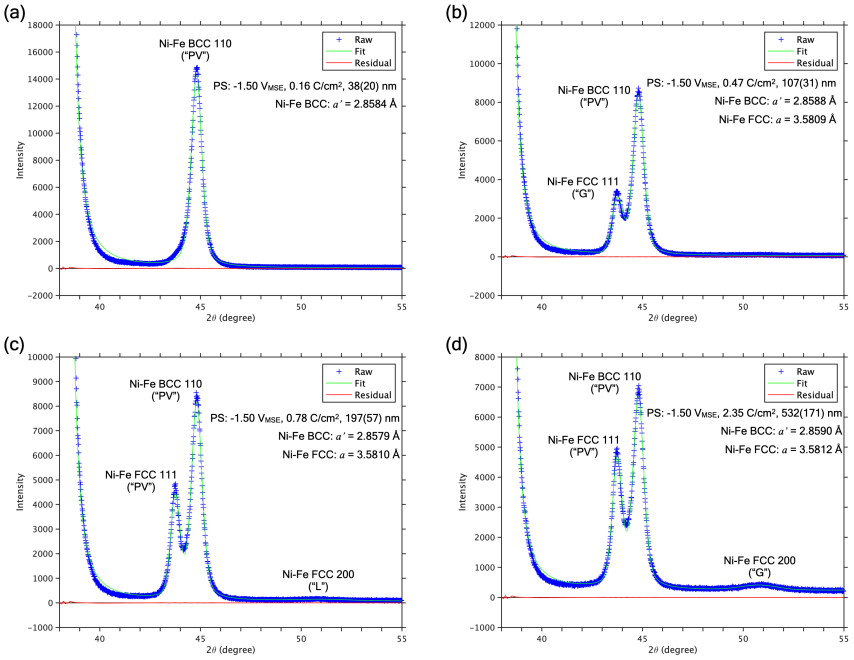

Figure 3.14. Individual profile-fitting of the XRD patterns of the films in set III.

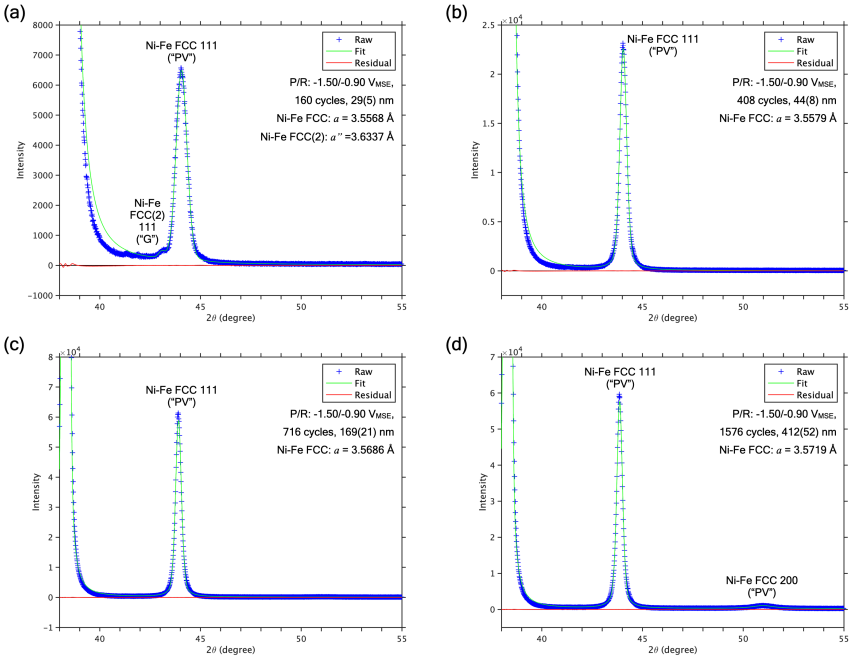

Figure 3.15. Individual profile-fitting of the XRD patterns of the films in set IV.

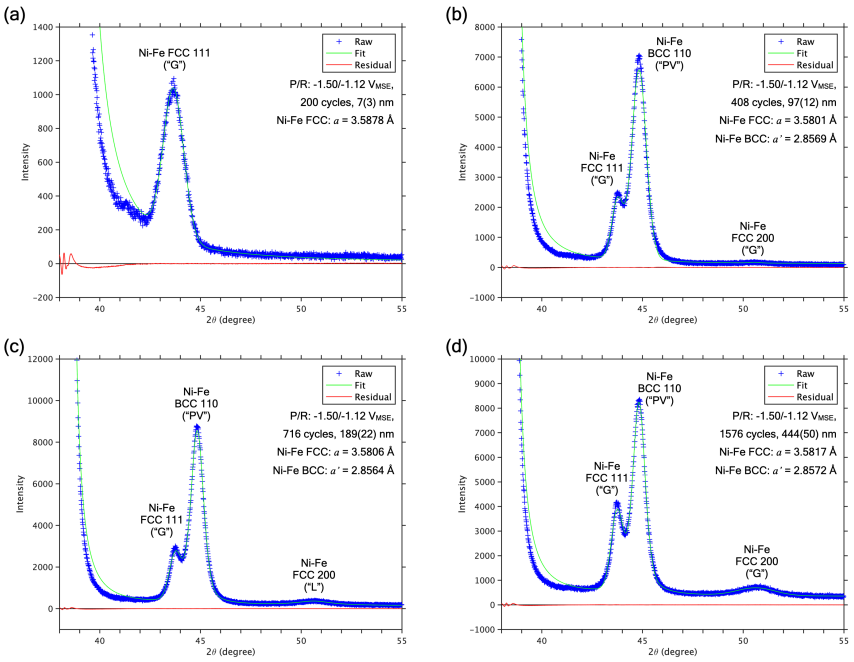

Figure 3.16. Individual profile-fitting of the XRD patterns of the films in set V.

Appendix A 3.4 The Rietveld Refinement of the XRD Patterns

Table 3.7. The weight fractions of the FCC phase and the BCC phase and the March coefficients extracted from the Rietveld refinement of the XRD patterns of the films (set II and III) from potentiostatic deposition that consist of both phases.

E **(VMSE)**	***σ*** **(C/cm²)**	**Thickness Level**	***h*** **(nm)**	**FCC (wt.%)**	**BCC (wt.%)**	**March Coefficient**
-1.42	0.4	"Thin"	112(18)	38	62	0.9909
-1.42	0.8	"Medium"	219(16)	43	57	0.9553
-1.42	2.0	"Thick"	579(30)	35	65	0.8426
-1.50	0.47	"Thin"	107(31)	30	70	1.0122
-1.50	0.78	"Medium"	197(57)	35	65	0.9743
-1.50	2.35	"Thick"	532(171)	26	74	0.7670

Table 3.8. The weight fractions of the FCC phase and the BCC phase extracted from the Rietveld refinement of the XRD patterns of the films (set V) from pulse-reverse potential deposition that consist of both phases.

E_P **(VMSE)**	E_R **(VMSE)**	***N***	***h*** **(nm)**	**FCC (wt.%)**	**BCC (wt.%)**
-1.50	-1.12	408	97(12)	22	78
-1.50	-1.12	716	189(22)	39	61
-1.50	-1.12	1576	444(50)	37	63

The Rietveld refinement of the XRD patterns (**Figure 3.18 – 3.20**) were obtained by the "NLINFIT" function of MATLAB, with the weight function specified by:

$w_i = 1/y_i$

where w_i is the weight of the ith data point, and y_i is the observed value of the ith data point, as in the individual profile-fitting method. The profile function of each Bragg reflection was labeled in **Figure 3.18** – **3.20**, with the same form as defined in the individual profile-fitting method. The calculated intensity was a weighted sum of the intensity contribution from each phase plus a flat background (*i.e.*, $y_{bi} = b$); the intensity contribution from each phase was a sum of the intensity contribution from each Bragg reflection; the intensity contribution from each Bragg reflection was a product of the Lorentz-Polarization factor (L), the multiplicity factor (M), the magnitude square of the structure factor (F), the profile function (Φ), and the preferred orientation function (P):

$$y_{ci} = \sum_j S_j \sum_K L_{j,K} M_{j,K} |F_{j,K}|^2 \Phi_{j,K} P_{j,K} + y_{bi}$$

where the weight of the intensity contribution from the jth phase (S_j) is called the Rietveld scale factor of the jth phase [11]. The March model [12, 13] was used as the preferred orientation function to account for the texture of the FCC phase:

$$P_K = (r^2 \cos^2 \alpha_K + r^{-1} \sin^2 \alpha_K)^{-3/2}$$

where r is the March coefficient that characterizes the strength of the preferred orientation, and α_K is the angle between the preferred orientation vector and the scattering vector of the Kth reflection. In this work, the preferred orientation vector of the FCC phase was assumed to be $[111]_{FCC}$, based on the XRD patterns shown in **Figure 3.9**. The local epitaxial relationship

demonstrated by the high-resolution transmission electron microscopy (HRTEM) image in **section 2.3.3** in **chapter 2** also supports such an assumption.

The weight fraction of the jth phase (W_j) was calculated from the Rietveld scale factors following the standard relationship in quantitative phase analysis (QPA):

$$W_j = S_j z_j m_j v_j / \Sigma_p S_p z_p m_p v_p$$

where z, m, and v are, respectively, the number of formula units per unit cell, the molar mass of the formula unit, and the unit cell volume of the respective phase [11].

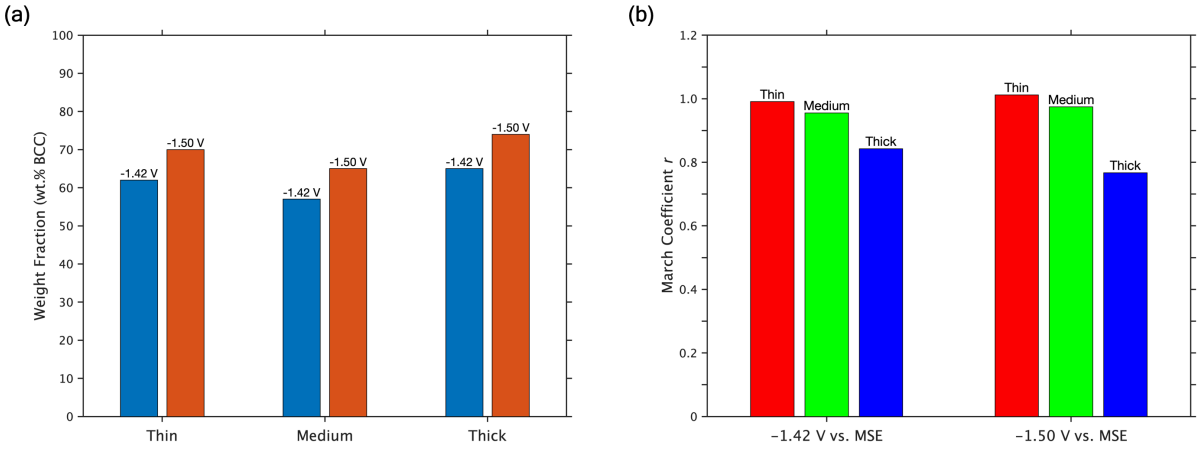

Figure 3.17. (a) Weight fractions (wt.% BCC) of the films (set II and III) from two potentiostatic deposition conditions (-1.42 and -1.50 V vs. MSE) at the three thickness levels as classified in **Table 3.7**. (b) The March coefficient of the films (set II and III) from two potentiostatic deposition conditions (-1.42 and -1.50 V vs. MSE) at the three thickness levels as classified in **Table 3.7**.

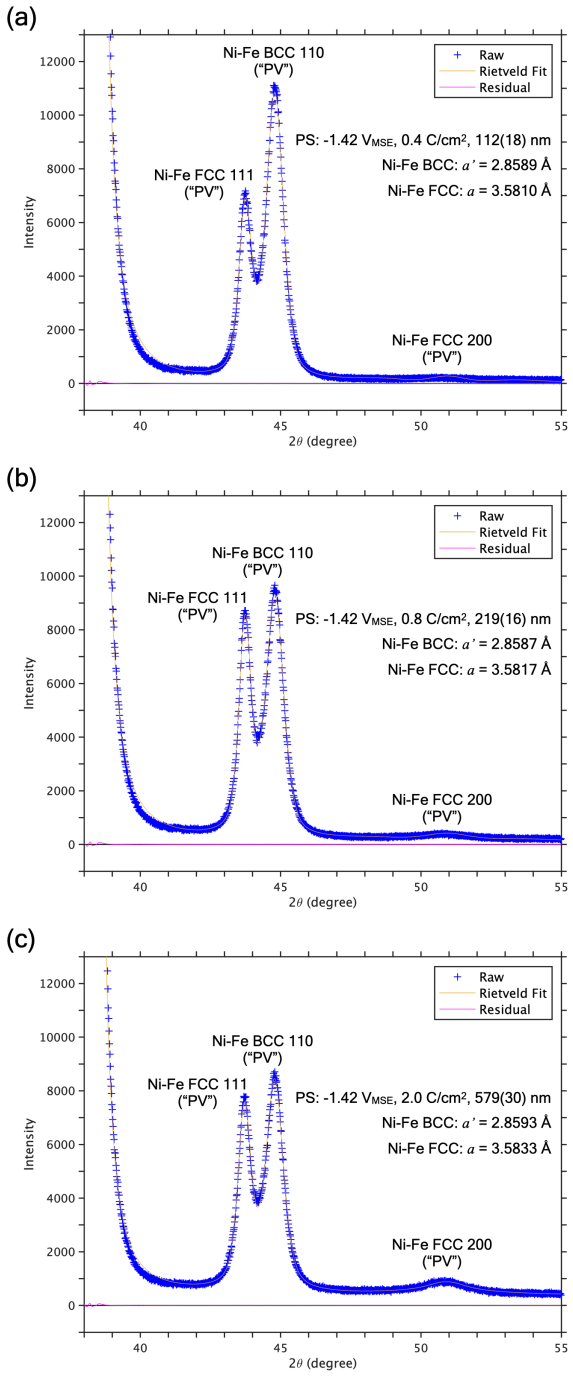

Figure 3.18. Rietveld refinement of the XRD patterns of the mix-phase films in set II.

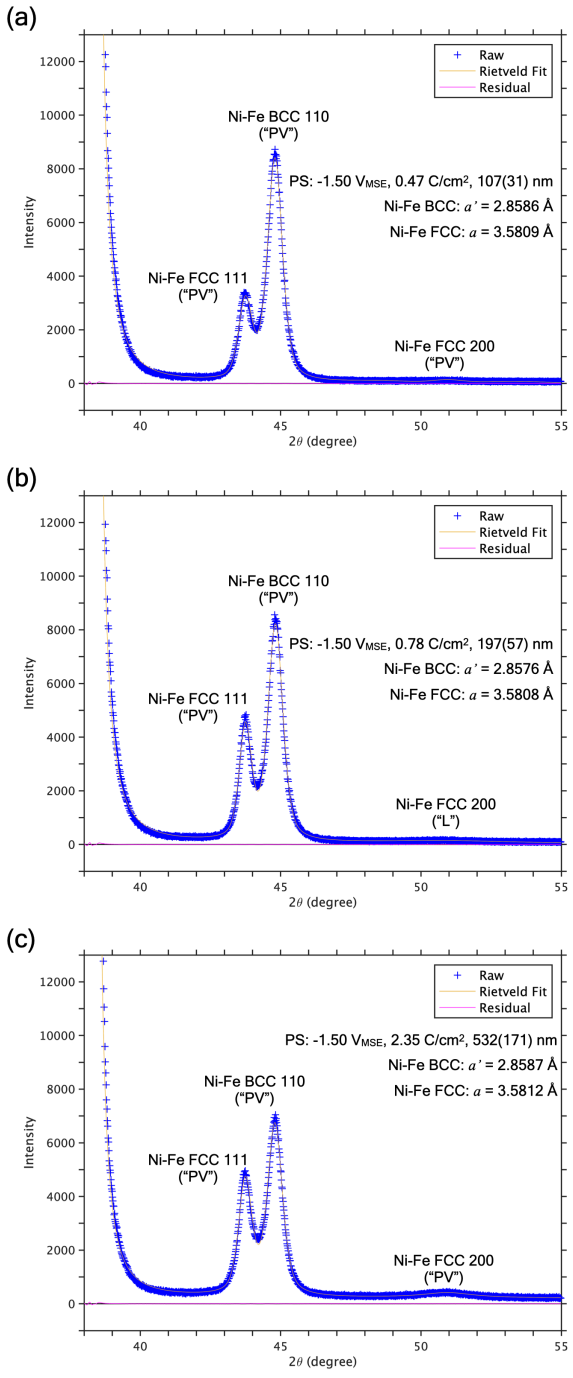

Figure 3.19. Rietveld refinement of the XRD patterns of the mix-phase films in set III.

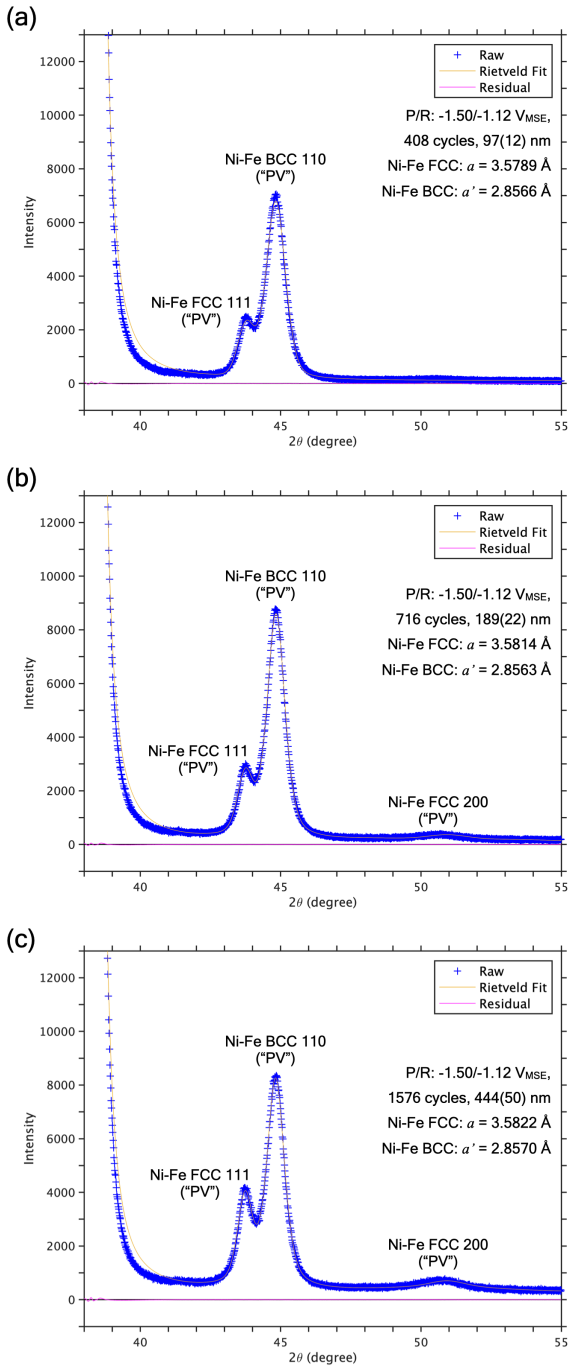

Figure 3.20. Rietveld refinement of the XRD patterns of the mix-phase films in set V.

Appendix A 3.5 The *j* vs. *t* Curves of the Pulse-Reverse Potential Deposition

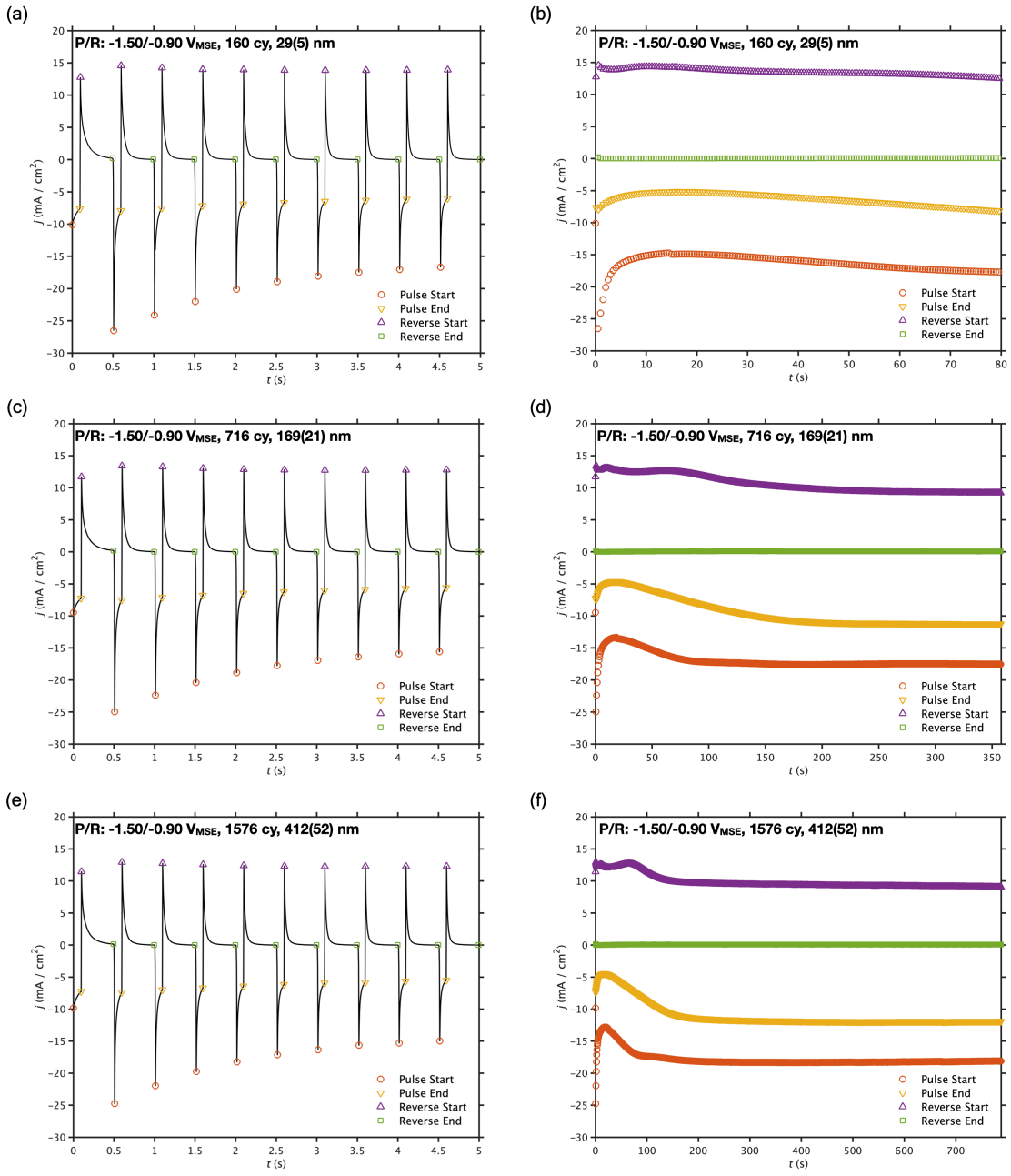

Figure 3.21. The current density vs. time curves of the films in set IV. (a, c, e) shows the temporal structure from which the data points at the pulse start, pulse end, reverse start, and reverse end were extracted. (b, d, f) shows the curves consisting of the data points extracted.

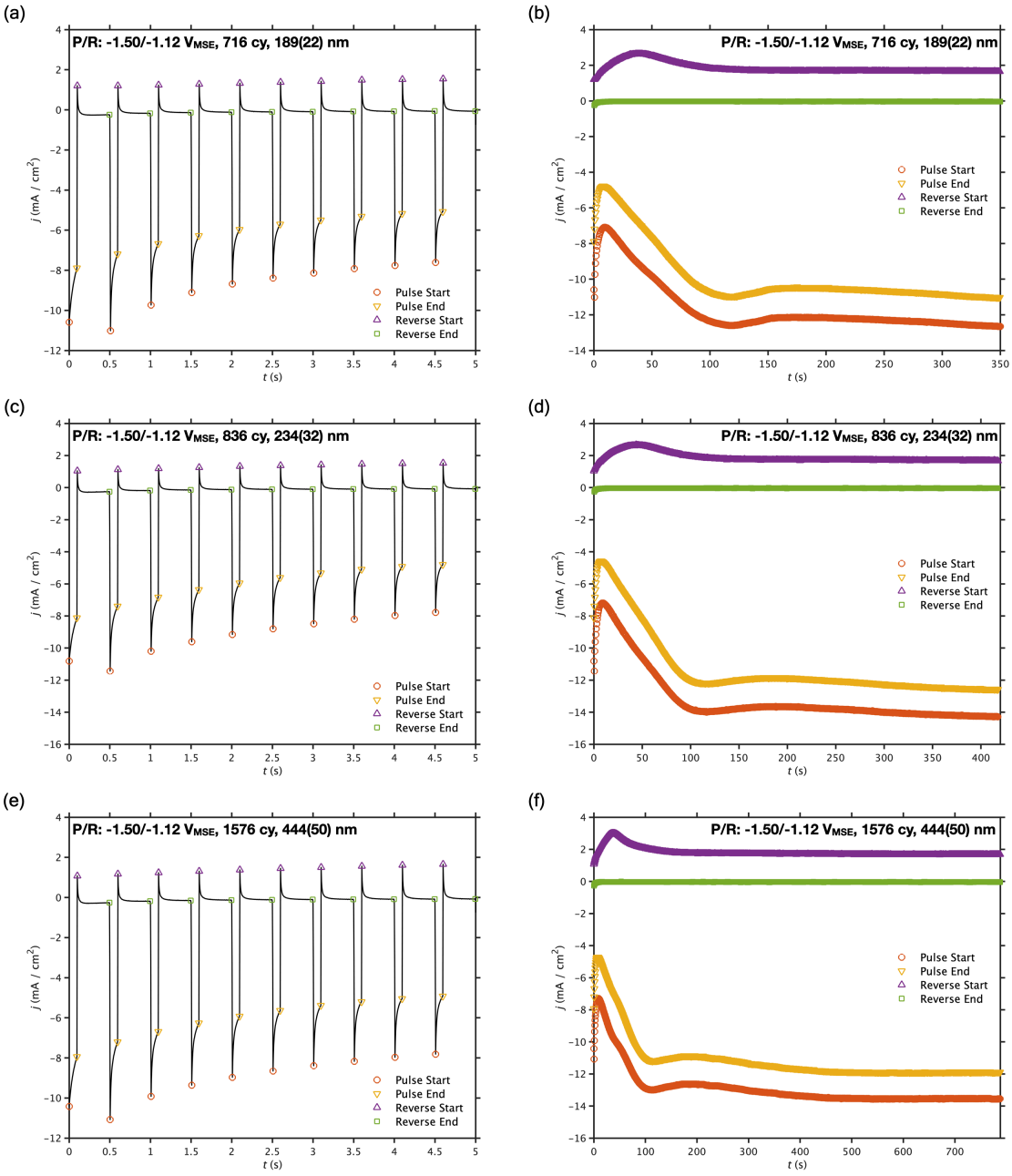

Figure 3.22. The current density vs. time curves of the films in set V. (a, c, e) shows the temporal structure from which the data points at the pulse start, pulse end, reverse start, and reverse end were extracted. (b, d, f) shows the curves consisting of the data points extracted.

Appendix A 3.6 The Cyclic Voltammogram

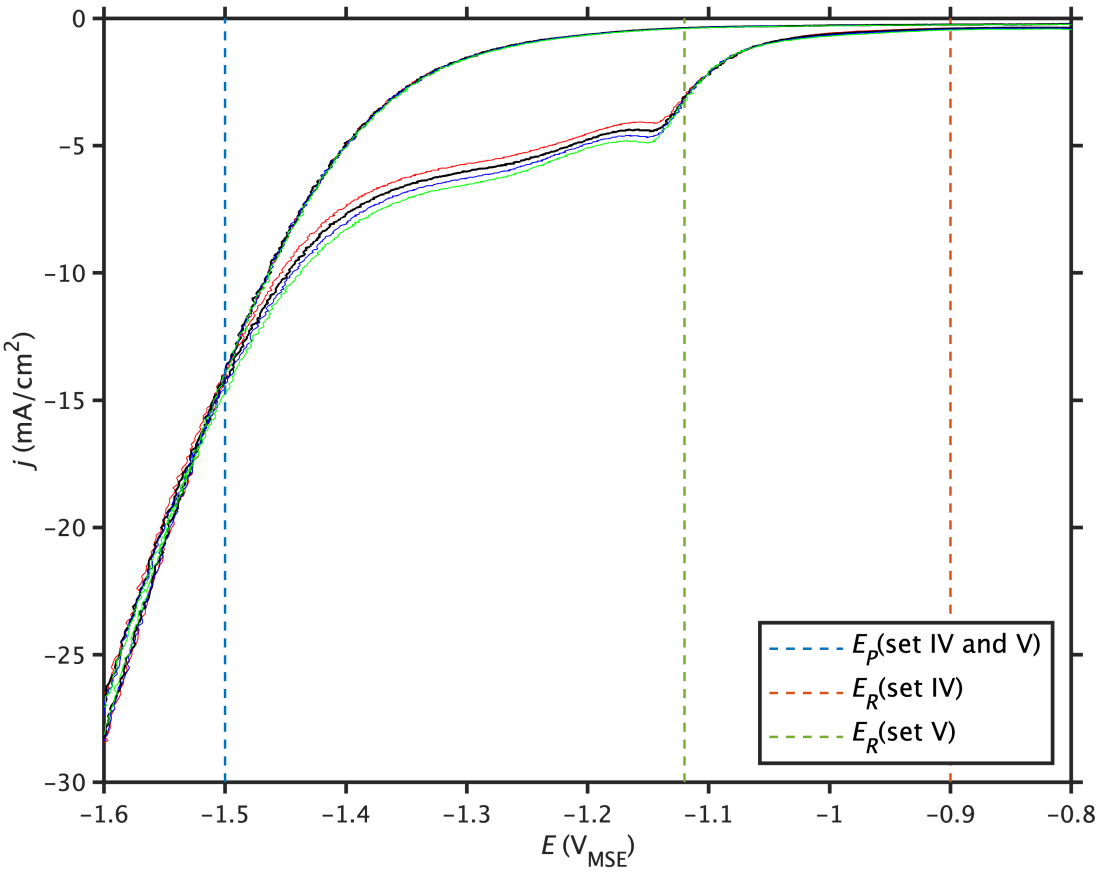

Figure 3.23. The magnified view of the CV loop (in black) shown in **Figure 3.10f**, along with a few other loops (red, blue, and green) collected right before or after.

Appendix A 3.7 EDS Spectra and Quantifications

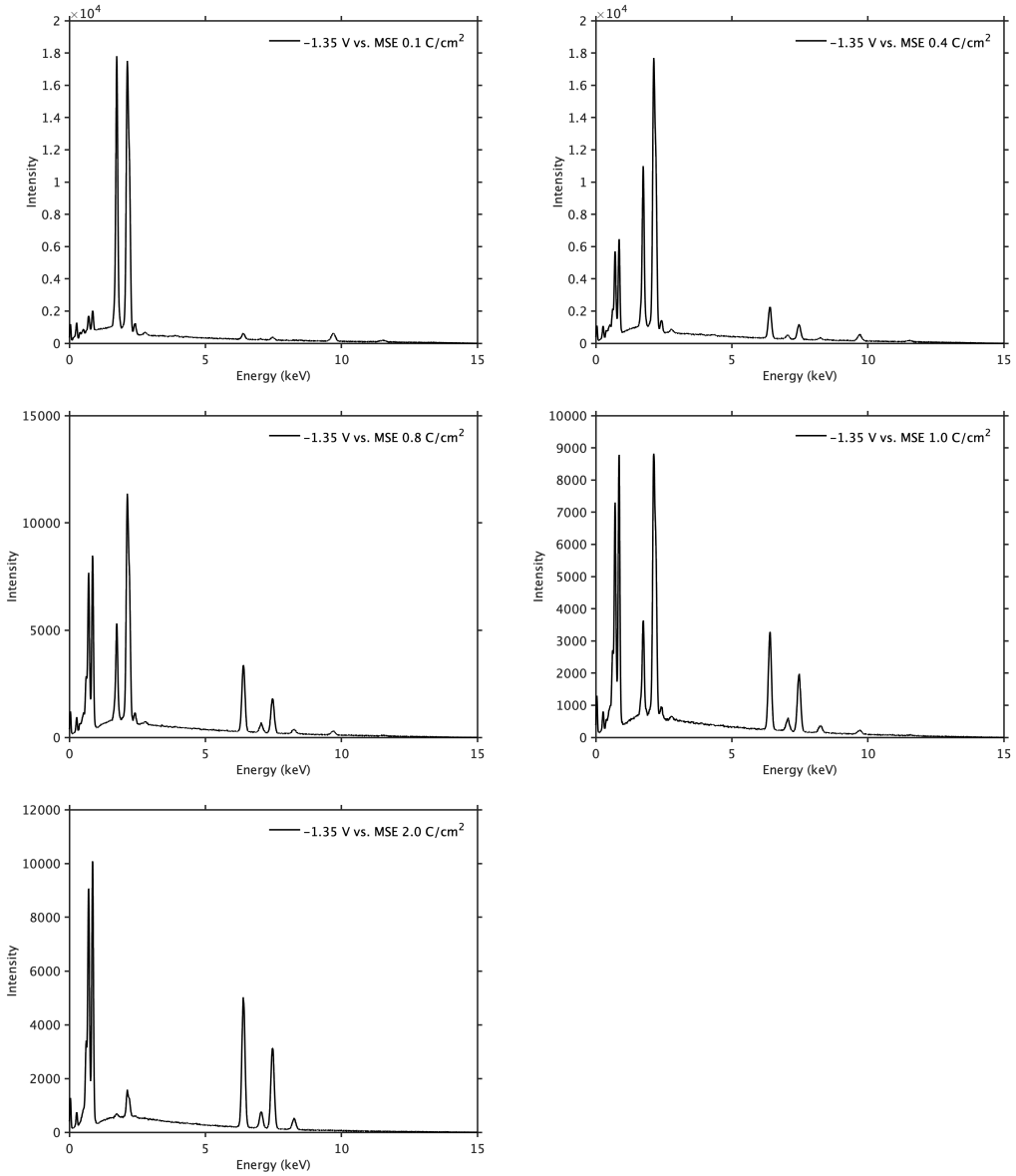

Figure 3.24. The EDS spectra of the Fe-Ni films (Set I) from the potentiostatic (PS) deposition at −1.35 V vs. MSE.

Set I -1.35 V vs MSE 0.1 C/cm2

Element	Line Type	Apparent Concentration	Intensity Correction	k Ratio	Wt%	Wt% Sigma	At%	Standard Label	Factory Standard
Fe	K series	7.02	1.05	0.07016	53.78	1.90	55.02	Fe	Yes
Ni	K series	5.51	0.96	0.05510	46.22	1.90	44.98	Ni	Yes
Total:					100.00		100.00		

Set I -1.35 V vs MSE 0.4 C/cm2

Element	Line Type	Apparent Concentration	Intensity Correction	k Ratio	Wt%	Wt% Sigma	At%	Standard Label	Factory Standard
Fe	K series	37.37	1.05	0.37374	53.80	0.54	55.04	Fe	Yes
Ni	K series	29.33	0.96	0.29326	46.20	0.54	44.96	Ni	Yes
Total:					100.00		100.00		

Set I -1.35 V vs MSE 0.8 C/cm2

Element	Line Type	Apparent Concentration	Intensity Correction	k Ratio	Wt%	Wt% Sigma	At%	Standard Label	Factory Standard
Fe	K series	59.71	1.06	0.59714	51.21	0.36	52.46	Fe	Yes
Ni	K series	51.85	0.96	0.51850	48.79	0.36	47.54	Ni	Yes
Total:					100.00		100.00		

Set I -1.35 V vs MSE 1.0 C/cm2

Element	Line Type	Apparent Concentration	Intensity Correction	k Ratio	Wt%	Wt% Sigma	At%	Standard Label	Factory Standard
Fe	K series	57.36	1.06	0.57365	47.81	0.34	49.06	Fe	Yes
Ni	K series	56.87	0.97	0.56872	52.19	0.34	50.94	Ni	Yes
Total:					100.00		100.00		

Set I -1.35 V vs MSE 2.0 C/cm2

Element	Line Type	Apparent Concentration	Intensity Correction	k Ratio	Wt%	Wt% Sigma	At%	Standard Label	Factory Standard
Fe	K series	91.59	1.07	0.91590	46.07	0.24	47.32	Fe	Yes
Ni	K series	97.17	0.97	0.97168	53.93	0.24	52.68	Ni	Yes
Total:					100.00		100.00		

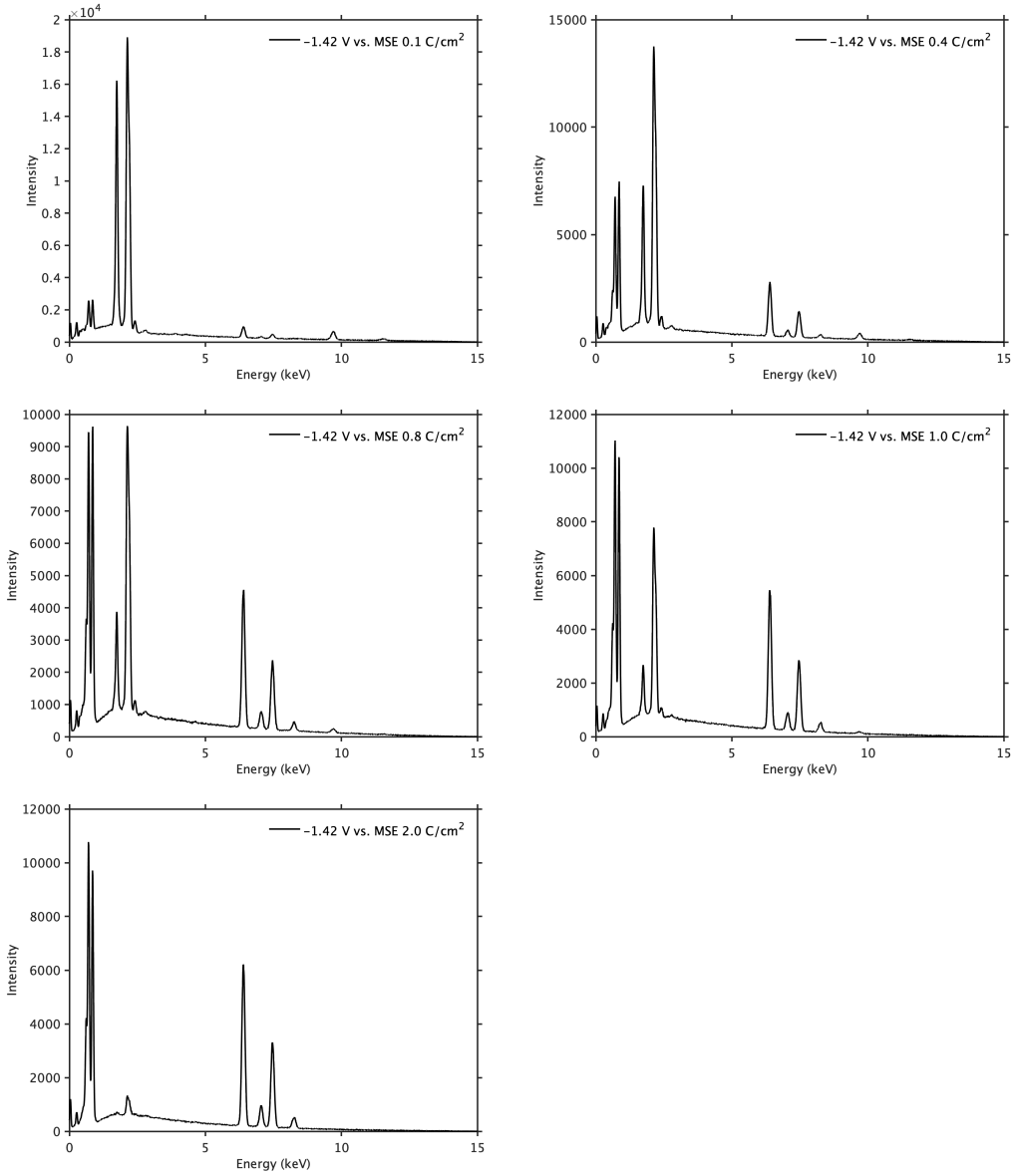

Figure 3.25. The EDS spectra of the Fe-Ni films (Set II) from the potentiostatic (PS) deposition at −1.42 V vs. MSE.

Set II -1.42 V vs MSE 0.1 C/cm2

Element	Line Type	Apparent Concentration	Intensity Correction	k Ratio	Wt%	Wt% Sigma	At%	Standard Label	Factory Standard
Fe	K series	13.14	1.04	0.13140	60.76	1.35	61.94	Fe	Yes
Ni	K series	7.80	0.96	0.07798	39.24	1.35	38.06	Ni	Yes
Total:					100.00		100.00		

Set II -1.42 V vs MSE 0.4 C/cm2

Element	Line Type	Apparent Concentration	Intensity Correction	k Ratio	Wt%	Wt% Sigma	At%	Standard Label	Factory Standard
Fe	K series	47.61	1.05	0.47605	52.48	0.43	53.72	Fe	Yes
Ni	K series	39.34	0.96	0.39342	47.52	0.43	46.28	Ni	Yes
Total:					100.00		100.00		

Set II -1.42 V vs MSE 0.8 C/cm2

Element	Line Type	Apparent Concentration	Intensity Correction	k Ratio	Wt%	Wt% Sigma	At%	Standard Label	Factory Standard
Fe	K series	81.97	1.05	0.81971	52.55	0.30	53.80	Fe	Yes
Ni	K series	67.54	0.96	0.67542	47.45	0.30	46.20	Ni	Yes
Total:					100.00		100.00		

Set II -1.42 V vs MSE 1.0 C/cm2

Element	Line Type	Apparent Concentration	Intensity Correction	k Ratio	Wt%	Wt% Sigma	At%	Standard Label	Factory Standard
Fe	K series	99.98	1.06	0.99980	51.66	0.27	52.91	Fe	Yes
Ni	K series	85.31	0.96	0.85312	48.34	0.27	47.09	Ni	Yes
Total:					100.00		100.00		

Set II -1.42 V vs MSE 2.0 C/cm2

Element	Line Type	Apparent Concentration	Intensity Correction	k Ratio	Wt%	Wt% Sigma	At%	Standard Label	Factory Standard
Fe	K series	115.01	1.06	1.15014	50.88	0.23	52.13	Fe	Yes
Ni	K series	101.16	0.96	1.01158	49.12	0.23	47.87	Ni	Yes
Total:					100.00		100.00		

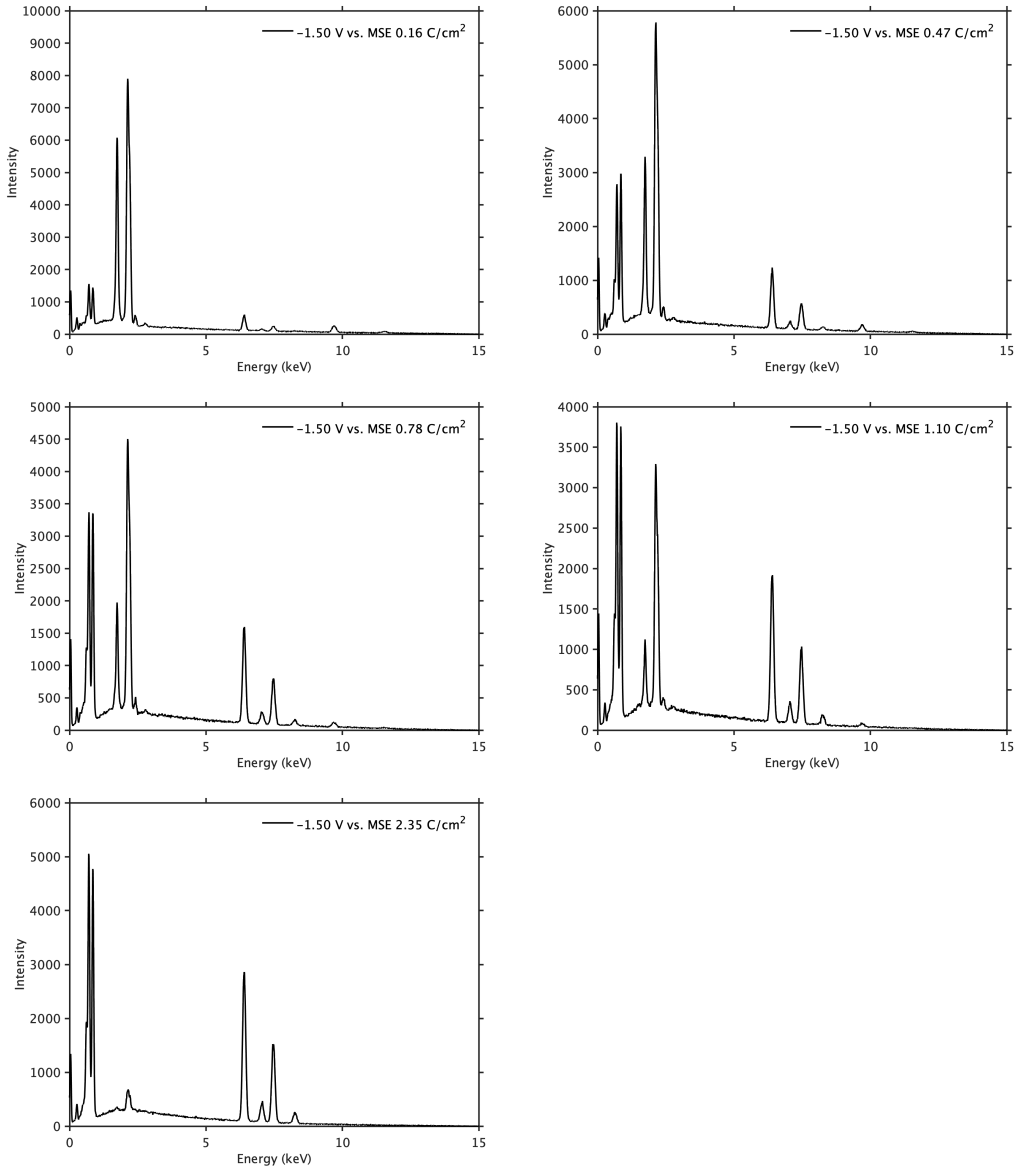

Figure 3.26. The EDS spectra of the Fe-Ni films (Set III) from the potentiostatic (PS) deposition at −1.50 V vs. MSE.

Set III -1.50 V vs MSE 0.16 C/cm2

Element	Line Type	Apparent Concentration	Intensity Correction	k Ratio	Wt%	Wt% Sigma	At%	Standard Label	Factory Standard
Fe	K series	8.81	1.04	0.08808	63.21	1.51	64.36	Fe	Yes
Ni	K series	4.72	0.96	0.04722	36.79	1.51	35.64	Ni	Yes
Total:					100.00		100.00		

Set III -1.50 V vs MSE 0.47 C/cm2

Element	Line Type	Apparent Concentration	Intensity Correction	k Ratio	Wt%	Wt% Sigma	At%	Standard Label	Factory Standard
Fe	K series	20.62	1.05	0.20619	54.98	0.69	56.22	Fe	Yes
Ni	K series	15.45	0.96	0.15450	45.02	0.69	43.78	Ni	Yes
Total:					100.00		100.00		

Set III -1.50 V vs MSE 0.78 C/cm2

Element	Line Type	Apparent Concentration	Intensity Correction	k Ratio	Wt%	Wt% Sigma	At%	Standard Label	Factory Standard
Fe	K series	28.22	1.05	0.28224	53.18	0.54	54.42	Fe	Yes
Ni	K series	22.70	0.96	0.22701	46.82	0.54	45.58	Ni	Yes
Total:					100.00		100.00		

Set III -1.50 V vs MSE 1.10 C/cm2

Element	Line Type	Apparent Concentration	Intensity Correction	k Ratio	Wt%	Wt% Sigma	At%	Standard Label	Factory Standard
Fe	K series	35.22	1.06	0.35222	51.83	0.45	53.08	Fe	Yes
Ni	K series	29.86	0.96	0.29865	48.17	0.45	46.92	Ni	Yes
Total:					100.00		100.00		

Set III -1.50 V vs MSE 2.35 C/cm2

Element	Line Type	Apparent Concentration	Intensity Correction	k Ratio	Wt%	Wt% Sigma	At%	Standard Label	Factory Standard
Fe	K series	52.93	1.06	0.52933	50.18	0.34	51.43	Fe	Yes
Ni	K series	47.87	0.96	0.47867	49.82	0.34	48.57	Ni	Yes
Total:					100.00		100.00		

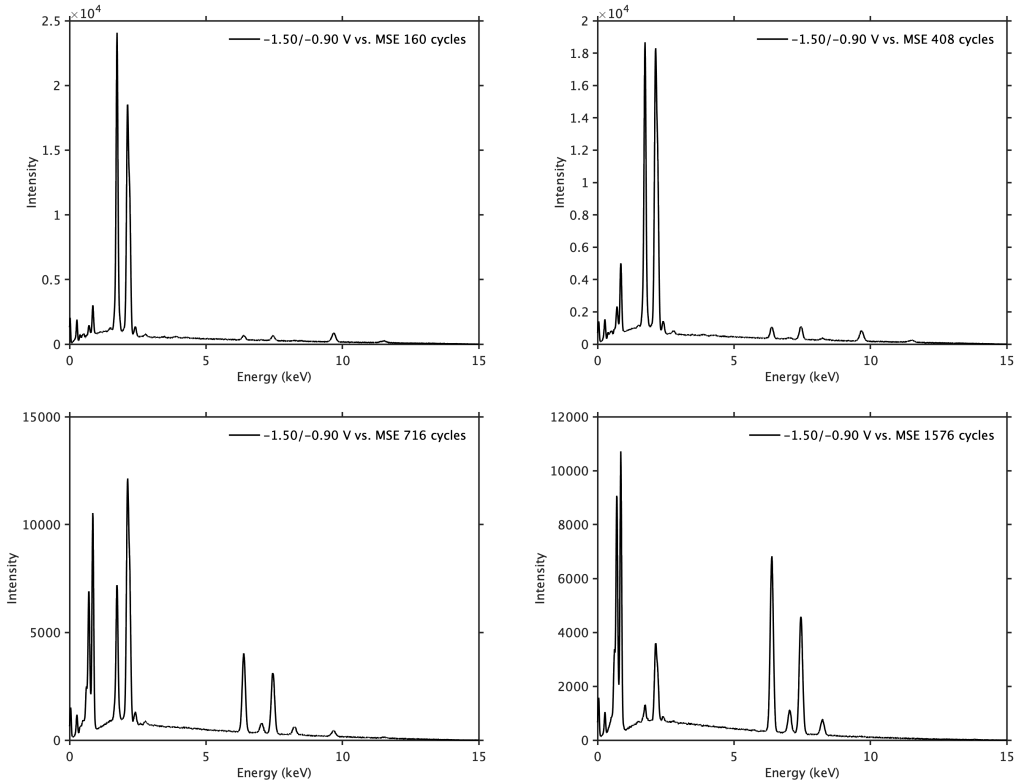

Figure 3.27. The EDS spectra of the Fe-Ni films (Set IV) from the pulse-reverse potential (P/R) deposition at −1.50 / −0.90 V vs. MSE

Set IV -1.50 / -0.90 V vs MSE 160 cycles

Element	Line Type	Apparent Concentration	Intensity Correction	k Ratio	Wt%	Wt% Sigma	At%	Standard Label	Factory Standard
Fe	K series	0.46	1.09	0.00461	33.17	1.38	34.29	Fe	Yes
Ni	K series	0.83	0.98	0.00828	66.83	1.38	65.71	Ni	Yes
Total:					100.00		100.00		

Set IV -1.50 / -0.90 V vs MSE 408 cycles

Element	Line Type	Apparent Concentration	Intensity Correction	k Ratio	Wt%	Wt% Sigma	At%	Standard Label	Factory Standard
Fe	K series	0.98	1.09	0.00981	32.26	0.74	33.36	Fe	Yes
Ni	K series	1.83	0.98	0.01833	67.74	0.74	66.64	Ni	Yes
Total:					100.00		100.00		

Set IV -1.50 / -0.90 V vs MSE 716 cycles

Element	Line Type	Apparent Concentration	Intensity Correction	k Ratio	Wt%	Wt% Sigma	At%	Standard Label	Factory Standard
Fe	K series	5.02	1.08	0.05021	41.44	0.30	42.65	Fe	Yes
Ni	K series	6.40	0.97	0.06397	58.56	0.30	57.35	Ni	Yes
Total:					100.00		100.00		

Set IV -1.50 / -0.90 V vs MSE 1576 cycles

Element	Line Type	Apparent Concentration	Intensity Correction	k Ratio	Wt%	Wt% Sigma	At%	Standard Label	Factory Standard
Fe	K series	8.89	1.07	0.08886	45.37	0.22	46.61	Fe	Yes
Ni	K series	9.69	0.97	0.09694	54.63	0.22	53.39	Ni	Yes
Total:					100.00		100.00		

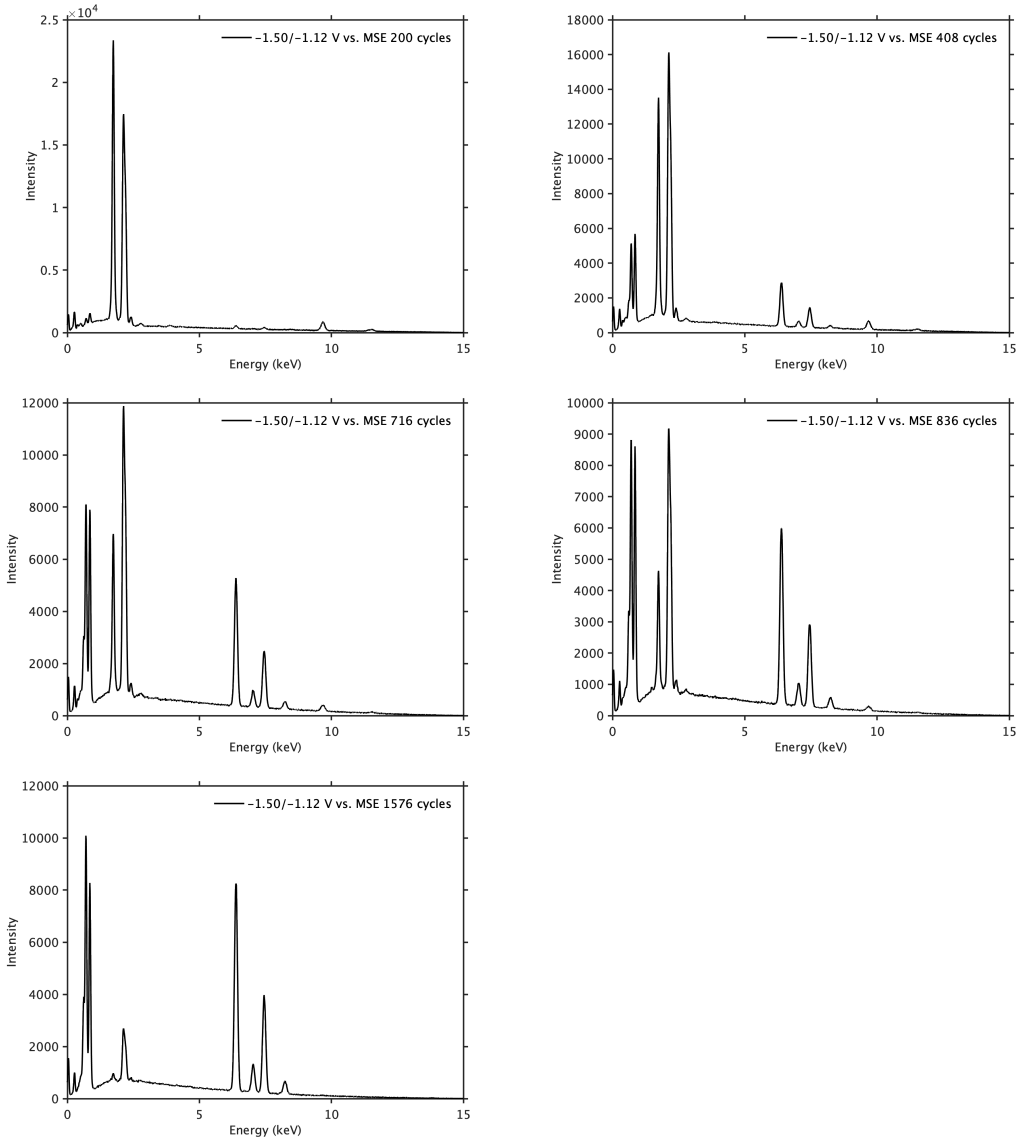

Figure 3.28. The EDS spectra of the Fe-Ni films (Set V) from the pulse-reverse potential (P/R) deposition at −1.50 / −1.12 V vs. MSE

Set V -1.50 / -1.12 V vs MSE 200 cycles

Element	Line Type	Apparent Concentration	Intensity Correction	k Ratio	Wt%	Wt% Sigma	At%	Standard Label	Factory Standard
Fe	K series	0.33	1.06	0.00334	47.90	2.70	49.15	Fe	Yes
Ni	K series	0.33	0.97	0.00331	52.10	2.70	50.85	Ni	Yes
Total:					100.00		100.00		

Set V -1.50 / -1.12 V vs MSE 408 cycles

Element	Line Type	Apparent Concentration	Intensity Correction	k Ratio	Wt%	Wt% Sigma	At%	Standard Label	Factory Standard
Fe	K series	3.48	1.05	0.03477	55.57	0.49	56.80	Fe	Yes
Ni	K series	2.55	0.96	0.02546	44.43	0.49	43.20	Ni	Yes
Total:					100.00		100.00		

Set V -1.50 / -1.12 V vs MSE 716 cycles

Element	Line Type	Apparent Concentration	Intensity Correction	k Ratio	Wt%	Wt% Sigma	At%	Standard Label	Factory Standard
Fe	K series	6.68	1.05	0.06680	55.36	0.32	56.59	Fe	Yes
Ni	K series	4.93	0.96	0.04932	44.64	0.32	43.41	Ni	Yes
Total:					100.00		100.00		

Set V -1.50 / -1.12 V vs MSE 836 cycles

Element	Line Type	Apparent Concentration	Intensity Correction	k Ratio	Wt%	Wt% Sigma	At%	Standard Label	Factory Standard
Fe	K series	7.85	1.05	0.07855	54.44	0.28	55.68	Fe	Yes
Ni	K series	6.01	0.96	0.06014	45.56	0.28	44.32	Ni	Yes
Total:					100.00		100.00		

Set V -1.50 / -1.12 V vs MSE 1576 cycles

Element	Line Type	Apparent Concentration	Intensity Correction	k Ratio	Wt%	Wt% Sigma	At%	Standard Label	Factory Standard
Fe	K series	10.99	1.05	0.10986	54.93	0.22	56.17	Fe	Yes
Ni	K series	8.25	0.96	0.08249	45.07	0.22	43.83	Ni	Yes
Total:					100.00		100.00		

References

[1] G. H. Cockett, E. S. Spencer-Timms, Variation of Composition with Thickness in Thin Electrodeposited Films of Nickel-Iron Alloys, Journal of The Electrochemical Society 108 (1961) 906.

[2] W. D. Doyle, Thickness Dependence of the Composition in Electroplated Ni–Fe Cylindrical Films, Journal of Applied Physics 38 (1967) 1441–1442.

[3] E. Bełtowska-Lehman, A. Riesenkampf, Effect of the Electrode Supply Mode on the Chemical Composition Gradient of Permalloy Thin Films, Thin Solid Films 71 (1980) 129–132.

[4] L. J. Gao, P. Ma, K. M. Novogradecz, P. R. Norton, Characterization of Permalloy Thin Films Electrodeposited on Si(111) Surfaces, Journal of Applied Physics 81 (1997) 7595–7599.

[5] K. Neuróhr, A. Csik, K. Vad, G. Molnár, I. Bakonyi, L. Péter, Near-Substrate Composition Depth Profile of Direct Current-Plated and Pulse-Plated Fe–Ni Alloys, Electrochimica Acta 103 (2013) 179–187.

[6] I. Tabakovic, J. Gong, S. Riemer, M. Kautzky, Influence of Surface Roughness and Current Efficiency on Composition Gradients of Thin NiFe Films Obtained by Electrodeposition, Journal of The Electrochemical Society 162 (2014) D102–D108.

[7] A. M. Białostocka, U. Klekotka, B. Kalska-Szostko, The Effect of a Substrate Material on Composition Gradients of Fe-Ni Films Obtained by Electrodeposition, Scientific Reports 10 (2020) 1029.

[8] J. O'M. Bockris, D. Drazic, A. R. Despic, The Electrode Kinetics of the Deposition and Dissolution of Iron, Electrochimica Acta 4, no. 2 (1961) 325–361.

[9] H. Dahms, I. M. Croll, The Anomalous Codeposition of Iron-Nickel Alloys, Journal of The Electrochemical Society 112 (1965) 771.

[10] S. Hessami, C. W. Tobias, A Mathematical Model for Anomalous Codeposition of Nickel-Iron on a Rotating Disk Electrode, Journal of The Electrochemical Society 136 (1989) 3611–3616.

[11] Young, R.A., and R.A. Young. The Rietveld Method. IUCr Monographs on Crystallography. Oxford University Press, 1995.

[12] March, Artur. "Mathematische Theorie Der Regelung Nach Der Korngestah Bei Affiner Deformation." Zeitschrift Für Kristallographie - Crystalline Materials 81, no. 1–6 (1932): 285–97.

[13] Dollase, W. A. "Correction of Intensities for Preferred Orientation in Powder Diffractometry: Application of the March Model." Journal of Applied Crystallography 19, no. 4 (August 1986): 267–72.

[14] Glaubitz, Benjamin, Stefan Buschhorn, Frank Brüssing, Radu Abrudan, and Hartmut Zabel. "Development of Magnetic Moments in Fe1 -XNix-Alloys." Journal of Physics: Condensed Matter 23, no. 25 (June 2011): 254210.

[15] Warren, B.E. X-Ray Diffraction. Dover Books on Physics. Dover Publications, 2012.

[16] Scharifker, Benjamin, and Graham Hills. "Theoretical and Experimental Studies of Multiple Nucleation." Electrochimica Acta 28, no. 7 (1983): 879–89.

[17] Jaya, S., T. Prasada Rao, and G. Prabhakara Rao. "Mono- and Multilayer Formation Studies of Thallium on Glassy Carbon Electrode." Electrochimica Acta 31, no. 12 (1986): 1601–4.

[18] Emery, Samuel B., Jennifer L. Hubbley, and Dipankar Roy. “Voltammetric and Amperometric Analyses of Electrochemical Nucleation: Electrodeposition of Copper on Nickel and Tantalum.” Journal of Electroanalytical Chemistry 568 (2004): 121–33.

[19] Zech, N., and D. Landolt. “The Influence of Boric Acid and Sulfate Ions on the Hydrogen Formation in Fe-Ni Plating Electrolytes.” Electrochimica Acta 45, no. 21 (2000): 3461–71.

[20] Yin, K.-M., and B.-T. Lin. “Effects of Boric Acid on the Electrodeposition of Iron, Nickel and Iron-Nickel.” Surface and Coatings Technology 78, no. 1 (1996): 205–10.

[21] Hassani, Sh., K. Raeissi, and M. A. Golozar. “Effects of Saccharin on the Electrodeposition of Ni–Co Nanocrystalline Coatings.” Journal of Applied Electrochemistry 38, no. 5 (May 1, 2008): 689–94.

[23] Wasekar, Nitin P., Prathap Haridoss, S. K. Seshadri, and G. Sundararajan. “Influence of Mode of Electrodeposition, Current Density and Saccharin on the Microstructure and Hardness of Electrodeposited Nanocrystalline Nickel Coatings.” Surface and Coatings Technology 291 (2016): 130–40.

4 Morphological Instability during Ni and Fe-Ni Electrodeposition

4.1 Introduction

Chapter 2 (**section 2.1.1**) introduced the anomalous codeposition mechanism in general. **Chapter 3** (**section 3.1.2**) proposed a more detailed mechanism to explain the origin of the through-thickness composition gradient occurred in both the potentiostatic mode and the pulse-reverse potential mode. Both mechanisms depend on the establishment of the hydrolysis equilibrium — reaction (2.1) or (3.1) (one and the same) — before the rate determining step — reaction (2.2) or (3.2) (not the same). If the hydrolysis equilibrium cannot be established, for example, as a result of the limited mass transport of the electroactive species, the anomalous codeposition mechanism should be prevented. However, as the limiting mass transport condition is approached, another growth behavior may arise, which is the morphological instability [1-3]. The morphological instability theory is described in Appendix **A 4.1**, following the analytical approach by C. P. Nielsen and H. Bruus [4]. The theoretical efforts on the subject has developed for more than two decades, a direct comparison between the theoretical predictions and the experimental measurements, however, is still missing. This chapter reports an attempt to achieve such a comparison.

4.2 Experimental Methods

4.2.1 Electrodeposition

The aqueous electrolyte (E-01) used for the Ni electrodepositions was made of 3 mM saccharin ($C_7H_5NO_3S$), 550 mM boric acid (H_3BO_3), 20 mM nickel (II) sulfate hexahydrate ($NiSO_4 \cdot$

$6H_2O$). The aqueous electrolyte (E-02) used for the Fe-Ni electrodepositions was made of 3 mM saccharin ($C_7H_5NO_3S$), 550 mM boric acid (H_3BO_3), 10 mM nickel (II) sulfate hexahydrate ($NiSO_4 \cdot 6H_2O$) and 10 mM iron (II) sulfate heptahydrate ($FeSO4 \cdot 7H_2O$). Milli-Q™ deionized (DI) water with a resistivity of 18.2 MOhm was used as the solvent of the electrolyte. The electrodepositions were carried out by potential control using an EG&G PAR (263A) potentiostat/galvanostat. A three-electrode setup was used. The reference electrode was oriented vertically. The working electrode and the counter electrode were oriented horizontally at the bottom and the top, respectively. The Ni and the Fe-Ni films were grown at the working electrode on the Ru / Ta / Si substrates. The exposure region at the working electrode was circular with a diameter of 0.8 cm defined by Kapton® tape. The counter electrode (*i.e.*, the anode) was a Pt mesh. The silver silver chloride (Ag/AgCl) electrode in saturated potassium chloride (sat'd KCl) was used as the reference electrode (0.00 V vs. Ag/AgCl = + 0.199 V vs. SHE). **Table 4.1** lists the deposition conditions of the films (2 Ni films and 2 Fe-Ni films) studied in this work. All the electrodepositions were performed at room temperature without intentional stirring.

Table 4.1 Electrodeposition conditions of the Ni and Fe-Ni films studied in this work.

Sample ID	Electrolyte	Metal Ion Concentration (mM)	Applied Charge Density (C/cm^2)	Applied Potential (V vs. Ag/AgCl)
Ni-01	E-01	20 mM Ni^{2+}	0.45	-1.35
Ni-02	E-01	20 mM Ni^{2+}	0.45	-1.45
FeNi-01	E-02	10 mM Ni^{2+}, 10 mM Fe^{2+}	0.45	-1.35
FeNi-02	E-02	10 mM Ni^{2+}, 10 mM Fe^{2+}	0.45	-1.45

4.2.2 Characterization

The height maps of the electrodeposited films were collected by scanning white light interferometry (SWLI) using the ZYGO NewView 7300 optical profiler at the University of Virginia and by atomic force microscopy (AFM) using the MFP-3D Origin+ AFM system in the research group of Prof. Filippo Mangolini at the University of Texas at Austin. The AFM height maps were collected by Robert Chrostowski with the assistance of Zixuan Li. The PSD analyses were performed by Robert Chrostowski. The composition map was collected by scanning electron microscopy and energy dispersive X-ray spectroscopy (SEM-EDS) using the Thermo Scientific Phenom scanning electron microscope. The Phenom 3D Roughness Reconstruction (Phenom 3DRR) software was used to reconstruct the height map at the field of view where the composition map was collected.

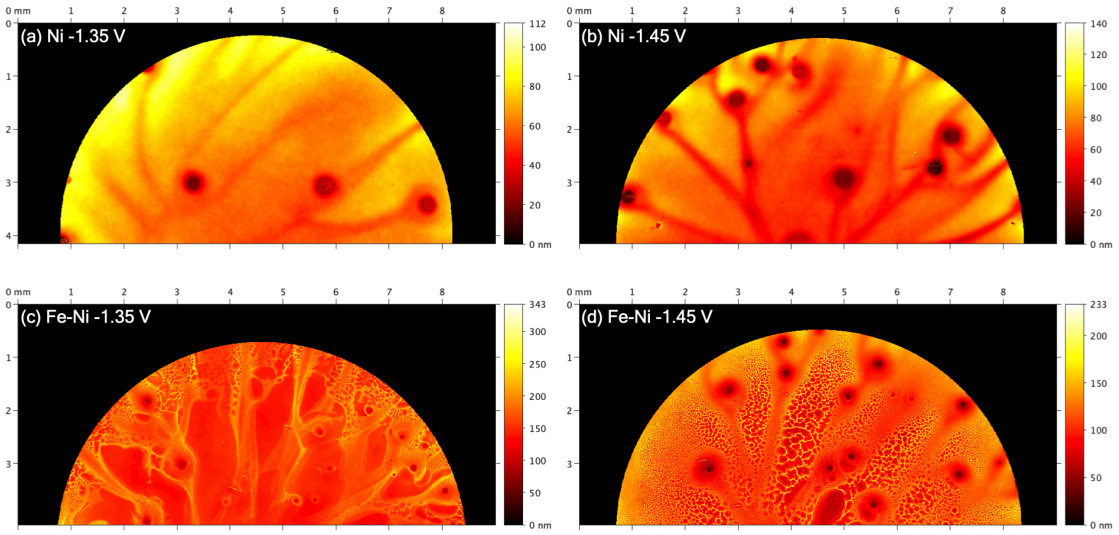

Figure 4.1. Scanning white light interferometry (SWLI) height maps of electrodeposited Ni and Fe-Ni films. **(a)** Ni-01 deposited at -1.35 V vs. Ag/AgCl. **(b)** Ni-02 deposited at -1.45 V vs. Ag/AgCl. **(c)** FeNi-01 deposited at -1.35 V vs. Ag/AgCl. **(d)** FeNi-02 deposited at -1.45 V vs. Ag/AgCl.

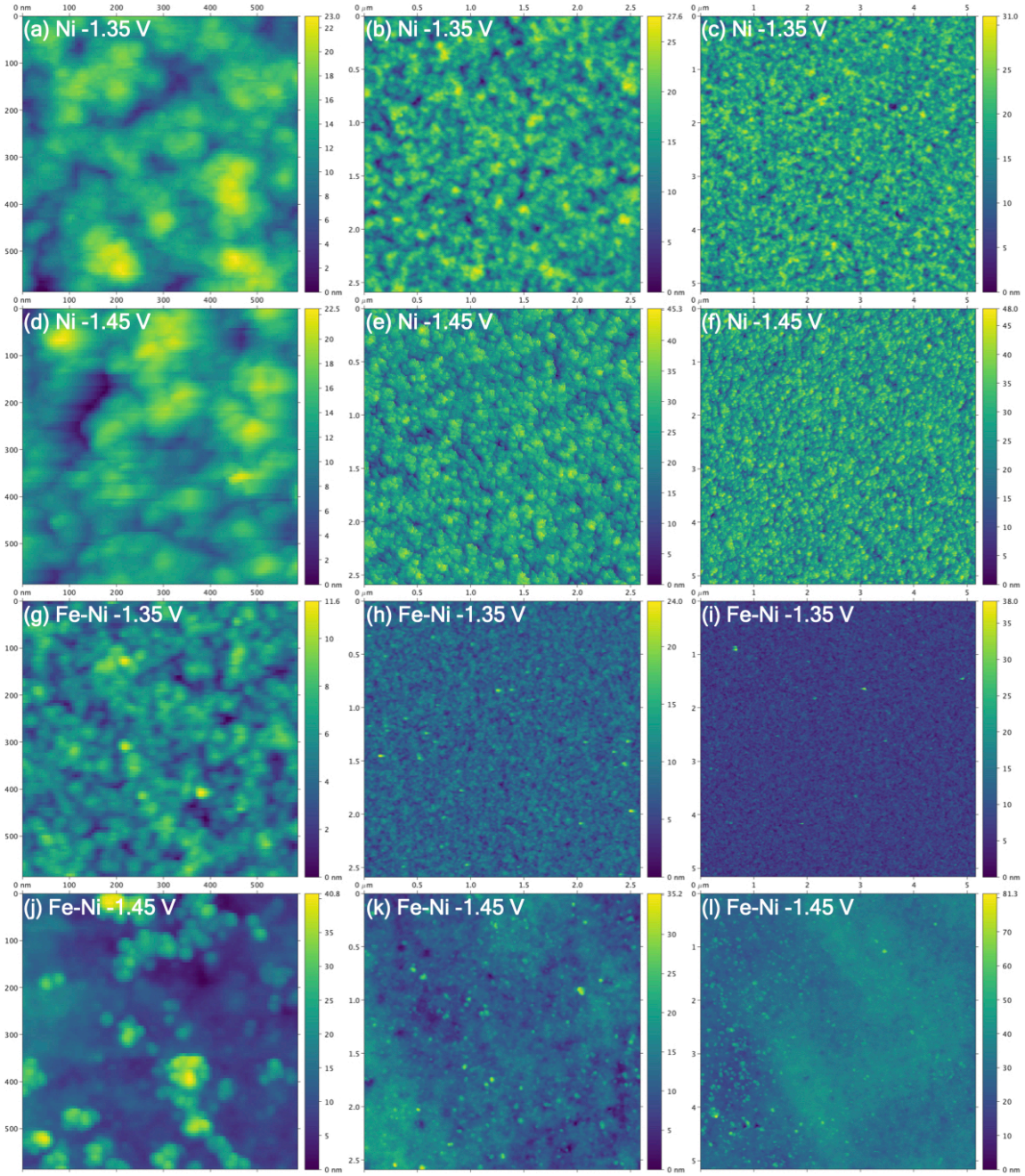

Figure 4.2. Atomic force microscopy (AFM) height maps of electrodeposited Ni and Fe-Ni films. **(a-c)** Ni-01 deposited at -1.35 V vs. Ag/AgCl. **(d-f)** Ni-02 deposited at -1.45 V vs. Ag/AgCl. **(g-i)** FeNi-01 deposited at -1.35 V vs. Ag/AgCl. **(j-l)** FeNi-02 deposited at -1.45 V vs. Ag/AgCl. The field of view of (a, d, g, j) is 586 nm. The field of view of (b, e, h, k) is 2.59 µm. The field of view of (c, f, i, l) is 51.4 µm.

4.3 Results and Discussion

Figure 4.1 shows the SWLI height maps of the Ni and the Fe-Ni films. A circular mask was imposed to exclude the region within ~ 0.5 mm from the step edge of the films, where the measured heights were most severely affected by overshoots and undershoots. All maps show pits resulted from the hydrogen bubbles attached on the film surface, generated by hydrogen evolution reaction (HER), during the electrodeposition process. As the applied potential varied from the less negative (-1.35 V vs. Ag/AgCl) to the more negative (-1.45 V vs. Ag/AgCl) value, more pits are seen on the height maps, for both Ni and Fe-Ni, suggesting that the HER process was more intense under the more negative applied potential. All maps show percolating networks, sometimes connecting one pit to another. The network in the Ni films consists of branches with a width on the order of 0.1 mm. The branches are valleys in the sense that they are lower in height than their exteriors. The orientations of the branches in the Ni films are more aligned with the radial direction than the tangential direction. The branches are denser in Ni-02 (**Figure 4.1b**) than in Ni-01 (**Figure 4.1a**), suggesting that the formation of the branches were affected by the applied potential, and thus by the electrochemical kinetics during the deposition process. The Fe-Ni films have a more hierarchical morphology. Around the pits, there are islands. Away from the pits, there are honeycombs. In between the pits, there are branches consisting of both the island and the honeycomb substructures. The honeycombs are more prominent in FeNi-02 (**Figure 4.1d**) than in FeNi-01 (**Figure 4.1c**), suggesting the morphological effect of the electrochemical kinetics. **Figure 4.2** shows the AFM height maps of the Ni and the Fe-Ni films. Ni clearly has a larger average grain size than Fe-Ni. Notice that the grains shown in the AFM height map are not necessarily single crystals. It follows that the grain

size extracted from the AFM height maps should be interpreted as an upper bound to the crystallite size, and the crystallite size of the Ni films is not necessarily larger than that of the Fe-Ni films.

Power spectral density (PSD) analysis was applied to both the SWLI height maps and the AFM height maps to provide a statistical description for the Ni and the Fe-Ni films. The Chow test statistics was used to estimate the critical wavenumber at which the slope of a PSD curve (in the log-log scale) changes statistically significantly. The mathematical details of the PSD analysis and the Chow test statistics applied in this work were described by R. Chrostowski et al. in *Applied Surface Science 581 (2022) 152092* [5]. The critical wavenumber is related to the length scale of the characteristic morphological feature. In the SWLI height maps (**Figure 4.1**), there are pits, islands, cell walls of the honeycomb structure, and branches of the percolating network. In the AFM height maps (**Figure 4.2**), there are grains and clusters of grains. The populations and the length scales of all these morphological features can affect the critical wavenumber being estimated.

Figure 4.3 shows the PSD curves of the Ni and the Fe-Ni films. The boundary between the yellow block and the blue block is positioned at the largest critical wavenumber (k_1), the magnitude of which is on the order of 4×10^7 rad/m, corresponding to a critical wavelength ($\lambda_1 = 2\pi/k_1$) on the order of 150 nm. The boundary between the blue block and the the red block is positioned at the second largest critical wavenumber (k_2), the magnitude of which is on the order of 3×10^6 rad/m, corresponding to a critical wavelength (λ_2) on the order of 2 μm. At each of the

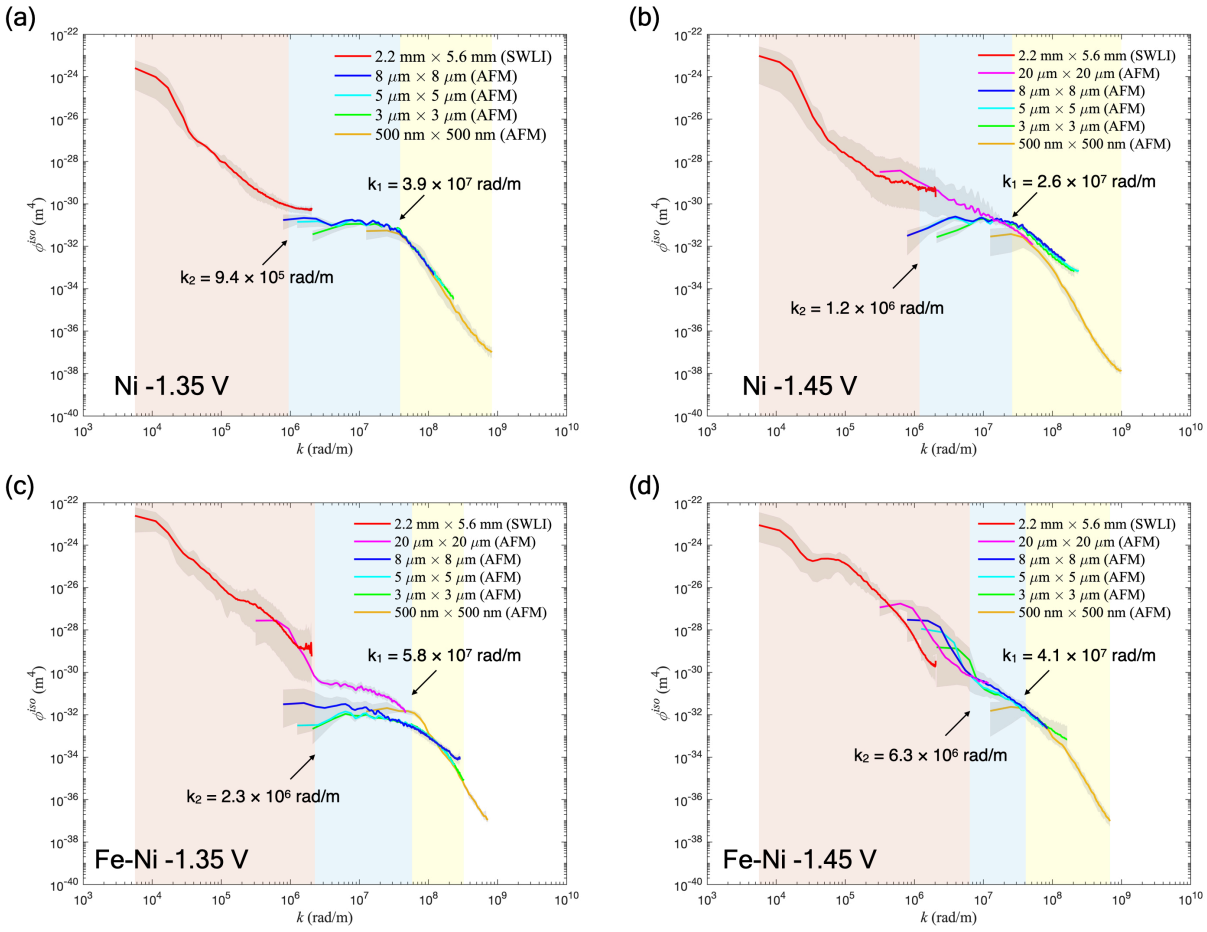

Figure 4.3. Power spectral density curves extracted from the SWLI and the AFM height maps of the electrodeposited Ni and Fe-Ni films. **(a)** Ni-01 deposited at -1.35 V vs. Ag/AgCl. **(b)** Ni-02 deposited at -1.45 V vs. Ag/AgCl. **(c)** FeNi-01 deposited at -1.35 V vs. Ag/AgCl. **(d)** FeNi-02 deposited at -1.45 V vs. Ag/AgCl. The boundaries of the colored blocks indicate the critical wavenumbers (k_1, k_2) determined by the Chow test.

two applied potentials, k_1 of the Fe-Ni film is larger than that of the Ni film, which is true for k_2 as well. At the same applied potential, the relative magnitude in k_1 between Ni and Fe-Ni is in qualitative agreement with the AFM height maps, in sense that the Fe-Ni films have smaller grains than the Ni films; the relative magnitude in k_2 is also in qualitative agreement with the SWLI height maps, in the sense that the Fe-Ni films show finer morphological features (cell

walls, islands) than the Ni films do (branches). In the same material system (either Ni or Fe-Ni), k_1 decreases as the applied potential varies from the less to the more negative value, while k_2 increases as the applied potential varies from the less to the more negative value. This suggests that k_1 and k_2 depends on the electrochemical kinetics via different mechanisms. While k_1 is very likely to determined by the nucleation and growth of grains or clusters, the physical origin of k_1 is less obvious, for the corresponding length scale involves more than one type of morphological features. In the following, we provide a direct comparison (**Figure 4.4**) between the experimental and the theoretical values to show that k_2 may arise as a result of morphological instability.

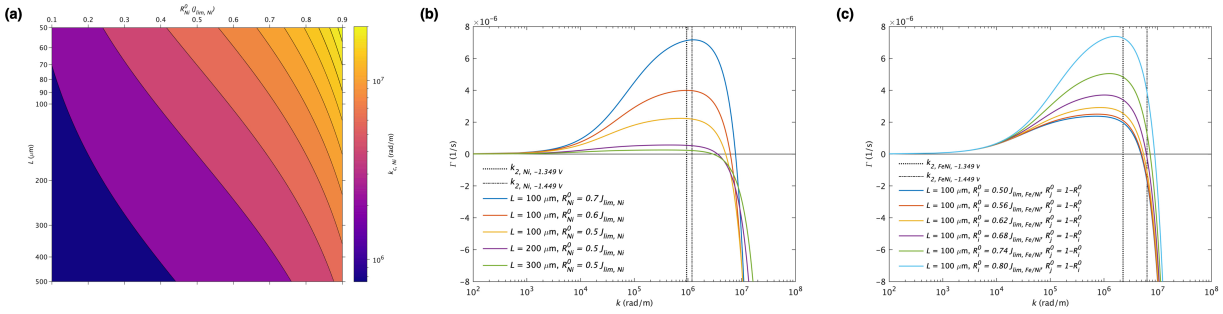

Figure 4.4. Theoretical predictions based on the morphological instability theory described in Appendix **A 4.1 (a)** Theoretical critical wavenumber as a map of the boundary layer thickness and the nondimensionalized zeroth order reaction rate. **(b)** Theoretical dispersion relation between the temporal frequency and the wavenumber for the Ni electrodeposition. The vertical lines indicate the experimental critical wavenumbers at the two applied potentials respectively. **(c)** Theoretical dispersion relation between the temporal frequency and the wavenumber for the Fe-Ni electrodeposition. The vertical lines indicate the experimental critical wavenumbers at the two applied potentials respectively. R^0_i is the partial reaction rate of the faster depositing cation. R^0_j is the partial reaction rate of the slower depositing cation. $J_{lim,\ Ni} = 2J_{lim,\ Fe/Ni}$ as a result of the difference in the electrolyte concentration described in **Table 4.1**.

Figure 4.4a shows the critical wavenumber for Ni electrodeposition ($k_{c,\ Ni}$) predicted by the morphological instability theory (**eq. A 4.74** described in Appendix **A 4.1**) as a map of the boundary layer thickness (L) and the nondimensionalized zeroth order reaction rate (R^0_{Ni}). The boundary layer thickness is varied between 50 μm and 500 μm. The experimental boundary layer thickness, though not measured experimentally, should fall within this range, according to the natural convection boundary layer thickness values reported in the literature [6]. The nondimensionalized zeroth order reaction rate is varied between 10% to 90% of the diffusion limiting flux. This is also realistic based on the following calculations. The diffusion limiting current density is estimated to be j_{lim} = 0.4 ~ 4.0 mA/cm^2 based on the boundary layer thickness range of L = 50 ~ 500 μm. The experimental steady state current density monitored by chronoamperometry is on the order of 3.7 mA/cm^2 at -1.35 V vs. Ag/AgCl, and 4.3 mA/cm^2 at -1.45 V vs. Ag/AgCl (see Appendix **A 4.2**). The current efficiencies estimated based on the mean heights extracted from the SWLI height maps (**Figure 4.1a** and **b**) , which are 69 nm and 72 nm respectively, are 45% at -1.35 V vs. Ag/AgCl, and 47% at -1.45 V vs. Ag/AgCl. Therefore the deposition current density are 1.7 mA/cm^2 at -1.35 V vs. Ag/AgCl, and 2.0 mA/cm^2 at -1.45 V vs. Ag/AgCl, given a boundary layer thickness of 500 μm, equivalent to 43% and 50% of the limiting current density, respectively, being within the specified range in **Figure 4.4a**. **Figure 4.4a** shows that the theoretical critical wavenumber is on the order of 10^6 ~ 10^7 rad/m, closely agreeing with the experimental values extracted by the Chow test from the PSD curves.

Figure 4.4b further compare the experimental critical wavenumber with the theoretical dispersion curves. The experimental values fall within the the theoretical wavenumber range in

vicinity of the wavenumber (k_{max}) at which the maximum temporal frequency (Γ_{max}) — the most unstable growth condition — is obtained, demonstrating the agreement between the theory and the experiment, and thus strongly suggesting that the morphological instability is the physical origin of k_2 in the Ni electrodeposition.

As in the Fe-Ni electrodeposition (**Figure 4.4c**), the experimental values are somewhat further away from k_{max}, but still falls within the range were the temporal frequency is positive — the unstable growth wavenumber range. Moreover, the morphological instability theory predicts that as the partial reaction rate of Ni and Fe deposition deviates more from each other, both the maximum temporal frequency (Γ_{max}) and the critical wavenumber (k_c) increase, both resulting in a more unstable growth. This theoretical insight may shed light to the physical origin of the dramatic difference in the morphological features between the Ni films and the Fe-Ni films shown by the SWLI height maps (**Figure 4.1**).

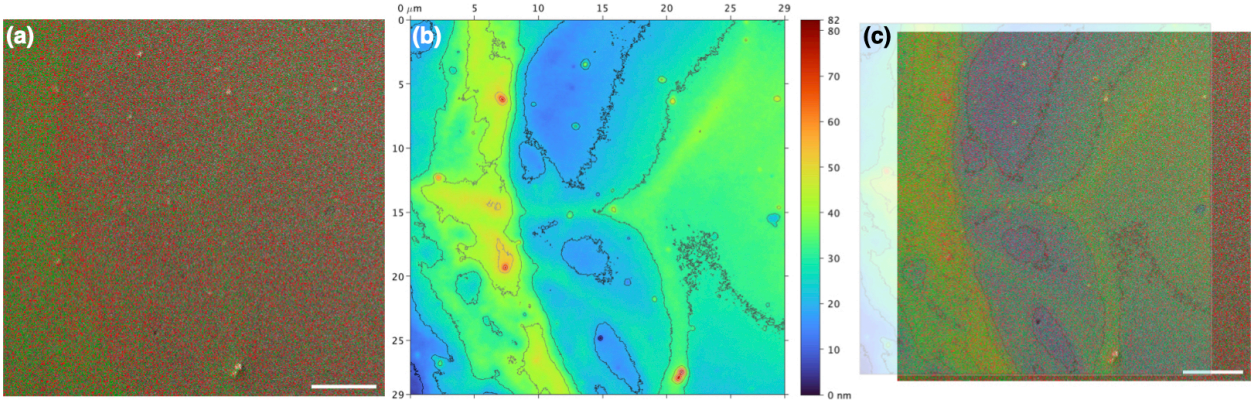

Figure 4.5. Composition map and height map of the electrodeposited Fe-Ni film deposited with -1.45 V vs. Ag/AgCl: (a) energy dispersive X-ray spectroscopy (EDS) composition map with Fe in red and Ni in green (5 μm scale bar); (b) height maps extracted from the back scattered electron (BSE) micrographs by the 3D roughness reconstruction (3DRR) software, which was collected from nominally the same location from which composition map in (a) was collected; (c) the height map (b) in 25% opacity superimposed with the composition map (a).

Evidence of deviation between the Ni and the Fe deposition rate was indeed detected by SEM-EDS. **Figure 4.5a** shows the SEM-EDS composition map of FeNi-02, which has the largest k_2 among all four samples. The average composition is 51 at.% Ni, nominally the same as the electrolyte composition, *i.e.*, $C_{Ni2+}/(C_{Ni2+}+C_{Fe2+})$ = 50%, indicating that the anomalous codeposition mechanism was mostly prevented. The composition map, however, shows local deviations from the equiatomic level (see Appendix **A 4.3**). The composition at the Ni-lean region can be as low as 44 at.%Ni (**Figure A 4.4**), and the composition of the Ni-rich region can be as high as 58 at.%Ni (**Figure A 4.5**). **Figure 4.5b** shows the height map collected from the nominally the same position where the composition map in **Figure 4.5a** was collected, and **Figure 4.5c** overlap the composition map and the height map. Interestingly, the composition deviation correlates very well with the height deviation — the troughs are Ni-lean, while the crests are Ni-rich. Such a correlation between compositional and topographical deviation is not captured by the morphological instability theory described in **Appendix A 4.1**. Another possibly important physical process that the morphological instability theory described in **Appendix A 4.1** does not capture is the migration contribution to the mass transport of the electroactive species. The ion concentration in the two electrolytes, E01 and E02 for the Ni and the Fe-Ni deposition respectively, are equivalent (**Table 4.1**). It follows that the ionic strength and the Debye screening length of the two electrolytes are also equivalent. Based on the Gouy-Chapman theory, the Debye screening length is estimated to be $\kappa^{-1} \sim 1$ nm, much smaller than the boundary layer thickness (50 ~ 500 μm), but still comparable to the size of a solvated cation. It follows that the mass transport in vicinity of the growth front may be affected by the migration driven by the electric field within the diffuse double layer (*i.e.*, the extended spaced charge region). A more

sophisticated model considering both migration and diffusion, particularly in vicinity of the growth front may shed light to the understanding of the correlation between composition and height shown in **Figure 4.5**.

4.4 Conclusion

The anomalous codeposition mechanism in Fe-Ni electrodeposition can be avoided when the deposition current density approached the diffusion limiting current density, providing a mean composition in the deposited alloy nominally the same as that of the electrolyte. In an electrolyte with a Debye screening length on the order of ~ 1 nm, however, the deposited growth front shows hierarchical morphological features, from grains and clusters of grains in the nano-scale (*i.e.*, in a field of view of ~ 500 nm) to pits, islands, honeycombs, and percolating networks in the macro-scale (*i.e.*, in a field of view of ~ 8 mm). PSD analysis was used to extract the largest two critical wavenumbers from the AFM and the SWLI height maps. The largest critical wavenumber (k_1) is shown to be on the order of 4×10^7 rad/m, corresponding to the characteristic length scale on the order of 150 nm, which is comparable to the size of grains or clusters of grains in the nanoscale. The second largest critical wavenumber (k_2) is shown to be on the order of 3×10^6 rad/m, corresponding to the characteristic length scale on the order of 2 μm. The morphological instability theory developed for metal and alloy electrodeposition was used to shed light to the physical origin of k_2. In both Ni and Fe-Ni films, the experimental critical wavenumbers (k_2) extracted from the AFM and the SWLI height maps by the PSD analysis fall under the theoretical critical wavenumbers (k_c), below which the morphological evolution is expected to be unstable, and close to the theoretical wavenumber at which the growth is

maximumly unstable (k_{max}), strongly suggesting the connection between k_2 and the characteristic wavenumbers (k_c, k_{max}) predicted by the morphological instability theory. In the micro-scale (*i.e.*, in a field of view of ~ 30 μm), the Fe-Ni film with the larger k_2 shows local composition deviations from the mean composition level that correlate with the heigh deviations from the mean height level. The morphological instability theory for alloy depositions expects a more unstable growth in case of a larger deviation in the partial current densities, connecting the composition deviation to the morphological instability. Thus the theory may be used to understand, though not directly, the micro-scale observations.

Though not directly related to the synthesis of $L1_0$ Fe-Ni, morphological instability is increasingly more important when the deposition condition is driven further away from the electrochemical equilibrium. Far-from-equilibrium deposition conditions designed to achieve the growth of metastable crystal structures or defect structures (possibly conducive to the synthesis of $L1_0$ Fe-Ni) may encounter morphological instability — a macroscopic break down of the growth front — before achieving the targeted microstructures or nanostructures. This work is one of the first attempts to connect the experiment and the theory towards the understanding of the morphological break down in far-from-equilibrium electrodeposition conditions.

A 4.1 Morphological Instability

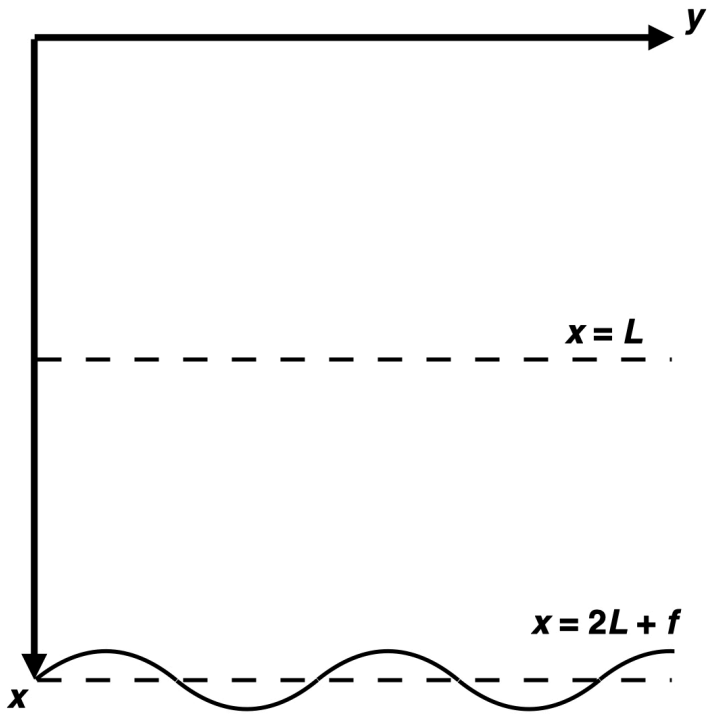

Figure A 4.1. The coordinate system.

A 4.1.1 Nondimensionalization

The spatial coordinate (x, y [=] m) are normalized by the boundary layer thickness (L [=] m). The time (t [=] s) is normalized by the diffusion time (L^2 / D [=] s), where the diffusivity (D [=] $m^2 \cdot s^{-1}$) of Ni^{2+} and Fe^{2+} are $D = D_{Ni2+} = D_{Fe2+} = 5 \times 10^{-10}$ $m^2 \cdot s^{-1}$ [7]. The concentration field (c_i [=] m^{-3}) is normalized by the bulk electrolyte concentration ($c_{0,i}$ [=] m^{-3}) determined by the electrolyte recipe, where the subscript i indicates the type of the cation (*i.e.*, $c_{0,Ni}$ for Ni^{2+}, $c_{0,Fe}$ for Fe^{2+}). For electrolyte E-01 (**Table 4.1**), the bulk electrolyte concentration is $c_{0,i} = c_{0,Ni} =$ (20 mM) (*Na*); for electrolyte E-02 (**Table 4.1**), the bulk electrolyte concentration is $c_{0,i} = c_{0,Ni} = c_{0,Fe} =$(10

mM) (*Na*), where *Na* = 6.02214086 mol^{-1} is the Avogadro constant. The flux field ($\boldsymbol{J_i}$ [=] s^{-1}·m^{-2}), the anodic and the cathodic reaction rate constant ($k^{+}_{0,i}$, $k^{-}_{0,i}$ [=] s^{-1}·m^{-2}), and the reaction rate (R_i [=] s^{-1}·m^{-2}) are normalized by the diffusion limiting flux ($J_{lim,i} = D\ c_{0,i} / L$ [=] s^{-1}·m^{-2}).

$$\tilde{x} = \frac{x}{L},\ \tilde{y} = \frac{y}{L} \qquad \text{eq. A 4.1}$$

$$\tilde{t} = \frac{t}{\frac{L^2}{D}} \qquad \text{eq. A 4.2}$$

$$\tilde{c_i} = \frac{c_i}{c_{0,i}} \qquad \text{eq. A 4.3}$$

$$\tilde{\mathbf{J}}_\mathbf{i} = \frac{\mathbf{J_i}}{\frac{Dc_{0,i}}{L}} \qquad \text{eq. A 4.4}$$

$$\tilde{k^{+}_{0,i}} = \frac{k^{+}_{0,i}}{\frac{Dc_{0,i}}{L}},\ \tilde{k^{-}_{0,i}} = \frac{k^{-}_{0,i}}{\frac{Dc_{0,i}}{L}} \qquad \text{eq. A 4.5}$$

$$\tilde{R_i} = \frac{R_i}{\frac{Dc_{0,i}}{L}} \qquad \text{eq. A 4.6}$$

The interface between the boundary layer and the bulk electrolyte is set to be located at $x = L$. The position of the growth front is located at $x = 2L + f$, where the growth front function (f [=] m) is normalized by the boundary layer thickness (L [=] m) (**Figure A 4.1**).

$$\tilde{f} = \frac{f}{L} \qquad \text{eq. A 4.7}$$

The rest potential (φ^i [=] V), and the bias voltage (V^i [=] V) are normalized by the thermal voltage (k_BT/e_0 [=] V), where k_B = 1.380649 × 10^{-23} J·K^{-1} is the Boltzmann constant, T = 298.15 K is the room temperature where the electrodepositions were conducted, and e_0 = 1.602 × 10^{-19} C is the elementary charge. The growth front interfacial energy (γ [=] J·m^{-2}) is normalized by k_BTL/a^3, where the atomic diameter (a [=] m) is derived from the lattice parameter (P [=] m) by $a = (\sqrt{2}/2)P$ in the FCC crystal structure. P = 3.51 Å for FCC Ni and P = 3.58 Å for FCC Fe-Ni. The surface tension of Ni is used to approximate the growth front interfacial energy (γ = 2.1 J·m^{-2}) [8], considering that it is much larger than the surface tension of water (γ_w = 0.0728 J·m^{-2}).

$$\tilde{\varphi}^i = \frac{\varphi^i}{\frac{k_BT}{e_0}} \qquad \text{eq. A 4.8}$$

$$\tilde{V}^i = \frac{V^i}{\frac{k_BT}{e_0}} \qquad \text{eq. A 4.9}$$

$$\tilde{\gamma} = \frac{\gamma}{\frac{k_BTL}{a^3}} \qquad \text{eq. A 4.10}$$

The spatial frequency (k [=] m^{-1}) is normalized by the boundary layer thickness. The temporal frequency (Γ [=] s^{-1}) is normalized by the diffusion frequency (D / L^2 [=] s^{-1}). The velocity of the moving coordinate system is set to be the mean growth velocity (U [=] m· s^{-1}), which is normalized by D / L.

$$\tilde{k} = \frac{k}{L} \qquad \text{eq. A 4.11}$$

$$\tilde{\Gamma} = \frac{\Gamma}{\frac{D}{L^2}} \qquad \text{eq. A 4.12}$$

$$\tilde{U} = \frac{U}{\frac{D}{L}} \qquad \text{eq. A 4.13}$$

A 4.1.2 Governing Equations

The mass conservation is

$$\partial t c_i = -\nabla \cdot \mathbf{J_i} \qquad \text{eq. A 4.14}$$

The nondimensionalized mass conservation is

$$\tilde{\partial} t \tilde{c}_i = -\tilde{\nabla} \cdot \tilde{\mathbf{J}}_\mathbf{i} \qquad \text{eq. A 4.15}$$

The Fick's 1st law is

$$\mathbf{J_i} = -D \nabla c_i \qquad \text{eq. A 4.16}$$

The nondimensionalized Fick's 1st law is

$$\tilde{\mathbf{J}}_{\mathbf{i}} = -\tilde{\nabla}\tilde{c}_i \qquad \text{eq. A 4.17}$$

The growth front normal ($\boldsymbol{n}$ [=] 1) is defined such that it always points out of the electrode

$$\mathbf{n} = \frac{-\mathbf{e_x} + \partial y f \mathbf{e_y}}{\sqrt{1 + (\partial y f)^2}} \qquad \text{eq. A 4.18}$$

The growth front curvature (κ [=] m^{-1}) is defined such that a crest is always positive and a trough is always negative

$$\kappa = \frac{\partial_y^2 f}{[1 + (\partial y f)]^{3/2}} \qquad \text{eq. A 4.19}$$

The nondimensionalized growth front curvature is

$$\tilde{\kappa} = \frac{\tilde{\partial}_y^2 \tilde{f}}{[1 + (\tilde{\partial} y \tilde{f})]^{3/2}} \qquad \text{eq. A 4.20}$$

The reaction rate is described by the Butler-Volmer electrochemical kinetics, where the charge transfer coefficient (α [=] 1) of the cathodic and the anodic reaction are assumed to be $\alpha = \alpha_c = \alpha_a = 0.5$, the valence numbers ($Z$ [=] 1) of Fe^{2+} and Ni^{2+} are equal to $Z = 2$, and the concentration

field is evaluated at growth front position (*i.e.*, $c_i = c_i(2L, y, t)$). The reaction rate is defined such that it is positive when the cathodic reaction rate dominates. Notice that the growth front interfacial energy term deactivates both the cathodic and the anodic reaction rate.

$$R_i = (c_i/m^{-3})\ k_{0,i}^{-}\ exp[-\frac{\alpha Z e_0(\varphi^i + V^i)}{k_B T} - \frac{a^3\gamma\kappa}{k_B T}] - k_{0,i}^{+}\ exp[+\frac{\alpha Z e_0(\varphi^i + V^i)}{k_B T} - \frac{a^3\gamma\kappa}{k_B T}]$$

eq. A 4.21

Denote (c_i/m^{-3}) as $<c_i>$ to simplify the equation. The nondimensionalized reaction rate is

$$\tilde{R}_i = < c_i >\ \tilde{k_{0,i}^{-}}\ exp[-\alpha Z(\tilde{\varphi^i} + \tilde{V^i}) - \tilde{\gamma}\tilde{\kappa}] - \tilde{k_{0,i}^{+}}\ exp[+\alpha Z(\tilde{\varphi^i} + \tilde{V^i}) - \tilde{\gamma}\tilde{\kappa}] \qquad \text{eq. A 4.22}$$

By the definition of the rest potential, the reaction rate equals zero when the bias voltage equals zero. This leads to the relation between the rest potential and the concentration field at the growth front position.

$$\varphi^i = \frac{k_B T}{Z e_0} ln(\frac{k_{0,i}^{-}}{k_{0,i}^{+}}) + \frac{k_B T}{Z e_0} ln < c_i > \qquad \text{eq. A 4.23}$$

Comparing to the Nernst equation, where the activity coefficient (γ_i [=] 1) is not to be confused with the growth front interfacial energy (γ [=] $\mathrm{J\cdot m^{-2}}$), m_0 = 1 mol·kg-1 is the standard molality, and ρ_s = 997 $\mathrm{kg\cdot m^{-3}}$ is the density of water at room temperature

$$\varphi^i = \varphi_0^i + \frac{k_B T}{Z e_0} ln[\frac{\gamma_i(m^{-3})}{m_0 Na \rho_s}] + \frac{k_B T}{Z e_0} ln < c_i > \quad \text{eq. A 4.24}$$

To simply the relation between the rest potential and the concentration field at the growth front position, the reference potential is chosen to be

$$\varphi_0^i = - \frac{k_B T}{Z e_0} ln[\frac{\gamma_i(m^{-3})}{m_0 Na \rho_s}] \quad \text{eq. A 4.25}$$

This implies $k^-_{0,i} = k^+_{0,i} = k_{0,i}$ under this choice of reference potential. It follows that the relation between the rest potential and the concentration field at the growth front is simplified to be

$$\varphi^i = \frac{k_B T}{Z e_0} ln < c_i > \quad \text{eq. A 4.26}$$

The nondimensionalized form of this relation is

$$\tilde{\varphi}^i = \frac{1}{Z} ln < \tilde{c}_i c_{0,i} > \quad \text{eq. A 4.27}$$

The flux field at the nominal growth front is related to the growth front function by

$$(\partial_t f - U)\mathbf{e_x} \cdot \mathbf{n} = -a^3 \sum_i [\mathbf{n} \cdot \mathbf{J_i}(2L, y, t)] \qquad \text{eq. A 4.28}$$

The nondimensionalized form of this relation is

$$(\tilde{\partial}_t \tilde{f} - \tilde{U})\mathbf{e_x} \cdot \mathbf{n} = -a^3 \sum_i [c_{0,i}\mathbf{n} \cdot \tilde{\mathbf{J}}_\mathbf{i}(2,\tilde{y}, \tilde{t})] \qquad \text{eq. A 4.29}$$

A 4.1.3 Boundary Conditions

At the electrode / electrolyte interface ($x = 2L$), the flux field is related to the reaction rate by

$$\mathbf{n} \cdot \mathbf{J_i}(2L, y, t) = -R_i \qquad \text{eq. A 4.30}$$

The nondimensionalized form of this relation is

$$\mathbf{n} \cdot \tilde{\mathbf{J}}_\mathbf{i}(2,\tilde{y}, \tilde{t}) = -\tilde{R}_i \qquad \text{eq. A 4.31}$$

At the boundary layer / bulk electrolyte interface ($x = L$), the concentration field equals to the bulk concentration

$$c_i(L, y, t) = c_{0,i} \qquad \text{eq. A 4.32}$$

The nondimensionalized form of this relation is

$$\tilde{c}_i(1,\tilde{y},\tilde{t}) = 1 \qquad \text{eq. A 4.33}$$

A 4.1.4 Perturbation Expansions

The concentration field, the rest potential, the flux field, the growth front position, the reaction rate are expanded as a sum of the zeroth order term (*i.e.*, the based state) and the first order term (*i.e.*, the perturbed state).

$$\tilde{c}_i(\tilde{x},\tilde{y},\tilde{t}) = \tilde{c_i^0}(\tilde{x}) + \tilde{c_i^1}(\tilde{x},\tilde{y},\tilde{t}) \qquad \text{eq. A 4.34}$$

$$\tilde{\varphi^i}(\tilde{x},\tilde{y},\tilde{t}) = \tilde{\varphi^{i,0}}(\tilde{x}) + \tilde{\varphi^{i,1}}(\tilde{x},\tilde{y},\tilde{t}) \qquad \text{eq. A 4.35}$$

$$\tilde{\mathbf{J}}_\mathbf{i}(\tilde{x},\tilde{y},\tilde{t}) = \tilde{\mathbf{J}}_\mathbf{i}^\mathbf{0}(\tilde{x}) + \tilde{\mathbf{J}}_\mathbf{i}^\mathbf{1}(\tilde{x},\tilde{y},\tilde{t}) \qquad \text{eq. A 4.36}$$

$$\tilde{f}(\tilde{y},\tilde{t}) = \tilde{f^1}(\tilde{y},\tilde{t}) \qquad \text{eq. A 4.37}$$

$$\tilde{R}_i(\tilde{y},\tilde{t}) = \tilde{R_i^0} + \tilde{R_i^1}(\tilde{y},\tilde{t}) \qquad \text{eq. A 4.38}$$

The first order terms are assumed to have the following spatial and temporal dependency (*i.e.*, the harmonic ansatz)

$$\tilde{c_i^1}(\tilde{x},\tilde{y},\tilde{t}) = \tilde{c_i^*}(\tilde{x})\ exp(\tilde{\Gamma}\tilde{t} + i\tilde{k}\tilde{y}) \qquad \text{eq. A 4.39}$$

$$\tilde{\varphi^{i,1}}(\tilde{x},\tilde{y},\tilde{t}) = \tilde{\varphi^{i,*}}(\tilde{x})\ exp(\tilde{\Gamma}\tilde{t} + i\tilde{k}\tilde{y}) \qquad \text{eq. A 4.40}$$

$$\tilde{\mathbf{J}}_\mathbf{i}^\mathbf{1}(\tilde{x},\tilde{y},\tilde{t}) = \tilde{\mathbf{J}}_\mathbf{i}^*(\tilde{x})\ exp(\tilde{\Gamma}\tilde{t} + i\tilde{k}\tilde{y}) \qquad \text{eq. A 4.41}$$

$$\tilde{f^1}(\tilde{y},\tilde{t}) = \tilde{F}\ exp(\tilde{\Gamma}\tilde{t} + i\tilde{k}\tilde{y}) \qquad \text{eq. A 4.42}$$

$$\tilde{R_i^1}(\tilde{y},\tilde{t}) = \tilde{R_i^*}\ exp(\tilde{\Gamma}\tilde{t} + i\tilde{k}\tilde{y}) \qquad \text{eq. A 4.43}$$

A 4.1.5 Taylor Expansions

The growth front normal is approximated as

$$\mathbf{n} = -\mathbf{e_x} + \tilde{\partial y}\tilde{f^1}\mathbf{e_y} \qquad \text{eq. A 4.44}$$

The growth front curvature is approximated as

$$\tilde{\kappa} = \tilde{\partial_y^2 f^1} \qquad \text{eq. A 4.45}$$

The concentration field at the growth front position is approximated as

$$\tilde{c_i}(2+\tilde{f^1},\tilde{y},\tilde{t}) = \tilde{c_i^0}(2) + \tilde{c_i^1}(2,\tilde{y},\tilde{t}) + \tilde{\partial}_x\tilde{c_i^0})_2\tilde{f^1} \qquad \text{eq. A 4.46}$$

The concentration field gradient at the growth front position is approximated as

$$\nabla\tilde{c_i}(2+\tilde{f^1},\tilde{y},\tilde{t}) = \mathbf{e_y}\tilde{\partial}_y\tilde{c_i^1})_{2,\tilde{y},\tilde{t}} + \mathbf{e_x}[\tilde{\partial}_x\tilde{c_i^0})_2 + \tilde{\partial}_x\tilde{c_i^1})_{2,\tilde{y},\tilde{t}} + \tilde{\partial_x^2}\tilde{c_i^0})_2\tilde{f^1}] \qquad \text{eq. A 4.47}$$

The rest potential at the growth front position is approximated as

$$\tilde{\varphi}^{i}(2+\tilde{f}^{1},\tilde{y},\tilde{t}) = \tilde{\varphi_i}^{i,0}(2) + \tilde{\varphi_i}^{i,1}(2,\tilde{y},\tilde{t}) + \tilde{\partial}_x \tilde{\varphi_i}^{i,0})_2 \tilde{f}^{1} \qquad \text{eq. A 4.48}$$

The rest potential gradient at the growth front position is approximated as

$$\nabla\tilde{\varphi}^{i}(2+\tilde{f}^{1},\tilde{y},\tilde{t}) = \mathbf{e_y}\tilde{\partial}_y \tilde{\varphi}^{i,1})_{2,\tilde{y},\tilde{t}} + \mathbf{e_x}[\tilde{\partial}_x \tilde{\varphi}^{i,0})_2 + \tilde{\partial}_x \tilde{\varphi}^{i,1})_{2,\tilde{y},\tilde{t}} + \tilde{\partial}_x^2 \tilde{\varphi}^{i,0})_2 \tilde{f}^{1}] \qquad \text{eq. A 4.49}$$

Substituting the approximated concentration field and the approximated rest potential into the Butler-Volmer equation, the zeroth order reaction rate is approximated as

$$\tilde{R_i^0} = < c_{0,i} > \tilde{k_{0,i}}\ \tilde{c_i^0}\ exp[-\alpha Z(\tilde{\varphi}^{i,0} + \tilde{V}^{i})] - \tilde{k_{0,i}}\ exp[+\alpha Z(\tilde{\varphi}^{i,0} + \tilde{V}^{i})] \qquad \text{eq. A 4.50}$$

And the first order reaction rate is approximated as

$$\tilde{R_i^1} = < c_{0,i} > \tilde{k_{0,i}}\ exp[-\alpha Z(\tilde{\varphi}^{i,0} + \tilde{V}^{i})]\ \{\tilde{c_i^1} + \tilde{\partial}_x \tilde{c_i^0})_2 \tilde{f}^{1} - \tilde{c_i^0}(\alpha+\alpha)Z[\tilde{\varphi}^{i,1} + \tilde{\partial}_x \tilde{\varphi}^{i,0})_2 \tilde{f}^{1}]\}$$
$$+ \tilde{R_i^0}\ \{-\tilde{\gamma}\tilde{\kappa} + \alpha Z[\tilde{\varphi}^{i,1} + \tilde{\partial}_x \tilde{\varphi}^{i,0})_2 \tilde{f}^{1}]\} \qquad \text{eq. A 4.51}$$

where all the x dependent variables are evaluated at $x = 2L$.

Substituting the harmonic ansatz into the first order reaction rate, the amplitude of the first order reaction rate is approximated as

$$\tilde{R_i^*} = < c_{0,i} > \tilde{k_{0,i}}\ exp[-\alpha Z(\tilde{\varphi^{i,0}} + \tilde{V^i})]\ \{\tilde{c_i^*} + \tilde{\partial}_x \tilde{c_i^0})_2 \tilde{F} - \tilde{c_i^0}(\alpha + \alpha) Z[\tilde{\varphi^{i,*}} + \tilde{\partial}_x \tilde{\varphi^{i,0}})_2 \tilde{F}]\}$$

$$+ \tilde{R_i^0}\ \{+\tilde{\gamma}\tilde{k}^2 \tilde{F} + \alpha Z[\tilde{\varphi^{i,*}} + \tilde{\partial}_x \tilde{\varphi^{i,0}})_2 \tilde{F}]\} \qquad \text{eq. A 4.52}$$

where all the x dependent variables are evaluated at $x = 2L$, and $\alpha + \alpha = 1$.

Substituting the perturbation expansions of the concentration field and the rest potential to the simplified Nernst equation, the zeroth order concentration field and rest potential are related by

$$\tilde{\varphi^{i,0}}(\tilde{x}) = \frac{1}{Z} ln[< c_{0,i} > \tilde{c_i^0}(\tilde{x})] \qquad \text{eq. A 4.53}$$

And the first order concentration field and rest potential are related by

$$\tilde{\varphi^{i,1}}(\tilde{x}, \tilde{y}, \tilde{t}) = \frac{1}{Z} \frac{\tilde{c_i^1}(\tilde{x}, \tilde{y}, \tilde{t})}{\tilde{c_i^0}(\tilde{x})} \qquad \text{eq. A 4.54}$$

Substituting the harmonic ansatz, the amplitudes are related by

$$\tilde{\varphi^{i,*}}(\tilde{x}) = \frac{1}{Z} \frac{\tilde{c_i^*}(\tilde{x})}{\tilde{c_i^0}(\tilde{x})} \qquad \text{eq. A 4.55}$$

Substituting the perturbation expansions of the flux field, the mean growth velocity is

$$\tilde{U} = a^3 \sum_i c_{0,i} \tilde{R}_i^0 \qquad \text{eq. A 4.56}$$

Further substituting the harmonic ansatz, the temporal frequency is

$$\tilde{\Gamma} \tilde{F} = - a^3 \sum_i c_{0,i} \tilde{R}_i^* \qquad \text{eq. A 4.57}$$

A 4.1.6 General Solutions

The zeroth order problem derived from the mass conservation and the Fick's 1st law is

$$0 = \tilde{\nabla}^2 \tilde{c_i^0}(\tilde{x}) \qquad \text{eq. A 4.58}$$

The general solution to the zeroth order problem is

$$\tilde{c_i^0}(\tilde{x}) = \tilde{C_i^{0,(1)}} \tilde{x} + \tilde{C_i^{0,(2)}} \qquad \text{eq. A 4.59}$$

And the first problem under the steady state assumption (*i.e.*, the time derivative of the first order concentration field is assumed to be zero) is

$$0 = \tilde{\nabla}^2 [\tilde{c_i^*}(\tilde{x}) \; exp(\tilde{\Gamma} \tilde{t} + i \tilde{k} \tilde{y})] \qquad \text{eq. A 4.60}$$

The general solution to the first order problem is

$$\tilde{c_i^*}(\tilde{x}) = C_i^{\tilde{*},(1)} exp[\tilde{k}(\tilde{x} - C_i^{\tilde{*},(2)})] + C_i^{\tilde{*},(3)} exp[-\tilde{k}(\tilde{x} - C_i^{\tilde{*},(4)})] \quad \text{eq. A 4.61}$$

Imposing the physical constraint that the maximum amplitude is obtained at the nominal growth front at $x = 2L$, the general solution to the first order problem is then reduced to

$$\tilde{c_i^*}(\tilde{x}) = C_i^{\tilde{*},(1)} exp[\tilde{k}(\tilde{x} - 2)] \quad \text{eq. A 4.62}$$

A 4.1.7 Special Solutions

The zeroth order boundary condition imposed at the electrolyte / electrode interface is

$$\mathbf{n} \cdot \tilde{\mathbf{J}}_{\mathbf{i}}^{\mathbf{0}}(2) = -\tilde{R}_i^0 \quad \text{eq. A 4.63}$$

Substituting the Fick's first law and the general solution, the first free variable is solved as

$$C_i^{\tilde{0},(1)} \tilde{x} = -\tilde{R}_i^0 \quad \text{eq. A 4.64}$$

Assuming that the first order term of the concentration field at the boundary layer/ bulk electrolyte interface is negligible in comparison to the zeroth order term, the boundary condition imposed at the boundary layer / bulk electrolyte interface is

$$\tilde{c_i^0}(1) = 1 \qquad \text{eq. A 4.65}$$

The second free variable is solved as

$$C_i^{\tilde{0},(2)}\tilde{x} = 1 + \tilde{R_i^0} \qquad \text{eq. A 4.66}$$

And the special solution to the zeroth order problem is

$$\tilde{c_i^0}(\tilde{x}) = 1 - \tilde{R_i^0}(\tilde{x} - 1) \qquad \text{eq. A 4.67}$$

A 4.1.8 Dispersion Relation

Substituting the special solution to the amplitude of the first order reaction rate, where the nondimensionalized amplitude of the growth front function is set equal to 1 (*i.e.*, $F = L$)

$$\tilde{R_i^*} = \tilde{R_i^0}\ (+\tilde{\gamma}\tilde{k}^2 + \alpha\frac{C_i^{\tilde{*},(1)} - \tilde{R_i^0}}{1 - \tilde{R_i^0}}) \qquad \text{eq. A 4.68}$$

The first order boundary condition imposed at the electrolyte / electrode interface is

$$\mathbf{n} \cdot \tilde{\mathbf{J}}_{\mathbf{i}}^{\mathbf{1}}(2) = -\tilde{R}_i^1 \qquad \text{eq. A 4.69}$$

Substituting the harmonic ansatz and then the Fick's first law, the amplitude of the first order reaction rate can also equal

$$\tilde{R}_i^* = -\tilde{k} C_i^{\tilde{*},(1)} \qquad \text{eq. A 4.70}$$

Combined the two expressions of the amplitude, the free variable is solved to be

$$C_i^{\tilde{*},(1)} = \tilde{R}_i^0 \frac{\alpha \frac{\tilde{R}_i^0}{1-\tilde{R}_i^0} - \tilde{\gamma}\tilde{k}^2}{\alpha \frac{\tilde{R}_i^0}{1-\tilde{R}_i^0} + \tilde{k}} \qquad \text{eq. A 4.71}$$

Substituting the solution to the amplitude of the first order reaction rate, and the amplitude to the expression for the temporal frequency, the dispersion relation between the temporal frequency and the spatial frequency is

$$\tilde{\Gamma} = a^3 \sum_i c_{0,i} \tilde{R}_i^0 \tilde{k} \frac{\tilde{\xi} - \tilde{\gamma}\tilde{k}^2}{\tilde{\xi} + \tilde{k}} \qquad \text{eq. A 4.72}$$

where

$$\tilde{\xi} = \alpha \frac{\tilde{R}_i^0}{1 - \tilde{R}_i^0} \qquad \text{eq. A 4.73}$$

The critical spatial frequency is obtained when the temporal frequency equals to zero

$$\tilde{k}_c = \sqrt{\frac{\tilde{\xi}}{\tilde{\gamma}}} \qquad \text{eq. A 4.74}$$

When the spatial frequency is larger than the critical spatial frequency ($k > k_c$), the temporal frequency is negative ($\Gamma < 0$), the exponential in the first order term diminishes over time, the morphological evolution is therefore stable. When the spatial frequency is smaller than the critical spatial frequency ($k < k_c$), the temporal frequency is positive ($\Gamma > 0$), the exponential in the first order term blows up over time, the morphological evolution is therefore unstable.

The spatial frequency ([=] m^{-1}) is related to the wavenumber ([=] $rad \cdot m^{-1}$) by a factor of 2π (wavenumber = $2\pi \times$ spatial frequency). The symbol k is used to represent the spatial frequency only in the derivation described here in Appendix **A 4.1**. In the main text, the symbol k is used to represent the wavenumber. The conversion was accounted when comparing the experimental wavenumber and the theoretical wavenumber.

This derivation described here is based on the work by C. P. Nielsen and H. Bruus [Nielsen 2015]. The most significant differences are (1) this derivation here incorporated the deposition of alloys, while the work by C. P. Nielsen and H. Bruus considers elementary metal only; (2) the mathematical expression for the ξ parameter is different — the derivation here follows the sign convention of potential used by experimental electrochemists; (3) the physical origin of the simplified Nernst equation is clearly stated here to be the choice of the reference potential; (4) the physical origin of the determination of the second free variable ($C^{0,(2)}{}_i$) to the zeroth order problem is clearly stated here to be the far-field boundary condition, instead of being related to the rest potential.

A 4.2 Chronoamperometry

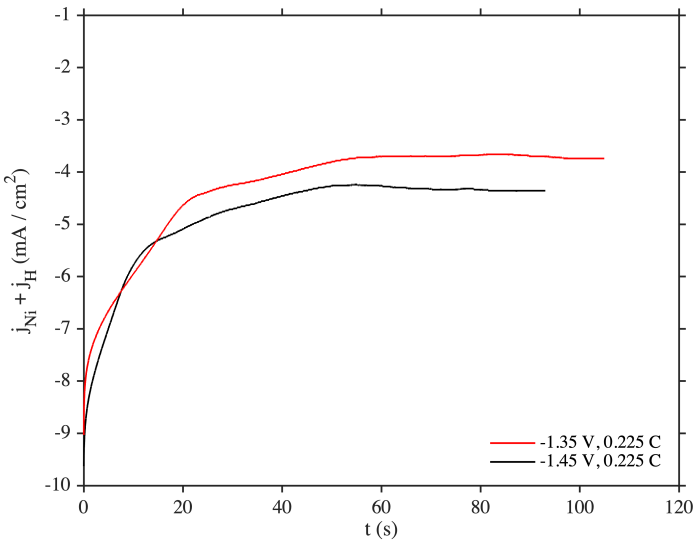

Figure A 4.2. Chronoamperometry of the Ni electrodepositions.

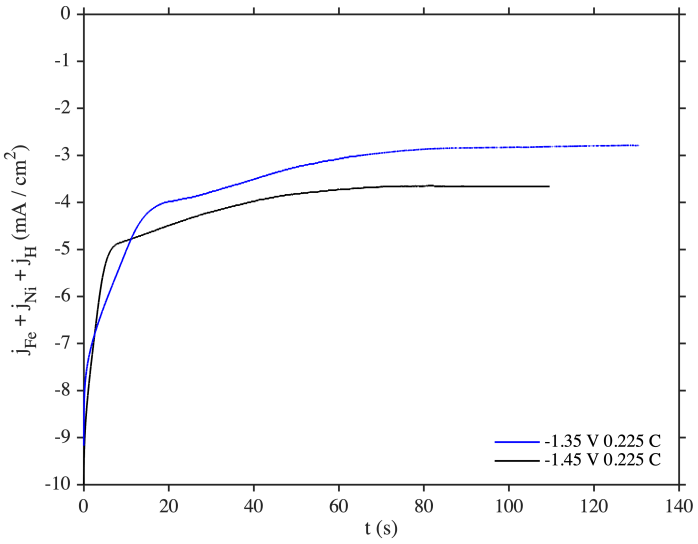

Figure A 4.3. Chronoamperometry of the Fe-Ni electrodepositions.

A 4.3 SEM-EDS Point ID

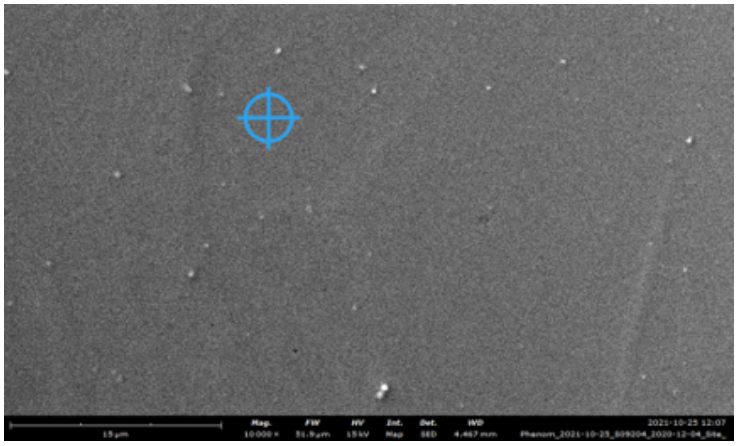

Element Symbol	Atomic Conc.	Weight Conc.
Fe	55.627	54.400
Ni	44.373	45.600

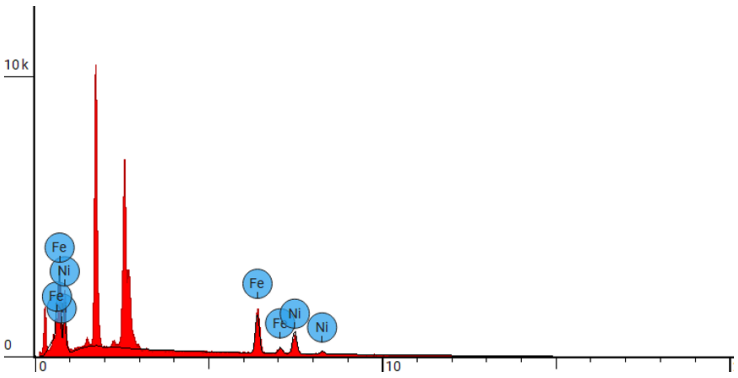

Figure A 4.4. SEM-EDS point ID on Ni-lean region in FeNi-02.

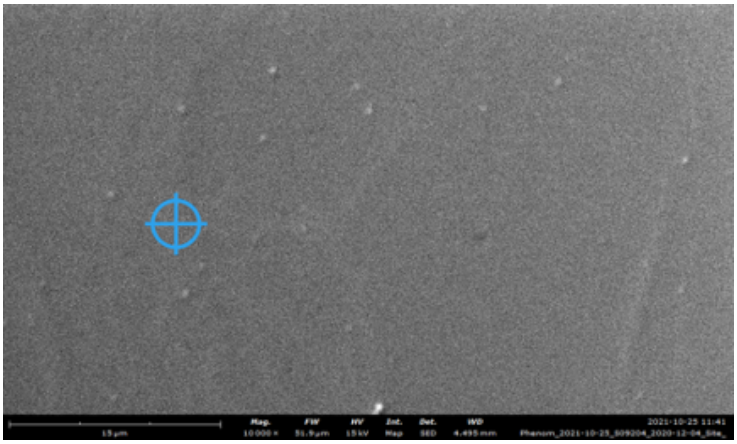

Element Symbol	Atomic Conc.	Weight Conc.
Fe	41.499	40.300
Ni	58.501	59.700

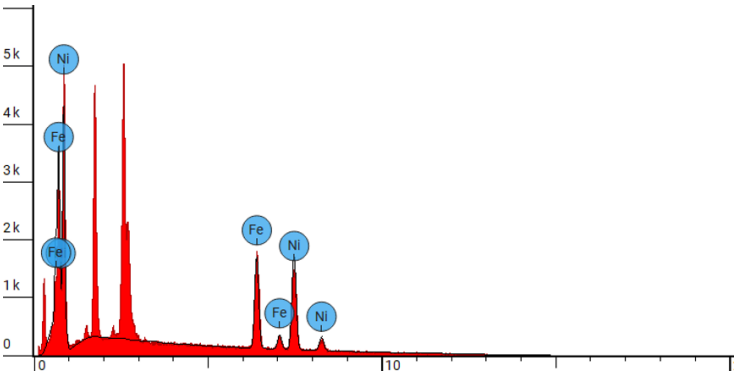

Figure A 4.5. SEM-EDS point ID on Ni-rich region in FeNi-02.

References

[1] Chazalviel, J.-N. “Electrochemical Aspects of the Generation of Ramified Metallic Electrodeposits.” Phys. Rev. A 42, no. 12 (December 1990): 7355–67.

[2] Chen, Chao-Peng, and Jacob Jorne. “The Dynamics of Morphological Instability during Electrodeposition.” Journal of The Electrochemical Society 138, no. 11 (November 1991): 3305–11.

[3] Sundström, Lars-Göran, and Fritz H. Bark. “On Morphological Instability during Electrodeposition with a Stagnant Binary Electrolyte.” Electrochimica Acta 40, no. 5 (April 1, 1995): 599–614.

[4] Nielsen, Christoffer P., and Henrik Bruus. “Morphological Instability during Steady Electrodeposition at Overlimiting Currents.” Phys. Rev. E 92, no. 5 (November 2015): 052310.

[5] Chrostowski, Robert, Zixuan Li, James Smith, and Filippo Mangolini. “Monte-Carlo Evaluation of Bias and Variance in Hurst Exponents Computed from Power Spectral Analysis of Atomic Force Microscopy Topographic Images.” Applied Surface Science 581 (April 15, 2022): 152092.

[6] Tobias, C. W., M. Eisenberg, and C. R. Wilke. “Fiftieth Anniversary: Diffusion and Convection in Electrolysis—A Theoretical Review.” Journal of The Electrochemical Society 99, no. 12 (1952): 359C.

[7] Hessami, Sholeh, and Charles W. Tobias. “A Mathematical Model for Anomalous Codeposition of Nickel-Iron on a Rotating Disk Electrode.” Journal of The Electrochemical Society 136, no. 12 (December 1989): 3611–16.

[8] Lee, J.-Y., M.P.J. Punkkinen, S. Schönecker, Z. Nabi, K. Kádas, V. Zólyomi, Y.M. Koo, et al. “The Surface Energy and Stress of Metals.” Surface Science 674 (August 1, 2018): 51–68.

5 Texture of Laser-Irradiated Electrodeposited Fe-Ni

5.1 Introduction

Section 1.4 in **chapter 1** reviews a few strategies to approach the challenge in synthesizing $L1_0$ Fe-Ni [1-3]. The characterization of the $L1_0$ Fe-Ni crystal structure is no trivial task either. The X-ray atomic form factor of Fe and Ni differ by ~ 10% at the momentum transfers of the first two superstructure reflections (i.e., 001 and 110). The electron atomic form factors differ by ~ 5% and ~ 2% at the momentum transfers of 001 and 110, respectively [4]. Since the structure factor at a superstructure reflection scales with the length square of the form factor difference, it is challenging to resolve the superstructure peaks from the background level, unless the ordered phase exists in a large quantity (e.g., in the meteorites [5] or the neutron irradiated samples [6]). On the other hand, the ordered structure deviates very little from its disordered counterpart (i.e., FCC Fe-Ni) in terms of the unit cell dimensions, which baffles the attempts to detect $L1_0$ Fe-Ni with atomic resolution imaging techniques. An indirect method to detect the $L1_0$ Fe-Ni phase in a polycrystalline, possibly multiphase sample is to characterize the coercivity of the sample. This is plausible in principle, based on the difference in the first-order magnetocrystalline anisotropy constant (K_1) between $L1_0$ Fe-Ni ($K_{1, L10} \sim 8.4 \times 10^5$ J/m^3) [7] and FCC Fe-Ni ($K_{1, FCC} \sim 3.6 \times 10^3$ J/m^3) [8, 9]. The coercivity values of $L1_0$ Fe-Ni containing samples reported in the literature range from ~ 56 kA/m (0.7 kOe) to ~ 143 kA/m (1.8 kOe) [1-3], at least an order of magnitude higher than the anisotropy field, $H_k \sim 5$ kA/m (0.06 kOe), of FCC Fe-Ni (see **eq. 1.5** in **chapter 1**), which is the upper bound of the coercivity of the disordered structure. The coercivity, however, is an extrinsic magnetic property very sensitive to the microstructure. Take the NWA

6259 meteorite as an example, the poorly textured region of the meteorite exhibits essentially zero coercivity, while the highly textured region exhibits a coercivity of 95.5 kA/m (1.2 kOe) [5]. In other words, a close-to-zero coercivity cannot disprove the existence of $L1_0$ Fe-Ni in the sample, but a coercivity on the order of 50 kA/m (0.6 kOe) or higher can be considered as an indicator that $L1_0$ Fe-Ni may exist in the sample. A control over the crystallographic texture is in this sense significant for tackling the synthetic challenge of $L1_0$ Fe-Ni. This chapter summarizes the preliminary work in affecting the texture of electrodeposited Fe-Ni films by single-pulse laser irradiation.

The research on pulsed laser irradiation of Fe-Ni is also motivated by the molecular dynamic simulation reported by He. et al [10], which shows that single-pulse (100 fs) laser irradiation introduces a high density of point, line, and planar defects to the region within ~ 15 nm in depth below the surface of equiatomic FCC Fe-Ni. The vacancy concentration in the highly defected region is on the order of $\sim 1.5 \times 10^{-4}$, which is higher than the equilibrium vacancy concentration ($\sim 0.7 \times 10^{-4}$) at the melting point ($T_m \sim 1430\ ^{o}C$) of FCC Fe-Ni. It is suggested that such a large amount of vacancies are generated due to the rapid motion of the re-solidification front (~ 80 m/s) under ultrafast cooling ($\sim 10^{24}$ K/s). The excess vacancies generated by the pulsed laser may accelerate the ordering transformation towards $L1_0$ Fe-Ni.

5.2 Experimental Methods

5.2.1 Electrodeposition

An Fe-Ni film was prepared by potentiostatic electrodeposition from an electrolyte consisting of

3 mM saccharin ($C_7H_5NO_3S$), 550 mM boric acid (H_3BO_3), 180 mM nickel (II) chloride hexahydrate ($NiCl_2 \cdot 6H_2O$), 820 mM nickel (II) sulfate hexahydrate ($NiSO_4 \cdot 6H_2O$), and 90 mM iron (II) sulfate heptahydrate ($FeSO_4 \cdot 7H_2O$). The recipe is the same as that of the electrolyte E-a in **Table 2.1** in **chapter 2** as well as the electrolyte used in **chapter 3**. All chemicals were used as purchased. Milli-Q™ deionized water with a resistivity of 18.2 MOhm was used as the solvent. The electrodeposition experiment was carried out with an EG&G PAR(263A) potentiostat/galvanostat. A three-electrode setup was used. The reference electrode was oriented vertically. The working electrode and the counter electrode were oriented horizontally at the bottom and the top, respectively. The Fe-Ni film was grown onto a Ru / Ta /Si substrate. The exposure area was 1.2 × 1.0 cm^2, defined by the Kapton® tape. The electrical contact was made from the front side of the substrate using the 3M™ copper conductive tape. The counter electrode (*i.e.*, the anode) was a Pt mesh. The silver silver chloride (Ag/AgCl) electrode in saturated potassium chloride (sat'd KCl) was used as the reference electrode (0.00 V vs. Ag/AgCl = + 0.199 V vs. SHE). The applied potential was − 0.984 V vs. Ag/AgCl. The applied charge density was 8.5 C/cm^2. The electrodeposition was performed at room temperature without intentional stirring.

5.2.2 Laser Irradiation

The single-pulse KrF laser (Lambda-Physik Compex) in the research group of Prof. James Fitz-Gerald at the University of Virginia was used to irradiate the electrodeposited Fe-Ni film (1.2 cm × 1.0 cm). The laser irradiation experiments were performed by Jonathan Skelton. The pulse duration of the laser was 20 ns. The wavelength of the laser was 248 nm. The laser power was

2.5 W. The laser frequency was 5 Hz, and the laser energy was 0.5 J (= 2.5 W / 5 Hz). The laser spot is approximately a rectangle with a fixed length of 2.9 cm. The laser fluence was controlled by varying the width of the laser spot, being measured from the irradiated site on a burn paper. The long side (2.9 cm) of the laser spot was oriented to be parallel to the short side (1.0 cm) of the electrodeposited Fe-Ni film, with the 1.0 cm short side of the film centered around the center of the long side of the laser spot. 5 single-pulse irradiation of 5 different fluence values were used to irradiate 5 separated sites on the surface of the same electrodeposited Fe-Ni film. The estimated effective fluence values (F) were 0.91, 1.02, 1.10, 1.17, 1.37 J/cm^2, respectively.

5.2.3 Characterization

The thickness of the as-deposited Fe-Ni film was checked by scanning white light interferometry (SWLI) using the ZYGO NewView 7300 optical profiler. The measured thickness was ~ 3 μm. The composition of the as-deposited Fe-Ni film was checked by energy dispersive X-ray spectroscopy (EDS) using the FEI Quanta LV200 scanning electron microscope (SEM). The measured composition was 46.2 at.%Ni. The compositions of the laser-irradiated sites were checked again by SEM-EDS. The measured compositions were between 45 and 47 at.% Ni, i.e., 46.4, 46.1, 46.2, 45.4, 45.0 at.%Ni for 0.91, 1.02, 1.10, 1.17, 1.37 J/cm^2, respectively, nominally the same as that of the as-deposited sample (see Appendix **A 5.3**).

The morphologies of the laser irradiated sites were characterized by the secondary electron images (SEI) and the backscattered electron images (BEI) collected with the FEI Quanta 650 SEM (acceleration voltage = 15 kV). EDS point ID and mapping were used to verify the

channeling contrast seen in the BEI. The nano-scale texture of the laser-irradiated site (1.37 J/ cm^2) was characterized by electron backscatter diffraction (EBSD) using the Helios UC G4 Dual Beam FIB-SEM. The data post-processing was conducted on the CHANNEL 5 software (Oxford Instruments HKL). The micro-scale textures of the laser-irradiated sites were characterized by X-ray diffraction (XRD) using the Empyrean multipurpose X-ray diffractometer (Cu Kα, λ = 1.5406 Å). The micro focus optics and the alignment camera were used to positioned the X-ray illuminated area (130 μm × 4.83 mm) to be within the laser-irradiated site being investigated. The GaliPIX3D detector was used in the area (2D) scanning mode to increase the count rate, but with a trade-off in instrumental peak broadening.

5.3 Results and Discussion

Figure 5.1-5.6 shows the morphologies of the as-deposited Fe-Ni site and the laser-irradiated Fe-Ni sites from low to high laser fluence. For the laser-irradiated sites, each of the SEM micrographs was collected near the center of the laser-irradiated site, where the maximum local fluence was located. Near the edge of the laser-irradiated site, the grain size was significantly smaller, as shown in **Figure 5.7**. Therefore, **Figure 5.2-5.6** represents maximum grain size in each of the fluence conditions. As the laser fluence increased from 0.91 J/m^2 (**Figure 5.2**) to 1.37 J/m^2 (**Figure 5.6**), the maximum grain size in the laser-irradiated site increased from ~ 90 nm to ~ 150 nm. The site-to-site grain size variation is therefore consistent with the edge-to-center intra-site grain size variation. Strong inter-grain contrasts are seen in the BSI of all the laser-irradiated sites but not in that of the as-deposited site. EDS point ID and mapping were used to show that the inter-grain contrasts in the BSI are not compositional by nature (Appendix **A 5.1** and **A 5.2**). The corresponding SEI shows that the inter-grain contrasts in the BSE are not topographical by nature. The arrow head in **Figure 5.6b** points at a grain that contains a set of planar defects (*i.e.*, crystal defects). All these observations indicate that the inter-grain contrasts are predominantly channeling contrasts [11].

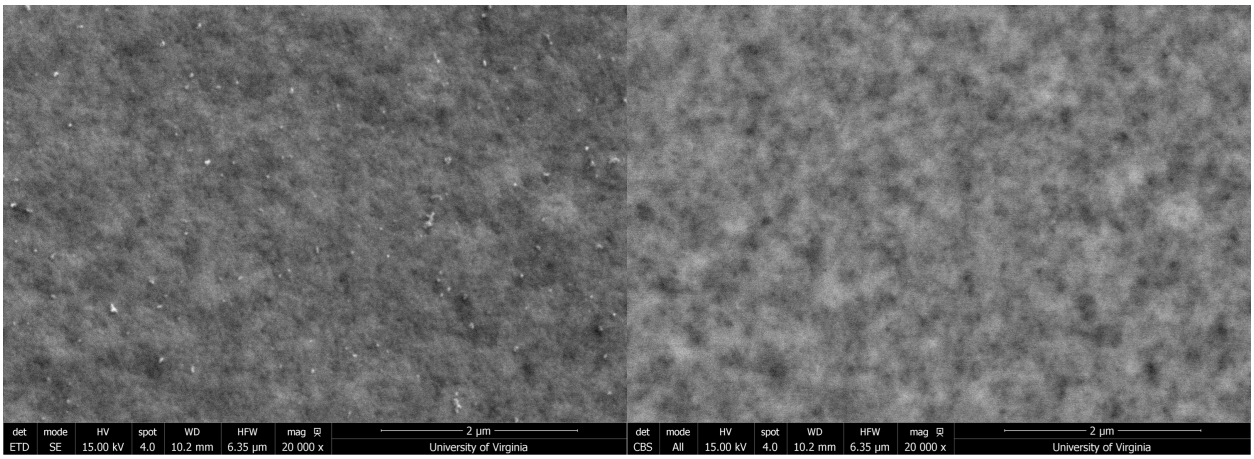

Figure 5.1. SEM micrographs of as-deposited Fe-Ni: **(a)** SEI. **(b)** BSI.

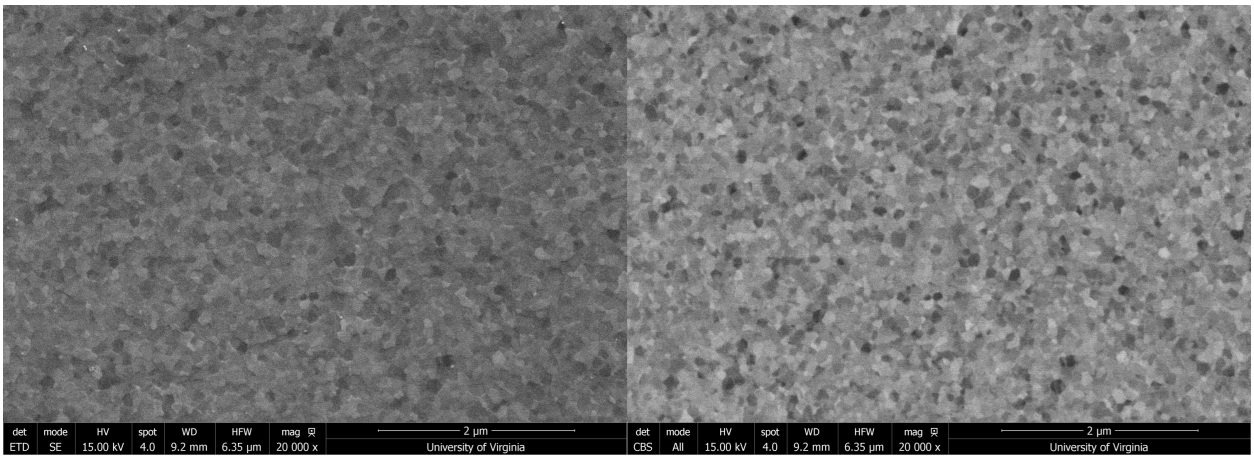

Figure 5.2. SEM micrographs of laser-irradiated (F = 0.91 J/m^2) Fe-Ni: **(a)** SEI. **(b)** BSI.

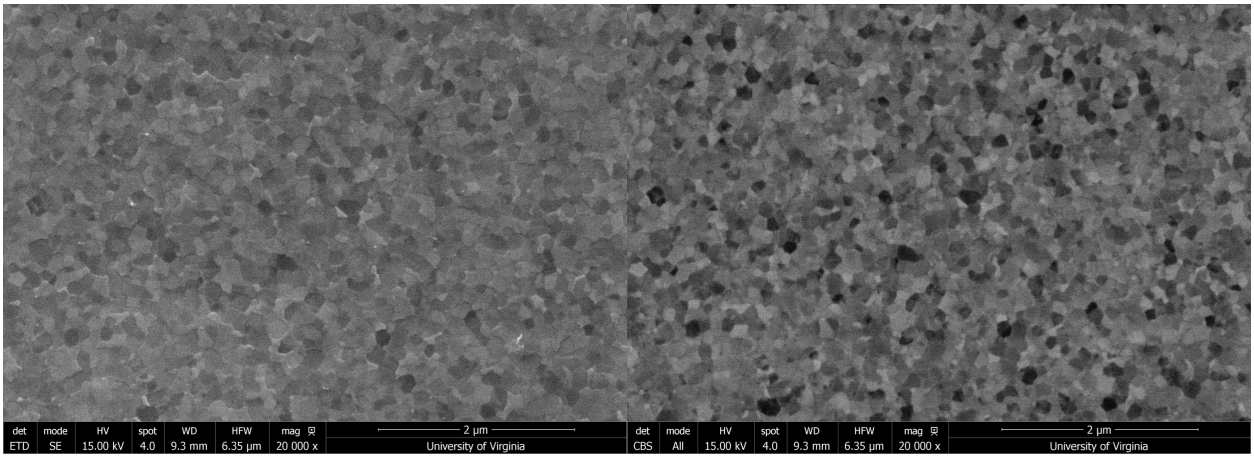

Figure 5.3. SEM micrographs of laser-irradiated (F = 1.02 J/m^2) Fe-Ni: **(a)** SEI. **(b)** BSI.

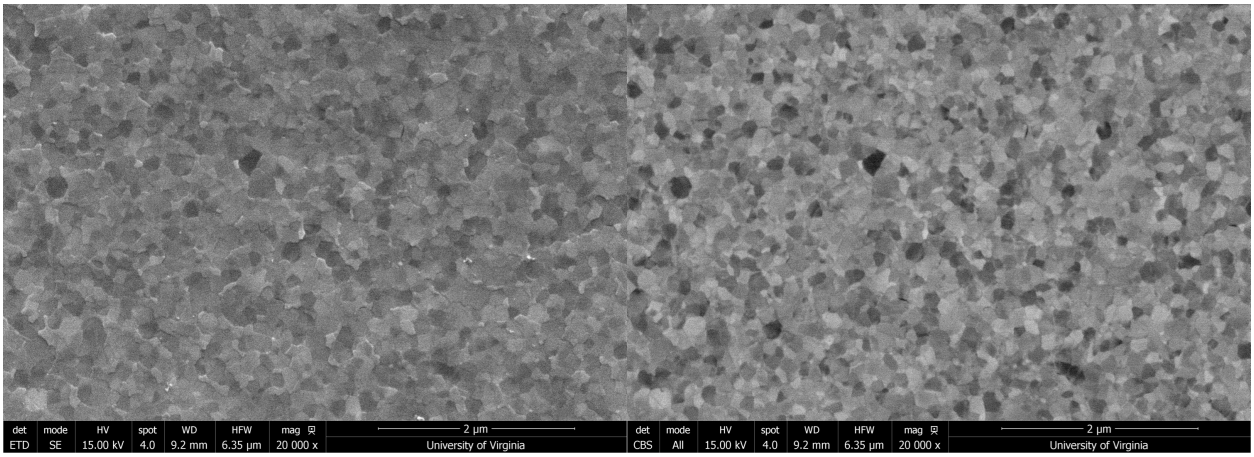

Figure 5.4. SEM micrographs of laser-irradiated (F = 1.10 J/m^2) Fe-Ni: **(a)** SEI. **(b)** BSI.

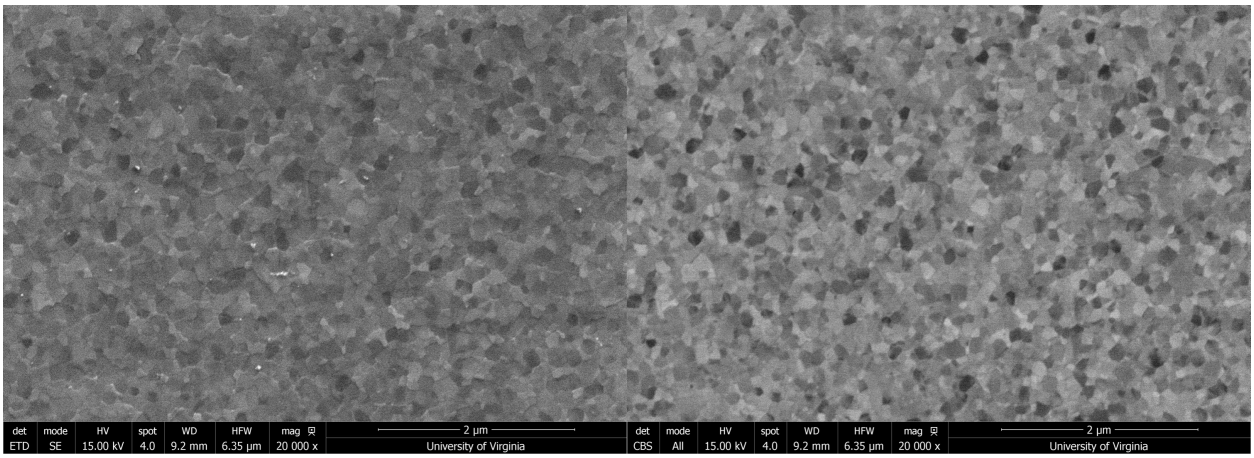

Figure 5.5. SEM micrographs of laser-irradiated (F = 1.17 J/m^2) Fe-Ni: **(a)** SEI. **(b)** BSI.

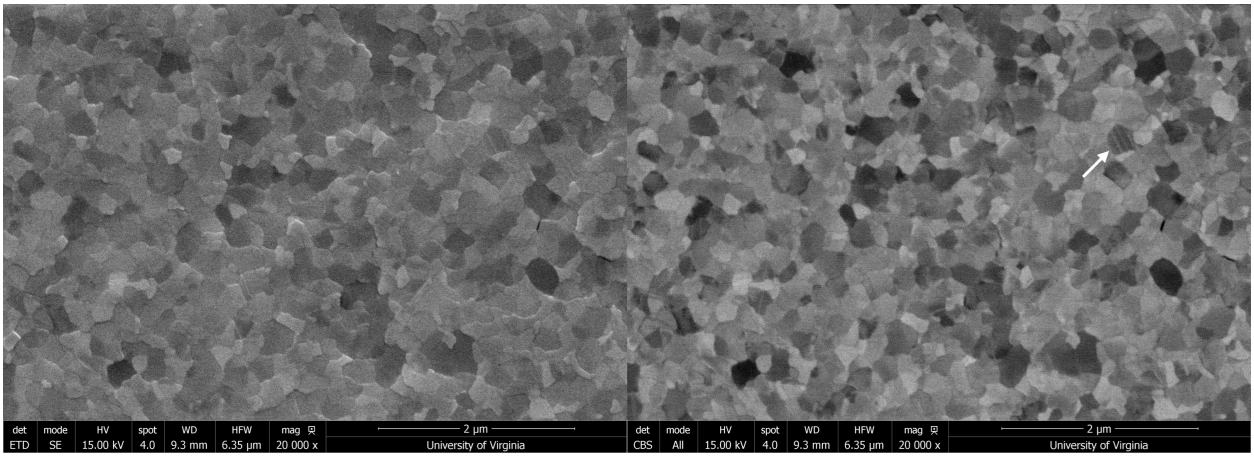

Figure 5.6. SEM micrographs of laser-irradiated (F = 1.37 J/m^2) Fe-Ni: **(a)** SEI. **(b)** BSI.

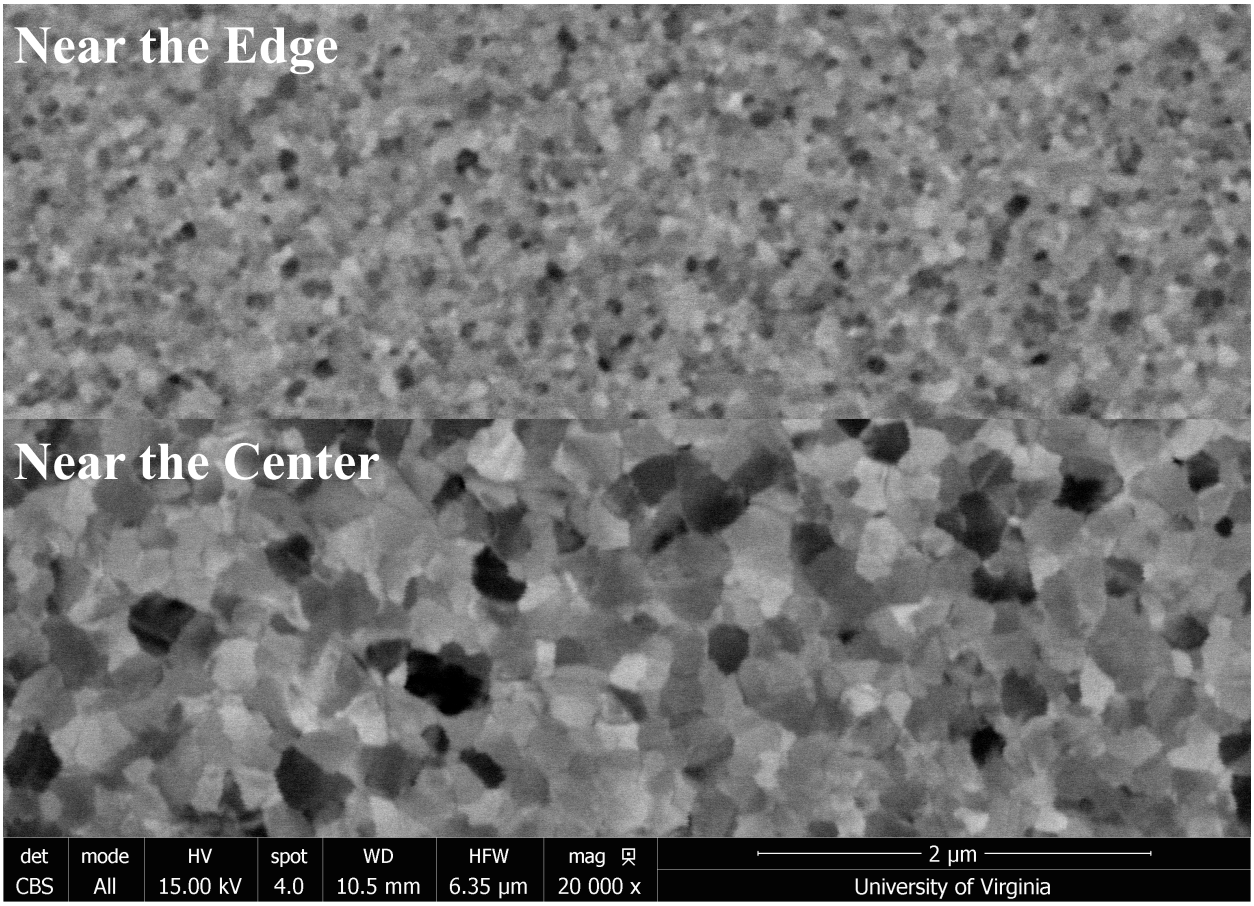

Figure 5.7. BSI micrograph of laser-irradiated (F = 1.37 J/m^2) Fe-Ni. The upper part was collected near the edge of the edge of the laser-irradiated site. The lower part was collected near the center of the laser-irradiated site.

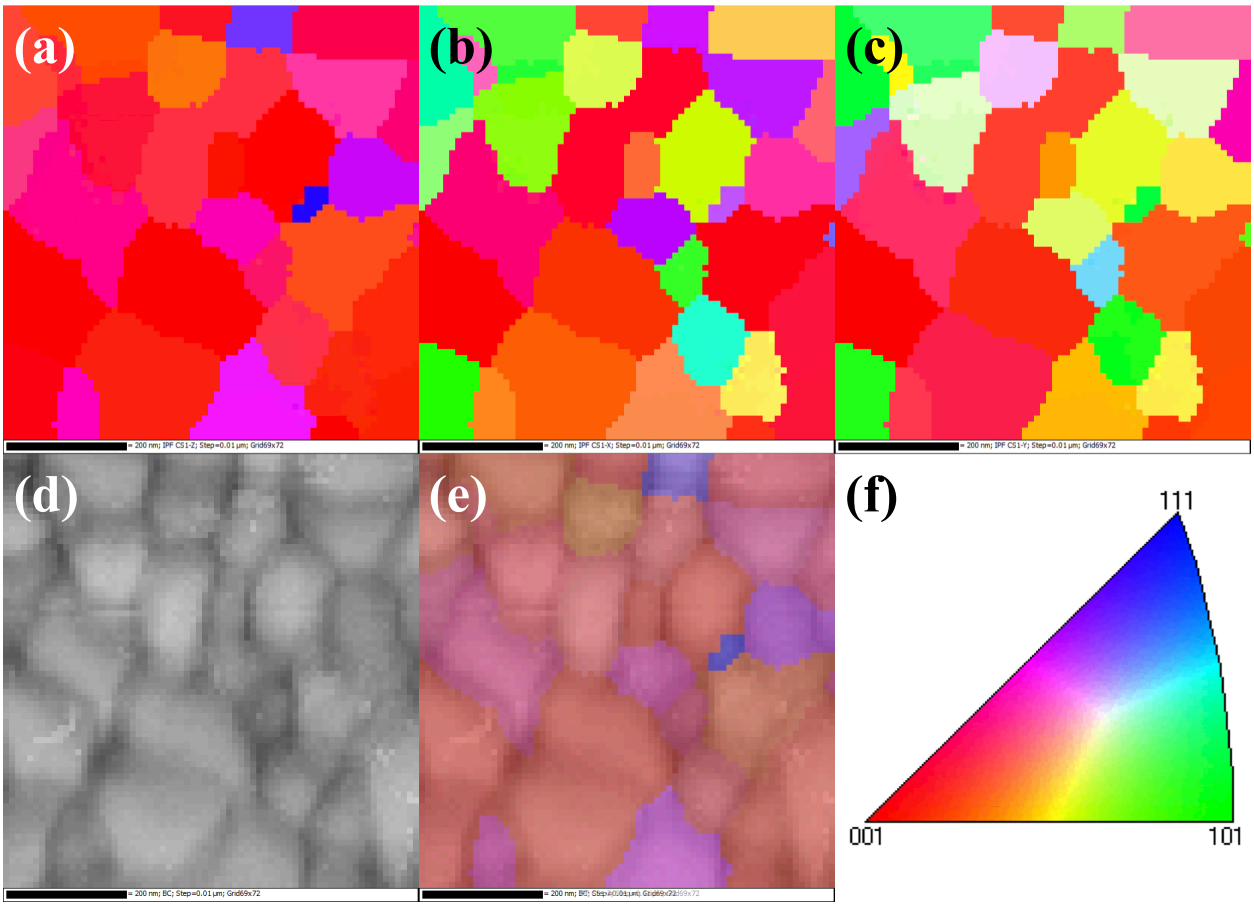

Figure 5.8. EBSD micrographs of laser-irradiated (F = 1.37 J/m^2) Fe-Ni. **(a)** Inverse pole figure map of the out-of-plane orientation. **(b, c)** Inverse pole figure maps of two orthogonal in-plane orientations. **(d)** Band contrast map. **(e)** The band contrast map overlapped. **(d)** with the inverse pole figure map of the out-of-plane orientation in 40% opacity. **(f)** Inverse pole figure of the FCC crystal structure. The scale bars are all 200 nm in length.

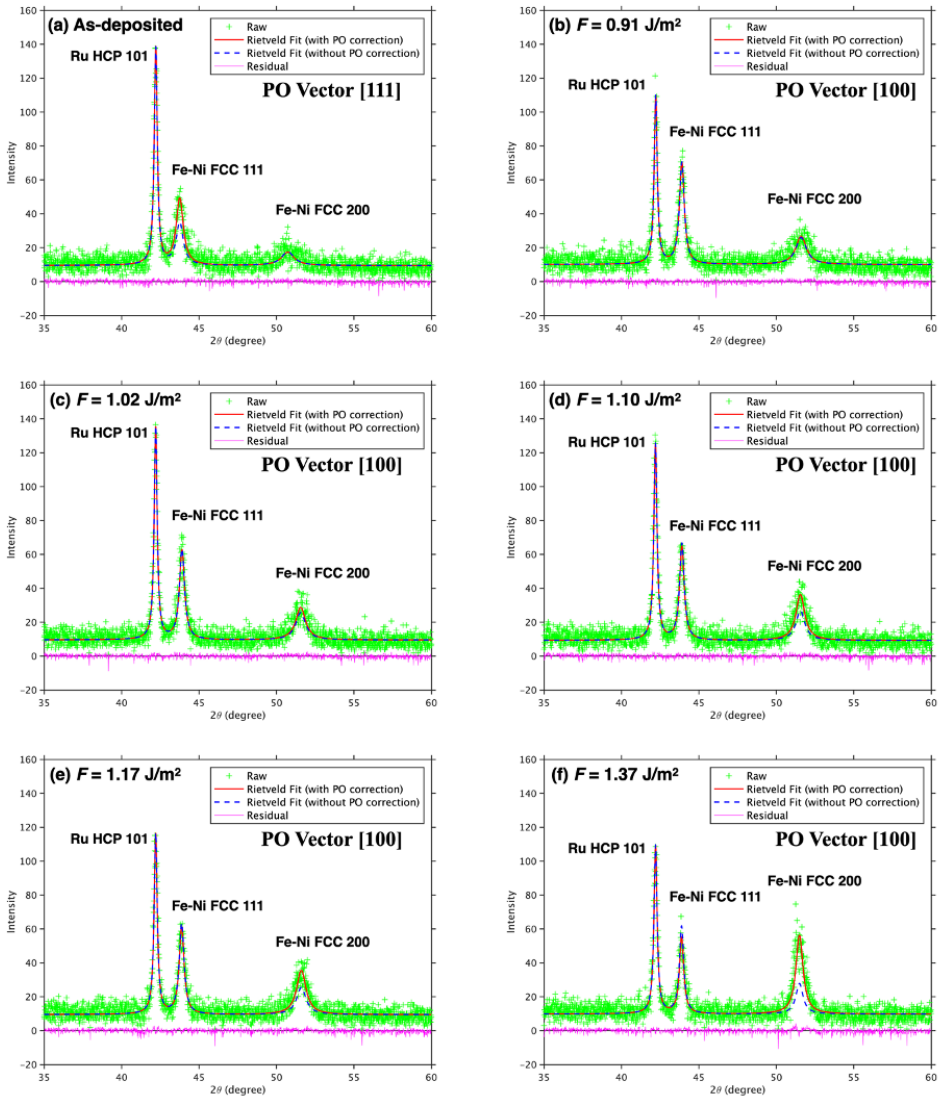

Figure 5.9. Rietveld refinements of experimental XRD patterns with and without the preferred orientation correction. **(a)** As-deposited Fe-Ni. **(b)** Laser-irradiated Fe-Ni (F = 0.91 J/m^2). **(c)** Laser-irradiated Fe-Ni (F = 1.02 J/m^2). **(d)** Laser-irradiated Fe-Ni (F = 1.10 J/m^2). **(e)** Laser-irradiated Fe-Ni (F = 1.17 J/m^2). **(f)** Laser-irradiated Fe-Ni (F = 1.37 J/m^2). The green crosses denote the experimental data. The red solid and blue dashed lines denote the Rietveld fitted pattern with and without the March preferred orientation (PO) correction, respectively. The magenta line shows the residual of the Rietveld fitted pattern with the PO correction.

Figure 5.8 shows the EBSD micrographs collected from the laser-irradiated (F = 1.37 J/m^2) Fe-Ni. The inver pole figure map of the out-of-plane orientation (**Figure 5.8a**) clearly shows that 001 is the dominant out-of-plane texture within the field of view. **Figure 5.9** shows the Rietveld refinements of the XRD patterns collected with the micro focus optics from the as-deposited site and the laser-irradiated sites. The March model (see Appendix **A 3.4** in chapter **3**) was used to account for intensity contribution from the preferred orientation (PO), i.e., the texture. Based on the EBSD characterization, the 001 direction was used as the PO vector in the March model for the laser-irradiated sites. The 111 direction was used as the PO vector for the as-deposited site. The Lorentzian function was used as the profile function. A shift parameter was refined to correct the peak position of the Fe-Ni FCC 200 reflection. The red solid lines show the Rietveld fitted patterns with the intensity contribution from the PO being accounted for by the March model. By setting the March coefficient to unity (r = 1), i.e., without accounting for the PO contribution, a reference profile (blue dashed line) was generated from the refined parameters, including the lattice parameter (a), the Rietveld scale factor (S), and the profile parameter (H_K). The parameters, r, S, and H_K, are all defined in Appendix **A 3.3** and **3.4** in **chapter 3**. The reference profile represents the XRD pattern of a hypothetical sample that is ideally polycrystalline, where each orientation is randomly distributed, but otherwise the same as the real one. The deviation of the Rietveld fitted profile from the reference profile (blue dashed line) describes the extent of the PO. For a certain orientation specified by the Bragg reflection, if the fitted profile is below the reference profile, the population of the orientation in the real sample is smaller than that in the ideally polycrystalline reference sample, where each orientation is randomly distributed. If the

fitted profile is above the reference profile, the population of the orientation in the real sample is larger than that in the reference sample.

As it is shown in **Figure 5.9**, the as-deposited site has a 111 PO — the probability of finding a 111 orientation in the as-deposited site is larger than that of finding one in the corresponding reference sample, where each orientation is randomly distributed. The laser-irradiated site of the lowest fluence (F = 0.91 J/m^2) is close to having no PO — the probability of finding a 111 orientation or a 001 orientation is close to that of finding one in the reference sample. As the laser fluence increases, the 001 PO increases monotonically. On the laser-irradiated site of the highest fluence (F = 1.37 J/m^2), the 001 PO is so strong that the 111 PO is significantly smaller than random, which agrees with the EBSD observation.

5.4 Conclusion

This chapter summarizes the results of a preliminary investigation on the single-pulse laser irradiation of electrodeposited Fe-Ni. The single-pulse laser irradiation changed the grain size as well as the texture of the laser-irradiated site. As the laser fluence was increased, the grain size of laser-irradiated site increased. At the same time, the 111 orientation was suppressed, while the 001 orientation was populated. The 001 direction in $L1_0$ Fe-Ni is the unique direction that defines the magnetocrystalline anisotropy, in exactly the sense that a magnetic moment aligned with the 001 direction has the minimum magnetocrystalline anisotropy energy. Developing the 001 texture of FCC Fe-Ni films may aid the detection of the $L1_0$ Fe-Ni phase via coercivity measurements.

Appendix A 5.1 EDS Point ID

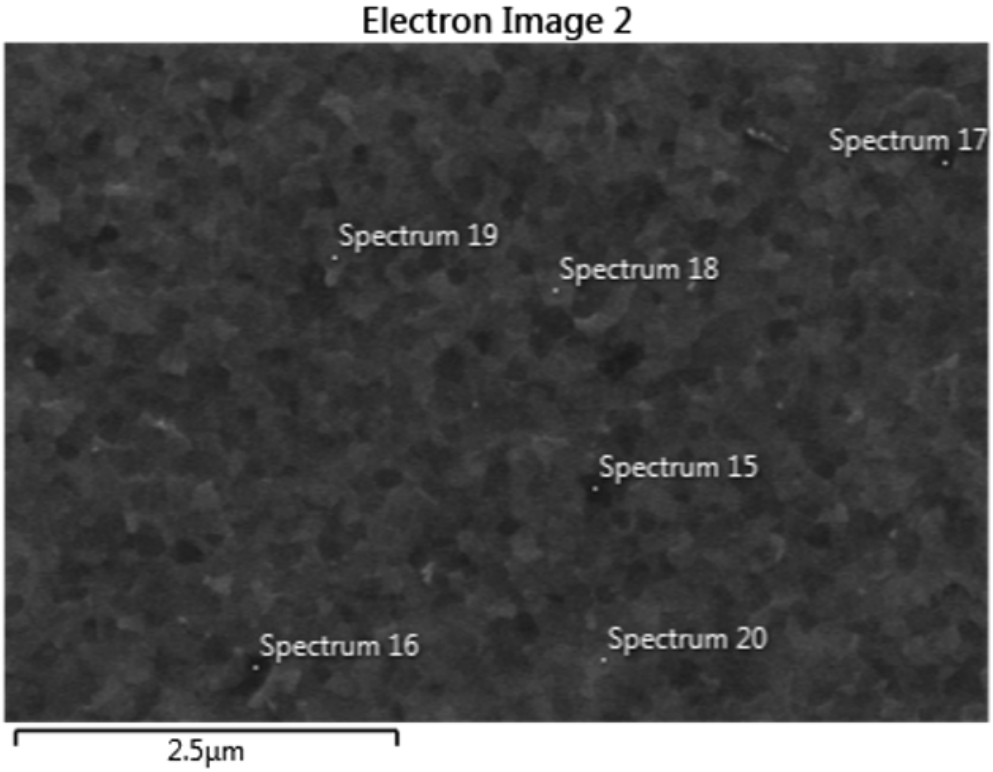

Figure 5.10. SEM micrograph (SEI) of the field of view on laser-irradiated Fe-Ni (F = 1.10 J/m^2) at which the EDS point IDs were performed.

Spectrum 15: 46.0 at.%Ni

Spectrum 16: 46.1 at.%Ni

Spectrum 17: 45.8 at.%Ni

Spectrum 18: 46.0 at.%Ni

Spectrum 19: 45.9 at.%Ni

Spectrum 20: 45.7 at.%Ni

Appendix A 5.2 EDS Map

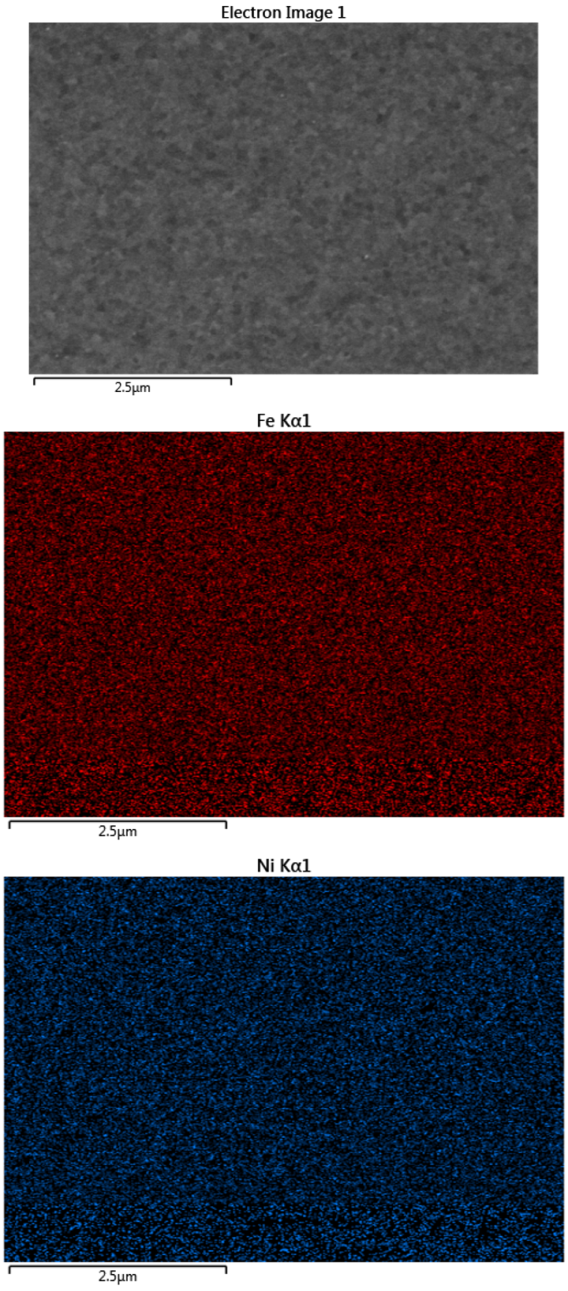

Figure 5.11. SEM micrograph (SEI) and EDS maps of laser-irradiated Fe-Ni (F = 1.02 J/m^2).

Appendix A 5.3 EDS Spectra and Quantifications

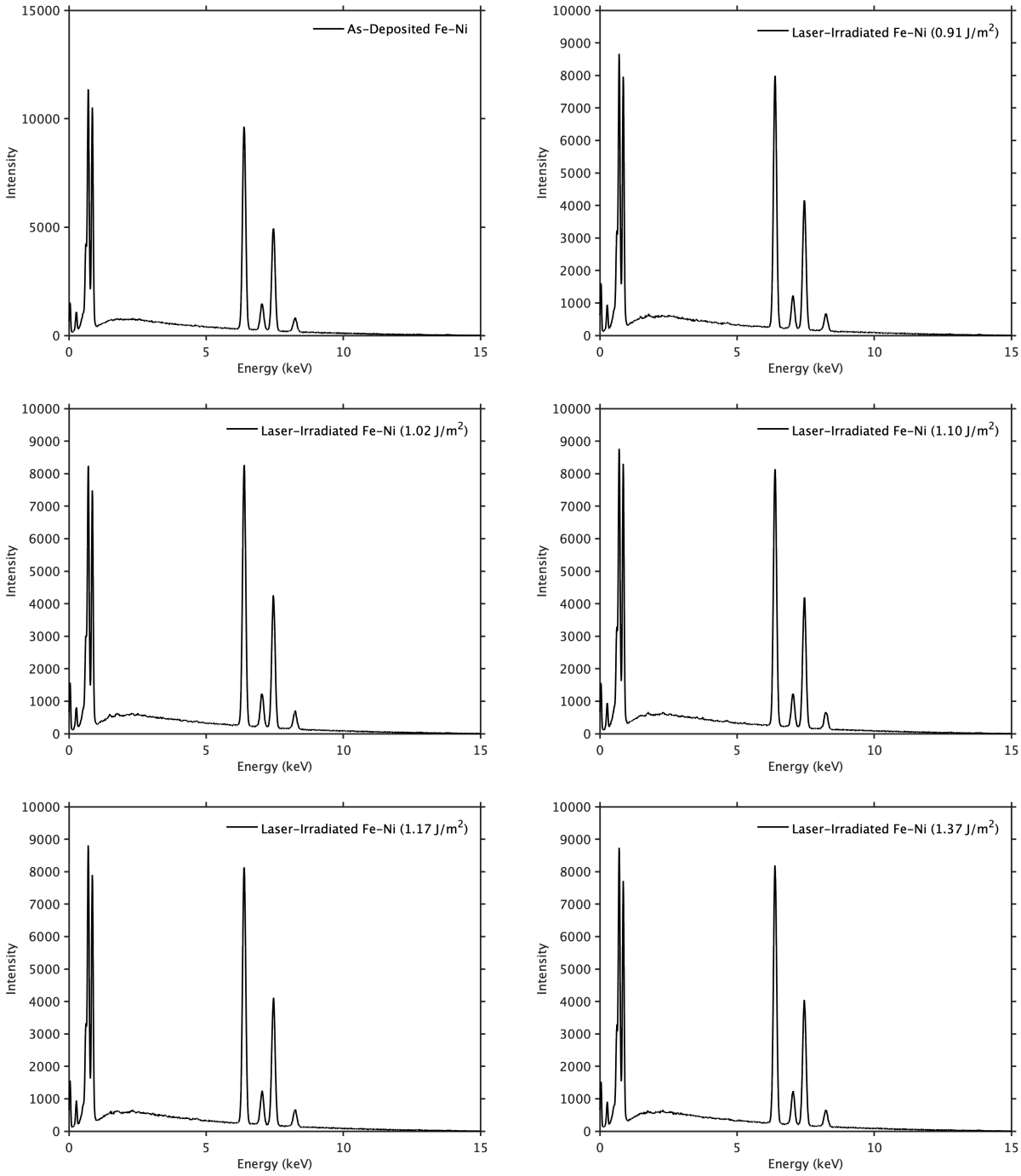

Figure 5.12. EDS spectra of as-deposited and laser-irradiated Fe-Ni.

As-deposited Fe-Ni

Element	Line Type	Apparent Concentration	Intensity Correction	k Ratio	Wt%	Wt% Sigma	At%	Standard Label	Factory Standard
Fe	K series	12.84	1.06	0.12835	52.58	0.20	53.82	Fe	Yes
Ni	K series	10.57	0.96	0.10572	47.42	0.20	46.18	Ni	Yes
Total:					100.00		100.00		

Laser-irradiated Fe-Ni (0.91 J/m2)

Element	Line Type	Apparent Concentration	Intensity Correction	k Ratio	Wt%	Wt% Sigma	At%	Standard Label	Factory Standard
Fe	K series	10.55	1.06	0.10553	52.41	0.22	53.65	Fe	Yes
Ni	K series	8.75	0.96	0.08751	47.59	0.22	46.35	Ni	Yes
Total:					100.00		100.00		

Laser-irradiated Fe-Ni (1.02 J/m2)

Element	Line Type	Apparent Concentration	Intensity Correction	k Ratio	Wt%	Wt% Sigma	At%	Standard Label	Factory Standard
Fe	K series	10.82	1.05	0.10817	52.63	0.21	53.87	Fe	Yes
Ni	K series	8.89	0.96	0.08892	47.37	0.21	46.13	Ni	Yes
Total:					100.00		100.00		

Laser-irradiated Fe-Ni (1.10 J/m2)

Element	Line Type	Apparent Concentration	Intensity Correction	k Ratio	Wt%	Wt% Sigma	At%	Standard Label	Factory Standard
Fe	K series	10.72	1.06	0.10722	52.61	0.21	53.85	Fe	Yes
Ni	K series	8.82	0.96	0.08822	47.39	0.21	46.15	Ni	Yes
Total:					100.00		100.00		

Laser-irradiated Fe-Ni (1.17 J/m2)

Element	Line Type	Apparent Concentration	Intensity Correction	k Ratio	Wt%	Wt% Sigma	At%	Standard Label	Factory Standard
Fe	K series	10.81	1.05	0.10807	53.41	0.22	54.65	Fe	Yes
Ni	K series	8.62	0.96	0.08616	46.59	0.22	45.35	Ni	Yes
Total:					100.00		100.00		

Laser-irradiated Fe-Ni (1.37 J/m2)

Element	Line Type	Apparent Concentration	Intensity Correction	k Ratio	Wt%	Wt% Sigma	At%	Standard Label	Factory Standard
Fe	K series	10.79	1.05	0.10795	53.75	0.22	54.99	Fe	Yes
Ni	K series	8.49	0.96	0.08491	46.25	0.22	45.01	Ni	Yes
Total:					100.00		100.00		

References

[1] Kojima, Takayuki, Misako Ogiwara, Masaki Mizuguchi, Masato Kotsugi, Tomoyuki Koganezawa, Takumi Ohtsuki, Taka-Yuki Tashiro, and Koki Takanashi. “Fe–Ni Composition Dependence of Magnetic Anisotropy in Artificially Fabricated L10-Ordered FeNi Films.” Journal of Physics: Condensed Matter 26, no. 6 (January 2014): 064207.

[2] Goto, Sho, Hiroaki Kura, Eiji Watanabe, Yasushi Hayashi, Hideto Yanagihara, Yusuke Shimada, Masaki Mizuguchi, Koki Takanashi, and Eiji Kita. “Synthesis of Single-Phase L10-FeNi Magnet Powder by Nitrogen Insertion and Topotactic Extraction.” Scientific Reports 7, no. 1 (October 16, 2017): 13216.

[3] Makino, Akihiro, Parmanand Sharma, Kazuhisa Sato, Akira Takeuchi, Yan Zhang, and Kana Takenaka. “Artificially Produced Rare-Earth Free Cosmic Magnet.” Scientific Reports 5, no. 1 (November 16, 2015): 16627.

[4] De Graef, M., & McHenry, M. (2012). Structure of Materials: An Introduction to Crystallography, Diffraction and Symmetry (2nd ed.). Cambridge: Cambridge University Press. doi:10.1017/CBO9781139051637.

[5] Lewis, L. H., A. Mubarok, E. Poirier, N. Bordeaux, P. Manchanda, A. Kashyap, R. Skomski, et al. “Inspired by Nature: Investigating Tetrataenite for Permanent Magnet Applications.” Journal of Physics: Condensed Matter 26, no. 6 (January 2014): 064213.

[6] Paulevé, J., A. Chamberod, K. Krebs, and A. Bourret. “Magnetization Curves of Fe–Ni (50–50) Single Crystals Ordered by Neutron Irradiation with an Applied Magnetic Field.” Journal of Applied Physics 39, no. 2 (February 1, 1968): 989–90.

[7] Poirier, Eric, Frederick E. Pinkerton, Robert Kubic, Raja K. Mishra, Nina Bordeaux, Arif Mubarok, Laura H. Lewis, Joseph I. Goldstein, Ralph Skomski, and Katayun Barmak. “Intrinsic Magnetic Properties of L10 FeNi Obtained from Meteorite NWA 6259.” Journal of Applied Physics 117, no. 17 (2015): 17E318.

[8] McDonald, Ian Joseph. “DESIGNING MAGNETIC ANISOTROPY IN FERROUS ALLOYS.” Doctor of Philosophy, Northeastern University, 2018.

[9] Einsle, Joshua F., Alexander S. Eggeman, Ben H. Martineau, Zineb Saghi, Sean M. Collins, Roberts Blukis, Paul A. J. Bagot, Paul A. Midgley, and Richard J. Harrison. “Nanomagnetic Properties of the Meteorite Cloudy Zone.” Proceedings of the National Academy of Sciences 115, no. 49 (2018): E11436–45.

[10] He, Miao, Chengping Wu, Maxim V. Shugaev, German D. Samolyuk, and Leonid V. Zhigilei. “Computational Study of Short-Pulse Laser-Induced Generation of Crystal Defects in Ni-Based Single-Phase Binary Solid–Solution Alloys.” The Journal of Physical Chemistry C 123, no. 4 (January 31, 2019): 2202–15.

[11] Joy, David C., Dale E. Newbury, and David L. Davidson. “Electron Channeling Patterns in the Scanning Electron Microscope.” Journal of Applied Physics 53, no. 8 (August 1, 1982): R81–122.

6 Far-From-Equilibrium Crystal and Defect Structures in Laser-Ablated Fe-Ni Nanoparticles

6.1 Introduction

In order to synthesize $L1_0$ FeNi, one has to circumvent the sluggish ordering kinetics and the limited driving force resulted from the low order-disorder temperature (T_{od} ~ 320 ^{o}C) of the system [1]. One strategy proposed (but not yet realized) by Lewis et al. was to trigger a martensitic transformation from the FCC phase to one of the non-cubic phases by high-strain processing methods [2]. Although the chemical ordering remained absent, the body-centered tetragonal (BCT) Fe-Ni obtained by this strategy was considered as a precursor of $L1_0$ Fe-Ni [2, 3]. The formation of BCT Fe-Ni via a displacive process was also implemented at the nanoscale by using tailored AuNi@FeNi core-shell particles. Ren et al. showed that the ordering of the Au-Ni core could impose an epitaxial strain on the Fe-Ni shell, transforming it into BCT Fe-Ni [4]. None of these proposed methods at their current stage of development are capable of obtaining $L1_0$ Fe-Ni. Nevertheless, considering the difficulties and the impacts of achieving $L1_0$ Fe-Ni, the lack of the cubic symmetry in the product phases of these synthesis and processing methods deserve a better understanding.

In this work, we report the structural and morphological characterization of near-equiatomic Fe-Ni nanoparticles prepared by the method of picosecond-pulsed laser ablation in liquids (ps-PLAL) [5, 6]. High-resolution transmission electron microscopy (HRTEM) imaging and nano-beam electron diffraction (NBED) were used to reveal a non-cubic Fe-Ni phase in the laser-

ablated nanoparticles as well as the orientation relationship between the non-cubic phase and the adjacent cubic phase, FCC Fe-Ni. Analyses base on Fast Fourier Transform (FFT) of the HRTEM images and HRTEM image simulations demonstrate that such a non-cubic phase could be identified as either the $L1_0$ Fe-Ni or the HCP Fe-Ni. Synchrotron X-ray diffraction (SXRD) was further used to verify that the laser-ablated nanoparticles contain a substantial amount of HCP Fe-Ni, which is a far-from-equilibrium phase absent in the Fe-Ni phase diagram at 1 atmosphere. The HRTEM images also reveal a high density of planar defects in the nanoparticles, suggesting that the characteristic defect structure of the system is also far-from-equilibrium. Scanning electron transmission electron microscopy with high-angle annular dark field imaging (STEM-HAADF) was further used to reveal the atomic arrangement in vicinity of the planar defects, including twins and stacking faults, as well as the intersections between these planar defects. The significances of the far-from-equilibrium crystal and defect structures revealed by the S/TEM characterizations reported in this work upon the synthesis of $L1_0$ Fe-Ni are discussed in **section 6.4**.

6.2 Experimental Methods and Simulations

6.2.1 Picosecond-pulsed laser ablation in liquids

The near-equiatomic Fe-Ni nanoparticles were prepared by pulsed laser ablation in acetone. A Nd:YAG laser (Ekspla, Atlantic Series) with a pulse duration of 10 ps and a pulse repetition rate of 100 kHz in the research group of Prof. Bilal Gökce at the University of Duisburg-Essen was used. The nanoparticle synthesis were performed by Ruksan Nadarajah with the help of Elisabeth Mühlhausen. The laser wavelength was centered at 1064 nm. The laser power was 8.1 watt, and

the laser fluence was 2.6 J/cm^2. An Fe-Ni foil (Sekels GmbH, Ober-Mörlen, Germany) with a composition of 50 at.% Ni was used as the target. The distance between the target and the lens was set to be 1.1 cm. The Fe-Ni target was ablated twice in 100 mL acetone. After the ablation process, the acetone was let to evaporate until the colloid reached a concentration of 298 mg/L.

6.2.2 Particle size distribution and composition

The size distribution of the nanoparticles was characterized by analytical disc centrifugation (ADC) with the CPS Disc Centrifuge (Model DC24000 UHR) by Ruksan Nadarajah at the University of Duisburg-Essen. The composition of the nanoparticles was characterized by inductively coupled plasma – optical emission spectrometry (ICP-OES) with the CIROS CCD (Spectro Analytical) by Milen Nachev at the University of Duisburg-Essen. The size distribution was corroborated by TEM imaging, and the composition was corroborated by TEM-EDS mapping and line-scanning. These corroborations were all performed with the JEOL 2200FS TEM (200 kV) by Ruksan Nadarajah at the University of Duisburg-Essen.

6.2.3 Transmission electron microscopy (TEM)

6.2.3.1 Experiments

The colloid of Fe-Ni particles in acetone prepared by ps-PLAL was drop-casted onto the copper grids with holey carbon film to enable the TEM studies performed on the TITAN TEM (FEI) with an acceleration voltage of 300 kV. On the TITAN TEM, the methods being used included high-resolution TEM (HRTEM) imaging, selected area diffraction (SAD), bright field (BF) imaging, dark field (DF) imaging, scanning transmission electron microscopy (STEM) imaging,

and nano-beam electron diffraction (NBED). The HRTEM imaging, the SAD, and the BF imaging were performed by Helge Heinrich with the assistance of myself at the University of Virginia. The DF imaging, the STEM imaging, and the NBED were performed by Eric Hoglund with the assistance of myself at the University of Virginia.

6.2.3.2 Simulations

Simulations of the HRTEM images based on the Bloch-wave approach were performed with the Java Electron Microscopy Simulation (JEMS) software [7]. The simulated specimens were 16-nm thick for both $L1_0$ Fe-Ni and HCP Fe-Ni. The thickness value was chosen to be comparable with the thickness of the experimentally observed non-cubic phase. The input parameters for the simulations include the acceleration voltage (E = 300 kV), the spherical aberration coefficient (C_s = 1.2 mm), the fifth-order spherical aberration coefficient (C_5 = 5.0 mm), the half convergence angle (1.0 mrad), the defocus spread (7.0 nm), the energy spread (0.8 eV), the acceptance angle (100.0 mrad), and the objective aperture diameter (40 nm^{-1}). For both $L1_0$ Fe-Ni and HCP Fe-Ni, thickness vs. defocus maps of HRTEM images were calculated and examined across the target specimen thickness (16 nm) from 2-nm to 30-nm thick, and across the Scherzer defocus (− 57 nm) from −150 nm to +50 nm defocus. The simulated cell of the $L1_0$ Fe-Ni structure contained two primitive unit cells stacked along the $[-110]_{L10}$ direction of the conventional cell, which is equivalent to the [100] direction of the primitive cell. The simulated cell of the HCP Fe-Ni structure was an orthogonalized unit cell that contained four atoms. All the presented images contain a 2×3 tile of the simulated image.

6.2.4 Scanning Transmission electron microscopy (STEM)

The colloid of Fe-Ni particles for the STEM studies was drop-casted onto a glider finder copper grid with holey carbon film. HRTEM performed on the TITAN TEM was first used to find and locate a nanoparticle with a diameter of ~ 50 nm or less, with the $[110]_{FCC}$ zone axis of the FCC Fe-Ni of which deviated as little as possible from the optic axis (i.e., with the α and the β tilt within ± 10^{o}). Aided by the glider finder grid as well as the images captured at different magnifications on the TITAN TEM, the same nanoparticle was found on the Themis TEM (Thermo Fisher Scientific). A beam shower treatment specified by a screen current of 11.1 nA and a probe diameter of 7.5 μm was performed around the particle for 10 min in order to mitigate the carbon built-up. High-angle annular dark field (HAADF) imaging was then performed to capture atomic resolution images of the planar defects in the Fe-Ni nanoparticle. The HRTEM imaging was performed by myself at the University of Virginia. The STEM-HAADF imaging was performed by Eric Hoglund with the assistance of myself at the University of Virginia.

6.2.5 Grazing Incidence X-ray Diffraction (GIXRD)

The GIXRD pattern of the nanoparticles was collected by using the PANalytical X'Pert Pro X-ray diffractometer, which has a Cu Kα (λ = 0.154 nm) radiation source. The grazing incidence angle was 0.5^{o}. The GIXRD pattern was collected by Ruksan Nadarajah at the University of Duisburg-Essen.

6.2.6 Synchrotron X-ray Diffraction (SXRD)

The colloid of Fe-Ni nanoparticles in acetone was loaded into a special glass 10 capillary with an outer diameter of 1.0 mm and a wall thickness of 0.01 mm (Hampton Research) with a syringe via a 25G needle (Tiger Medical, Inc.). The loaded capillary was sealed by melted and re-solidified beeswax (Hampton Research). SXRD was performed in the transmission geometry (i.e., the Debye-Scherrer geometry) on the capillary sample at beamline 33-BM-C in the Advanced Photon Source (APS) in Argonne National Laboratory, with an incident beam energy of ~ 16 keV, using the Pilatus 100K detector. The SXRD pattern of a LaB_6 NIST Standard (SRM 660a) was collected in order to extract the accurate incident beam energy (16.015 keV). The capillary SXRD samples were prepared by myself at the University of Virginia and then shipped to the beamline at the APS. The SXRD patterns were collected by Evguenia Karapetrova at the APS.

6.2.7 Magnetic Properties

The magnetometry measurements on the nanoparticles were performed by using the Quantum Design PPMS DynaCool system. The measured magnetic moment was normalized by the mass of the sample. The measurements were performed by Anna Semisalova at the University of Duisburg-Essen.

6.3 Results

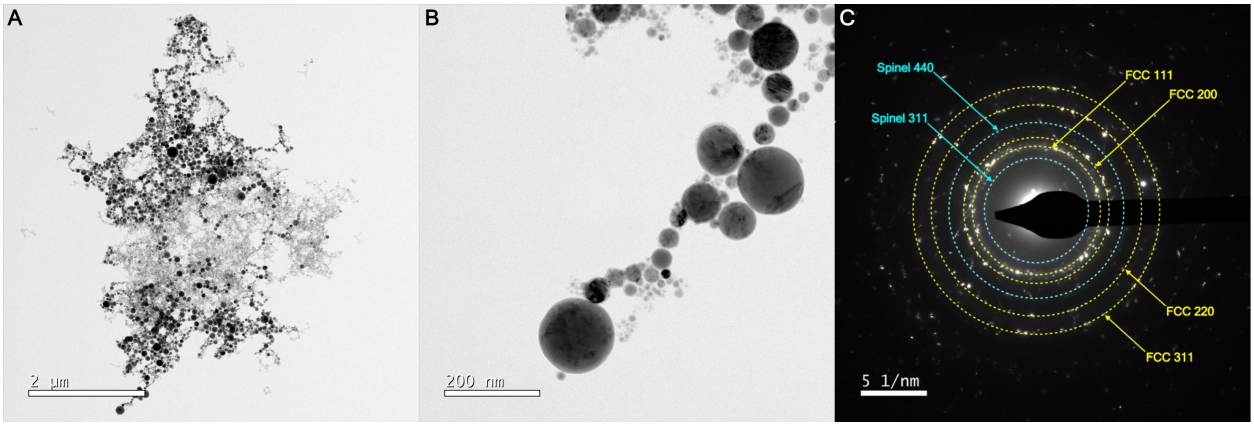

Figure 6.1. Fe-Ni nanoparticles synthesized by ps-PLAL. **(A)** Bright field TEM image of the Fe-Ni nanoparticles. **(B)** Bright field TEM image that shows a chain of nanoparticles. **(C)** Selected area diffraction pattern corresponding to the TEM image in (A).

The size distribution of the Fe-Ni nanoparticles was characterized by ADC, which shows that the nanoparticles have a number-weighted mean hydrodynamic diameter of ~ 24 nm (**Figure A 6.1**). The alloy composition of the Fe-Ni nanoparticles was characterized by ICP-OES and TEM-EDS. Both techniques confirm that the alloy composition was 48 ~ 50 at.%Ni (**Figure A 6.2**). **Figure 6.1** shows the BF TEM images and the SAD pattern of the Fe-Ni nanoparticles prepared by ps-PLAL. The first four reflections of FCC Fe-Ni can all be identified in the SAD pattern. The lattice parameter was extracted to be a = 3.58 Å (**Table A 6.1**). This value is on top of that of the bulk equiatomic FCC-FeNi (a = 3.575 Å) [8], and is consistent with the composition measured by ICP-OES and TEM-EDX (**Figure A 6.2**). In addition to the FCC Fe-Ni rings (yellow dashed lines), **Figure 6.1C** shows two other low-angle rings (blue dashed lines) that are relatively diffuse (also see **Figure A 6.3**). They can be identified as the $(311)_{spinel}$ ring and the $(440)_{spinel}$ ring of spinel FeNi oxide (MgAl2O4-type) [9-11]. The lattice parameter of the spinel Fe-Ni

oxide was extracted from the positions of these two diffuse rings to be a_s = 8.46 Å (**Table A 6.1**). This value is close to the reported value of $Fe_{2.6}Ni_{0.4}O_4$ (a_s = 8.37 Å) [10]. The presence of the $(311)_{spinel}$ reflection makes the detection of any possibly existing $L1_0$ Fe-Ni even more challenging. Based on the lattice parameters extracted from the $L1_0$ Fe-Ni found in meteorites [12], the $(110)_{L10}$ reflection is expected to appear at 3.95 nm^{-1} in the electron diffraction pattern. The $(311)_{spinel}$ ring in **Figure 6.1C** appeared at 3.92 nm^{-1}, a position that is virtually indistinguishable from that of the $(110)_{L10}$ reflection.

Figure 6.2A shows the HRTEM image of a nanoparticle of ~ 32 nm in diameter. A thin shell less than ~ 4 nm thick wrapped around the surface of the nanoparticle, which was identified as the spinel FeNi oxide that contributed to the diffuse rings shown in **Figure 6.1C**. **Figure 6.2B** shows a region of interest within the nanoparticle. The arrowheads in **Figure 6.2B** mark the bright-and-dark contrast. This type of contrast can only result either from a composition modulation that signifies chemical ordering, or from the dynamical interaction between the electron wave and a specimen of moderate thickness. The green square in **Figure 6.2B** marks a region from which the FFT pattern in **Figure 6.2C** was obtained, while the blue square in **Figure 6.2B** marks a region from which the FFT pattern in **Figure 6.2D** was obtained.

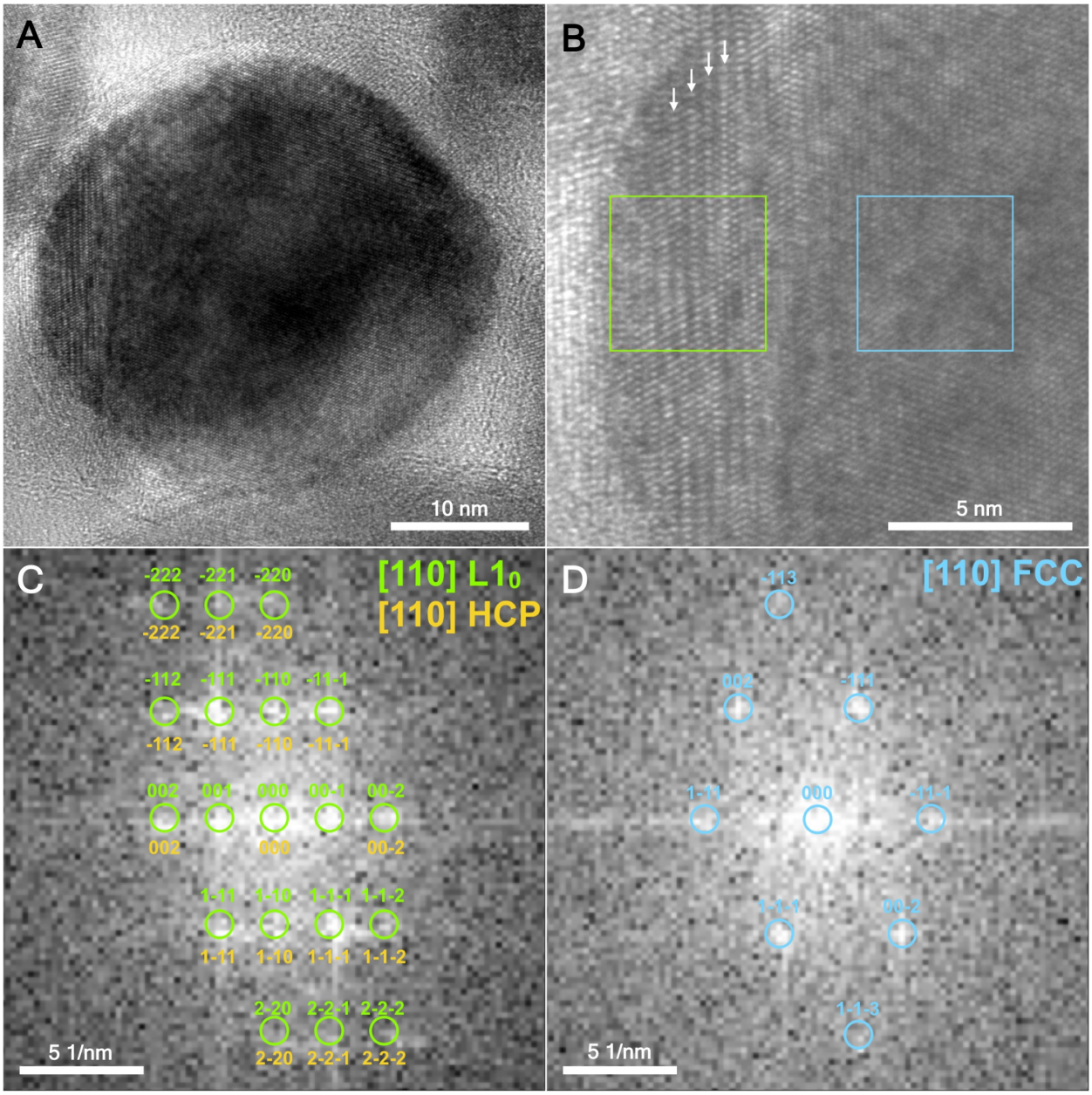

Figure 6.2. High-resolution TEM image of an Fe-Ni nanoparticle. **(A)** Overview of the Fe-Ni nanoparticle. **(B)** A region of interest in (A) including the non-cubic phase around the green (left) square region and the cubic phase around the blue (right) square region. The arrows indicate the bright-and-dark contrast in the image. **(C)** Fast Fourier Transform (FFT) pattern of the green (left) square region in (B). **(D)** FFT pattern of the blue (right) square region in (B).

The FFT pattern in **Figure 6.2C** can be identified as either the $[110]_{L10}$ zone of $L1_0$ Fe-Ni or the $[110]_{HCP}$ zone (i.e., the $[11\text{-}20]_{HCP}$ zone) of HCP Fe-Ni. It is shown by the indices in **Figure 6.2C** that the only feature differentiating the $[110]_{L10}$ zone from the $[110]_{HCP}$ zone is the presence of the $(001)_{L10}$ spots. However, double diffraction can occur in the HCP structure and give rise to the $(001)_{HCP}$ spots [13], rendering the patterns of the two zones virtually indistinguishable. Although **Figure 6.2C** also resembles the $[110]_{BCC}$ zone of BCC Fe-Ni, assuming the structure to be BCC Fe-Ni leads to an unrealistically large lattice parameter of $a_{BCC} \sim 5.19$ Å, too far away from the lattice parameter of BCC Fe-Ni ($a_{BCC} = 2.861 \sim 2.870$ nm) [14]. Notice that unlike HCP Fe-Ni, which has a two-atom basis, FCC Fe-Ni, BCC Fe-Ni, and BCT Fe-Ni are all crystal structures with a single-atom basis, and thus cannot give rise to any forbidden reflections through double diffraction. The possibility that **Figure 6.2C** can be identified as the $[111]_{spinel}$ zone was also ruled out based on the discrepancy in the lattice parameter. Therefore, the FFT pattern in **Figure 6.2C**, whether it was identified as the $[110]_{L10}$ zone or the $[110]_{HCP}$ zone, evidenced an unambiguous absence of the cubic symmetry.

On the other hand, the FFT pattern in **Figure 6.2D** shows a $[110]_{FCC}$ zone of FCC Fe-Ni. It is evidenced by the FFT patterns (**Figure 6.2C and D**) that the $[1\text{-}11]_{FCC}$ direction of the FCC Fe-Ni phase was parallel to the unique axis of the non-cubic phase (i.e., either $[001]_{L10}$ or $[001]_{HCP}$). The orientation relationship across the interphase interface was then determined from the two FFT patterns to be either $(1\text{-}11)_{FCC}[110]_{FCC} \parallel (001)_{L10}[110]_{L10}$ if the non-cubic phase was $L1_0$ Fe-Ni, or $(1\text{-}11)_{FCC}[110]_{FCC} \parallel (001)_{HCP}[110]_{HCP}$ if the non-cubic phase was HCP Fe-Ni.

The lattice parameter of the FCC Fe-Ni phase was extracted from **Figure 6.2D** to be a = 3.61 Å (**Table A 6.2**). Assuming that the non-cubic phase was $L1_0$ Fe-Ni, the lattice parameters extracted from **Figure 6.2C** were a' = 3.14 Å and c' = 4.36 Å with c'/a' = 1.391 (**Table A 6.2**). These values deviate considerably from the lattice parameters of $L1_0$ Fe-Ni in bulk, which are a'_{bulk} = 3.58 Å and c'_{bulk} = 3.59 Å (c'_{bulk}/a'_{bulk} = 1.003) [12]. The relative deviations are calculated to be:

$$\varepsilon_a = (a' - a'_{bulk}) / a'_{bulk} = -12.3\% \quad \text{e.q. 6.1}$$

$$\varepsilon_c = (c' - c'_{bulk}) / c'_{bulk} = +21.4\% \quad \text{e.q. 6.2}$$

Interestingly, these relative deviations are close to the typical Bain strains of a BCT martensite with respect to a BCC martensite, which are −12% along the $[100]_{BCT}$ direction and +20% along the $[001]_{BCT}$ direction [15]. Alternatively, assuming that the non-cubic phase was HCP Fe-Ni, the lattice parameters extracted from **Figure 6.2C** were a_h = 2.56 Å and c_h = 4.36 Å with c_h/a_h = 1.703 (**Table A 6.2**). These values are close to those of the HCP Fe-Ni (31 at.%Ni) that emerged during the reverse martensitic transformation reported by Kabanova et al., which were a_h = 2.535 Å and c_h = 4.132 Å with c_h/a_h = 1.630 [14, 16].

Figure 6.3 shows another nanoparticle with a similar two-phase microstructure. Once again, the non-cubic phase in **Figure 6.3** can only be either $L1_0$ Fe-Ni or HCP Fe-Ni, and the orientation relationship between the non-cubic phase and the adjacent cubic phase was the same as the one in **Figure 6.2**.

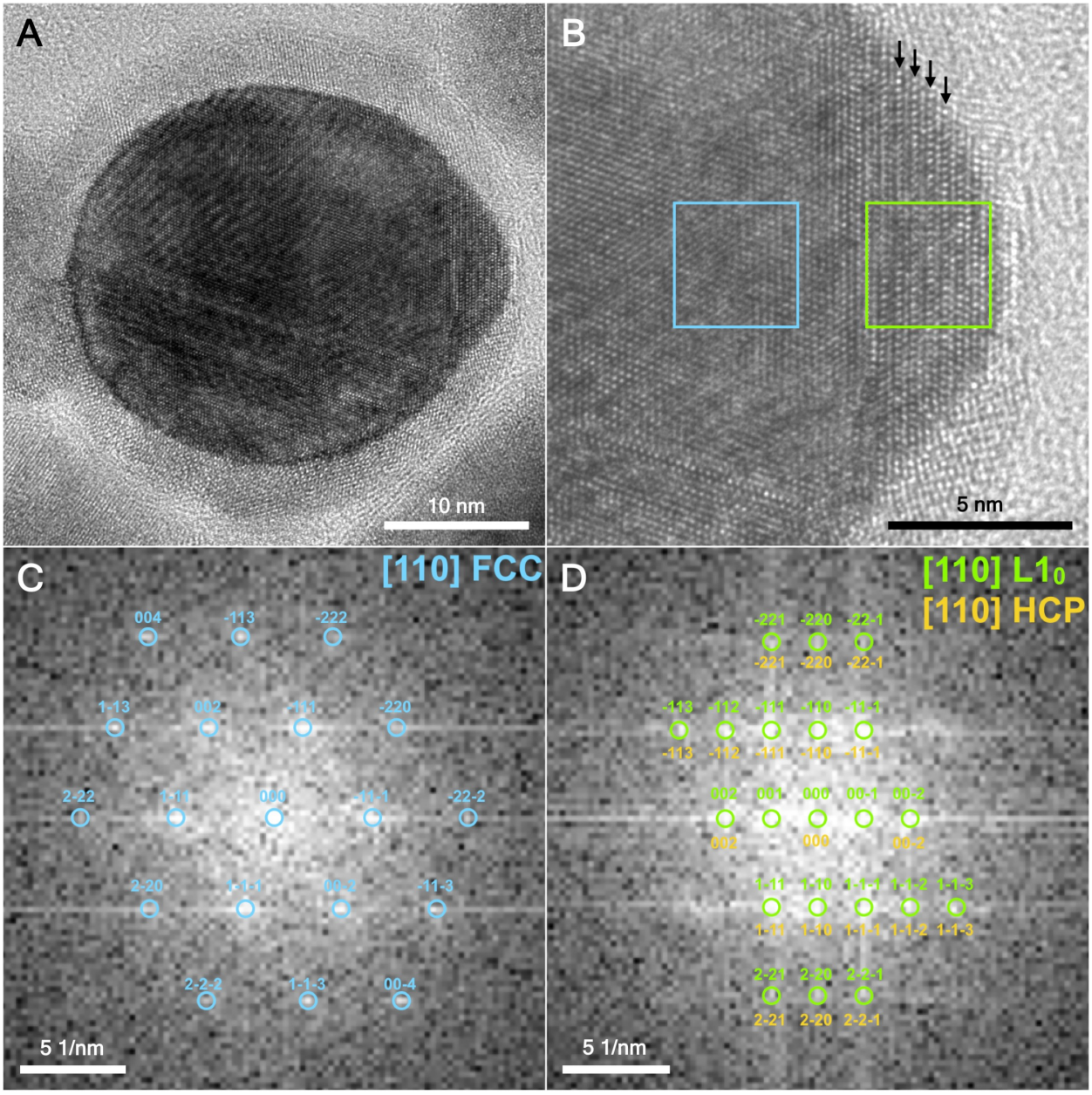

Figure 6.3. High-resolution TEM image of an Fe-Ni nanoparticle **(A)** Overview of the Fe-Ni nanoparticle. **(B)** A region of interest in (A) including the cubic phase around the blue (left) square region and the non-cubic phase around the green (right) square region. The arrows indicate the bright-and-dark contrast in the image. **(C)** Fast Fourier Transform (FFT) pattern of the blue (left) square region in (B). **(D)** FFT pattern of the green square (right) region in (B).

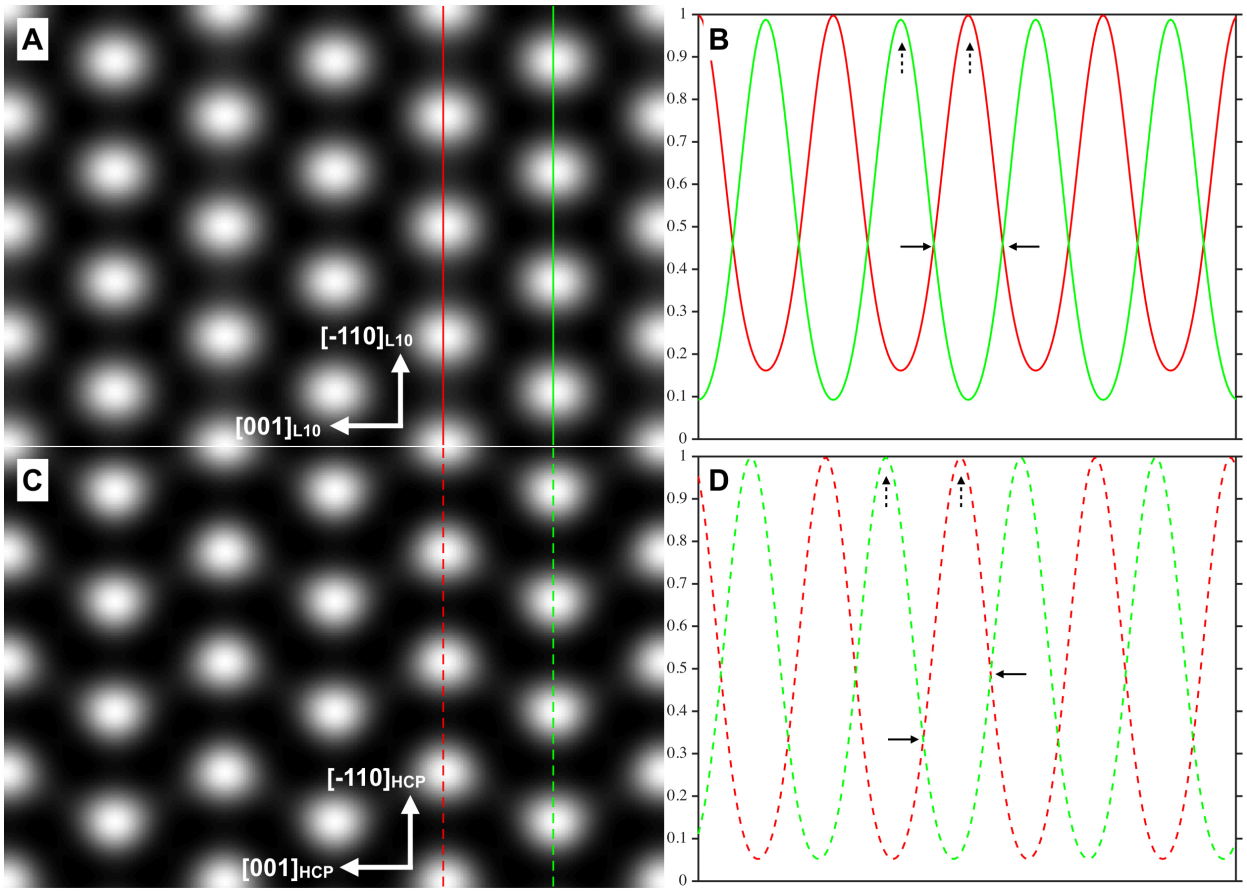

Figure 6.4. Simulated HRTEM images without beam tilt. **(A)** $L1_0$ Fe-Ni viewed along the $[110]_{L10}$ zone axis with the direction of the 4-fold rotation axis (i.e., $[001]_{L10}$) aligned horizontally. The thickness of the simulated specimen was 16 nm. **(B)** Line profiles of the intensities along two rows of atomic columns denoted by the red solid line (left) and the green solid line (right) in (A). The red solid line and the green solid line went across the Fe monoatomic layer and the Ni monoatomic layer, respectively. **(C)** HCP Fe-Ni viewed along the $[110]_{HCP}$ zone axis with the direction of the 6-fold rotation axis (i.e., $[001]_{HCP}$) aligned horizontally. The thickness of the simulated specimen was 16 nm. **(D)** Line profiles of the intensities along two rows of atomic columns denoted by the red dashed line (left) and the green dashed (right) line in (C).

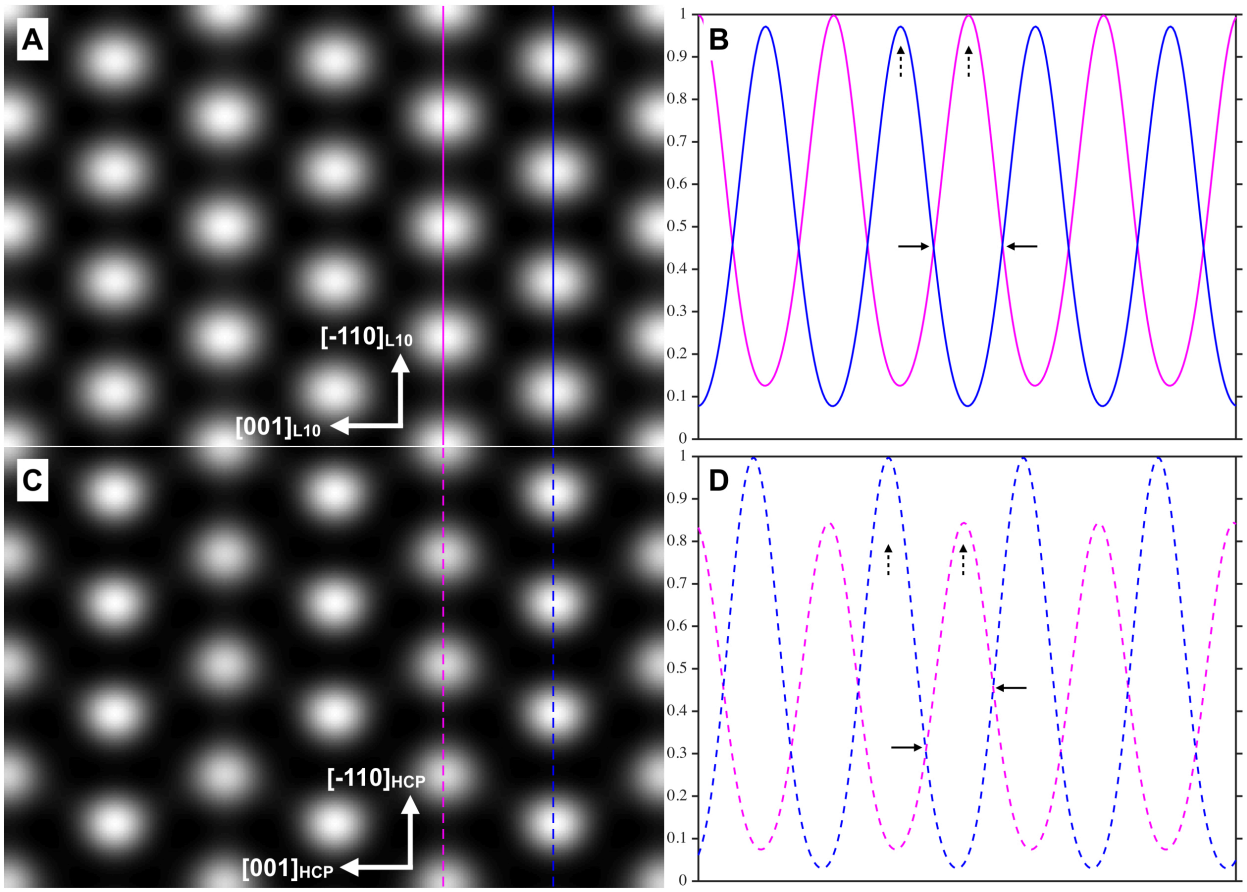

Figure 6.5. Simulated HRTEM images with beam tilt. **(A)** $L1_0$ Fe-Ni viewed along the $[110]_{L10}$ zone axis with the direction of the 4-fold rotation axis (i.e., $[001]_{L10}$) aligned horizontally. The simulation was performed with a 1.05 mrad beam tilt inclined towards the $[-110]_{L10}$ direction (i.e., beam tilt ~ 0.25 $2\theta_{-110}$). The thickness of the simulated specimen was 16 nm. **(B)** Line profiles of the intensities along two rows of atomic columns denoted by the purple solid line (left) and the blue solid line (right) in (A). The purple solid line and the blue solid line went across the Fe monoatomic layer and the Ni monoatomic layer, respectively. **(C)** HCP Fe-Ni viewed along the $[110]_{HCP}$ zone axis with the direction of the 6-fold rotation axis (i.e., $[001]_{HCP}$) aligned horizontally. The simulation was performed with a 1.05 mrad beam tilt inclined towards the $[-110]_{HCP}$ direction (i.e., beam tilt ~ 0.25 $2\theta_{-110}$). The thickness of the simulated specimen was 16 nm. **(D)** Line profiles of the intensities along two rows of atomic columns denoted by the purple dashed line (left) and the blue dashed line (right) in (C).

The simulated HRTEM images are presented in **Figure 6.4** and **Figure 6.5** to provide more insights for the interpretation of the experimental ones. **Figure 6.4A and C** show the simulated images of $L1_0$ Fe-Ni viewed along the $[110]_{L10}$ direction and HCP Fe-Ni viewed along the $[110]_{HCP}$ direction, respectively. The atomic arrangements shown in the two simulated images both agree well with those experimentally observed in the non-cubic phase (**Figure 6.2B** and **Figure 6.3B**). However, **Figure 6.4A** does show a subtle but non-vanishing bright-and-dark contrast along the $[001]_{L10}$ direction, which results from the chemical ordering of the structure. Corresponding to **Figure 6.4A**, the line profiles in **Figure 6.4B** show the intensities across a row of slightly brighter atomic columns (red solid line) and a row of slightly darker atomic columns (green solid line). The dashed arrows in **Figure 6.4B** point to the apexes of the peaks, showing the subtle but non-vanishing bright-and-dark contrast. The solid arrows point to the crossovers between the two profiles. The crossovers are on the same height, which indicates the presence of a mirror plane along the $[-110]_{L10}$ direction. As for the simulated image of HCP Fe-Ni shown in **Figure 6.4C**, the bright-and-dark contrast is completely absent, which can be verified by examining the apexes pointed by the dashed arrows in **Figure 6.4D**. The crossovers pointed by the solid arrows are not on the same height, indicating the absence of a mirror plane along the $[-110]_{HCP}$ direction. Overall, **Figure 6.4** demonstrates how the two crystal structures, i.e., $L1_0$ Fe-Ni and HCP Fe-Ni, can result in HRTEM images that are very similar to each other.

Figure 6.5A and C show another pair of simulated HRTEM images of the two structures. The simulations here were performed with a 1.05 mrad beam tilt along the vertical direction, i.e., $[-110]_{L10}$ in $L1_0$ Fe-Ni or $[-110]_{HCP}$ in HCP Fe-Ni. In comparison to **Figure 6.4B and D**, the line

profiles in **Figure 6.5B and D** show the dramatic effects of the beam tilt: (1) the bright-and-dark contrast in the simulated image of $L1_0$ Fe-Ni intensified; (2) as for the simulated image of HCP Fe-Ni, an artificial bright-and-dark contrast, completely absent in **Figure 6.4D**, shows up in **Figure 6.5D**. The mirror plane along the vertical direction remains present and absent in the $L1_0$ Fe-Ni and the HCP Fe-Ni structure, respectively. **Figure 6.5**, in short, demonstrates that the dynamical effects of electron scattering can give rise to an artificial bright-and-dark contrast without smearing out the apparent atomic resolution. Therefore, both $L1_0$ Fe-Ni and HCP Fe-Ni are valid interpretations of the non-cubic phase found in the HRTEM images (**Figure 6.2** and **Figure 6.3**).

The orientation relationship between the cubic phase and the non-cubic phase was corroborated in a third nanoparticle with a different set of TEM techniques. SAD and BF/DF imaging were first used to identify a nanoparticle of interest. **Figure 6.6A** shows the SAD pattern of a group of nanoparticles. The solid circle and the dashed circle in **Figure 6.6A** indicate two objective aperture positions (OA-1 and OA-2). The position indicated by the solid circle (OA-1) selects diffraction spot “A” only, while the position indicated by the dashed circle (OA-2) selects both spot “A” and spot “B”. The corresponding BF/DF TEM images are shown in **Figure 6.6B-D**. **Figure 6.6B** is the BF image with the objective aperture centered at the zero beam (OA-0). **Figure 6.6C** is the DF image with the objective aperture located at the position of the solid circle (OA-1), brightening those crystallites that contributed to the intensity of spot “A” in the SAD pattern. **Figure 6.6D** is another DF image with the objective aperture located at the position of the dashed circle (OA-2), brightening those crystallites that contributed to the intensities of both

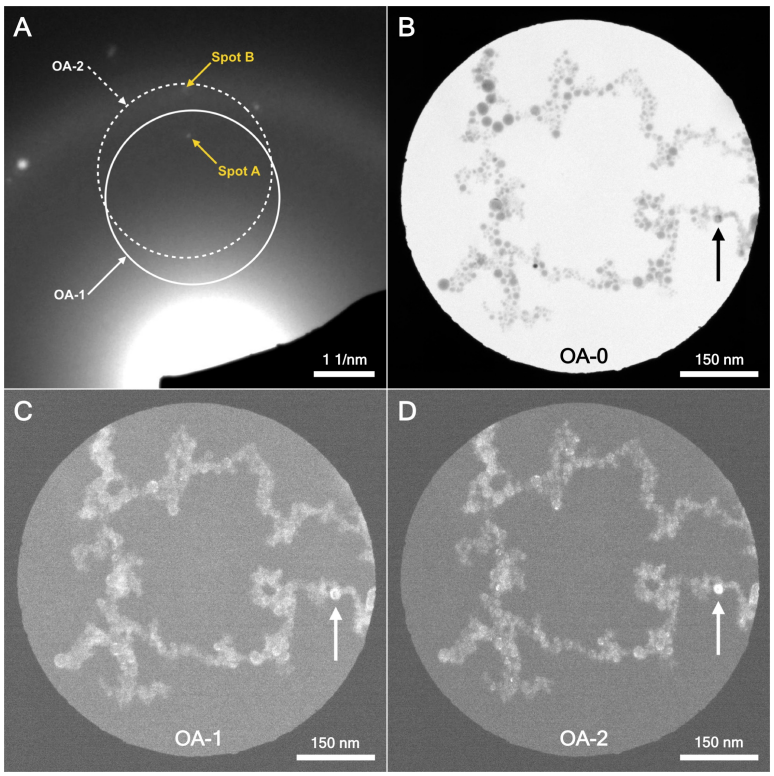

Figure 6.6. Mix-phase Fe-Ni nanoparticle identified by bright-field (BF) and dark-field (DF) TEM images. **(A)** SAD pattern of a group of Fe-Ni nanoparticles. The solid circle and the dashed circle indicate two objective aperture positions, OA-1 and OA-2, respectively. OA-1 includes spot A only, while OA-2 includes both spot A and spot B. **(B)** BF image with the objective aperture centered at the zero beam (OA-0). **(C)** DF image with the objective aperture at OA-1. **(D)** DF image with the objective aperture at OA-2. The arrows in (B-D) point to the same particle identified as the mix-phase Fe-Ni nanoparticle.

spot "A" and spot "B". As shown in **Figure 6.6B-D**, the particle indicated by an arrow turned from dark in the BF image to bright in the DF images. This indicates that both spot "A" and spot "B" originated from the same particle, and that the particle is the one indicated by the arrows in **Figure 6.6B-D**. Diffraction spot "B" was further identified to be the $(1\text{-}11)_{FCC}$ spot of FCC Fe-

Ni. Diffraction spot "A" was identified to be either the $(002)_{L10}$ spot of $L1_0$ Fe-Ni or the $(002)_{HCP}$ spot of HCP Fe-Ni (**Table A 6.4**). The particle indicated by the arrows in **Figure 6.6B-D** was thus a third particle shown in this work that consisted of both the cubic phase and the non-cubic phase. Notice that spot "A" and spot "B" in **Figure 6.6A** are located along the same radial direction, which indicates that the (002) plane of the non-cubic phase and the (1-11) plane of the cubic phase were parallel to each other. This observation is consistent with the orientation relationship extracted from the HRTEM images in **Figure 6.2** and **Figure 6.3**.

Figure 6.7 shows the scanning transmission electron microscope (STEM) image of the nanoparticle of interest indicated by the arrows in **Figure 6.6B-D**, which had been identified as the particle that gave rise to the two diffraction spots (i.e., spot "A" and spot "B") in **Figure 6.6A**. This nanoparticle has a diameter of ~ 20 nm. NBED patterns were collected from five different sites (i.e., site 1 to 5 in **Figure 6.7A**) on this particle in order to corroborate the orientation relationship between the cubic phase and the non-cubic phase. Based on the orientation relationship extracted from **Figure 6.2** and **Figure 6.3**, a schematic of the NBED pattern viewed along the [110] common zone axis was shown in **Figure 6.7**. The NBED patterns collected from the five sites on the nanoparticle are shown in **Figure 6.7C-G** (also see **Figure A 6.4**). They closely resemble the pattern highlighted by the red frame in **Figure 6.7B**. Specifically, **Figure 6.7C and D** both show the (001) disc and the (003) disc. They can only arise either from $L1_0$ Fe-Ni as a result of chemical ordering, or from HCP Fe-Ni when double diffraction was present. **Figure 6.7D-G** all show the $(002)_{L10|HCP}$ disc and the $(1\text{-}11)_{FCC}$ disc. Their positions in the NBED patterns match up with the positions of spot "A" and spot "B" in the SAD pattern

(**Figure 6.6A**). This confirms our previous statement that both spot "A" and spot "B" originated from this nanoparticle of interest. The observations presented in **Figure 6.6** and **Figure 6.7** demonstrate two points: (1) the nanoparticle of interest contained both the FCC Fe-Ni phase and the non-cubic phase that could be either $L1_0$ Fe-Ni or HCP Fe-Ni; (2) the (002) plane of the non-cubic phase and the (1-11) plane of the FCC Fe-Ni phase are parallel to each other. Both are consistent with the microstructures presented by the HRTEM images in **Figure 6.2 and 6.3**.

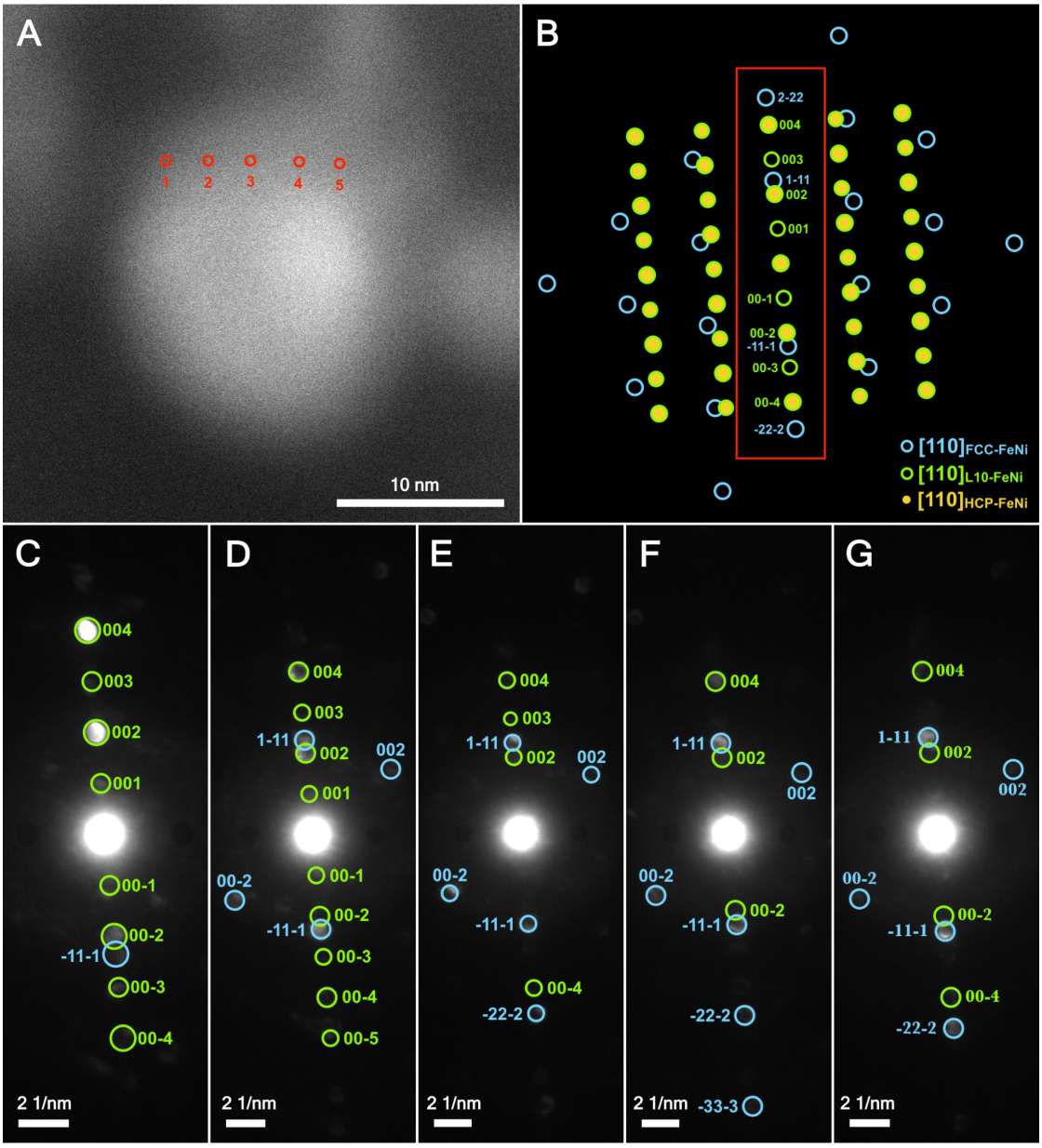

Figure 6.7. Nano-beam electron diffraction (NBED) patterns that show the orientation relationship between the cubic phase and the non-cubic phase in an Fe-Ni nanoparticle. **(A)** STEM image of the Fe-Ni nanoparticle from which the NBED patterns in (C-G) were collected. **(B)** Schematic of the $[110]_{FCC\text{-}FeNi}$, the $[110]_{L10\text{-}FeNi}$, and the $[110]_{HCP\text{-}FeNi}$ zone being overlapped. **(C-G)** NBED patterns collected from site 1 to 5 on the nanoparticle in (A).

The GIXRD pattern of the nanoparticles (**Figure A 6.5**) provides a further evidence for the existence of the non-cubic Fe-Ni phase. Apart from the main peaks at 43.5° and 50.5°, which were identified as the $(111)_{FCC}$ and the $(200)_{FCC}$ reflection of the FCC Fe-Ni phase, three other peaks at 39.5°, 42.8°, and 44.9° were decomposed from the diffraction pattern by the individual profile fitting method. These peaks were identified as the Bragg reflections of the non-cubic Fe-Ni phase. Assuming these peaks to be the $(110)_{L10}$, the $(002)_{L10}$, and the $(111)_{L10}$ reflection of the $L1_0$ FeNi phase, the lattice parameters of the $L1_0$ FeNi phase were calculated to be a' = 3.23 Å and c' = 4.22 Å with c'/a' = 1.307. Assuming these peaks to be the $(100)_{HCP}$, the $(002)_{HCP}$, and the $(101)_{HCP}$ reflection of the HCP Fe-Ni phase, the corresponding lattice parameters were calculated to be a_h = 2.64 Å and c_h = 4.22 Å with c_h/a_h = 1.601. These two sets of lattice parameters were comparable to those values extracted from the FFT patterns in **Figure 6.2C and 6.3D** (also see Table **A 6.2** and Table **A 6.3**). The lattice parameter of the FCC Fe-Ni phase was calculated to be a = 3.60 Å, close to the values extracted from the SAD pattern in **Figure 6.1C** and from the FFT patterns in **Figure 6.2D and Figure 6.3C**. The broad peak at 35.3° was identified as the $(311)_{spinel}$ reflection of the spinel Fe-Ni oxide, and the corresponding lattice parameter was calculated to be a_s = 8.43 Å, close to the value extracted from the SAD pattern in **Figure 6.1C**.

A much higher resolution diffraction pattern was provided with SXRD. **Figure 6.8** shows two SXRD patterns collected from two different positions (1 and 2) on the same capillary sample loaded with the colloid of Fe-Ni nanoparticles in acetone from ps-PLAL. The two patterns were collected to demonstrate the sample homogeneity. The HCP Fe-Ni phase was clearly identified

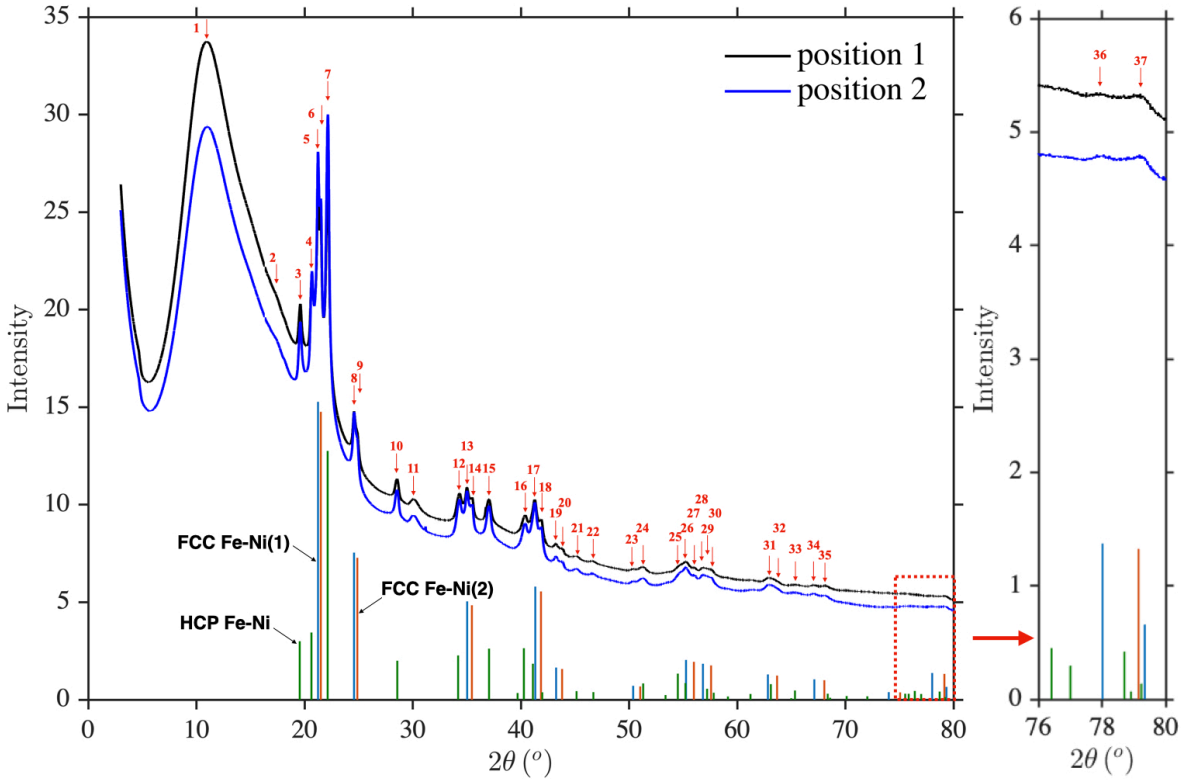

Figure 6.8. Synchrotron X-ray Diffraction (SXRD) patterns of the colloid of Fe-Ni nanoparticles in acetone prepared by ps-PLAL. Green lines: the calculated SXRD pattern of HCP Fe-Ni. Blue lines: the calculated SXRD pattern of FCC Fe-Ni(1). Red lines: the calculated SXRD pattern of FCC Fe-Ni(2).

(see peak 3, 4, 7, 10, 12, 15, 16, 21, 22, 25, 29, 33). The lattice parameters were extracted to be a_h = 2.63 Å and c_h = 4.31 Å, with c_h/a_h = 1.639. What was not revealed in the GIXRD pattern was the coexistence of two FCC Fe-Ni phases of a slightly different lattice parameter — $a_{(1)}$ = 3.64 Å and $a_{(2)}$ = 3.59 Å. Such a phase composition — 1 HCP Fe-Ni phase + 2 FCC Fe-Ni phases — was found in the SXRD patterns of another colloid sample prepared under similar ps-PLAL conditions (see **Figure A 6.6**). The physical origin of such a re-occurring phase composition, however, is not clear. Besides the Fe-Ni phases, the SXRD patterns in **Figure 6.8** also show the spinel Fe-Ni oxide peaks (see peak 2 and 11).

To investigate the possible existence of $L1_0$ Fe-Ni in the nanoparticles, magnetic hysteresis loops of the nanoparticles were collected in the temperature range between 10 K and 300 K (**Figure A 6.7**). The specific saturation magnetization reached 58 ± 2 A·m^2/kg at 300 K and increased up to 67 ± 2 A·m^2/kg at 10 K. Assuming a density of 8.275 × 10^3 kg/m^3, the saturation magnetization was 4.80 × 10^5 A/m (= 480 emu/cm^3) at 300 K and 5.54 × 10^5 A/m (= 554 emu/cm^3) at 10 K. The 300 K saturation magnetization was considerably smaller than that of either $L1_0$ Fe-Ni or FCC Fe-Ni (i.e., on the order of 1.17 × 10^6 A/m = 1170 emu/cm^3, see **section 1.1** in **chapter 1**). It is not clear if such a reduction in the magnetization is due to the HCP Fe-Ni phase, the spinel Fe-Ni oxide phase, or both of them. The coercivity gradually changed from 3.8 ± 0.1 mT (3.0 kA/m = 0.038 kOe) at 300 K to 21.8 ± 0.3 mT (17.3 kA/m = 0.218 kOe) at 10 K. The 300 K coercivity is less than the anisotropy field of FCC Fe-Ni (H_k ~ 5 kA/m = 0.063 kOe) (see **section 5.1** in **chapter 5**). The magnetic characterization therefore did not indicate the existence of $L1_0$ Fe-Ni.

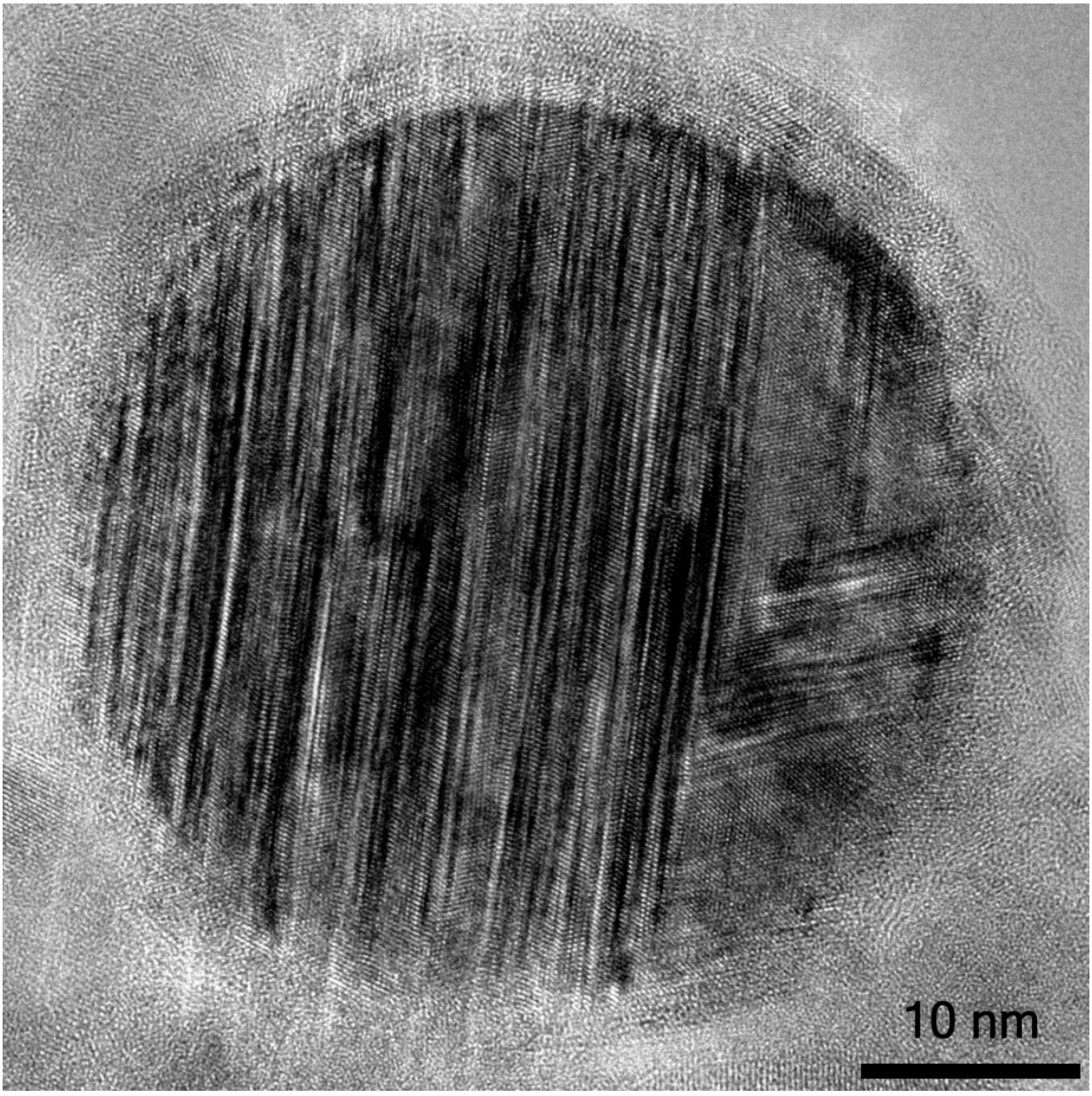

Figure 6.9. HRTEM image of an Fe-Ni nanoparticle (~ 43 nm in diameter) showing 2 sets of planar defects. Figure 6.9, 6.10, and 6.11 were collected from the same particle.

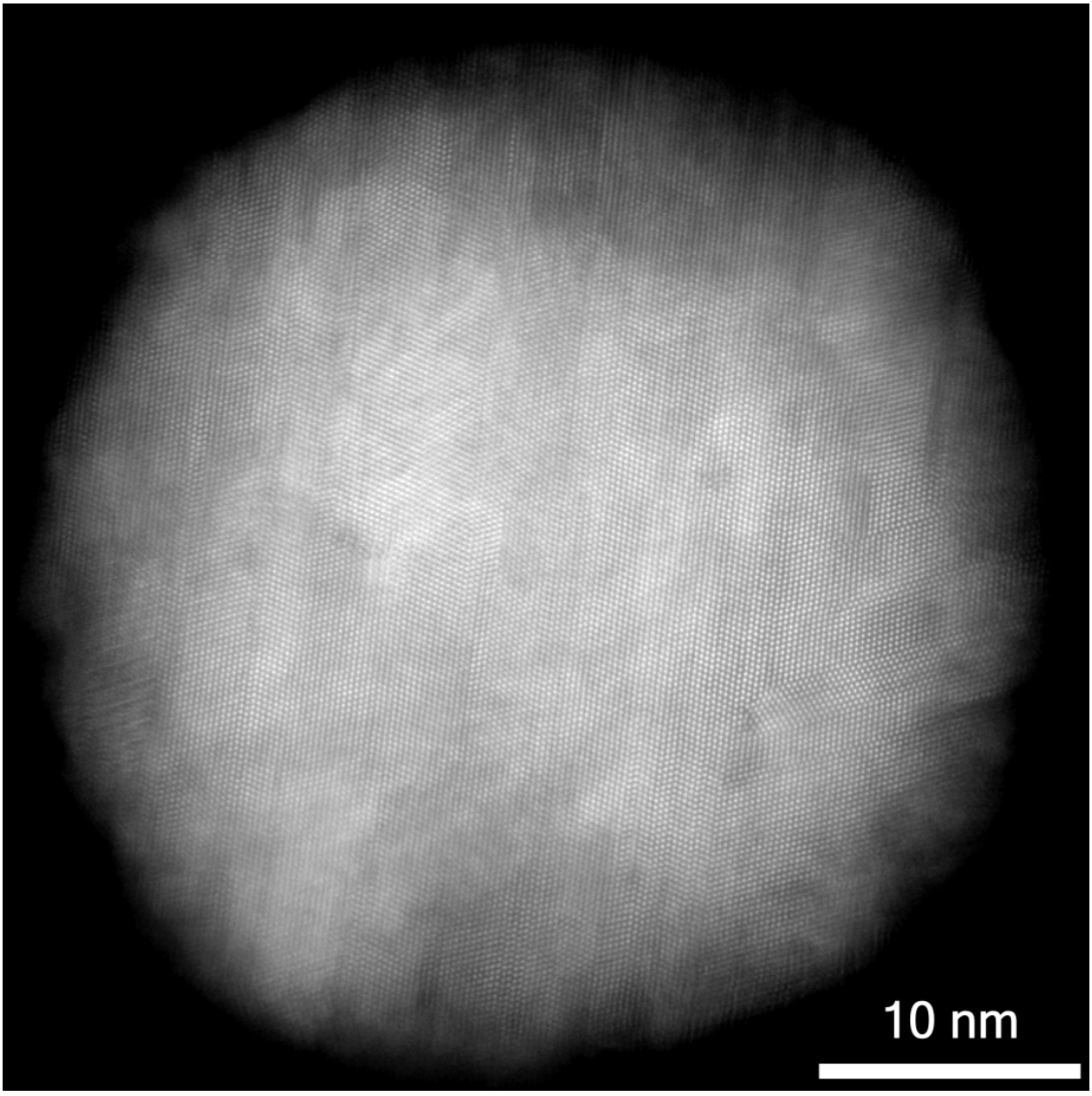

Figure 6.10. STEM-HAADF image of an Fe-Ni nanoparticle (~ 43 nm in diameter) showing 2 sets of planar defects. Figure 6.9, 6.10, and 6.11 were collected from the same particle.

Figure 6.11. STEM-HAADF image showing the intersection between 2 sets of planar defects. Figure 6.9, 6.10, and 6.11 were collected from the same particle.

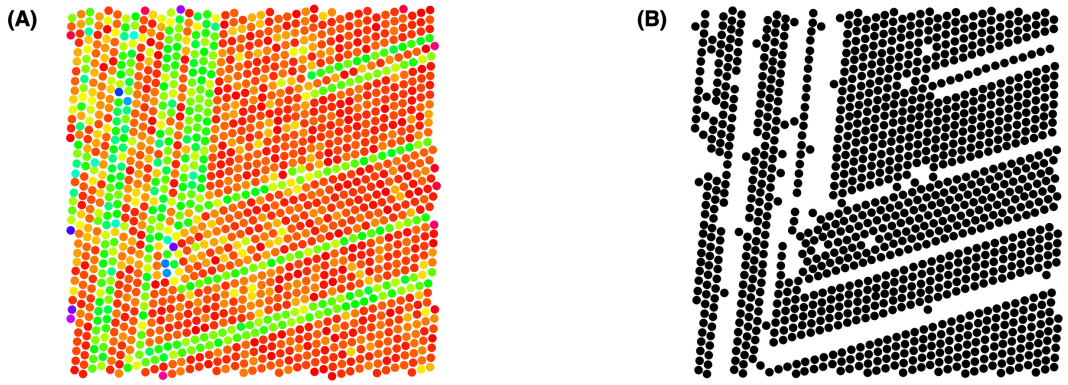

Figure 6.12. (A) Length square map extracted from the region around the intersection between 2 sets of planar defects in Figure 6.11. **(B)** Figure 6.12A with atoms with a length square ≥ 20 pixel^2 being excluded (1 pixel = 0.0057718 nm). The field of view is 1600 pixel × 1600 pixel (~ 10 nm × 10 nm) in both (A) and (B). There are 1570 atoms (1570 atomic columns) in the field of view.

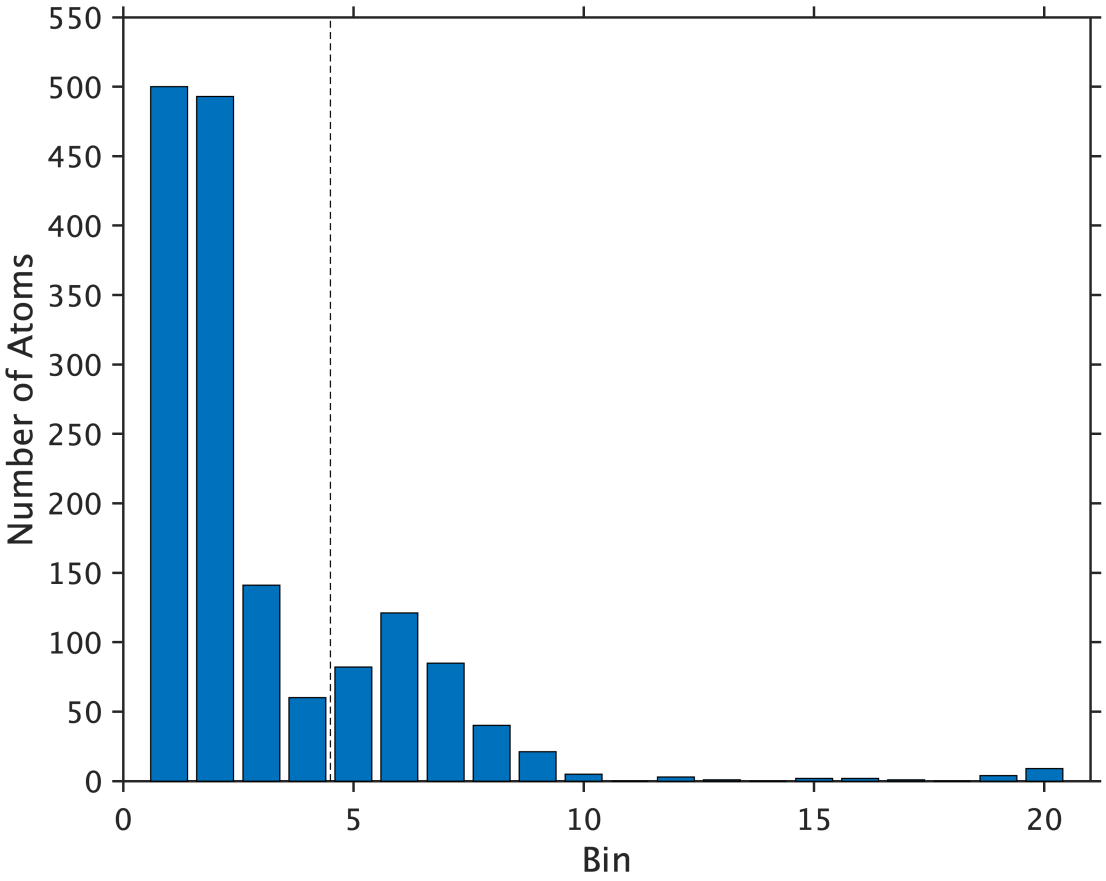

Figure 6.13. Distribution of atoms of different length squares. The i^{th} bin ($i < 20$) defines a length square window of $5(i\text{-}1) \leq$ length square $< 5i$. The last bin ($i = 20$) defines a length square window of $5(i\text{-}1) \leq$ length square $\leq 5i$. Among the 1570 atoms shown in Figure 6.12, there are 376 atoms with a length square larger than or equal to the threshold of 20 pixel^2, there are 1194 atoms with a length square smaller than the threshold of 20 pixel^2.

Figure 6.9 and 6.10 show the HRTEM and the STEM-HAADF image of the same nanoparticle (~ 43 nm in diameter) which had two sets of planar defects. The first set extended nominally from the surface on top to the surface at the bottom. The second set started from the surface on the right but terminated inside the particle at or near the intersection against the first set. **Figure 6.11** shows a higher magnification image of the intersection between the two sets of planar defects, where the local atomic configuration deviates the most from the perfect crystal. The 2D positions of 1716 atoms, atomic columns more rigorously speaking, around the intersection were extracted from the STEM-HAADF image by a program using the tools in the HyperSpy [17] library and the Atomap [18] library. The field of view occupied by the atoms is ~ 10 nm × 10 nm (~ 1600 pixel × 1600 pixel, where 1 pixel = 0.0057718 nm). For each of the 1716 atoms, the length square of the vector sum of the 6 nearest-neighbor vectors was calculated. If the 6 nearest neighbors of an atom are symmetrical about the atom, the length square assigned to the atom equals to zero. The length square defined as such was used as an indicator to gauge the local symmetry of each atom. A length square threshold of 100 pixel^2 excluded the atoms at the boundary of the field of view. **Figure 6.12A** shows the length square map, which clearly highlights the atoms on the planar defects. Quantitatively, a length square threshold of 20 pixel^2 further excluded the atoms on the planar defects (**Figure 6.12B and Figure 6.13**). With respect to this threshold, ~ 24% of the atoms are on a planar defect (appearing green in **Figure 6.12A**) while ~ 76% of the atoms (appearing red in **Figure 6.12A**) are not. The planar defect density estimated in this way can be directly compared to the theoretical defect density obtained by molecular dynamic (MD) simulations. Therefore, the effort here in quantifying the planar defect

density by STEM-HAADF represents the first step in connecting the theoretical prediction and the experimental observation of the atomic arrangements in Fe-Ni nanoparticles from ps-PLAL.

6.4 Discussion

Although not disproven, the hypothesis of the non-cubic phase observed in the HRTEM images (**Figure 6.2 and 6.3**) being $L1_0$ Fe-Ni can be challenged by the following arguments: (1) the lattice parameters extracted from **Figure 6.2 and 6.3** deviate significantly from the bulk values extracted from the meteorites [12]; (2) the orientation relationship, i.e., $(1\text{-}11)_{FCC}[110]_{FCC} \parallel (001)_{L10}[110]_{L10}$, has not been observed before; (3) the $L1_0$-type chemical ordering is in general considered to require a long diffusional process over a cosmic timescale [19]. On the contrary, the hypothesis of the non-cubic phase being HCP Fe-Ni can be supported by the following: (1) the lattice parameters extracted from **Figure 6.2 and 6.3** are close to the reported values [14, 16]; (2) the orientation relationship — $(1\text{-}11)_{FCC}[110]_{FCC} \parallel (001)_{HCP}[110]_{HCP}$ — is more common, e.g., this orientation relationship was found in Co-32 at.%Ni across the interface between the HCP phase and the FCC phase, where the HCP phase was formed through thermally induced martensitic transformation; (3) the SXRD patterns verify the existence of HCP Fe-Ni in the nanoparticles.

Based on the microstructures shown in **Figure 6.2 and 6.3**, it is reasonable to further speculate that the formation of the aforementioned non-cubic phase involves a martensitic transformation process. Our investigation also revealed that a relatively high density of planar defects (i.e., twins and/or stacking faults) can be found in some of the nanoparticles, which can be recognized from

the lower left region of the nanoparticle shown in **Figure 6.3A** and from the nanoparticle in **Figure 6.9**. G. B. Olson *et al.* presented a formalism that described the FCC-to-HCP martensitic transformation as a nucleation and growth process. Within their formalism, a stacking fault was generalized as a HCP martensite embryo in the size of two atomic planes [22]. The formalism was used by L. M. Guerrero *et al.* to describe the FCC-to-HCP martensitic transformation in Fe-Mn-Cr steels and yielded a critical size (4 ~ 6 atomic planes) consistent with their experimental observations [23]. However, unlike Cr- or Mn-containing steels, the HCP phase of the Fe-Ni system in bulk can only be stabilized by high pressures on the order of at least 10 GPa [24]. I. G. Kabanova *et al.* detected the formation of HCP-FeNi in the BCC Fe-31at.%Ni martensite during a reverse martensitic transformation process [14, 16]. Y. Liang *et al.* reported the detection of HCP Fe-Ni in the nanoparticles synthesized by nanosecond-pulsed laser ablation in liquids (ns-PLAL) [25]. The composition of the particles was not quantified, and their HRTEM studies did not reveal the coexistence of different Fe-Ni phases within the same particle. In direct contrast to the Co-Ni system, the formation of HCP FeNi during thermally induced martensitic transformation has not been detected in FCC Fe-Ni with a Ni fraction larger than 30 at.%Ni. As for the defect structure, FCC-FeNi alloys with a Ni fraction larger than ~ 30 at.%Ni have a significantly higher stacking fault energy (> ~ 100 mJ/m^2) [26] in comparison to those of the Cr- or Mn-containing steels (< ~ 50 mJ/m^2) [23, 27, 28]. All these considerations suggest that the microstructures being observed in the nanoparticles shown in **Figure 6.2, 6.3, and 6.9** involve configurations that are far-from-equilibrium.

Furthermore, the grain boundary diffusivity measured by K. Barmak *et al.* suggested that the ordering towards $L1_0$ Fe-Ni was limited by driving force instead of diffusivity in FCC Fe-Ni with an ultra-fine grain size of ~ 10 nm [29, 30]. The synthesis of nanoscale $L1_0$ Fe-Ni nitride from FCC Fe-Ni nitride by S. Goto et al. and Y. Sakanaka et al. also suggested that diffusion below T_{od} can be activated under a larger driving force [31, 32]. The far-from-equilibrium microstructures reported in this work may therefore hold significance for the direct synthesis of $L1_0$ FeNi, in the sense that they may provide a larger thermodynamic driving force for the ordering transformation than the ones that are fault-free or consisting of the cubic phases only.

6.5 Conclusions

We report the nanoscale structural investigation of near-equiatomic FeNi nanoparticles synthesized by picosecond-pulsed laser ablation in liquids. A non-cubic Fe-Ni phase was revealed by HRTEM images in the nanoparticles synthesized by this method. The crystal structure of the non-cubic phase could only be $L1_0$ Fe-Ni or HCP Fe-Ni. In either case, the absence of cubic symmetry was unequivocal. The same orientation relationship between the non-cubic phase and the adjacent cubic phase was detected in different nanoparticles and corroborated by different TEM techniques. The orientation relationship was identified to be either $(1\text{-}11)_{FCC}[110]_{FCC} \parallel (001)_{L10}\ [110]_{L10}$ if the non-cubic phase was $L1_0$ Fe-Ni, or $(1\text{-}11)_{FCC}[110]_{FCC} \parallel (001)_{HCP}\ [110]_{HCP}$ if the non-cubic phase was HCP Fe-Ni. The existence of HCP Fe-Ni was further verified by GIXRD and SXRD, but the existence of $L1_0$ Fe-Ni was not. Within a ~ 10 nm × 10 nm field of view in a nanoparticle with ~ 43 nm in diameter that

contained a high density of planar defects, it was estimated that the planar defects were accounted for by ~ 24% of all the atoms within the field of view.

Appendix A 6.1 Size Distribution

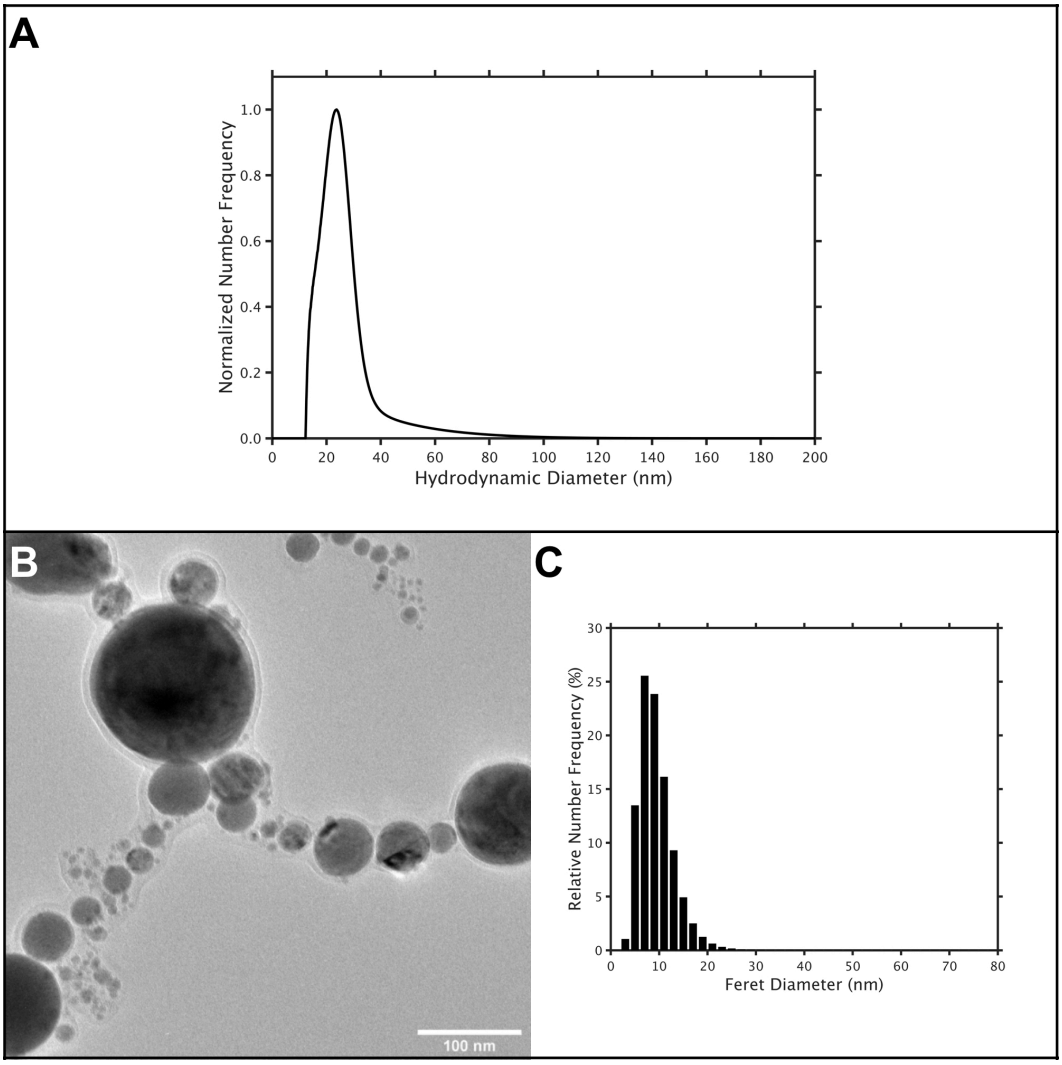

Figure A 6.1. Hydrodynamic/Feret diameter distribution of the Fe-Ni nanoparticles. (**A**) Number frequency distribution obtained by analytical disc centrifugation. All data were normalized by the maximum value. (**B**) TEM image from which the size distribution was corroborated. (**C**) Number frequency distribution extracted from the TEM image in (B).

Appendix A 6.2 Composition

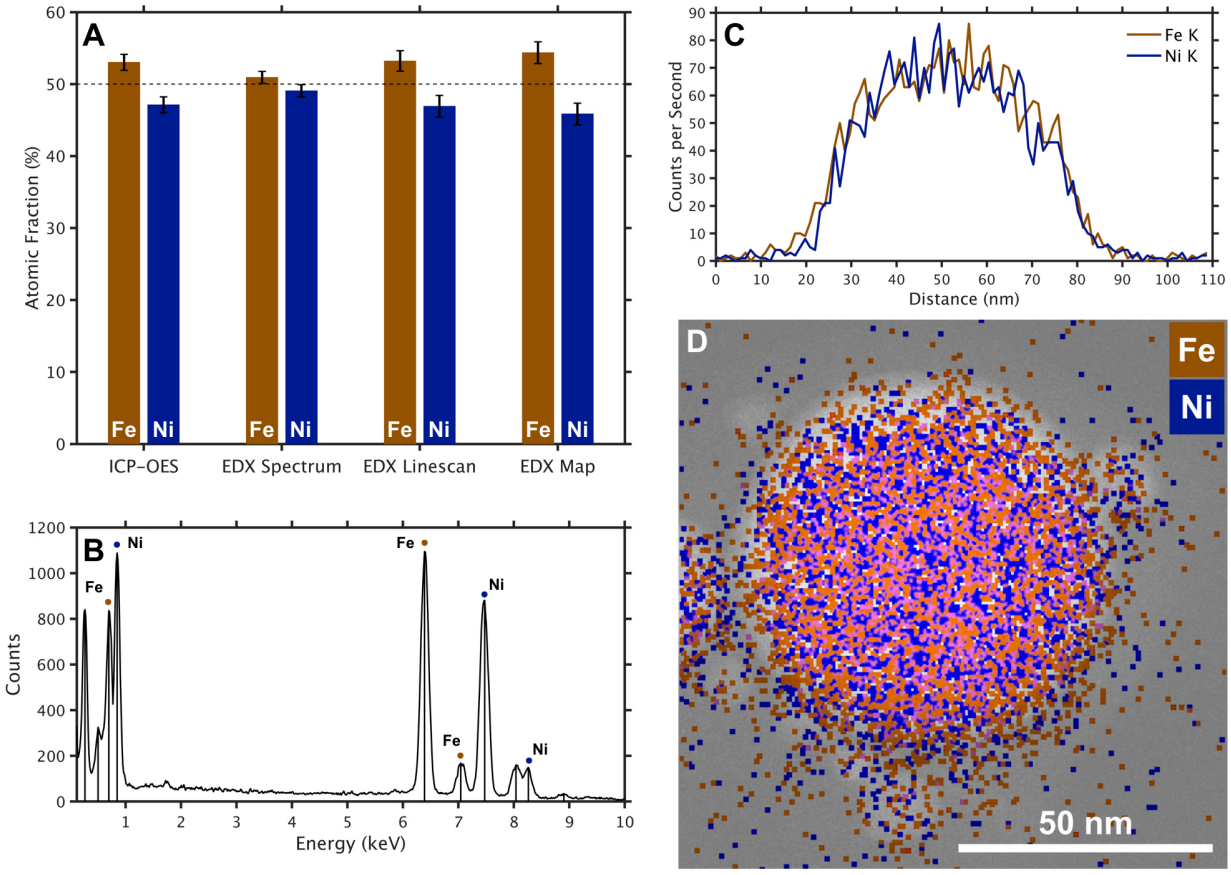

Figure A 6.2. Composition of the Fe-Ni nanoparticles. (A) Alloy composition values obtained by ICP-OES and TEM-EDX (spectrum acquisition / line scanning / mapping). (**B**) TEM-EDX spectrum. (**C**) TEM-EDX line scan profile. (**D**) TEM-EDX map.

Appendix A 6.3 Selected Area Diffraction

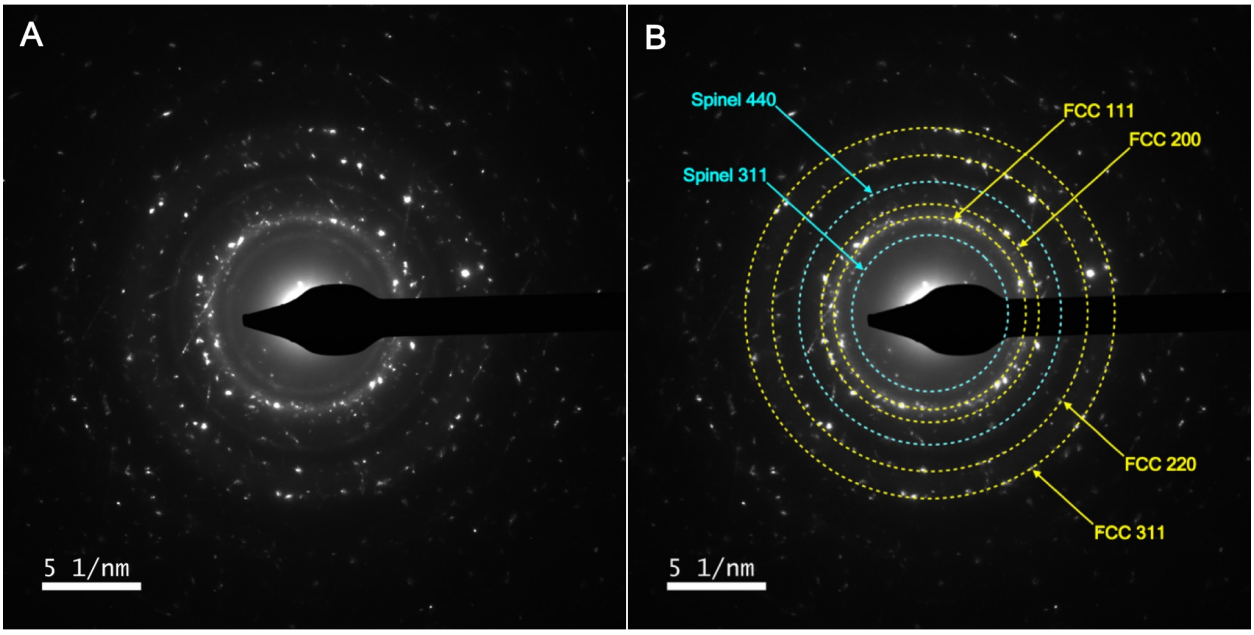

Figure A 6.3. Selected area diffraction (SAD) pattern. (**A**) The labels and indices were excluded for a clearer presentation of the features. (**B**) The same SAD pattern with labels and indices included.

Appendix A 6.4 Nano-Beam Electron Diffraction

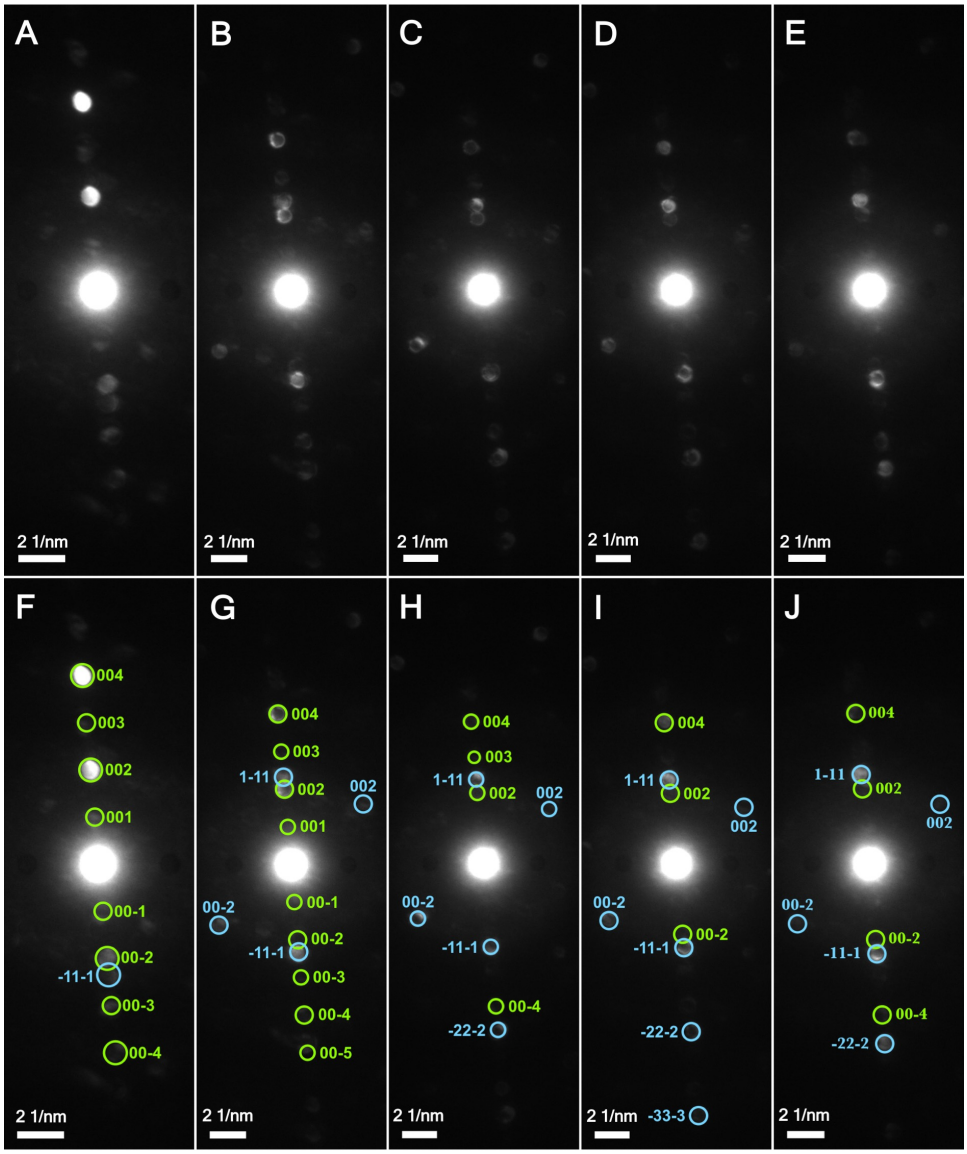

Figure A 6.4. Nano-beam electron diffraction (NBED) patterns. (**A-E**) The labels and indices were excluded for a clearer presentation of the features. (**F-J**) The same set of NBED patterns with labels and indices included.

Appendix A 6.5 Grazing Incidence X-ray Diffraction

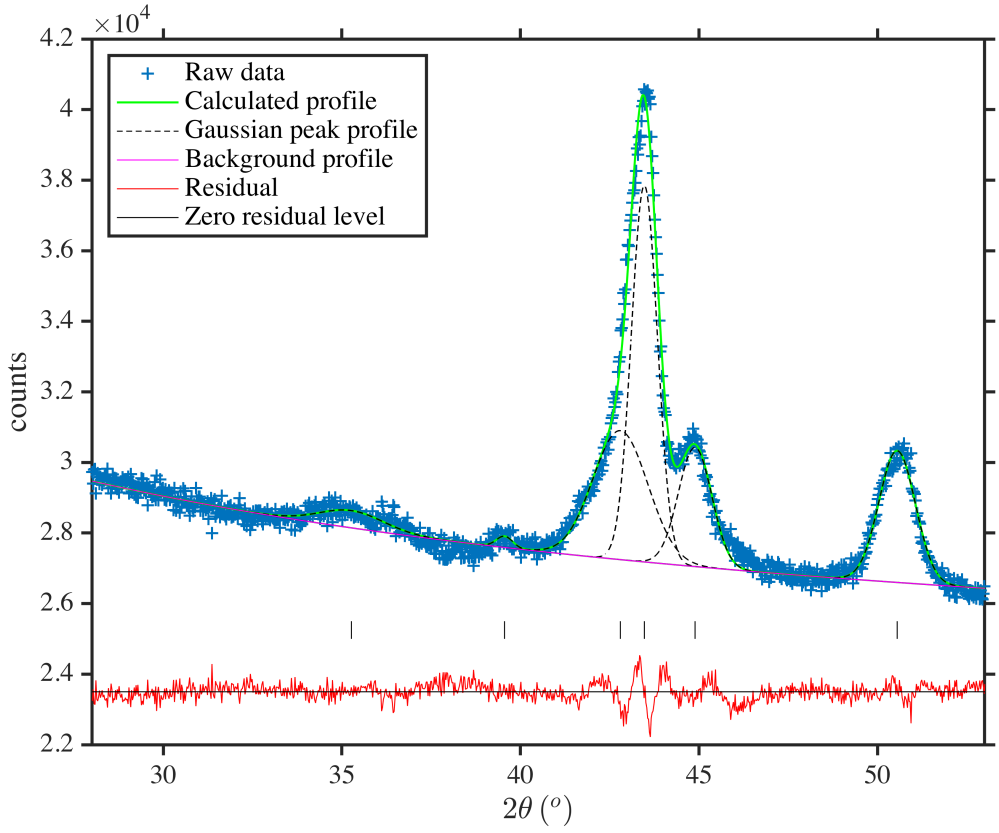

Figure A 6.5. Grazing incidence X-ray diffraction (GIXRD) pattern of the Fe-Ni nanoparticles. The blue crosses show the raw data. The green solid curve shows the calculated profile extracted with the individual profile fitting method, which is a superposition of the Gaussian peak profiles and the background profile. The black dashed curves show the Gaussian peak profiles. The magenta solid curve shows the background profile. The vertical bars show the center positions of the Gaussian peak profiles. The red solid curve shows the residual resulted from the difference between the raw data and the calculated profile. The horizontal line shows the level of zero residual. Both the residual and the zero residual level were lifted in order to cut the empty space on the graph.

Appendix A 6.6 Synchrotron X-ray Diffraction

The SXRD patterns were collected by Evguenia Karapetrova at the APS. The capillary samples for the SXRD measurements were prepared by myself at the University of Virginia and then shipped to the beamline at the APS. The nanoparticle synthesis was performed by Inna Yusnila Khairani in the research group of Prof. Bilal Gökce at the University of Wuppertal.

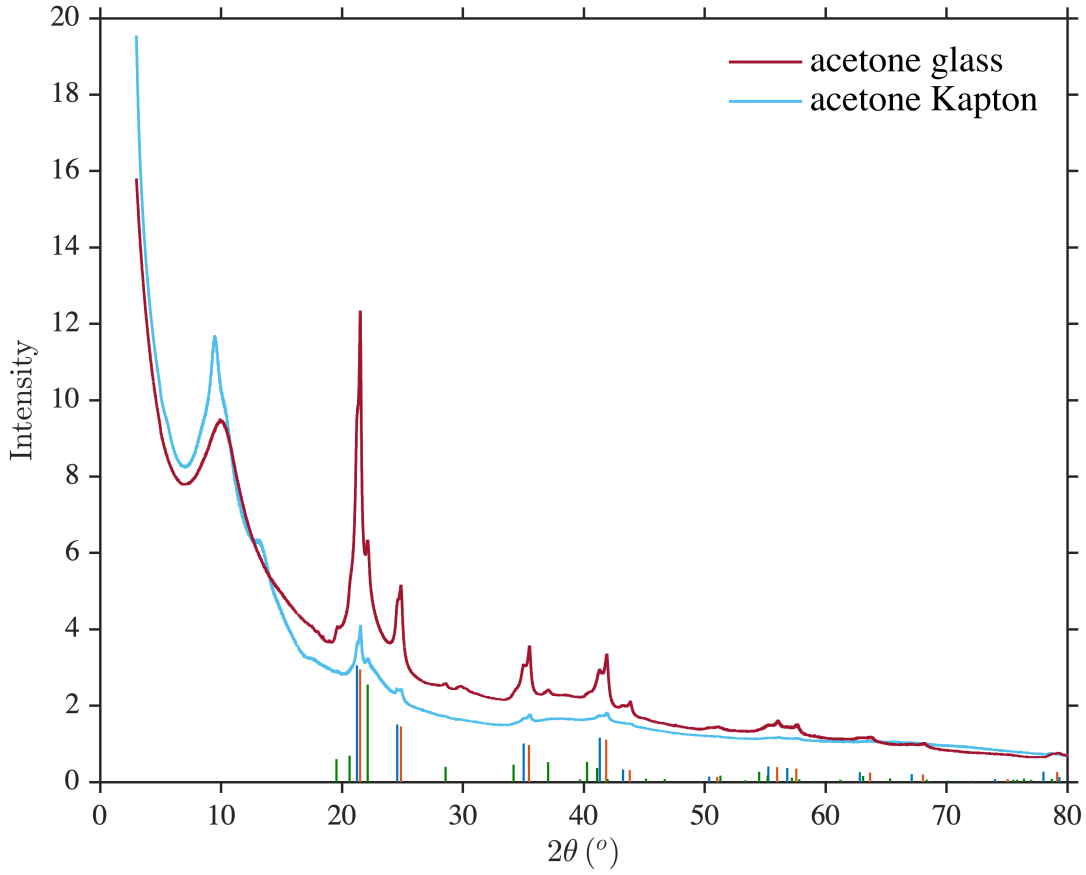

Figure A 6.6. Synchrotron X-ray Diffraction (SXRD) patterns of the colloid of Fe-Ni nanoparticles in acetone prepared by ps-PLAL. Green lines: the calculated SXRD pattern of HCP Fe-Ni. Blue lines: the calculated SXRD pattern of FCC Fe-Ni(1). Red lines: the calculated SXRD pattern of FCC Fe-Ni(2).

Appendix A 6.7 Magnetic Hysteresis

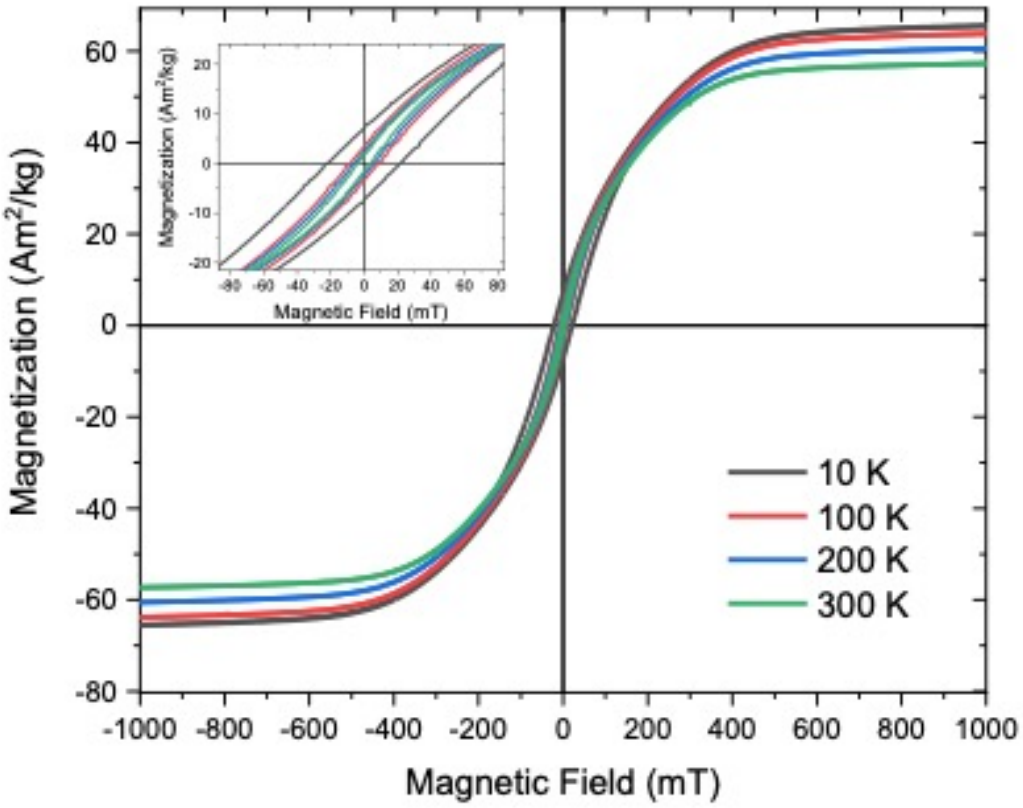

Figure A 6.7. Magnetic characterization of the Fe-Ni nanoparticles. The hysteresis loops were recorded at the temperatures of 10 K (black), 100 K (red), 200 K (blue) and 300 K (green). Inset shows a magnified low-field region.

Appendix A 6.8 Lattice Parameters

Table A 6.1. D-spacings of the phases measured from Figure 6.1C and the corresponding lattice parameter(s) extracted from the d-spacings by the non-linear least squares (NLS) method.

Phase	Miller Index	D-spacing / nm
FCC-FeNi	111	0.2083
	200	0.1808
	220	0.1262
	311	0.1079
	***a* / nm**	**0.358**
Spinel FeNi Oxide	311	0.2485
	440	0.1500
	a_s / nm	**0.846**

Table A 6.2. D-spacings of the phases measured from Figure 6.2C and D and the corresponding lattice parameter(s) extracted from the d-spacings by the non-linear least squares (NLS) method.

Phase	Miller Index	D-spacing / nm
FCC-FeNi	-11-1	0.1986
	-111	0.1934
	002	0.1808
	-113	0.1100
	***a* / nm**	**0.361**
$L1_0$-FeNi	001	0.4494
	-110	0.2309
	-111	0.1984
	-11-1	0.1984
	002	0.2309
	-112	0.1635
	-220	0.1139
	-221	0.1080
	-222	0.0958
	***a′* / nm**	**0.314**
	***c′* / nm**	**0.436**
HCP-FeNi	001	0.4494
	-110	0.2309
	-111	0.1984
	-11-1	0.1984
	002	0.2309
	-112	0.1635
	-220	0.1139
	-221	0.1080
	-222	0.0958
	a_h / nm	**0.256**
	c_h / nm	**0.436**

Table A 6.3. D-spacings of the phases measured from Figure 6.3C and D and the corresponding lattice parameter(s) extracted from the d-spacings by the non-linear least squares (NLS) method.

Phase	Miller Index	D-spacing / nm
FCC-FeNi	1-11	0.2130
	-111	0.2123
	002	0.1791
	-220	0.1245
	-113	0.1058
	1-13	0.1074
	2-22	0.1034
	-222	0.1048
	004	0.0896
	***a* / nm**	**0.358**
$L1_0$-FeNi	001	0.4684
	-110	0.2345
	-111	0.1940
	-11-1	0.2119
	002	0.2198
	-112	0.1589
	-220	0.1134
	-221	0.1098
	-22-1	0.1093
	-113	0.1208
	***a′* / nm**	**0.321**
	***c′* / nm**	**0.432**
HCP-FeNi	001	0.4684
	-110	0.2345
	-111	0.1940
	-11-1	0.2119
	002	0.2198
	-112	0.1589

-220	0.1134
-221	0.1098
-22-1	0.1093
-113	0.1208
a_h / nm	**0.262**
c_h / nm	**0.432**

Table A 6.4. Lattice parameters extracted from spot "A" and spot "B" in Figure 6.6A.

Miller Index	Lattice Parameter / nm	
Spot A: $(002)_{L10}$ or $(002)_{HCP}$	$c_{L10\text{-}FeNi} = c_{HCP\text{-}FeNi}$	0.486
Spot B: $(1\text{-}11)_{FCC}$	$a_{FCC\text{-}FeNi}$	0.353

References

[1] K. B. Reuter, D. B. Williams, J. I. Goldstein, Determination of the Fe-Ni phase diagram below 400°C. *Metallurgical Transactions A* **20**, 719-725 (1989).

[2] A.M. Montes-Arango, L.G. Marshall, A.D. Fortes, N.C. Bordeaux, S. Langridge, K. Barmak, L.H. Lewis, Discovery of process-induced tetragonality in equiatomic ferromagnetic FeNi. *Acta Materialia* **116**, 263-269 (2016).

[3] N. Maât, I. McDonald, R. Barua, B. Lejeune, X. Zhang, G. M. Stephen, A. Fisher, D. Heiman, I. V. Soldatov, R. Schäfer, L. H. Lewis, Creating, probing and confirming tetragonality in bulk FeNi alloys. *Acta Materialia* **196**, 776-789 (2020).

[4] Maogang Gong, Shenqiang Ren, Phase Transformation-Driven Surface Reconstruction of FeNi Nanostructures. *Chemistry of Materials* **27**, 7795-7800 (2015).

[5] Dongshi Zhang, Bilal Gökce, Stephan Barcikowski, Laser synthesis and processing of colloids: fundamentals and applications, *Chem. Rev.* **117**, 3390-4103 (2017).

[6] Stephan Barcikowski, Thomas Baranowski, Yigit Durmus, Ulf Wiedwald, Bilal Gökce, Solid solution magnetic FeNi nanostrand-polymer composites by connecting-coarsening assembly. *J. Mater. Chem. C* **3**, 10699-10704 (2015).

[7] E. I. Suvorova, P. A. Stadelmann, P.-A. Buffat, HRTEM Simulation in determination of thickness and grain misorientation for hydroxyapatite crystals, *Kristallografiya* **49**, 407-417 (2004).

[8] V. D. Dobroeol'skii, S. M. Karal'nik, A. V. Koval', X-ray spectroscopic study of some alloys in relation with deviations from the additivity rule. *Metallofizika (Akademiya Nauk Ukrainskoi SSR, Institut Metallofiziki)* **41**, 73-77 (1972).

[9] M. C. Blesa, U. Amador, E. Morán, N. Menéndez, J. D. Tornero, J. Rodríguez-Carvajal, Synthesis and characterization of nickel and magnesium ferrites obtained from alpha-$NaFeO_2$. *Solid State Ionics* **63-65**, 429-436 (1993).

[10] Katsuhiro Tsukimura, Satoshi Sasaki, Noboru Kimizuka, Cation distributions in nickel ferrites. *Jpn. J. Appl. Phys.* **36**, 3609-3612 (1997).

[11] M. C. Blesa, E. Morán, U. Amador, N. H. Andersen, Crystal and Magnetic Structures of a Nickel-rich Ferrite obtained by ionic exchange from alpha-$NaFeO_2$. *Journal of Solid State Chemistry* **129**, 123-129 (1997).

[12] Khanam, S., Zakaria, A., Ahsan, M., Datta, T., Aktar, S., Liba, S., Hossain, S., Das, A., Kamal, I., Yunus, S., Saha, D., Eriksson, S., Study of the crystallographic and magnetic structure in the nickel substituted cobalt ferrites by neutron diffraction. *Materials Sciences and Applications* **6**, 332-342 (2015).

[13] J. F. Albertsen, Tetragonal lattice of tetrataenite (ordered Fe-Ni, 50 - 50) from 4 meteorites. *Physica Scripta* **23**, 301-306 (1981).

[14] Brent Fultz, James M. Howe, "Electron Diffraction and Crystallography" in *Transmission Electron Microscopy and Diffractometry of Materials* (Springer, ed. 3, 2007), pp. 302-303.

[15] I. G. Kabanova, V. V. Sagaradze, N. V. Kataeva, V. E. Danil'chenko, Detection of the ε phase and the Headley-Brooks orientation relationships upon α-γ transformation in the Fe-32% Ni alloy. *The Physics of Metals and Metallography* **112**, 381-388 (2011).

[16] H. K. D. H. Bhadeshia, C. M. Wayman, “Phase Transformations: Nondiffusive” in *Physical Metallurgy* (Elsevier, 2014), pp. 1021-1071.

[17] V. V. Sagaradze, N. V. Kataeva, I. G. Kabanova, V. A. Zavalishin, A. I. Valiullin, M. F. Klyukina, Structural mechanism of reverse alpha-gamma transformation and strengthening of Fe-Ni Alloys. *The Physics of Metals and Metallography* **115**, 661-671 (2014).

[18] Francisco de la Peña, Eric Prestat, Vidar Tonaas Fauske, Pierre Burdet, Jonas Lähnemann, Tom Furnival, Petras Jokubauskas, Magnus Nord, Tomas Ostasevicius, Katherine E. MacArthur, Duncan N. Johnstone, Mike Sarahan, Thomas Aarholt, Joshua Taillon, pquinn-dls, Vadim Migunov, Alberto Eljarrat, Jan Caron, Timothy Poon, … DENSmerijn. (2021). hyperspy/ hyperspy: Release v1.6.5 (v1.6.5). Zenodo.

[19] Nord, M., Vullum, P.E., MacLaren, I. *et al.* Atomap: a new software tool for the automated analysis of atomic resolution images using two-dimensional Gaussian fitting. *Adv Struct Chem Imag* **3,** 9 (2017).

[20] N. Bordeaux, A. M. Montes-Arango, J. Liu, K. Barmak, L. H. Lewis, Thermodynamic and kinetic parameters of the chemical order-disorder transformation in $L1_0$ FeNi (tetrataenite). *Acta Materialia* **103**, 608-615 (2016).

[21] D. W. Bray, J. M. Howe, High-resolution transmission electron microscopy investigation of the face-centered cubic/hexagonal close-packed martensite transformation in Co-31.8 wt pct Ni alloy: Part 1. Plate interfaces and growth ledges. *Metallurgical and Materials Transactions A* **12**, 3362-3370 (1996).

[22] D. W. Bray, J. M. Howe, High-resolution transmission electron microscopy investigation of the face-centered cubic/hexagonal close-packed martensite transformation in Co-31.8 wt pct Ni

alloy: Part 2. Plate intersections, extended defects, and nucleation mechanisms. *Metallurgical and Materials Transactions A* **27**, 3371-3380 (1996).

[23] G. B. Olson, Morris Cohen, A general mechanism of martensitic nucleation: Part I. General concepts and the FCC-HCP transformation. *Metallurgical Transactions A* **7**, 1897-1904 (1976).

[24] L. M. Guerrero, P. La Roca, F. Malamud, A. Baruj, M. Sade, Experimental determination of the driving force of the fcc-hcp martensitic transformation and the stacking fault energy in high Mn Fe-Mn-Cr steels. *Journal of Alloys and Compounds* **797**, 237-245 (2019).

[25] Tetsuya Komabayashi, Kei Hirose, Yasuo Ohishi, In situ X-ray diffraction measurements of the fcc-hcp phase transition boundary of an Fe-Ni alloy in an internally heated diamond anvil cell. *Phys. Chem. Minerals* **39**, 329-338 (2012).

[26] Ying Liang, Pu Liu, Guowei Yang, Fabrication of one-dimensitional chain of iron-based bimetallic alloying nanoparticles with unique magnetizations. *Cryst. Growth Des.* **14**, 5847-5855 (2014).

[27] Raymond E. Schramm, Richard P. Reed, Stacking fault energies of fcc Fe-Ni alloys by X-ray diffraction line profile analysis. *Metallurgical transactions A* **7**, 359-363 (1976).

[28] R. P. Reed, The spontaneous martensitic transformations in 18% Cr, 8% Ni steels. *Acta Metallurgica* **10**, 865-877 (1962).

[29] Toshio Yonezawa, Ken Suzuki, Suguru Ooki, Atsushi Hashimoto, The effect of chemical composition and heat treatment conditions on stacking fault energy for Fe-Cr-Ni austenitic stainless steel. *Metallurgical and Materials Transactions A* **44**, 5884-5896 (2013).

[30] Jiaxing Liu, Katayun Barmak, Interdiffusion in nanometric Fe/Ni multilayer films. *Journal of Vacuum Science & Technology A* **33**, 021510 (2015).

[31] Jiaxing Liu, Katayun Barmak, Method for measurement of diffusivity: Calorimetric studies of Fe/Ni multilayer thin films. *Scripta Materialia* **104**, 1-4 (2015).

[32] Sho Goto, Hiroaki Kura, Eiji Watanabe, Yasushi Hayashi, Hideto Yanagihara, Yusuke Shimada, Masaki Mizuguchi, Koki Takanashi, Eiji Kita, Synthesis of single-phase $L1_0$-FeNi magnet powder by nitrogen insertion and topotactic extraction. *Scientific Reports* **7**, 13216 (2017).

[33] Y. Sakanaka, E. Watanabe, Y. Hayashi, T. Goto, New Route of the Formation of Ordered FeNi by Electrochemical Nitriding and De-Nitriding Processes. *Journal of the Electrochemical Society* **164**, E525-E528 (2017).

7 Summary

The synthesis of $L1_0$ Fe-Ni is a high-reward high-risk challenge. The reward side of the challenge can be understood based on the intrinsic magnetic properties of the crystal structure, which was introduced in **section 1.1** in **chapter 1**. The magnetic properties of $L1_0$ Fe-Ni indicate the possibility of engineering the system into a rare-earth-free permanent magnet, potentially of no little economic impacts, particularly in the clean energy sector. The risk side of the challenge can be understood based on the thermodynamics and the kinetics of the ordering transformation, which were introduced in **section 1.2 and 1.3** in **chapter 1**, respectively. The kinetics of the ordering transformation is limited by the order-disorder temperature of the crystal structure. The ordering transformation is diffusional by nature, and thus sensitive to the vacancy concentration. However, routinely characterizing vacancy concentration is in-so-far inaccessible for most if not all the research institutions over the world. As long as such a technical barrier remains, the challenge of developing an economical and scalable method to synthesize $L1_0$ Fe-Ni remains a challenge to invent rather than a challenge to optimize. One can always envision a new strategy, but until she or he succeeds for the first time, one can only proceed by trial and error.

In comparison to the vacancy concentration, structural information in the nanoscale — a few to a few tens of nanometers — is more accessible. Structures in such a length scale are not too small to be characterized by the more common characterization methods (e.g., SEM, EBSD, and TEM). Yet, they are not too big to bear significance for the vacancy concentration of the material. Motivated by the significance of the structural information in the nanoscale, this dissertation explores the structure and synthesis relationship of three different synthesis methods

(i.e., electrodeposition, pulsed laser irradiation, and pulsed laser ablation in liquids), with a focus on the nanoscale crystal and defect structures in near-equiatomic Fe-Ni. The main conclusions are summarized in the following.

(1) **Pulsed laser ablation in liquids generated HCP Fe-Ni.** Via SXRD, a far-from-equilibrium crystal structure — HCP Fe-Ni — was identified in near-equiatomic Fe-Ni nanoparticles prepared by ps-PLAL. With HRTEM and NBED, a non-cubic Fe-Ni phase was identified, which could only be either HCP Fe-Ni or $L1_0$ Fe-Ni. Based on the orientation relationship between the non-cubic phase and the cubic phase obtained from the nanoscale characterizations, the non-cubic phase was more likely to be HCP Fe-Ni. As a near-equiatomic far-from-equilibrium crystal structure, the HCP Fe-Ni being identified may provide a larger thermodynamic driving force for the ordering transformation to occur.

(2) **Pulsed laser ablation in liquids generated highly twinned / faulted FCC Fe-Ni.** The local density of the planar defects within a near-equiatomic Fe-Ni nanoparticle with a diameter of ~ 43 nm prepared by ps-PLAL was extracted from atomic-resolution electron micrograph collected with STEM-HAADF imaging. Approximately 24% of the atomic columns within a field of view of ~ 10 nm × 10 nm contributed to the planar defects, while the rest of the atomic columns followed the perfect FCC stacking sequence with respect to their first nearest neighbors. Based on the atomic fraction of the planar defects being extracted experimentally, a direct comparison between the real structure and the structure computed by atomistic simulations (e.g., molecular dynamics) can be quantified. The quantification can

then be used to evaluate the vacancy concentrations derived from the atomistic simulations. A method that combined atomic-resolution characterizations and atomistic simulations can be used to aid the search of synthesis conditions that promote the creation of excess vacancies, which are critical for the acceleration of the ordering transformation kinetics. This dissertation does not include any atomistic simulation results.

(3) **Pulsed laser irradiation promoted the 001 crystallographic texture of FCC Fe-Ni.** In the laser-irradiated sites on the electrodeposited near-equiatomic Fe-Ni film, a correlation between the texture and the laser fluence was found by XRD equipped with the micro-focus optics. While the as-deposited Fe-Ni films had the 111 texture, the 001 texture was developed when an increasingly higher laser fluence was applied. A control over the texture of near-equiatomic Fe-Ni bears significance for the detection of $L1_0$ Fe-Ni by means of coercivity measurements.

(4) **Fast electrodeposition promoted the growth of near-equiatomic BCC Fe-Ni.** In near-equiatomic Fe-Ni thin films (with a thickness of 10 ~ 30 nm) electrodeposited on Au (111) substrates, it was found that the phase fraction ratio of BCC Fe-Ni versus FCC Fe-Ni can be increased by applying a more negative applied potential. Among the deposition conditions being investigated, it was found with EQCM that a more negative potential was correlated with a faster deposition, suggesting a relationship between the phase fraction and the overall deposition rate. The compositions of the films with different phase fractions were similar and close to 40 at.% Ni, suggesting that the formation of the near-equiatomic BCC Fe-Ni was

promoted by the deposition kinetics rather than the composition thermodynamics. A control over the phase fraction of near-equiatomic Fe-Ni may be used to vary the thermodynamic driving force, which could bear significance for the ordering kinetics towards $L1_0$ Fe-Ni.

(5) **Pulsed and static modes of electrodeposition generated opposite composition gradients.** In Fe-Ni films (with a thickness of 30 nm ~ 500 nm) deposited under the constant potential mode, a through-thickness composition gradient with increasing Ni fraction was observed. Under the pulse-reverse potential mode, a through-thickness composition gradient with decreasing Ni fraction was observed, suggesting that the composition control over the Fe-Ni films can be optimized by tuning the parameters of the pulse-reverse cycles.

(6) **Near-diffusion-limit electrodeposition may encounter morphological instability.** Near-equiatomic Fe-Ni films were electrodeposited in conditions close to the diffusion limit, resulting in a breakdown of the planar growth front, which was observed ex-situ both by AFM in a field of view on the order of 500 nm and by SWLI in a field of view on the order of 5 mm. The PSD analysis that characterizes the growth front topography shows at least two critical wavenumbers. While the highest critical wavenumber is comparable to the characteristic wavenumber related to the grain size, the second highest critical wavenumber is comparable to the critical wavenumber estimated based on the morphological instability theory.